Direct Bonding of Wafers on Non-Planar Optical Substrates and Bonding Energy Measurement via the Novel κ-Method

Dissertation

zur Erlangung des akademischen Grades
doctor rerum naturalium (Dr. rer. nat.)

vorgelegt dem Rat der Physikalisch-Astronomischen-Fakultät
der Friedrich-Schiller-Universtät Jena

von Pascal BIRCKIGT, M. Sc.,
geboren am 10. Juni 1992 in Bremen

Abstract

In this thesis, the novel concept of direct bonding of wafers on non-planar substrates – in particular, convex cylindrical and convex spherical substrates – is explored, challenging the paradigm that direct bonding requires both surfaces to be highly planar. The motivation stems from the desire to combine advanced diffractive optical elements (DOEs) – which can lithographically only be written into planar substrates – with optical lenses in order to obtain new optical functionalities. As part of this effort, mathematical models to predict complete area stable contacting success are developed and the mechanical stressed bonding interface is investigated through time-resolved contact front propagation experiments. Also, a novel, highly accurate method for measuring the bonding energy in non-planar interfaces is introduced. It was found that direct bonding success can be predicted for a large range of use cases as a function of the wafer's and the substrate's geometry. Also, it was discovered that the bonding energy of a mechanically stressed interface stabilizes at a consistent level regardless of the surface waviness. A reaction kinetics model for explaining this phenomenon has been proposed. A demonstrator combining an optical lens and a DOE is manufactured to showcase the potential of direct bonding of wafers on non-planar substrates for the field of advanced optics.

Kurzzusammenfassung

Diese Arbeit befasst sich mit dem neuartigen Konzept des direkten Fügens von Wafern auf nicht-planare – insbesondere konvexe zylindrische und konvexe sphärische – Substrate. Es wird das Paradigma in Frage gestellt, dass das direkte Fügen eine hohe Planarität beider Oberflächen erfordere. Motiviert wird diese Arbeit durch die Idee, fortschrittliche diffraktive optische Elemente (DOEs) – die lithografisch nur in planare Substrate eingeschrieben werden können – mit optischen Linsen zu kombinieren, um neue optische Funktionalitäten zu erhalten. Es wurden mathematische Modelle zur Vorhersage einer vollflächigen, stabilen Fügeverbindung entwickelt und mechanisch vorgespannte Grenzflächen durch zeitaufgelöste Kontaktfrontausbreitungsexperimente untersucht. Zudem wurde eine neuartige, sehr genaue Methode zur Messung der Fügeenergie nicht-planarer Grenzflächen eingeführt. Es wurde herausgefunden, dass für eine Vielzahl von Anwendungsfällen vorhergesagt werden kann, ob Fügen als Funktion von Wafer- und Substrat-Geometrie möglich ist. Außerdem, dass sich die Fügeenergie mechanisch vorgespannter Grenzflächen auf dem gleichen Niveau stabilisiert – unabhängig von der Oberflächenwelligkeit. Zur Erklärung dieses Phänomens wurde ein reaktionskinetisches Modell vorgestellt. Ein Demonstrator, der eine optische Linse mit einem DOE kombiniert, wurde hergestellt, um das Potential des direkten Fügens von Wafern auf nicht-planare Substrate für die moderne Optik aufzuzeigen.

Contents

Nomenclature

For each entry, the page of its first appearance is given.

Abbreviations

4PT   four-point flexural test, see p.

AFM   atomic force microscopy, see p.

CMP   chemical mechanical polishing, see p.

DCB   double cantilever beam, see p.

DIW   de-ionized water, see p.

DOE   diffractive optical element, see p.

FEM   finite element method, see p.

HSFR   high spatial frequency range, see p.

LSFR   low spatial frequency range, see p.

MSFR   mid spatial frequency range, see p.

PAB   plasma-activated bonding, see p.

PSD   power spectral density, see p.

PV   peak-to-valley, see p.

RT   room temperature, see p.

WLI   white light interferometry, see p.

Latin Symbols

a gap opening length when applying the DCB-method, see p.

A_c contacted surface area, see p.

B extensional rigidity, see p.

C_J molar concentration of a substance J, see p.

D flexural rigidity, see p.

Greek Symbols

1 Introduction

1.1 Motivation

In the field of optics and opto-mechanics, much research is focused on reducing the size and weight of optical instruments [1, Chap. 1.1]. This can be achieved by combining several optical functionalities into a single component. For example, modern imaging spectrometers rely on curved mirrors inscribed with a diffraction grating to combine reflective and diffractive properties.

The technological capabilities to inscribe a diffraction grating, or more generally, a diffractive optical element (DOE) in the surface of non-planar optical substrates, such as curved mirrors or lenses, are still limited as compared to that on planar substrates, such as wafers. In fact, non-planar DOEs, which must operate efficiently over a wide range of wavelengths, are a critical technology in the case of many applications. These applications are imaging spectrometers [2–4], extreme ultraviolet lithography optics [5–7], illumination systems [8] and anamorphic imaging systems [9], to name but a few.

The combination of advanced DOEs with non-planar optical substrates is expected to help create smaller and more light-weight optical systems, reduce stray light, improve optical correction methods and enable new optical functionalities. In other words, it would be a significant extension to the classical applications.

Currently, the manufacture of a number of advanced DOEs is only well established for surfaces of planar substrates, in particular, glass and semiconductor wafers. For surfaces on non-planar substrates, such as curved mirrors or lenses, manufacture is still challenging. The approach proposed here to address this challenge is to use direct bonding to combine a thin, initially planar wafer, into whose surface a DOE has been inscribed, with a non-planar optical substrate. Direct bonding is a bonding technique that can achieve unique interface properties such as very low reflectance, long term stability, no outgassing and high bonding strength.

In the following, direct bonding of wafers on non-planar substrates with height deviations *larger* than the wafer's thickness is referred to as *non-planar direct bonding*. To the best of the author's knowledge, no research has yet addressed the issue of predicting non-planar direct bonding success in that sense. In this thesis, non-planar direct bonding is investigated, with particular focus on convex cylindrical and spherical lenses, which are the most important geometries.

1.2 Exemplary Possible Applications

There are recent advanced optical applications where a combination of a DOE with a non-planar optical substrate via direct bonding could be beneficial. Two examples are presented in the following.

1.2.1 Imaging Spectrometers

Spectrometry is the key analytical method to study material composition and related processes. Measurement is performed remotely, that is, without physical contact [3]. Imaging spectrometers provide additional spatial information about features that lie in the instrument's field of view. Space-based imaging spectrometers on satellites have been in use since the early 1980s [3, 10]. In this context, the most important designs are the DYSON spectrometer and the OFFNER spectrometers [11–13]. They were both originally developed for microlithography [14–16]. Their advantages are simplicity, low imaging errors and high spatial resolution [17].

The basic OFFNER design has two concave mirrors and a convex (usually large curvature), reflective grating in the center [4, 18]. Here, the optical axis is vertical to the object and image planes. It has a better spectral resolution in a relatively compact form and a high range of angles over which the system can accept light, as required for remote sensing [19, 20]. In the basic DYSON design, the object and image planes are located at the center of curvature of a concave, reflective diffraction grating. That curvature is usually small. Furthermore, a thick plano-convex lens can be used to compensate for imaging errors [21]. An advantage is the near-normal angle of incidence which reduces polarization sensitivity.
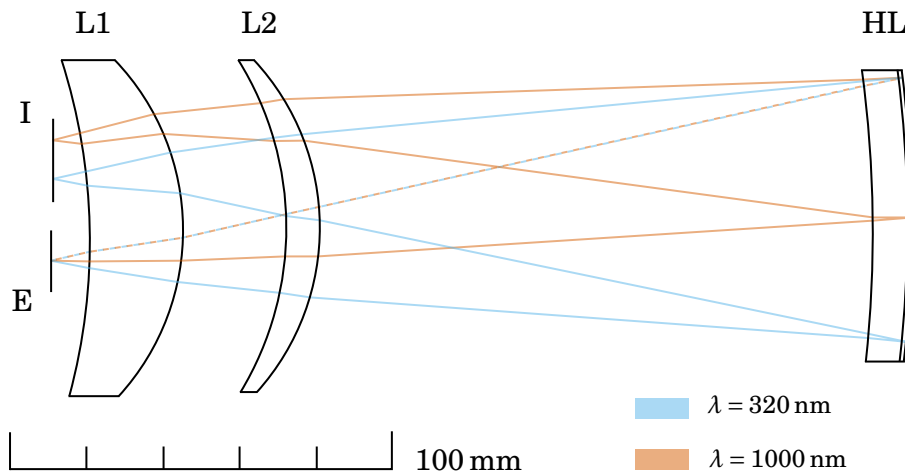
Figure 1.1: Schematic layout of the proposed DYSON spectrometer optical design by WU et al. [22]. The design consists of concavo-convex spherical lenses (L1, L2), the image plane (I), the entrance slit (E), and the hybrid lens (HL), that is, a combination of an optical lens and a diffraction grating. Here, λ is the wavelength of the light .

The combination of more advanced diffraction gratings with these curved mirrors is considered crucial for future missions [23–25]. Wu et al. [22] have proposed a novel Dyson spectrometer design to address two important requirements of space-based imaging spectrometers, namely small assembly space and large field of view. A concavo-convex lens with a diffraction grating and a reflective coating on the convex side is used, with a curvature radius of 200 mm and a diameter of 74 mm. The light is transmitted from the concave side so that both diffractive and refractive properties are in effect. The proposed optical design is shown in Fig. 1.1. The diffraction grating was made by diamond turning. In the current version, its diffraction efficiency does not yet meet typical remote imaging requirements.

A conceivable solution for meeting those requirements is to use advanced lithography technology to inscribe a diffraction grating into the surface of a planar substrate, such as a wafer. Then, that wafer would be directly bonded on the convex surface of an optical lens.

1.2.2   Manufacture Tool for Fiber and Volume Bragg Gratings

A fiber Bragg grating (FBG) is an optical fiber waveguide in which guidance is created by a periodic variation of the refractive index in the fiber core. It is commonly manufactured via ultraviolet light illumination [26]. FBGs have enabled compact fiber lasers. In this context, they are used for integrated cavity mirrors, distributed sensor systems and strong narrow band filters for quantum applications, to name but a few [27–29]. In contrast, a volume Bragg grating (VBG)is a periodic variation of the refractive index through the volume of a bulk material. VBGs show a unique set of properties which enable narrow band stabilization of high power laser diodes, highly efficient spectral beam combination and highly compact chirped pulse amplification (CPA) compressor systems [30–32].

FBGs and VBGs are two very popular commercial devices. Their manufacture process relies on ultraviolet light illumination of photo-sensitive materials. The application range is limited when it comes to other spectral ranges (in particular, beyond 2.5 µm) or high power laser applications [33, 34]. Ultrashort laser pulses can be a helpful tool for overcoming these limitations. There are different approaches for the manufacture via ultrashort laser pulses. A very powerful one is the phase mask inscription technique [26]. Here, the interference pattern of a phase mask is imprinted into the material of the target device via a cylindrical lens. Mainly chromatic aberrations are a limiting factor. Thus, there is room for optimization.
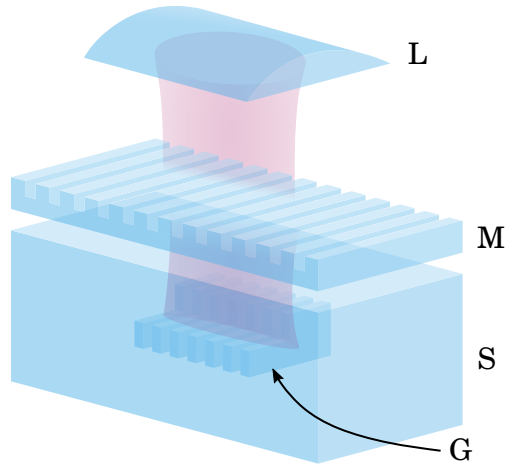
Figure 1.2: Schematic illustration of the VBG inscription tool which applies the multilayer scanning phase-mask technique by TALBOT et al. [35]. It makes use of a cylindrical lens (L). A laser pulse is focused trough a phase mask (M) into a bulk glass sample (S) into which the BRAGG grating (G) is inscribed.

1.3 Non-Planar Structured Optical Surfaces

The motivation of this thesis is to help realize diffractive optical elements (DOEs) on non-planar optical substrates which surpass the technological state of art via direct bonding. There are alternative approaches to realize DOEs on non-planar substrates. The most relevant ones are presented in the following.

Diffraction gratings on non-planar surfaces have first been described and manufactured in the 1880s [36, 37]. Since the second half of the last century, concave and convex gratings have been industrially produced by holographic illumination [38] or mechanical ruling [39] to create a sinusoidal or blazed profile, respectively, where both transmission and reflection setups are used [40, 41]. A transmission setup can be used, for example, to reduce chromatic aberration in optical systems [9, 42]. A recent example for a reflection setup is a convex blazed grating for high throughput OFFNER type spectrometers [43] which is manufactured by applying an elastic grating replica onto the non-planar substrate and finally transferring it by reactive ion etching.

Similarly advanced gratings have been produced by diamond turning on a metallic mirror. This technique is applicable for line densities up to 500 lines per millimeter [44]. Is has been used for extreme ultraviolet lithography applications [5] and space based imaging spectrometer applications [44]. More general DOEs on non-planar substrates have also been realized by mounting the inscription tool on a multi-axis table [45]. The resulting spatial resolution is insufficient for some applications.

Since the 2010s, other approaches have been pursued for a variety of applications. For example, miniature compound eye imaging devices have been realized by placing micro lens arrays on a stretchable circuit board [46, 47], or by inscribing micro lens arrays directly into a non-planar rigid substrate [48]. While these designs provide a large field of view, they have poor spatial resolution. Another approach is the stacking of wedged optical elements [49], but the resulting surface geometry has unfavorable discontinuities.

More recent approaches use the principle of inscribing a DOE in an initially planar membrane, which is then placed on a mold and pressed into it by a correspondingly shaped non-planar flexible stamp. Finally, permanent bonding is achieved by adhesive bonding, high temperature direct bonding, or anodic bonding [50–52]. This approach has two major drawbacks. First, it introduces adhesives, heat or voltage. This prohibits the use of mechanically or chemically sensitive DOEs and may adversely modify the bonding interface. Second, the pressing step introduces significant residual stresses and in-plane grating deformations.

1.4   Research Questions

Modern optical instruments benefit from reduced weight and assembly space. A combination of advanced diffractive optical elements (DOEs) with non-planar optical substrates would significantly expand the possibilities of classical applications. The process chain of direct bonding, in particular of plasma-activated bonding which is a low-temperature direct bonding technique, is established only for planar substrates, in particular glass and semiconductor wafers. Also, there is no method that allows to measure the bonding energy of a non-planar interface. A current direct bonding research topic is the prediction of complete area stable contacting success based on wafer surface topography data. It is suggested that if a wafer allows sufficient elastic deformation, the planarity requirement can be relaxed. Direct bonding of a thin, initially planar wafer, in which a DOE is inscribed, to a non-planar optical substrate is proposed to address the challenge of the manufacture of optical components required to surpass state-of-the-art technology.

The key research questions are outlined in the following.

1. How can direct bonding of an initial planar wafer to a convex cylindrical (and more generally acylindrical) lens substrate and to a spherical lens substrate be modeled as a function of wafer and substrate geometry?
2. How can the bonding energy of a non-planar interface be accurately measured?
3. How does wafer surface quality, which is known to be strongly correlated with wafer thickness due to manufacture limitations, affect glass interface properties?

4. What are the physics or chemical mechanisms at a bonded glass interface subjected to a significant amount of residual stress stored in the deflected wafer?

The boundary conditions for the experimental approach are the availability of a direct bonding process suitable for temperature sensitive DOEs and, because of its relevance to optics, the investigation of glass-to-glass direct bonding. The research focuses on cylindrical and spherical lens substrates because these are the most important optical geometries. Finally, the process must be suitable for transmissive applications. Therefore, it is reasonable to study primarily convex and not concave substrate geometries.

From a practical point of view, the goal is to find a workable theory for the principle manufacture of novel hybrid lenses that combine advanced DOEs and non-planar optical lens substrates.

1.5 Thesis Structure

This thesis consists of nine more sections.

In Sec. 2, direct bonding is introduced in detail, with particular emphasis on recent findings with regard to the surface physics mechanisms and the mechanical aspects. Note that direct bonding on *planar* substrates is considered as the state-of-the-art technology.

In Sec. 3, mathematical models are derived to predict the success of direct bonding of wafers on *non-planar* substrates. Two substrate geometries are considered, namely, cylindrical (and more generally, acylindrical) and spherical substrates. The general procedure for the direct bonding experiments is then presented in Sec. 4.

In the following, this thesis covers three main topics. First, the development of a novel method for determining the bonding energy (κ-method), see Sec. 5, second, the investigation of the direct bonding mechanism, see Sec. 6, and third, the investigation of direct bonding of wafers on spherical substrates, see Sec. 7.

An overview and assessment of the practical application of the obtained results for non-planar direct bonding is given in Sec. 8, where also the manufacture of a combination of an optical lens and a DOE is demonstrated.

The conclusion of this thesis is given in Sec. 9. Finally, the acknowledgment is stated in Sec. 10.

2 Theoretical Foundations

In this section, common glass bonding technologies are introduced and it is shown that direct bonding is best suited to meet the requirements for advanced optical instruments. Then, the theoretical foundations of direct bonding of planar surfaces are presented. In particular, the surface physics mechanisms and mechanical aspects are discussed.

2.1 Comparison of Bonding Techniques

The manufacture process to permanently bring together two workpieces where adhesion is created locally and increased in the whole is referred to as *bonding* [53]. The resulting workpiece has a permanently joined interface. In the following, bonding techniques for optical materials, such as oxide glasses or crystalline Si, are presented.

2.1.1 Adhesive Bonding

Adhesive bonding uses an organic solution as initially liquid and finally solid intermediate layer (that is, the adhesive) in order to hold two surfaces together. The conversion from a liquid to a solid state, which is referred to as curing, can be realized for example via annealing or radiation. The bonding strength is high.

> ***Advantages:*** Irregularly shaped surfaces can be bonded with ease and at relatively low cost. The adhesive material, which is usually relatively soft, can help distribute stress more evenly and damps mechanical oscillations. This makes the bonded workpiece mechanically very resilient.

> ***Disdvantages:*** The bonded workpiece has an operating temperature range that is limited, it lacks chemical and thermal resistance and it has a limited long-term stability [54]. Also, misalignment may occur during the adhesive's curing due to anisotropic [55]. In the case of transmissive optical applications, an adaption of the adhesive's refractive index is important. In the case of opto-mechanical resonators, mechanical oscillation damping is undesired, cf. Ref. [56, 57].

2.1.2 Silicate Bonding

Silicate bonding, also known as hydroxide-catalysis bonding, uses an inorganic aqueous SiO_2 solution to build a molecular network of covalent bonds between the surfaces of the workpieces to be bonded. Curing is accomplished over time or by annealing. It

has been developed for the purpose of joining fused silica workpieces for space-based optical systems [58–61].

Advantages: Silicate bonding yields a high bonding strength, long-term stability, thermal cycling resistance [62] and precise alignment.

Disdvantages: Surfaces of workpieces with rigid geometries, for example, large prisms, must have a surface planarity with PV value below 200 nm in order to achieve a homogeneous void-free bonding interface [58, 61]. Refractive index adaption is challenging and reflectances are around 10^{-3} [63]. In high power laser applications, damage at the bonding interface may occur [64]. Because water migration out of the edges is required while curing [65], the bondable area is limited.

2.1.3   Laser Welding

Laser welding employs the heat generated by focused, ultra-short laser pulses directed onto the surface to be bonded [54], creating localized melting and solidification of the material. Each heat affected zone has an extent of a few 10 µm. A lot of oxide glasses (such as fused silica, CORNING ULE® or SCHOTT borofloat®) can be bonded.

Advantages: The bonded workpiece has a high bonding strength.

Disdvantages: Local optical distortions are generated [66] which comes with the generation of mechanical stress fields and consequently refractive index variations.

2.1.4   Optical Contact Bonding

Optical contact bonding is a process in which two closely conformal surfaces are joined together without any intermediate layer, being held together solely by intermolecular forces. Since the 19$^{\text{th}}$ century, optical contact bonding has been used to manufacture optical components for transmissive applications such as prism pairs [67, 68].

Advantages: The reflectance at the interface is as small as 10^{-5} because there is no optically undesirable space between the workpieces [69]. Other advantages are precise alignment, no out-gassing and chemical resistance [70, Chap. 1.2].

Disdvantages: Bonded workpieces have a relatively low bonding strength and high requirements on the surfaces' smoothness, planarity and cleanliness [67, 69, 71], because an interface separation smaller than 10 nm is required [72].

2.1.5   Direct Bonding

Direct bonding refers to any type of optical contact bonding with additional surface treatment steps *before* the contacting and an annealing step *after* the contacting. Research has most extensively been conducted on samples in wafer geometry, that is,

circular slices in a range below around 1 mm in thickness, typically with diameters between 100 and 200 mm made of materials which are used as a substrate for the manufacture of electronic devices [70, Chap. 1].

Advantages: Both the interface reflectance [73] and the bonding strength [74, Chap. 1.3] is distinctly enhanced as compared to optical contact bonding. Besides precise alignment, no out-gassing and chemical resistance, the interface ensures long-term stability.

Disdvantages: Similar to optical contact bonding, there are high requirements on the surfaces' smoothness, planarity and cleanliness.

If a workpiece has a non-rigid geometry (for example, wafers), surface planarity requirements are a few 10 μm because such geometries allow for sufficient elastic deformation [75, Chap. 6]. For workpieces with rigid geometries (for example, large prisms), a surface planarity with a peak-to-valley value of several 10 nm is required [76].

In view of the advantages explained above, direct bonding is of particular interest for the manufacture of optics and opto-mechanical instruments. Particularly for temperature-sensitive workpieces, plasma-activated bonding (PAB) has been developed, which is a low temperature direct bonding technique. It will be introduced in detail later in Sec. 2.4. The application of PAB has become important for the manufacture of optical instruments [73, 77–80]. This thesis will therefore focus on direct bonding, in particular, PAB.

2.2   Intermolecular Forces between Surfaces

Whenever direct bonding is applied to join optical glasses, the surfaces to be contacted are required to be highly smooth, planar and clean. If these requirements are met, there are different types of chemical bonds governing the intermolecular forces between the contacted surfaces. They are presented in the following.

2.2.1   VAN DER WAALS Bonds

VAN DER WAALS bonds are created by induced dipole moments between atoms or molecules. The potential energy per molecule is very weak (several meV), and its interaction potential, V, operates over long distances, r, taking on the form $V = -C/r^6$, where C is a constant [81, Chap. 6]. From this, it can be calculated that the interaction potential per unit area between two planar surfaces of macroscopic bodies with a homogeneous atom density, ϱ, exhibits a quadratic decay [81, Chap. 11].

The work of separation, W_{sep}, is defined as the energy per unit area needed to separate two planar surfaces from contact distance, $r = r_0$, to infinity, $r = \infty$, see Ref. [82, Chap. 2]. It can be shown that

$$W_{\text{sep}} = \frac{A_{\text{H}}}{12\pi r_0^2}. \tag{1}$$

Here, $A_{\text{H}} = \pi^2 C \varrho^2$ is the HAMAKER constant. The contact distance, r_0, is defined phenomenologically as a cut-off value which considers the center-to-center distance between the molecules, where typically $r_0 = 0.165\,\text{nm}$ is assumed [81, Chap. 11.10].

A numerical value for the HAMAKER constant is required to calculate the work of separation using Eq. (1). By incorporating the influence of neighboring atoms, the HAMAKER constant is a function of temperature and complex permittivities of the considered material [83]. For example, for fused silica (that is, synthetic amorphous SiO_2 of high purity), which has a relatively simple molecular structure, a typical value is $A_{\text{H}} = 65 \times 10^{-21}\,\text{mJ}$ at room temperature (RT) [84, 85]. Substituting this value into Eq. (1) yields a work of separation of $64\,\text{mJ}\,\text{m}^{-2}$. Experiments obtained at RT find values ranging from 24 to $72\,\text{mJ}\,\text{m}^{-2}$ [86, 87]. This is consistent.

If water is assumed to be present as medium between the two fused silica surfaces, typical values for the HAMAKER constant range from 4.6 to $8.3 \times 10^{-21}\,\text{mJ}$ at RT [84, 88, 89], yielding a very small work of separation ranging from 4.2 to $8.2\,\text{mJ}\,\text{m}^{-2}$. Experimental values are much higher. Therefore, VAN DER WAALS bonds are not able to fully explain the surfaces' attraction in the case of aqueous conditions.

2.2.2   Hydrogen Bonds

In the case of aqueous conditions, for example when experiments are conducted in humid air, the work of separation is governed by the prevalence of molecules that form hydrogen bonds [86]. On an untreated fused silica's surface there are hydroxy groups (that is, –OH) adsorbed on the surface. At RT, their estimated areal density ranges from 3.4 to $4.8\,\text{nm}^{-2}$ [90–92]. They act as primary sites to form bonds with water molecules or other hydroxy groups [93, 94]. Measured values of the potential energy of such type of hydrogen bonds range from 0.22 to $0.25\,\text{eV}$ per molecule [92, 95]. This yields a work of separation ranging from 120 to $192\,\text{mJ}\,\text{m}^{-2}$. Experiments find values ranging from 142 to $167\,\text{mJ}\,\text{m}^{-2}$ [69, 96, 97]. This is consistent.

Thus, a combination of hydrogen bonds and VAN DER WAALS bonds cause two polished planar surfaces to spontaneously stick together, see Ref. [97]. This phenomenon relates to optical contact bonding, which has been introduced in Sec. 2.1.4.

Table I: Measured values of the work of separation, W_{sep}, of selected materials. Here, W_{sep} has partly been calculated according to Ref. [98] from fracture toughness data.

material	$W_{\mathrm{sep}}/\mathrm{J\,m}^{-2}$	Refs.
Si	4.3 to 5.7	[99, 100]
fused silica	6.8 to 8.2	[101–104]
borofloat	10.6 to 11.6	[105, 106]
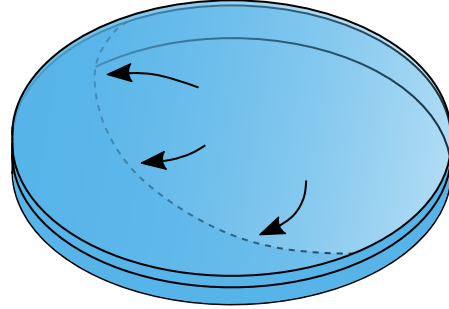
Figure 2.1: Propagation direction (arrows) of the contact front (dashed line), as typically observed during the direct bonding contacting process.

2.2.3   Covalent Bonds

Covalent bonds involve the sharing of electrons to form electron pairs between atoms or molecules [107, Chap. 1]. The potential energy per molecule is high, typically several eV. The corresponding work of separation can be determined by fracture experiments. Table I lists measured work of separation values of selected optical materials. Here, the material SCHOTT Borofloat® 33, in the following referred to as borofloat, is a commonly used versatile industrial oxide glass.

While optical contact bonding makes use of weak adhesion due to hydrogen bonds or VAN DER WAALS bonds, direct bonding aims for the creation of covalent bonds at the contacted interface in order to increase the work of separation. This can be done, among other process steps, via annealing.

2.2.4   Distinction between Adherence and Adhesion

Surface separation requires a sufficiently large external force. This is equivalent to saying that in order for the interface's contact front to continue propagating (such that the separated surface area increases), the amount of change in accumulated elastic strain energy, $\mathrm{d}U_E$, must exceed the amount of change in work required for surface separation, $W_{\mathrm{sep}}\,\mathrm{d}A_c$. Here, A_c is the contacted surface area. The quantity $G := \mathrm{d}U_E/\mathrm{d}A_c$ is referred to as strain energy release rate, a term well known from fracture mechanics. The work of separation, W_{sep}, which has already been introduced in Sec. 2.2.1, is in this context also referred to as *critical* strain energy release rate, G_c. In the context of direct bonding, it is also referred to as *bonding energy*. As such, the criterion for the surfaces to *not* separate is

$$G_c \geq G := \frac{\mathrm{d}U_E}{\mathrm{d}A_c} \qquad (2)$$

which is applicable under the assumption that the workpieces deform elastically and that the interaction potential rapidly decreases with increasing contact distance.

In this context, the term *adherence* is introduced as the resistance to surface separation due to an external force. It is quantified by the work of separation, that is, bonding energy, see Eq. (2). In contrast, the term *adhesion* refers to the strength of chemical bonds during the contacting process [108, 109], that is, during surface closure where the contact front often propagates by itself, see Fig. 2.1. It is quantified by the work of adhesion, W_{adh}. The contact front between two partly contacted surfaces will continue advancing and pull the surfaces together if $W_{\text{adh}} > \text{d}U_E/\text{d}A_c$ [110].

For direct bonding, it has been shown that W_{sep} differs from W_{adh}. There is a hysteresis between surface closure and surface separation [111, 112]. The surface closure process is driven by short-range intermolecular forces such as weak hydrogen- and VAN-DER-WAALS-bonds where a thin air film has to be pushed away [113, 114] and the inhomogeneous H_2O layer distribution needs to rearrange according to the local surface waviness and roughness [115], and also, after contacting, some chemical reactions already occur at RT [116].

In direct bonding literature, often the surface energy (with the symbol γ) is used for bonding strength quantification, being defined as twice as the work of separation. Strictly, this is only possible for reversible fracture of virgin monolithic solids [117]. For direct bonding of optical glasses, surface separation involves chemical reactions, as stated above. To be unambiguous, G_c will be used for bonding strength quantification.

2.2.5 Measurement of the Bonding Energy

Bonding energy measurements are essentially fracture tests [111]. Therefore, their results depend on the loading geometry which correspond to different fracture modes. A tensile stress being applied normal to the plane of the crack corresponds to "mode I", a shear stress being applied parallel to the plane of the crack corresponds to "mode II" and out-of-plane tearing corresponds to "mode III", see Fig. 2.2. As such, the critical
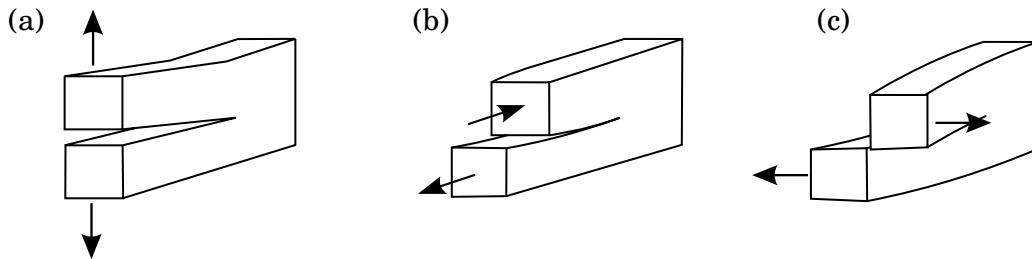
Figure 2.2: Schematic depiction of the three independent fracture modes, where (a) shows the opening mode, (b) shows the in-plane shearing mode and (c) shows the out-of-plane shearing mode.

strain energy release rate can be split according to

$$G_c = G_{Ic} + G_{IIc} + G_{IIIc}. \tag{3}$$

For direct bonding of workpieces in wafer geometry, the measurement of the bonding energy, G_c, is most commonly conducted using the double cantilever beam (DCB) method, also referred to as razor blade method. It has been introduced by MASZARA et al. [118, 119]. Here, two planar, thin and rectangular wafer beams are directly bonded, and then, a razor blade (with a certain thickness, w) is inserted in between of these beams [120]. Figure 2.3 shows a schematic of the DCB-method. As an alternative to the razor blade, a steel foil can be used. Then, the length of the resulting gap, a, is measured, and the bonding energy, G_c, is calculated from a. If both wafer beams have the same stiffness, the DCB-method corresponds to pure mode I. It can be shown that G_c is proportional to a^{-4} [119]. The quartic proportionality makes G_c very sensitive to a. In other words, any measurement error in a leads to an even larger calculated measurement error in G_c. This is a major disadvantage of the DCB-method.

Another example for a bonding energy measurement method is the end-notched flexural test, which is described in the ASTM 7905 standard [121]. Here, a bonded specimen is prepared with an end-notch, that is, an already separated part at one of the edges. Then, by conducting a common three-point flexural test, the end-notch length, a, increases with increasing load, P. From the load-displacement curve, the bonding energy is calculated. The end-notched flexural test corresponds to pure mode II. Therefore, the resulting bonding energy is *not* comparable with that of the DCB-method.

Another method for a bonding energy measurement method is the four-point flexural test (4PT) method [122]. It has recently been adapted for direct bonding by TABATA
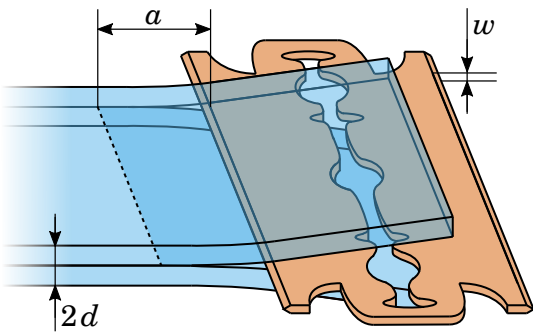
Figure 2.3: Schematic of the commonly known DCB-method, where both wafer beams have the same thickness, d. The contact front is drawn as a dashed line. Here, by reading the gap opening length, a, the bonding energy can be directly calculated in a closed-form formula.
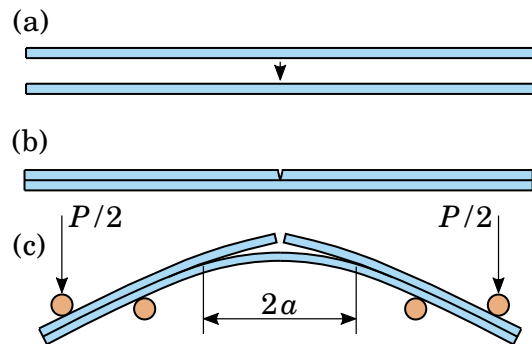
Figure 2.4: Schematic of the 4PT-method. Here, (a) a wafer pair is directly bonded in a planar way, (b) then a cut through the upper wafer beam is prepared, and finally (c) the sample pair is bent in a four-point flexural test setup such that the separated area increases.

et al. [123]. Here, a bonded wafer beam pair is prepared with a centered cut through the top wafer beam. It is then placed in a conventional four-point flexural test setup where the upper wafer beam begins to separate, see Figs. 2.4 (a) to (c). As in the previous method, the load-displacement curve is recorded. However, the loading geometry corresponds to mixed mode I and II [124]. Mode I stems from a bending moment, mode II stems from a shear stress. The shearing is introduced due to the fact that the contacting step takes place in a planar way, see (a), and *afterwards* the wafer beam pair is bent such that the upper wafer beam is stretched while the lower one is compressed (that is, squeezed), see (c). It is possible to explicitly calculate the share of mode I bonding energy in the total bonding energy. The result is $G_{Ic}/G_c = 4/7$ [125]. As such, the 4PT-method allows to calculate a value for the bonding energy corresponding to mode I only. This allows a comparison with measurements from the DCB-method.

The disadvantage of the previous two methods is the need of a high-resolution compression test machine with a specialized three-point or four-point test setup.

2.3 Surface Topography

Direct bonding requires highly smooth and planar surfaces. Real surfaces are never perfectly planar or perfectly smooth. This is due to manufacture limitations. Therefore, it is useful to take a look at how to describe the topography of a surface. Deviations from a perfect surface can be separated into roughness, waviness and shape variations [126] which are discussed in the following.

2.3.1 Roughness and Waviness

Roughness refers to local deviations in the high spatial frequency range (HSFR), which manifest as grooves, cracks or the crystalline structure. If these deviations are large, the surface is considered as rough, if they are small, the surface is considered as smooth. Only for smooth surfaces or for elastically soft materials, spontaneous adhesion can be observed for macroscopic solid workpieces [127]. This is why direct bonding requires smooth surfaces. The roughness can be quantified, for example, as root mean square value of the ordinate values, $z(x, y)$, within a definition area, $\mathscr{A}$, [128]

$$S_q := \sqrt{\frac{1}{A} \iint_{\mathscr{A}} z(x, y)^2 \, \mathrm{d}x \, \mathrm{d}y}. \tag{4}$$

Waviness refers to local deviations in the mid spatial frequency range (MSFR), which extend over up to several tenths of millimeters and can occur during the surface polishing step due to machine deflections or vibrations [126]. Waviness is often quantified by the S_q-value according to Eq. (4), too.
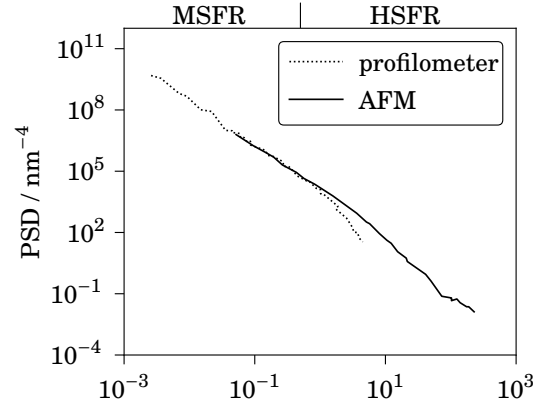
Figure 2.5: A typical measured PSD-function of a polished fused silica surface. The *x*-axis shows the spatial frequency in μm^{-1}. Data in the MSFR, that is, the waviness, was obtained by a profilometer. Data in the HSFR, that is, the roughness, by AFM. Note that both curves overlap. Taken from Ref. [129].

If the capability of different surface profile measurement instruments with regard to their measuring area and resolution is considered, it is found that S_q-values of the same surface differs for different measurement instruments [129]. For example, the S_q-value of a surface characterized by white light interferometry (WLI) at a one square millimeter test area differs from that characterized by atomic force microscopy (AFM) at a one square micrometer test area. Therefore, it is important to measure a surface's roughness and waviness over different spatial frequency ranges.

A way to combine the roughness and waviness data into a single diagram is the calculation of the combined power-spectral-density (PSD) function. A PSD-function gives the surface's power spectrum, that is, the FOURIER transform of the areal profile, $z(x, y)$, squared, as a function of the spatial frequency [130, Chap. 3]. The area beneath the curve (evaluated within a given spatial frequency range) is equal to the S_q-value in that range. Figure 2.5 shows a typical measured PSD-function of a polished fused silica surface. PSD-functions of real surfaces often show power-law behavior over many orders of magnitude [131, 132], thus, on a log-log scale, they appear as a straight line, indicating that the surface is self-affine. An example is shown in Fig. 2.5. The absolute value of the slope is also referred to as the surface's fractal dimension, ζ [133].

2.3.2 Shape Variations

Shape variations refer to deviations in the low spatial frequency range (LSFR), which may extent over the complete surface, such as roundness and cylindricity. A convenient method to describe shape variations is to approximate the ordinate values, $z(x, y)$, by a polynomial. In the field of optics, the ZERNIKE polynomials have become established because they represent typical optical imaging errors [134, 135]. An alternative, more simple description is the peak-to-valley (PV) value which is defined as $\max(z) - \min(z)$. If the shape variations are sufficiently small, the surface is considered as planar.

2.4   Application of Direct Bonding

Direct bonding enables high strength bonding of two workpieces without introducing any intermediate layer. Its technical development history with an overview of typical process steps is outlined in the following.

2.4.1   Technical Development History

To employ direct bonding, hydrophobic and hydrophilic techniques have been developed since the 1980s. The terms hydro*phobic* and *-philic* refer to surfaces *repelling* and *adsorbing* water molecules, respectively [81, Chap. 8]. An untreated fused silica surface at RT, which is characterized by its adsorbed hydroxy groups, is an example for a hydrophilic surface [81, Chap. 8], as pointed out in Sec. 2.2.2.

Hydrophobic direct bonding has been developed to join two oxide-free Si wafer surfaces typically at annealing temperatures above 700 °C [136]. The development of lower temperature hydrophobic direct bonding techniques that still result in high bonding strengths turned out to be challenging. By using foreign atom implantation techniques [137], direct bonding at temperatures below 400 °C has been reported.

In contrast, hydrophilic direct bonding has originally been developed to join a chemically untreated Si wafer surface with a thermally oxidized Si wafer surface at annealing temperatures above 700 °C [138]. Due to more temperature sensitive parts in the fields of microelectronics, three-dimensional device integration, microelectromechanical systems [139, 140], microfluidics [141], and optical, opto-mechanical and photonics applications [76, 142–145], a particular progress has been made with regard to low-temperature hydrophilic direct bonding techniques. In this context, the term *low-temperature* refers to annealing temperatures below 450 °C [146]. (For higher temperatures, the term *fusion bonding* has become established [147].) Since the 2010s, low-temperature hydrophilic direct bonding has increasingly been adapted to various substrate materials other than Si, for example, Ge, Ti, fused silica, cf. Ref. [118], other optical glasses [64, 148] and laser crystals [149, 150].

2.4.2   Process Steps

In the following, only *hydrophilic* direct bonding is considered due to its importance for the bonding of commonly deployed optical materials. Both chemical and physical surface treatment steps have been established to decrease the temperature of the subsequent annealing step while remaining a sufficiently high bonding strength.

By using a preceding chemical surface treatment, also referred to as *chemical cleaning*, direct bonding at temperatures of around and below 300 °C has been made possible [151, 152]. The chemical cleaning commonly consists of a mixture of de-

ionized water (DIW), ammonia water and aqueous hydrogen peroxide [70, Chap. 4.2.1]. This mixture has been found to reduce the amount of organic and in some cases inorganic contaminants on the surface, maintain surface smoothness [153] and, in the case of Si, create a hydrophilic surface by oxidation [154] and by increasing the number of hydroxy groups [97]. Most low-temperature direct bonding methods employ a static load [155, 156] and a vacuum environment, cf. Ref. [152, 156], during the annealing step. To further prevent contamination, that vacuum environment can be already used during the contacting step, as well [157, 158].

Direct bonding at temperatures of around and below 200 °C and even at RT has been achieved by adding preceding physical surface treatment steps. For example, UV activation bonding uses ultraviolet (UV) radiation for introducing O_3 and O_2 radicals which remove remaining contaminants and promote surface oxidation. But, it may introduce nano-asperities and create interface micro-gaps [159, 160]. This is considered as a risk when a homogeneously distributed high bonding strength on a large surface area, for example, for large-scale opto-mechanical applications, is required.

An alternative method to apply temperatures of around and below 200 °C which yield a high bonding strength is plasma-activated bonding (PAB). It employs plasma ions from specific process gases, for example, O_2, CF_4, N_2, Ar or mixtures, being accelerated towards the surface. This takes place in a reaction chamber operating at low-pressures. A useful plasma mode for PAB has been shown to be the reactive ion etching mode where the samples are connected to the powered electrode and the plasma ions approach the surface nearly normally, as well as modes that use similar operating principles, cf. Refs. [161–165]. Considering the process gases, O_2 is reported to remove remaining contaminants and promote surface oxidation, too, while preserving, or even enhancing [166], surface smoothness [162]. A combination of O_2 and CF_4 has recently been proposed to enable reliable bonding at RT [167]. N_2 is reported to soften nano-asperities on SiO_2 surfaces [168]. Several authors find a significantly higher resulting bonding energy when using N_2 as compared to O_2, as a process gas [169–171]. Si surfaces have successfully been bonded using O_2, N_2 and Ar plasma [169, 172–176]. The effect of the process gas strongly depends on the used material, cf. Refs. [148, 177].

Prior to the plasma-activation, the surface to be bonded needs to be clean. Plasma-activation is usually performed immediately after chemical cleaning [75, Chap. 6], although chemical cleaning may be omitted [176, 178]. In addition, many authors apply a DIW rinse step immediately prior to the contacting step [79, 161, 169, 176, 177, 179–182] which is proposed to increase the hydrogen bonding interaction distance and thus to improve the spontaneity of adhesion [183, 184]. A general PAB process flow chart is shown in Fig. 2.6.
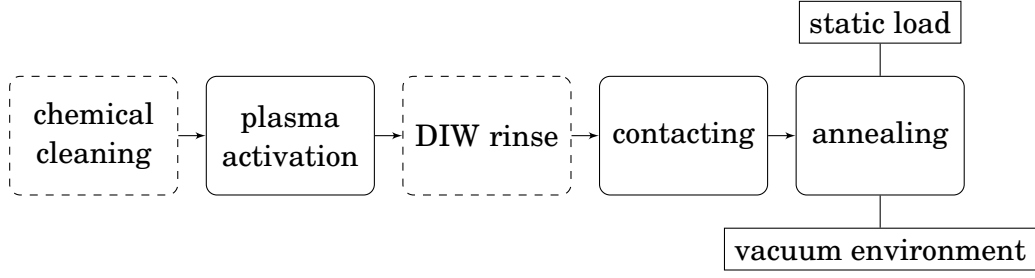
Figure 2.6: General PAB process flow chart, with necessary (straight boxes and lines) and optional (dashed boxes and lines) process steps and external conditions.

2.5 Surface Physics Mechanisms

For direct bonding, the high bonding strength results from the formation of covalently bonded molecules at the bonding interface during the annealing step. In the following, the underlying chemical reaction is investigated: The silanol condensation. Also, the impact of the plasma-activation step is discussed. When a bonding interface is subjected to mechanical stress, which is the case while measuring the bonding energy, another chemical reaction takes place: The water stress corrosion. It is discussed in the following, too.

2.5.1 Silanol Condensation

The surface physics mechanisms of classical direct bonding (that is, direct bonding without the plasma-activation step) can be understood by considering a reversible chemical reaction between *weak* and *strong* intermolecular bonds,

$$\text{A} \underset{k_2}{\overset{k_1}{\rightleftharpoons}} \text{B}, \tag{5}$$

where k_1 and k_2 are the reaction rate constants in each direction. Chemical equilibrium occurs when both the reactants and products have no further tendency to change with time, that is, it occurs for $t \to \infty$. Then, the reaction and its reverse reaction proceed at the same rate. Then, the equation $k_1/k_2 = C_A^\alpha / C_B^\beta$ holds, where α and β are the order of reaction for A and B, respectively [185, Chap. 20C]. Here, C_J is the molar concentration of a substance J. The reaction rate constants are temperature-dependent [185, Chap. 20A]. As it has been found by ARRHENIUS for electrolytes in 1889 [186] and for many other chemical reactions thereafter [185, Chap. 20D], the temperature dependency of the reaction rate constants, k_i, with $i = 1, 2$, can be approximated by

$$k_i \propto \exp\left(-\frac{E_{\text{a},i}}{k_\text{B} T}\right), \tag{6}$$
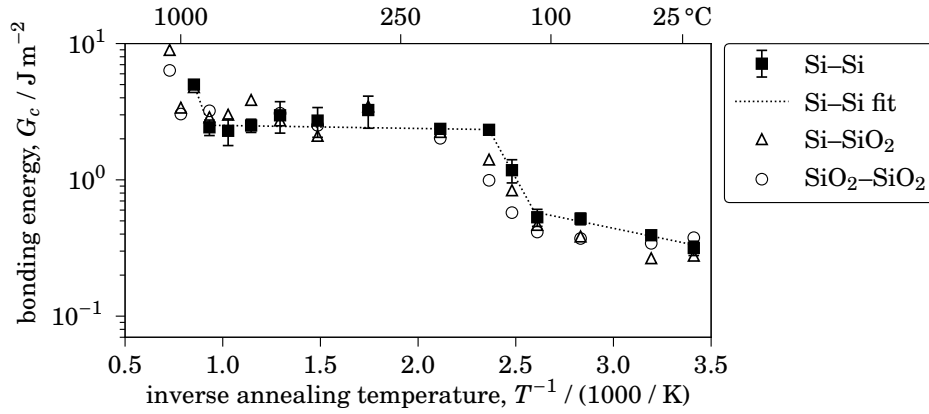
Figure 2.7: Bonding energy, G_c, vs. annealing temperature, T, measured for classical hydrophilic direct bonding of Si and of SiO$_2$ wafer pairs. Note that data is depicted as $\log(G_c)$ vs. T^{-1}. Data points have been taken from Refs. [190] and [70, Chap. 5.2.1].

where T is the temperature, $E_{\mathrm{a},i}$ is the activation energy, that is, the minimum energy needed for that chemical reaction to occur, and k_B is the fundamental BOLTZMANN constant from the kinetic theory of gases. Consequently, Eqs. (5) and (6) imply that

$$\frac{C_A}{C_B} \propto \exp\left(\frac{\text{const.}}{k_\mathrm{B}T}\right). \tag{7}$$

Based on preliminary work by GRUNDNER et al., LASKY et al., SHIMBO et al. and STENGL et al. [138, 187–189], the first systematic investigations of the surface physics mechanisms of direct bonding have been conducted by TONG and GÖSELE in 1996 [190]. They annealed each two Si wafers at different annealing temperatures, T, and measured the resulting bonding energy, G_c. Each annealing step was performed for a sufficient period of time in order to achieve chemical equilibrium. They assumed that the ratio of C_A and C_B from above is approximately proportional to the bonding energy. Thus, if Eq. (7) holds, the quantity $\log(G_c)$ as a function of T^{-1} would appear as a straight line. The experimental results are shown in Fig. 2.7 where for now the data points with ■-symbol (labeled as "Si–Si") are considered. Here, straight lines are indeed observed. But there are four temperature ranges, each with a straight line of different slope. This indicates that the direct bonding process consists of four (consecutive) stages. Three of these stages have a non-zero slope and can be clearly assigned to an underlying chemical reaction.

A few years later, TONG and GÖSELE repeated the experiment by contacting a chemically untreated Si wafer with a thermally oxidized Si wafer, as well as by contacting two thermally oxidized Si wafers [70, Chap. 5.2.1]. The results are shown in Fig. 2.7, too, labeled as "Si–SiO$_2$" and as "SiO$_2$–SiO$_2$". Both results are similar to "Si–Si". This is expected because the increase of bonding energy is governed by chemical reactions of *near-surface* molecules, and chemically untreated as well as thermally oxi-

19
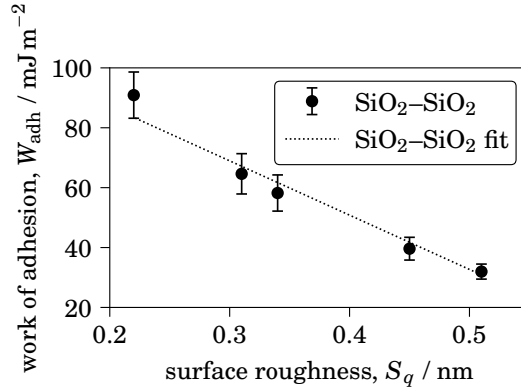
Figure 2.8: Work of adhesion, W_{adh}, which has been calculated from contact front propagation velocity measurements vs. surface roughness, S_q, measured with atomic force microscopy (AFM) at a one square micrometer test area. Data points have been taken from Ref. [112].

dized Si wafers both have a SiO_2 surface layer. Only the thickness of that layer differs, which is several nm [191, 192] and up to several 100 nm [176, 193, 194], respectively.

Based on these results, TONG and GÖSELE proposed the following four steps.

(a) Formation of stable clusters of hydrogen bonds between H_2O and adsorbed hydroxy groups across the interface from RT up to 110 °C.

(b) Removal of the interface H_2O and formation of some isolated covalent Si–O–Si bonds from 110 °C up to 150 °C.

(c) Energetically *stagnant* arrangement from 150 °C up to 800 °C, where the bonding energy is limited by the effectively contacted surface area.

(d) Complete direct bonding via viscous flow of the interface SiO_2 from 800 °C.

The effectively contacted surface area, that is, the contact point density, is determined by surface roughness [127, 195–198]. Already at RT, some covalent bonds are created according to the contact point density, which increases the bonding energy, as shown by FOURNEL et al. [199]. In stage (a), the bridging of local asperities by H_2O molecules plays a role, too, where a separation of up to 1.4 nm can be bridged in the case of full wetting [112, 183, 197] and a separation of up to 0.5 nm is proposed to contribute to adhesion [200]. In fact, surface roughness and work of adhesion are highly correlated, see Fig. 2.8. Structural formulae of the four stages are shown in Fig. 2.9. The complete chemical reaction is often referred to as silanol condensation [76, 151, 177, 201].

The summarizing chemical equation is

$$\text{Si–OH} + \text{HO–Si} \longrightarrow \text{Si–O–Si} + H_2O \tag{8}$$
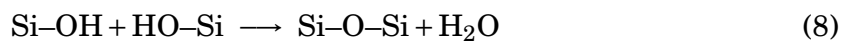
where the water is proposed to be stored at the bonding interface [202], or, at the edges, to diffuse away [203] during the annealing step.
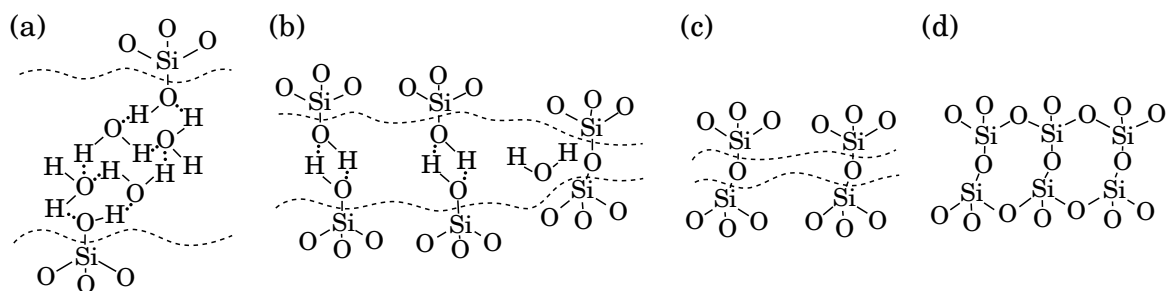
Figure 2.9: Structural formulae of the four stages of classical hydrophilic direct bonding, taken from Ref. [70, Chap. 5.2.1]. In stage (c), it is rather the intermolecular arrangement than the bonding energy which is changing.

2.5.2 The Impact of the Plasma-Activation Step

In Sec. 2.5, classical direct bonding has been considered. Now, plasma-activated bonding (PAB) is considered. As introduced in Sec. 2.4.2, PAB is a hydrophilic direct bonding technique using a plasma-activation step for decreasing the temperature of the annealing step while still obtaining a high bonding energy. In 2013, in order to investigate the surface physics mechanisms of PAB, PLACH et al. repeated the experiments by TONG and GÖSELE in a slightly modified way by introducing a plasma-activation step, using N_2 or O_2 as a process gases, and then a DIW rinse step prior to the contacting step [176]. They found a significant increase of bonding energy as a function of annealing temperature already at RT, with slightly, yet not significantly, higher values when using N_2 as a process gas. This is shown in Fig. 2.10. Note that in this diagram, the annealing time (or storage time in the case of RT) differs for each data point, being several months, a few days and a few hours at RT, 50 °C and 300 °C, respectively. PLACH et al. conclude that stages (a) to (c), as shown in Fig. 2.9, already set in at RT, and that stage (d) sets in from 150 °C to 200 °C.

Although for PAB the underlying chemical reactions have been described as complex [176, 178] and there is yet no consensus on the precise impact of different process gases, DIW rinse or the substrate material, five qualitative surface physics mechanisms of the plasma-activation step have been proposed [158, 166, 204–206], namely

1. removal of remaining contaminants of the surface,
2. increase in the amount of adsorbed hydroxy groups after the DIW rinse,
3. improvement of the diffusivity of water trapped at the bonding interface,
4. enhancement of viscous flow, and
5. preservation or even enhancement of surface smoothness.

To give a few examples for the application of PAB in the field of optics and optomechanics, EICHLER et al. bonded both fused silica and SCHOTT Borofloat® wafers using PAB and found that both the process gases N_2 and Ar yield a higher resulting bond-
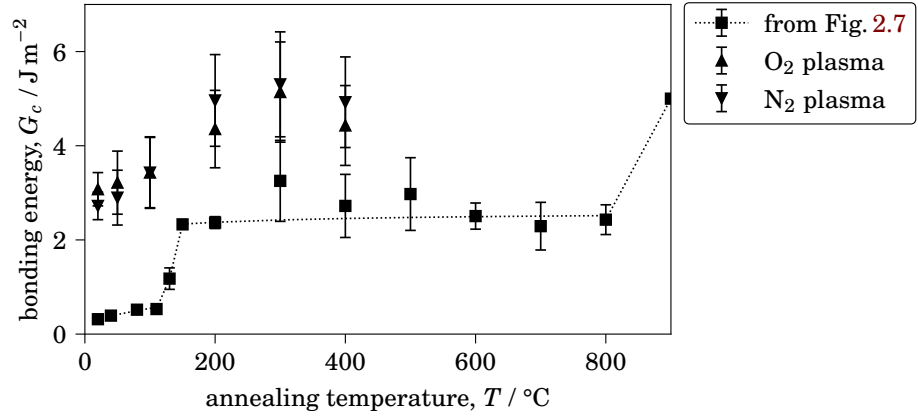
Figure 2.10: Relation between bonding energy, G_c, and annealing temperature, T, for classical hydrophilic direct bonding and for PAB, both performed at Si wafers. Data has been taken from Ref. [176].

ing energy as compared to O_2 [148]. KALKOWSKI et al. bonded both fused silica and CORNING ULE® substrates with large geometries using PAB with the process gases O_2 and N_2 being applied consecutively, proving that even large scale optical workpieces can be joined with a spatially homogeneous small interface reflection and high bonding strength [62, 181]. Taking all this into account, there is reason to consider PAB as a suitable bonding technique for joining optical materials. In particular, PAB is suitable for workpieces that hold temperature-sensitive parts.

2.5.3 Water Stress Corrosion

In the 1940s, BAKER and PRESTON reported that if glass is exposed to humidity, it rapidly loses strength under stress [207]. In the 1960s, WIEDERHORN reported an increase in crack propagation velocity in mechanically stressed bulk glass pieces as a function of the surrounding atmosphere's humidity [208]. Later, MICHALSKE et al. introduced the term *water stress corrorion* for describing the phenomenon of corresponding crack propagation velocity increase with increasing humidity and increasing mechanical stress [209]. In the 1990s, PETZOLD et al. have noticed while performing the DCB-method at directly bonded silicon and SiO_2 glass wafer pairs that over time, the gap opening length increases, that is, the bonding energy decreases [210].

As proposed by FOURNEL et al. in the 2010s for direct bonding, the proposed molecular mechanism is a *reversed* silanol condensation reaction, that is, when a mechanical stress is applied and humidity is present, Equation (8) occurs in a reversed way [199]. The summarizing chemical equation is

$$Si–O–Si + H_2O \longrightarrow Si–OH + HO–Si. \tag{9}$$

As demonstrated by TAKEUCHI and SUGA in the 2020s, the required water stems from

both the surrounding atmosphere's humidity as well as from the residual water stored at the bonding interface [202].

2.6   Mechanics of Direct Bonding

For direct bonding, the surface planarity requirements depend on the workpieces' geometry. If sufficient elastic deformation is possible, the contact front will spontaneously propagate outwards from the point of initial contact and pull the surfaces together [110]. Contacting may fail if planarity deviations are too large, if the surfaces' shapes do not match or if the workpieces are too rigid [110]. Spontaneous contact front propagation often applies to workpieces in wafer geometry, cf. Ref. [211]. Wafer deformation can be mathematically described with plate theory. It is introduced in the following. Also, models that predict direct bonding success are presented.

2.6.1   Preliminary Assumptions for Modeling Wafer Deformation

Deformation of a solid material can be described by a displacement vector $\mathbf{u} = \mathbf{x}' - \mathbf{x}$, where $\mathbf{x} = (x, y, z)$ and $\mathbf{x}' = (x', y', z')$ denote the position of some point in that material *before* and *after* the deformation, respectively. For a relatively small displacement, CAUCHY's strain tensor,

$$\varepsilon_{ij} = \begin{bmatrix} \varepsilon_{xx} & \varepsilon_{xy} & \varepsilon_{xz} \\ \varepsilon_{yx} & \varepsilon_{yy} & \varepsilon_{yz} \\ \varepsilon_{zx} & \varepsilon_{zy} & \varepsilon_{zz} \end{bmatrix} := \frac{1}{2} \left(\frac{\partial u_i}{\partial x_j} + \frac{\partial u_j}{\partial x_i} \right), \tag{10}$$

is a convenient quantity for describing that deformation. Note that even for a large displacement of *some* parts of that material, the local strain itself may be small. An example is a wafer being bent to form a cylindrical surface. In general, deformation is a respond to a mechanical force field, $\mathbf{f}$. For reasons of convenience, the force element per surface area element [212] is considered. It is given by the stress tensor

$$\sigma_{ij} := \frac{\partial f_i}{\partial A_j} = \frac{\partial^2 f_i}{\partial x_k \partial x_l}, \tag{11}$$

with (j, k, l) being pairwise different. Both strain and stress tensor are symmetric, that is, they satisfy $\varepsilon_{ij} = \varepsilon_{ji}$ and $\sigma_{ij} = \sigma_{ji}$ [213, Chap. 1–2]. Latin indices represent x, y and z. A solid material which responds to a mechanical force field by deforming in a linear way suffices HOOKE's law [214, Chap. 4]. For a homogeneous and isotropic solid material, HOOKE's law is given by

$$\sigma_{ij} = \frac{E}{1+\nu} \left(\varepsilon_{ij} + \delta_{ij} \frac{\nu}{1-2\nu} \sum_k \varepsilon_{kk} \right). \tag{12}$$

The elastic strain energy is given by the equation

$$dU_E = \frac{1}{2}\sum_i \sum_j \varepsilon_{ij}\sigma_{ij}\,dV. \tag{13}$$

Here, $E = \sigma_{zz}/\varepsilon_{zz}$ is YOUNG's modulus, $\nu = \varepsilon_{xx}/\varepsilon_{zz}$ is POISSON's ratio and δ_{ij} is KRO-NECKER's delta function which is equal to one for $i = j$ and equal to zero elsewise [213, Chap. 4 – Chap. 5]. HOOKE's law models the elastic behavior of brittle materials, for example, optical glasses, very well.

Planar workpieces with thickness much smaller than their lateral dimensions, for example, wafers, are referred to as plates, for which there are four fundamental deformation types, namely bending and twisting, as well as stretching or squeezing and shearing. These can be modeled to result from moments per unit length, M, as well as from longitudinal forces per unit length, N, respectively, see Fig. 2.11. In literature, N is also referred to as membrane force, cf. Refs. [215, 216]. In general, all four deformation types contribute to the plate's *total* strain energy, U_E. For a *local* consideration, it is useful to define Ψ_M and Ψ_N as the strain energy *per unit area* due to bending and twisting and due to stretching or squeezing and shearing, respectively, such that

$$dU_E = \left(\Psi_M + \Psi_N\right)dA \tag{14}$$

holds [213, Chap. 14]. When plates experience small strains only, the stress components σ_{xz}, σ_{yz} and σ_{zz} are small compared to the remaining stress components and may be neglected [213, Chap. 11]. This is referred to as plane stress condition. Thus,

$$\varepsilon_{xz} = 0, \quad \varepsilon_{yz} = 0, \quad \text{and} \quad \varepsilon_{zz} = -\frac{\nu}{1-\nu}\left(\varepsilon_{xx} + \varepsilon_{yy}\right). \tag{15}$$

Taking into account all four deformation types, VON KÁRMÁN derived a system of non-linear differential equations describing the displacement field, $\mathbf{u}$, for any given force field, $\mathbf{f}$, and for any fixed boundary condition [217]. Unfortunately, this system is highly complicated and even for simple cases not exactly solvable [213, Chap. 14]. To overcome this inconvenience it is considered that as a rule of thumb [216, Chap. 7.4]

1. Ψ_M predominates for small deflections, that is, $u_z < d/5$, and

2. Ψ_N predominates for large deflections, that is, $u_z > d$, with the additional condition
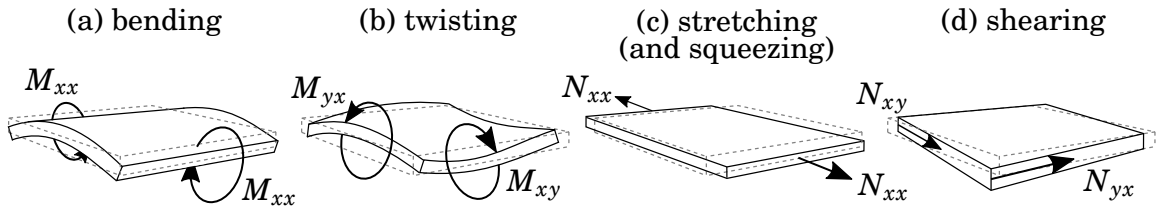
Figure 2.11: Schematic of the four fundamental plate deformation types. In each drawing, the dashed gray lines show the geometry of the plate prior to deformation. M_{ij} are moments and N_{ij} are longitudinal forces (per unit length). Plates are defined such they lie in the x-y-plane prior to deformation.

that there is bending or twisting in both the x- and y-direction (which is equivalent to a non-zero GAUSSian curvature, that is, $\kappa_{xx}\kappa_{yy} \neq 0$).

2.6.2   Energetic Relations for Modeling Wafer Deformation

In the following, plates are assumed to have a homogeneous thickness, d.

In order to derive an explicit expression for Ψ_M, the surface's curvature, $\kappa_{\alpha\beta}$, and moment per unit length, $M_{\alpha\beta}$, are considered as the variables. Greek indices represent x and y. It can be shown that in the case of the curvature, $\kappa_{\alpha\beta}$, the linear relation

$$\kappa_{\alpha\beta} = \kappa_{\beta\alpha} = \varepsilon_{\alpha\beta}/z \tag{16}$$

holds. This implies that the moment per unit length, $M_{\alpha\beta}$, can be expressed as

$$M_{\alpha\beta} = D(1-\nu)\left(\kappa_{\alpha\beta} + \delta_{\alpha\beta}\frac{\nu}{1-\nu}\sum_{\gamma}\kappa_{\gamma\gamma}\right), \tag{17}$$

with flexural rigidity

$$D := \frac{Ed^3}{12(1-\nu^2)}. \tag{18}$$

Equation (17) can be regarded as HOOKE's law of plate bending and twisting. Here, $\delta_{\alpha\beta}$ is the KRONECKER delta which is equal to one for $\alpha = \beta$ and equal to zero elsewise. From this, it can be shown that the corresponding strain energy per unit area is equals

$$\Psi_M = \frac{D}{2}\left(\kappa_{xx}^2 + \kappa_{yy}^2 + 2\nu\kappa_{xx}\kappa_{yy} + 2(1-\nu)\kappa_{xy}^2\right), \tag{19}$$

which is valid for small and large deflections. In fact, all findings presented in Sec. 2.6 are based on a consideration of Ψ_M only. A detailed derivation of Eqs. (16) to (19) is given in the appendix, see Sec. A.1.1.

In literature, mostly special cases of Eqs. (17) and (19) are found [213, 215, 216] that use the small deflection approximation

$$\kappa_{\alpha\beta} \approx \frac{\partial^2 u_z}{\partial x_\alpha \partial x_\beta}. \tag{20}$$

In order to derive an explicit expression for Ψ_N, a plate experiencing longitudinal strains only is considered. Deformation may be regarded as uniform over the plate's thickness. Here, the new variables are longitudinal strain, $\varepsilon_{\alpha\beta}$, and longitudinal force per unit length, $N_{\alpha\beta}$, as variables. The first variable has already been defined by Eq. (10), but, whenever taking into account plate bending and twisting, too, this definition becomes imprecise. This is because the directions represented by dx and dy are not necessarily in line with the plate's surface, anymore.

Typically, the KIRCHHOFF-LOVE plate theory is applied in such cases, in which the correction term $-z\kappa_{\alpha\beta}$ is added to $\varepsilon_{\alpha\beta}$ for considering local curvature [218, 219]. This approximation, however, may not work for large deflections [216, Sec. 12.3]. A more precise approximation is the FÖPPL-VON KÁRMÁN plate theory, where yet another correction term is added, namely $\frac{1}{2}\frac{\partial u_z}{\partial x_\alpha}\frac{\partial u_z}{\partial x_\beta}$, for considering local slope [217, 220]. This may, however, become inconvenient for analytical calculations. Therefore, in the following, whenever longitudinal strains are considered, directional derivatives with respect to the plate's surface are calculated.

Apart from that, for homogeneous materials the longitudinal force per unit length is given by $N_{\alpha\beta} = \sigma_{\alpha\beta}d$. Thus, with Eqs. (13) and (14), and the identity $\mathrm{d}V = d\,\mathrm{d}x_\alpha\,\mathrm{d}x_\beta$, the equation $\Psi_N = \frac{1}{2}\sum_\alpha\sum_\beta N_{\alpha\beta}\varepsilon_{\alpha\beta}$ is obtained [213, Chap. 14]. Subsequently, by using Eqs. (12) and (15), it can be shown [221, Chap. 4] that the corresponding strain energy per unit area is given by

$$\Psi_N = \frac{B}{2}\left(\varepsilon_{xx}^2 + \varepsilon_{yy}^2 + 2\nu\varepsilon_{xx}\varepsilon_{yy} + 2(1-\nu)\varepsilon_{xy}^2\right), \tag{21}$$

with extensional rigidity

$$B := \frac{Ed}{1-\nu^2}. \tag{22}$$

In conclusion, by regarding the plate's mid-plane, the plate can now fully be described in two dimensions only.

2.6.3 Predicting Direct Bonding Success

With Eq. (2), see p. 11, an energetic criterion has been presented as condition for a mechanically stressed interface to start separating. It relates the work of separation, W_{sep}, which is also referred to as bonding energy, G_c, with the strain energy release rate, G, which is defined as $\mathrm{d}U_E/\mathrm{d}A_c$. The key to use that criterion is to develop an expression for U_E as a function of A_c [222]. To do so, plate theory is required. Relevant findings from literature which made use of plate theory are presented in the following.

There has been interest since the early 1990s in predicting surface contacting success on the basis of the surfaces' planarity data [223–225]. In 1999, TONG and GÖSELE [70, Chap. 3.3] considered two wafers ($i = 1, 2$) that have circular, continuous and shallow gaps (with radius R_{gap} and height h_{gap}) caused by planarity deviations, see Fig. 2.12. As criterion for the gap to remain closed after contacting, they found

$$G_c \geq \frac{2}{3}\left(\frac{2h_{\mathrm{gap}}}{R_{\mathrm{gap}}^2}\right)^2\left[\frac{E_1 d_1^3 \times E_2 d_2^3}{E_1 d_1^3 + E_2 d_2^3}\right]. \tag{23}$$

Here, E_i is the YOUNG's modulus of each wafer. The term in square brackets implies that gap closure is governed by that wafer with the smaller $E_i d_i^3$-value.
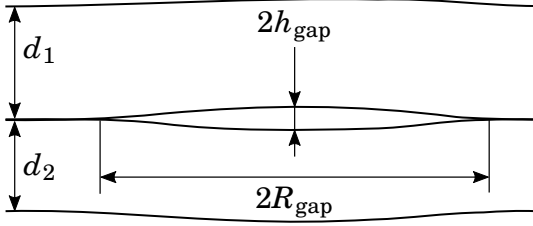
Figure 2.12: Schematic of a circular, continuous and shallow gap between two contacted wafers. Taken from Ref. [224].
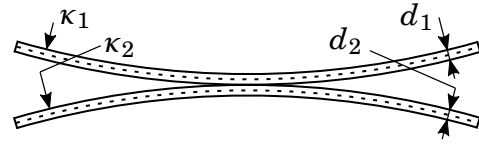
Figure 2.13: Schematic of a cross-sectional view of the initial contact between two bowed wafers. Taken from Ref. [222].

TURNER and SPEARING considered two circular wafers made of a material with the same POISSON's ratio, v, having each a small, constant radial-symmetric curvature κ_1, κ_2 [222], see Fig. 2.13. (Note that the curvature is equals the inverse of the curvature radius.) They found that wafers will spontaneously contact with one another either *completely* or *not at all*, because G takes on its maximum value,

$$G_{\mathrm{max}} = \frac{(\kappa_2 - \kappa_1)^2}{6(1-v)} \left[\frac{E_1 d_1^3 \times E_2 d_2^3}{E_1 d_1^3 + E_2 d_2^3} \right], \tag{24}$$

in the moment of the initial contact [110]. Note that Eq. (23) can directly be derived from Eq. (24) by considering $(\kappa_2 - \kappa_1)$ as the curvature of one of the gaps' surfaces, applying the small sagitta approximation, $(\kappa_2 - \kappa_1) \approx 2 h_{\mathrm{gap}}/R_{\mathrm{gap}}^2$, cf. Ref. [73], changing h_{gap} to $2 h_{\mathrm{gap}}$ to account for both gaps and assuming a vanishing POISSON's ratio.

Another application of Eq. (2) has recently been proposed by ROTHHARDT in 2019 [226]. She defined the wafers' *joint* surface planarity data, u_z, as $u_{z,2}(x,y) + u_{z,1}(-x,y)$, where both wafers are considered as equally thin. Then, she calculated the strain energy, U_E, for each rectangular area element, S, by using the equation

$$U_E = \frac{E d^3}{24(1-v^2)} \iint_S \left[\left(\frac{\partial^2 u_z}{\partial x^2} + \frac{\partial^2 u_z}{\partial y^2} \right)^2 + 2(1-v) \left(\left(\frac{\partial^2 u_z}{\partial x \partial y} \right)^2 - \frac{\partial^2 u_z}{\partial x^2} \frac{\partial^2 u_z}{\partial y^2} \right) \right] \mathrm{d}x \, \mathrm{d}y. \tag{25}$$

Equation (25) is commonly found in literature for approximating the strain energy of a thin plate subjected to small deflections, see, for example, Refs. [213, Chap. 11], [215, Chap. 2] and [216, Chap. 2.6.1]. As an important novelty, by comparing U_E with the area of S multiplied by G_c according to Eq. (2), a prediction can be made about the *local* surface contacting success. Although each individual area element is considered to be independent of neighboring area elements, this model agrees very well with the experiments.

In general, many authors emphasize that a preferably almost ideally planar surface is a key requirement for direct bonding success [67, 68, 117, 118, 139, 227–230]. However, note that this restriction cannot strictly be derived from plate theory.

3 Modeling Non-Planar Direct Bonding Success

In the following, models will be derived for predicting non-planar direct bonding success. The term non-planar direct bonding refers to direct bonding of wafers on substrates with height deviations larger than the wafer's thickness.

3.1 Plate Theory Applicability

The equations derived within this thesis are applicable for *convex* substrate geometries. Concave substrate geometries would present challenges in establishing an initial point contact and in the contact front propagation behavior during the direct bonding process.

In all cases, plates, that is, wafers, are considered as initially perfectly planar. The substrates are considered as infinitely rigid.

3.1.1 Substrate Planarity Deviations and Energetic Contributions

The total strain energy stored in a deformed wafer, U_E, can be modeled to be composed of Ψ_M and Ψ_N, that is, the strain energy per unit area due to wafer bending and twisting and due to wafer stretching or squeezing and shearing, respectively, see Eq. (14). When considering special cases of wafer deformation, it is proposed that certain contributions can be neglected. An example is a circular wafer being pressed onto a spherical substrate, where its diameter increases and circumference reduces [213, Chap. 14] so that Ψ_N becomes *much* larger than Ψ_M. Table II shows a classification of relevant energetic contributions for different substrate types.

Models that predict direct bonding success in the case of small deflections have been presented in Sec. 2.6.3. In this thesis, medium as well as large cylindrical (and acylindrical) and spherical deflections are considered.

Table II: Relevant energetic contributions to the resulting total strain energy, U_E, based on Eq. (19), for different substrate geometry types and different extents of the wafer's deflection.

substrate geometry	extent of the wafer's deflection		
	small	medium	large
cylindrical	Ψ_M	Ψ_M	Ψ_M
acylindrical	Ψ_M	Ψ_M	Ψ_M
spherical	Ψ_M	$\Psi_M + \Psi_N$	Ψ_N
arbitrary	Ψ_M	$\Psi_M + \Psi_N$	$\Psi_M + \Psi_N$

3.1.2   Static Equilibrium Condition

In order to predict direct bonding success, it is required to express the strain energy release rate, G, as a function of the contacted area, A_c. The first step is to consider how to make the underlying equations easier to work with. To do so, a wafer which is (partly) in contact with a non-planar substrate is regarded where the surfaces have (partly) been separated by an external force. The wafer's bonding surface, $\mathscr{A}$, is modeled as a differentiable manifold, and its already contacted part, $\mathscr{A}_c \subseteq \mathscr{A}$, as a connected subset. Their corresponding surface areas are given by A and A_c, respectively. The not contacted part is given by $\mathscr{A} \setminus \mathscr{A}_c$. By assuming static equilibrium, that is, the contact front has come to halt, and by using Eqs. (2) and (14) and splitting the integral into two parts, the equation

$$G_c = \frac{\mathrm{d}U_E}{\mathrm{d}A_c} = \underbrace{\frac{\mathrm{d}}{\mathrm{d}A_c} \int_{\mathscr{A}_c} \left(\Psi_M + \Psi_N\right) \mathrm{d}A}_{=:G^{(\mathrm{c})}} + \underbrace{\frac{\mathrm{d}}{\mathrm{d}A_c} \int_{\mathscr{A} \setminus \mathscr{A}_c} \left(\Psi_M + \Psi_N\right) \mathrm{d}A}_{=:G^{(\mathrm{nc})}} \tag{26}$$

is obtained, with partial strain energy release rates, $G^{(\mathrm{c})}$ and $G^{(\mathrm{nc})}$, resulting from the already contacted and the not anymore contacted part of the wafer, respectively. Here, $G^{(\mathrm{c})}$ is *only* a function of the coordinates which are element of $\mathscr{A}_c$, whereas $G^{(\mathrm{nc})}$ is *also* a function of the boundary line of the already contacted part of the wafer, $\partial \mathscr{A}_c$, that is, the contact front. So, for $G^{(\mathrm{c})}$, STOKES' theorem can be applied [231, Chap. 5]. Consequently,

$$G^{(\mathrm{c})} = \left(\Psi_M + \Psi_N\right)\Big|_{\partial \mathscr{A}_c} \tag{27}$$

is obtained, which offers the great advantage of greatly simplifying the consideration of those contact front propagation problems where $G^{(\mathrm{nc})}$ can be neglected.

3.2   Direct Bonding on Cylindrical and Acylindrical Substrates

In the following, it is considered that a wafer is directly bonded to a non-planar substrate with a *vanishing* curvature along the y-direction, that is, $\kappa_{yy} = 0$. During direct bonding, only bending moments in one direction will act on the wafer, even in the case of large deflections. Therefore, this type of wafer deformation is referred to as uni-axial. A trivial example of a substrate that gives rise to uni-axial deformation is a cylindrical lens where the substrate's curvature along the x-direction, κ_{xx}, is constant. A drawing of such a substrate is shown in Fig. 3.1. A more general geometry, where the substrate's curvature is a function of the x-position is referred to as acylindrical.
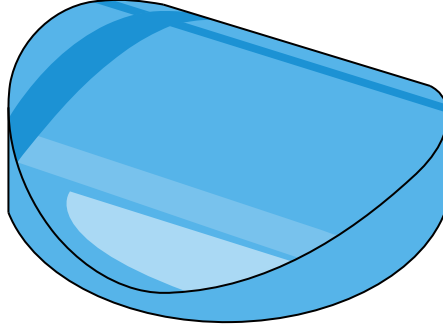
Figure 3.1: Schematic depiction of a convex cylindrical lens.

3.2.1 Condition for Direct Bonding of a Wafer on a Cylindrical Surface

When it comes to direct bonding of a wafer on a lens substrate which has a convex cylindrical or acylindrical surface, there will be complete area stable contact if the bonding energy, G_c, is larger than the strain energy release rate, G.

In order to find an expression for G, it is considered that the wafer is subjected to bending in one direction only, therefore, $\Psi_N = 0$ and $\kappa_{yy} = \kappa_{xy} = 0$, furthermore, that part of the wafer which is not in contact with the substrate will not be subjected to any moments or forces, therefore, $G^{(\mathrm{nc})} = 0$. For relating the strain energy release rate, G, with the curvature, κ_{xx}, Eqs. (19) and (27) are applied, such that

$$G = \Psi_M\Big|_{\partial \mathscr{A}_c} = \frac{D}{2}\left[\kappa_{xx}(x = x_c)\right]^2 = \frac{D}{2}\kappa_{xx,c}^2 \tag{28}$$

is obtained, where x_c is the contact front position and $\kappa_{xx,c} := \kappa_{xx}(x = x_c)$ is the corresponding curvature at that position, assuming that the contact front propagation takes place only in the x-direction.

In the case of a cylindrical lens, where κ_{xx} is constant, it follows with Eq. (2) that direct bonding is successful if the condition

$$G_c \geq \frac{D}{2\rho_{\mathrm{cyl}}^2} \tag{29}$$

is fulfilled. Here, the cylindrical lens's curvature radius, ρ_{cyl}, has been defined as the inverse of κ_{xx}.

3.2.2 Bending Stress as a Function of the Substrate's Curvature

A consideration of the wafer's bending stress may become important. The bending stress must not exceed the material's bending strength, σ_{b}. Otherwise, the wafer might break into pieces. In the following, a condition for the wafer to *not* break into pieces is derived.
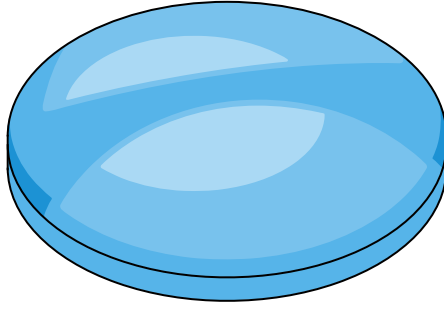
Figure 3.2: Schematic depiction of a convex spherical lens.

By applying HOOKE's law, see Eq. (12), and by using Eq. (15), as well as by considering only that stress contribution which emerges in the x-direction, the equation

$$\sigma_{xx} = \frac{E}{1 - \nu^2} \left(\varepsilon_{xx} + \nu \, \varepsilon_{yy} \right) \tag{30}$$

is obtained. From Sec. 2.6.2, it is known that for a wafer which is subjected to pure bending the maximum tensile strain is located exactly at $z = d/2$, that is, directly at the wafer's surface. From Eq. (16) follows that this value is given by $\varepsilon_{xx} = d \, \kappa_{xx}/2$. Also, $\kappa_{yy} = 0$ implies $\varepsilon_{yy} = 0$. For brittle materials, the tensile stress, σ_{xx}, which is in this case equivalent to the bending stress, is considered as the relevant stress contribution [232, Chap. 5.2]. Thus, the wafer is expected to *not* break into pieces if

$$\sigma_{\mathrm{b}} \leq \frac{B}{2} \kappa_{xx}. \tag{31}$$

3.3   Direct Bonding on Spherical Substrates

In the following, it is considered that a wafer is directly bonded to a convex spherical substrate, that is, to a non-planar substrate with non-vanishing and equal curvatures in the x- and y-direction. During direct bonding, both moments and longitudinal forces will act on the wafer. As bending moments in both directions will arise, this type of deformation is referred to as bi-axial.

A drawing of such a substrate is shown in Fig. 3.2. Spherical substrates are technologically the most important geometry for optical applications.

When a circular wafer (with radius R) is placed in a centered position on top of a convex spherical lens (with curvature κ or curvature radius $\rho = 1/\kappa$), the wafer will either remain in the state of having a point-contact, or it will spontaneously increase its contacted area while undergoing a deformation. The outcome depends on the work of adhesion, W_{adh}. Likewise, an already completely contacted wafer will either remain in the state of being completely contacted, or it will spontaneously reduce its contacted area. The outcome depends on the work of separation, that is, the bonding energy, G_c.

3.3.1   Small Deflection Approximation

For the case of small deflections, only bending moments need to be considered. For that case, TURNER and SPEARING have proposed complete area stable contact if

$$G_c \geq \frac{D\,(1+v)}{\rho^2} \tag{32}$$

holds [110], which follows from their result presented as Eq. (24) in Sec. 2.6, where the derivation is performed by taking into account the contribution of only one wafer and by assuming an infinitely rigid substrate, that is, $E_2 d_2^3 \to \infty$. An alternative derivation is presented in the appendix, see Sec. A.1.3.

In the case of large deflections, longitudinal forces need to be considered, too. In the following, different analytical and semi-analytical modeling approaches are presented. All of these approaches have in common that they only consider energetic contributions from longitudinal forces, Ψ_N, while neglecting those from bending and twisting moments, Ψ_M, as they are comparatively small, cf. Tab. II. It is convenient to use cylinder coordinates, (r, φ, z), where $dA = r\,dr\,d\varphi$. Equation (21) is still valid after substituting x and y with r and φ, respectively, cf. Refs. [213, §4–§5] and [233, Chap. 2.2]. Due to radial symmetry, shearing, $\varepsilon_{r\varphi}$, can be neglected.

3.3.2   Naïve Azimuthal Strain Model

By assuming that a wafer is completely contacted with a spherical substrate, it may be proposed that the wafer's strained circumference, $\tilde{p}$, is smaller than its original circumference, $p = 2\pi R$, due to squeezing in the azimuthal direction. It can be shown that $\tilde{p} = 2\pi\rho\sin(R/\rho)$. Thus, not only for the wafer radius, R, but for any radius variable, r, with $0 < r \leq R$, the azimuthal strain as a function of r is given by

$$\varepsilon_{\varphi\varphi} \approx \frac{1}{r}\frac{\partial u_\varphi}{\partial \varphi} = \frac{\tilde{p}-p}{p} = \frac{\rho}{r}\sin\left(\frac{r}{\rho}\right) - 1. \tag{33}$$

This is an approximation because in reality, there is also stretching in the radial direction. The *naïve* approach is to ignore that stretching, that is, $\varepsilon_{rr} = 0$, and to assume that there are no longitudinal forces acting on that part of the wafer which could already have separated from the substrate, that is, $G^{(\mathrm{nc})} = 0$. By regarding Eqs. (21) and (26), the equation $G = \Psi_N|_{\partial\mathscr{A}_c} = B\left[\varepsilon_{\varphi\varphi}(r = r_c)\right]^2/2$ is found, where r_c is the contact front position. By inserting Eq. (33),

$$G = G^{(\mathrm{c})} = \frac{B}{2}\left[1 - \frac{\rho}{r_c}\sin\left(\frac{r_c}{\rho}\right)\right]^2 = \frac{B}{2}\left[1 - \frac{2\rho\sin(r_c/\rho)}{r_c} + \frac{\rho^2\sin^2\left(r_c/\rho\right)}{r_c^2}\right] \approx \frac{B}{72}\left(\frac{r_c}{\rho}\right)^4 \tag{34}$$

(a)

(b)
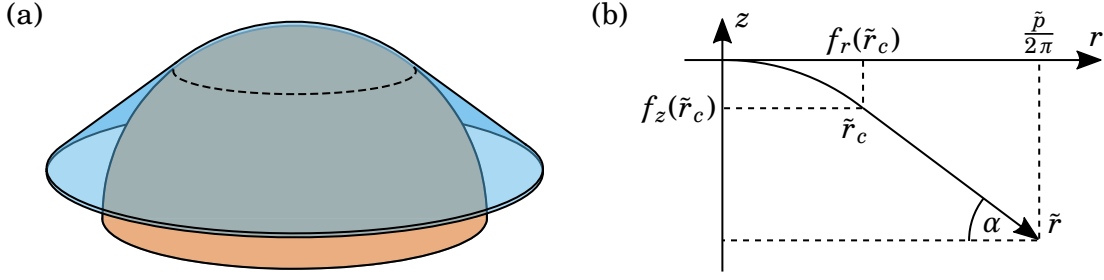
Figure 3.3: Schematic of the truncated cone model, with (a) an illustration, where the contact front is drawn as a dashed curve, and (b) its geometric abstraction.

is obtained, where a fifths order TAYLOR approximation, with $r_c \ll \rho$, has been performed. By considering that G takes on its maximum value, $G_{\max}$, at $r_c = R$ and by applying Eq. (2), it is found that complete area contact between wafer and substrate is stable if

$$G_c \geq G_{\max} = \frac{B}{72} \left(\frac{R}{\rho} \right)^4 \approx \left(138.9 \times 10^{-4} \right) \times B \left(\frac{R}{\rho} \right)^4 . \tag{35}$$

According to this model, for smaller bonding energies, G_c, there is a *partial* contact between wafer and substrate possible. This is in contrast to the model by TURNER and SPEARING, cf. Eq. (24). As mentioned above, for finding Eq. (35), it was neglected that, for one thing, there is radial strain, ε_{rr}, and for another thing, there are longitudinal forces acting on that part of the wafer which is not anymore contacted with the substrate. It is unclear whether the naïve azimuthal strain model overestimates or underestimates the real strain energy release rate, G.

3.3.3 Truncated Cone Model

As compared to the previous model, the radial strain, ε_{rr}, and the longitudinal forces acting on the part of the wafer which is not in contact with the substrate are now taken into account. To model the completely contacted wafer's strain distribution, it is necessary to model the wafer's contact front propagation starting from point contact. In this context, the quantity G is referred to as the strain energy *accumulation* rate. (Note that this mathematical "trick" allows to calculate the strain distribution stored in the wafer. Eventually, surface separation from complete contact will be assumed again, where G will be compared with strain energy *release* rate, G_c.)

For the not yet contacted part of the wafer, it is assumed that it takes on the form of a truncated cone. This allows some analytical calculations. A schematic drawing is shown in Fig. 3.3 (a). The truncated cone will presumably experience radial stretching, ε_{rr}, and azimuthal squeezing, $\varepsilon_{\varphi\varphi}$. A calculation of G requires four steps.

In the first step, a relation between ε_{rr} and $\varepsilon_{\varphi\varphi}$ is derived. To this end, the strained wafer's radial arc length and the strained wafer's circumference as a function of r, with $0 < r \leq R$, are introduced as

$$\tilde{r} = \int_0^r \left(1 + \varepsilon_{rr}(s) \right) \mathrm{d}s \quad \text{and} \tag{36}$$

33

$$\tilde{p} = 2\pi r\left(1 + \varepsilon_{\varphi\varphi}(r)\right), \tag{37}$$

respectively. As shown in Fig. 3.3 (b), from a geometrical point of view it is found that the strained wafer's circumference can also be written as

$$\tilde{p} = 2\pi\left((\tilde{r} - \tilde{r}_c)g + f_r(\tilde{r}_c)\right), \quad \text{with} \tag{38}$$

$$g = \cos\alpha, \tag{39}$$

where the cone's angle is given by $\alpha = \arctan\left(\mathrm{d}f_z(\tilde{r})/\mathrm{d}\tilde{r}\big|_{\tilde{r}_c}\right)$. Equation (38) is valid for $\tilde{r} \in [\tilde{r}_c, \tilde{R}]$, where $\tilde{r}_c$ is the contact front's radial position. The auxiliary quantity

$$\mathbf{f}(\tilde{r}) = \begin{bmatrix} f_r(\tilde{r}) \\ f_z(\tilde{r}) \end{bmatrix} = \int_0^{\tilde{r}} \begin{bmatrix} \cos\beta(s) \\ -\sin\beta(s) \end{bmatrix} \mathrm{d}s, \quad \text{with} \quad \beta(s) = \int_0^s \kappa_{rr}(t)\,\mathrm{d}t, \tag{40}$$

is, according to the fundamental theorem of space curves [234], an explicit function of the substrate's local radial curvature, $\kappa_{rr}(\tilde{r})$. In Eq. (38), $\tilde{r}_c$ can be evaluated via Eq. (36). So, for a spherical substrate, where $\kappa_{rr} = 1/\rho$, it is found that

$$g = \cos\left(\arctan\left(\sin\left(\tilde{r}_c/\rho\right)\right)\right) = \sqrt{\frac{1}{1 + \sin^2\left(\tilde{r}_c/\rho\right)}}. \tag{41}$$

The previous equations can easily be combined and rearranged for $\varepsilon_{\varphi\varphi} = \varepsilon_{\varphi\varphi}(r, \varepsilon_{rr})$. Unfortunately, this function would contain a lot of integrals and trigonometric functions, ruling out further analytical considerations. In order to make progress anyway, the key idea is to regard the *geometrical* parameters, g and $\mathbf{f}$, as constant values, at least for now. By doing this, combining Eqs. (37) and (38), solving for $\tilde{r}$, applying Eq. (36), using the second fundamental theorem of calculus [231, Chap. 4] and rearranging gives

$$\varepsilon_{rr} = \frac{1 + \varepsilon_{\varphi\varphi} + r\,\varepsilon'_{\varphi\varphi}}{g} - 1 \tag{42}$$

which provides a simple relation between ε_{rr}, $\varepsilon_{\varphi\varphi}$ and its derivative $\varepsilon'_{\varphi\varphi} := \mathrm{d}\varepsilon_{\varphi\varphi}/\mathrm{d}r$. The only remaining variable is r, and the offset term $-g\,r_c + f_r(\tilde{r}_c)$ has vanished. Because of Eq. (38), the domain of both ε_{rr} and $\varepsilon_{\varphi\varphi}$ is $(r_c, R]$. The domain of g is $(0, 1)$.

In the second step, a formula for $\varepsilon_{\varphi\varphi}$ will be framed. According to Eqs. (21), (26) and (42), the strain energy accumulation rate resulting from the truncated cone is

$$\begin{aligned}
G^{(\mathrm{nc})} &= \frac{\mathrm{d}}{\mathrm{d}A_c} \int_{\mathscr{A}\setminus\mathscr{A}_c} \Psi_N\,\mathrm{d}A = \frac{\mathrm{d}}{\mathrm{d}A_c}\left(\frac{B}{2}\int_0^{2\pi}\int_{r_c}^R \left(\varepsilon_{\varphi\varphi}^2 + \varepsilon_{rr}^2 + 2\nu\,\varepsilon_{\varphi\varphi}\,\varepsilon_{rr}\right) r\,\mathrm{d}r\,\mathrm{d}\varphi\right) \\
&= \frac{\mathrm{d}}{\mathrm{d}A_c}\left(\pi B \int_{r_c}^R \left\{r\left[\varepsilon_{\varphi\varphi}^2 + \left(\frac{1 + \varepsilon_{\varphi\varphi} + r\,\varepsilon'_{\varphi\varphi}}{g} - 1\right)^2 + 2\nu\,\varepsilon_{\varphi\varphi}\left(\frac{1 + \varepsilon_{\varphi\varphi} + r\,\varepsilon'_{\varphi\varphi}}{g} - 1\right)\right]\right\}\mathrm{d}r\right) \\
&= \frac{B}{2r_c}\frac{\mathrm{d}}{\mathrm{d}r_c}\left(\int_{r_c}^R \mathscr{L}\,\mathrm{d}r\right)
\end{aligned} \tag{43}$$

where the integrand, $\{\dots\}$, is now referred to as $\mathscr{L}$. Here, the function $\varepsilon_{\varphi\varphi} = \varepsilon_{\varphi\varphi}(r)$ is of interest. It has to be chosen such that the integral takes on its minimum value. Finding such a function corresponds to minimizing the total strain energy of the truncated cone. Following the established terminology, the function $\mathscr{L}$ is referred to as the Lagrangian. A necessary condition for the integral to take on its minimum value is given by the EULER-LAGRANGE equation, cf. Refs. [235, Chap. 12] and [236, Chap. 4.1], that is,

$$\frac{\partial \mathscr{L}}{\partial \varepsilon_{\varphi\varphi}} - \frac{\mathrm{d}}{\mathrm{d}r}\frac{\partial \mathscr{L}}{\partial \varepsilon'_{\varphi\varphi}} = 0 \tag{44}$$

which in the present case yields the ordinary differential equation (ODE) $g^2 \varepsilon_{\varphi\varphi} - g^2 v + g v + g - r^2 \varepsilon''_{\varphi\varphi} - 3 r \varepsilon'_{\varphi\varphi} - \varepsilon_{\varphi\varphi} - 1 = 0$. This is a CAUCHY-EULER type ODE, thus, the exact solution is given by

$$\varepsilon_{\varphi\varphi} = c_1 \left(\frac{r}{r_c}\right)^{g-1} + c_2 \left(\frac{r}{r_c}\right)^{-g-1} + \frac{g v - 1}{g + 1}, \tag{45}$$

with constants $c_1 = \left(1 - g v + g \varepsilon_{\varphi\varphi,c} + r_c \varepsilon'_{\varphi\varphi,c} + \varepsilon_{\varphi\varphi,c}\right)\big/(2g)$,

$$c_2 = \left(g^2 \varepsilon_{\varphi\varphi,c} - g^2 v - g r_c \varepsilon'_{\varphi\varphi,c} + g v + g - \varepsilon_{\varphi\varphi,c} - r_c \varepsilon'_{\varphi\varphi,c} - 1\right)\big/\left(2 g (g+1)\right),$$

and boundary conditions $\varepsilon_{\varphi\varphi,c} := \varepsilon_{\varphi\varphi}(r = r_c)$, $\varepsilon'_{\varphi\varphi,c} := \varepsilon'_{\varphi\varphi}(r = r_c)$ [237, Chap. 61]. With this solution at hand, ε_{rr} can be solved exactly, too, see Eq. (42). This implies that the truncated cone's strain distribution is fully determined by those strains which are present at the contact front position as well as by the truncated cone's slope, g.

In the third step, $\varepsilon_{\varphi\varphi}$ is calculated iteratively. To this end, by starting at point contact, that is, $r_c = 0$, Eq. (45) and its derivative are evaluated at $r_c + \mathrm{d}r_c$, where $\mathrm{d}r_c$ is a small increment. Then, the resulting values are assigned as updated boundary conditions, then, $\varepsilon_{\varphi\varphi}$ is updated, and then this process is repeated for the next increment. The geometrical parameter, g, is updated in each step, too, according to Eq. (39). The algorithm is shown in Fig. 3.4. Here, not only $\varepsilon_{\varphi\varphi}$ but also $G^{(\mathrm{nc})}$ is computed.
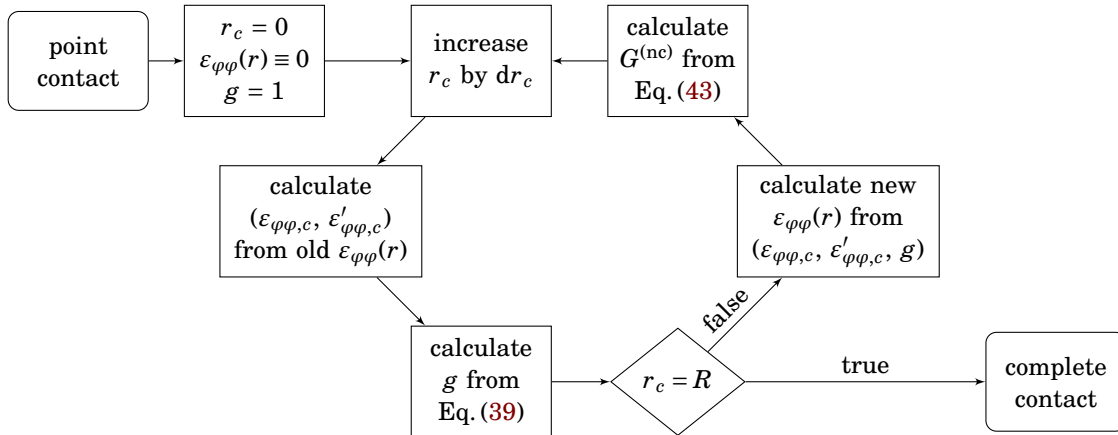
Figure 3.4: Flowchart of the iterative algorithm, starting with point contact and ending with complete area stable contact, for finding $\varepsilon_{\varphi\varphi}(r)$ and $G^{(\mathrm{nc})}$ for any given contact front position $r_c \in [0,R]$. The corresponding computer code is given in the appendix, see Sec. A.3.1.
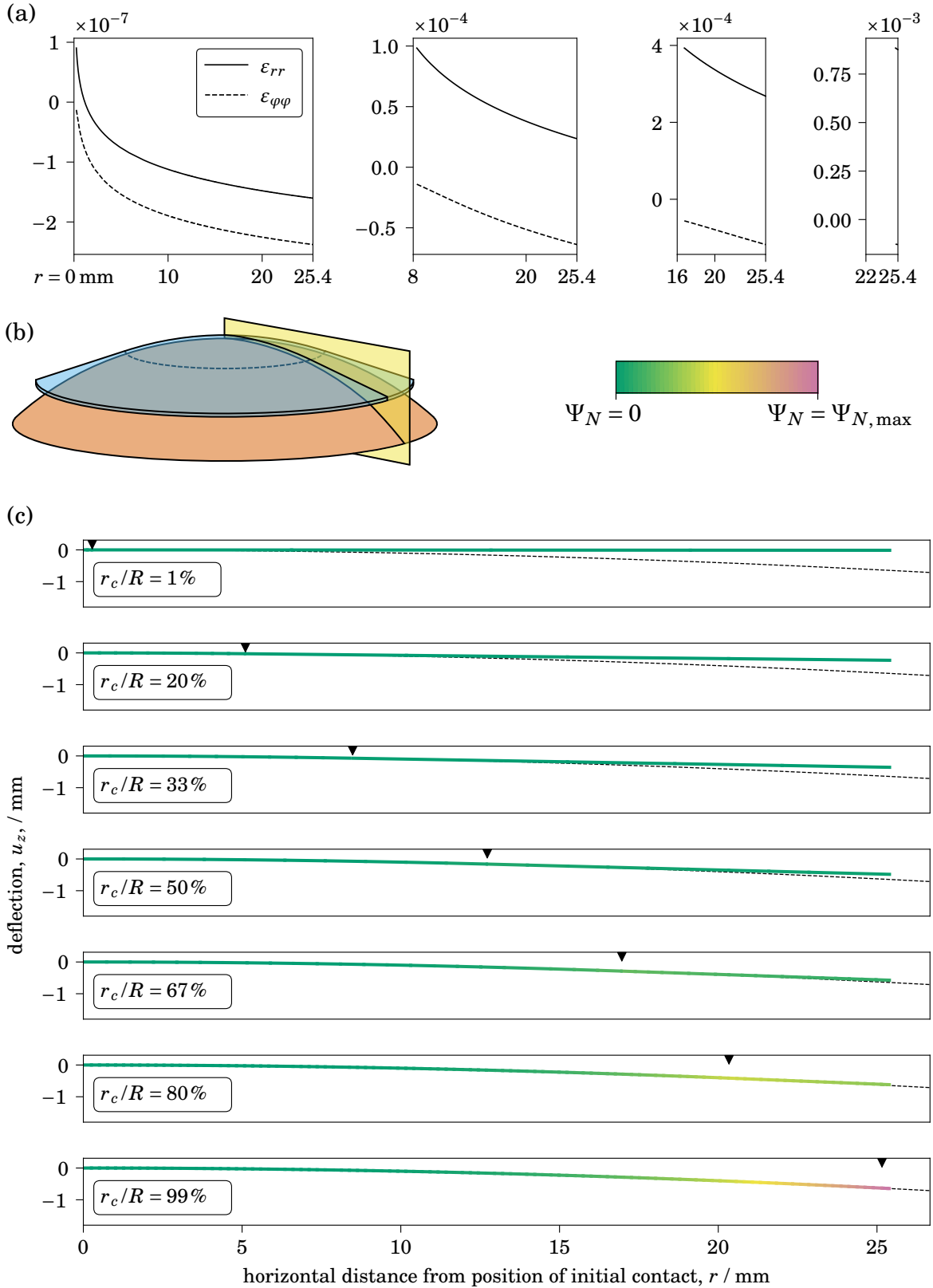
Figure 3.5: Visualization of the contact front propagation behavior for truncated cone model. Here, (a) shows the calculated curves of the strains $\varepsilon_{\varphi\varphi}$ and ε_{rr}, for $r_c/R = 1\%$, 33%, 67% and 99% (from left to right), (b) shows the considered cross-section as a yellow plane, and (c) shows the resulting wafer geometry with corresponding strain energy per unit area, Ψ_N, with color legend depicted directly above on the right hand side. The contact front position, r_c, is indicated by the ▼-symbol. In all cases, $\rho = 0.5\,\mathrm{m}$, $R = 25.4\,\mathrm{mm}$ and $\nu = 0.2$, which gives $\Psi_{N,\mathrm{max}} = 7.42 \times 10^{-7} \times B$.

An exemplary calculation of $\varepsilon_{\varphi\varphi}$ and ε_{rr} is shown in Fig. 3.5 (a). It shows that very soon after the contact front has begun to propagate outwards, ε_{rr} is always positive and $\varepsilon_{\varphi\varphi}$ is always negative, corresponding to radial stretching and azimuthal squeezing, respectively, as expected. The absolute values of ε_{rr} and $\varepsilon_{\varphi\varphi}$ increase very drastically with increasing r_c. There is an alternative way to visualize this finding. Rather than displaying the calculated curves of the strains, $\varepsilon_{\varphi\varphi}$ and ε_{rr}, separately, it may be useful to display wafer shape and underlying strain distribution simultaneously. One way to do this is shown in Figs. 3.5 (b) and (c). It becomes evident that in the case of a completely contacted wafer, essentially all the elastic strain energy is stored in the outer perimeter of the wafer.

In the fourth step, G is calculated. It consists of two parts, see Eq. (26). The first part, $G^{(\mathrm{nc})}$, that is, the strain energy accumulation rate resulting from the truncated cone, is given by Eq. (43). The second part, $G^{(\mathrm{c})}$, that is, the strain energy accumulation rate resulting from the already contacted part of the wafer, is given by

$$G^{(\mathrm{c})} = \frac{B}{2} \left[\varepsilon_{\varphi\varphi,c}^2 + \left(\frac{1 + \varepsilon_{\varphi\varphi,c} + r\,\varepsilon_{\varphi\varphi,c}'}{g} - 1 \right)^2 + 2\,\nu\,\varepsilon_{\varphi\varphi,c} \left(\frac{1 + \varepsilon_{\varphi\varphi,c} + r\,\varepsilon_{\varphi\varphi,c}'}{g} - 1 \right) \right] \qquad (46)$$

which is a function of the boundary conditions. Equation (46) directly follows from the Eqs. (21), (26) and (42). Both $G^{(\mathrm{nc})}$ and the boundary conditions have already been computed by the algorithm presented in Fig. 3.4. As such, $G^{(\mathrm{c})}$ is fully determined for any given value $r_c \in [0,R]$, as well. In conclusion, also the total strain energy accumulation rate, G, is fully determined.

An exemplary calculation of G is shown in Fig. 3.6. It shows that there is an initial increase of G with increasing contact front position, r_c, and then, after reaching its maximum value, $G_{\max}$, there is a rapid decrease back to $G = 0$.

The final concern is to establish a condition for predicting complete area stable contact between wafer and substrate. It is proposed that this criterion is given by $G_c \geq G_{\max}$. In Fig. 3.6, $G_{\max}$ has been highlighted by a small circle. The objective is to estimate the value of $G_{\max}$ as a function of the two geometrical parameters, namely, the wafer radius, R, and the substrate curvature radius, ρ. By running the algorithm as presented in Fig. 3.4 for more than a hundred input values (in the range of $R \in [0.5\,\mathrm{mm}, 1000\,\mathrm{mm}]$ and $\rho \in [0.05\,\mathrm{m}, 5\,\mathrm{m}]$, with the condition $\rho > 5R$), an interesting empirical result was found: First, $G_{\max}$ is proportional to ρ^{-4}, and second, $G_{\max}$ is proportional to R^4. The pre-factor is $\left(320.4 \times 10^{-4}\right) \times B$.
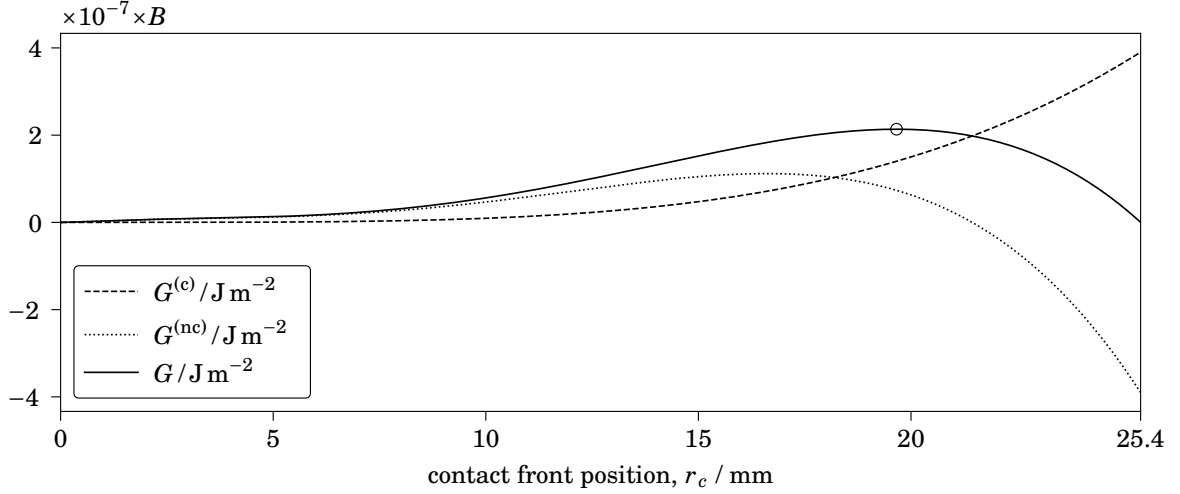
Figure 3.6: Calculated strain energy accumulation rate values of the contacted and not yet contacted part of the wafer, and its sum, $G^{(c)}$ and $G^{(nc)}$, and G, respectively, drawn as function of the radial contact front position r_c. Here, $\rho = 0.5$ m, $R = 25.4$ mm and $\nu = 0.2$. Circle: Maximum value of G, that is, G_{max}.

In conclusion, the final outcome of the truncated cone model can be written as the short and simple formula

$$G_c \geq G_{max} = \left(320.4 \times 10^{-4}\right) \times B \left(\frac{R}{\rho}\right)^4. \tag{47}$$

The deviation between the numerical result and Eq. (47) is smaller than 2 % (in a range of $R \in [0.5\,\text{mm}, 1000\,\text{mm}]$ and $\rho \in [0.05\,\text{m}, 5\,\text{m}]$, with the condition $\rho > 5R$). A visualization of the curve fitting process is shown in the appendix, see Sec. A.2.1.

The truncated cone model is expected to overestimate the real G_{max}. This is because the truncated cone's geometry is very limited as it does not consider radial bending. In reality, the not yet contacted part of the wafer would bend upwards such that its outer perimeter is less squeezed. As such, the longitudinal forces are acting against an accumulation of Ψ_M. From a mathematical point of view, at least *two* independent functions would be required to model the shape of the not yet contacted part of the wafer, namely $\varepsilon_{\varphi\varphi}(r)$ and $\kappa_{rr}(r)$. This makes a minimization of the total strain energy much more complicated. To following model tackles this challenge.

3.3.4 Truncated Torus Model

In order to make progress modeling the upwards bending of the not yet contacted part of the wafer, the simple but approximately realistic assumption

$$\kappa_{rr} = \text{const.} \ \text{ for all } \ r \in (r_c, R] \tag{48}$$

is made. This is equivalent to assuming that the not yet contacted part of the wafer takes on the form of a truncated torus, see Fig. 3.7 (a). Furthermore, it is assumed that
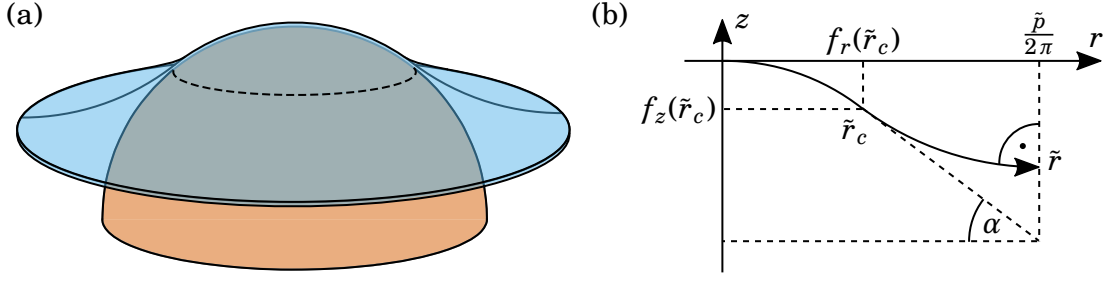
Figure 3.7: Schematic of the truncated torus model, with (a) an illustration, where the contact front is drawn as a dashed curve, and (b) its geometric abstraction.

the slope at the outer perimeter vanishes, see Fig. 3.7 (b). This assumption is realistic because it corresponds to a minimization of the longitudinal strain energy, Ψ_N, at the wafer's outer perimeter, which is exactly the position where Ψ_N takes on its maximum value, cf. Fig. 3.5 (c).

This assumption has the impact that only a single change in the mathematical derivation – as compared to the previous model – is required: Equation (39), which defines the geometrical parameter g, takes on the form

$$g = \frac{\sin(\alpha)}{\alpha}. \tag{49}$$

Now, by re-running the algorithm as presented in Fig. 3.4 and re-calculating $G_{\max}$, it is found that the final outcome is now given by

$$G_c \geq G_{\max} = \left(35.6 \times 10^{-4}\right) \times B \left(\frac{R}{\rho}\right)^4. \tag{50}$$

3.3.5 Quartic Proportionality Explained by Geometrical Considerations

Up to now, three models have been presented to predict complete area stable contact between a circular wafer and a spherical substrate. In all cases, for the calculated maximum value of the strain energy release rate, $G_{\max}$, it has been found that

$$G_{\max} \propto \left(\frac{R}{\rho}\right)^4. \tag{51}$$

It will be shown that this result can be derived by purely geometric considerations under the assumption that only longitudinal forces, Ψ_N, are considered.

It is evident that the spatial distribution of the elastic strain, ε, is the same for all those setups that are similar (in a geometrical sense). In other words, the value (R/ρ) fully determines the elastic strain distribution. This is due to the fact that the elastic strain is defined as a relative quantity, cf. Eq. (10). Such setups are shown in Figs. 3.8 (a) to (d).
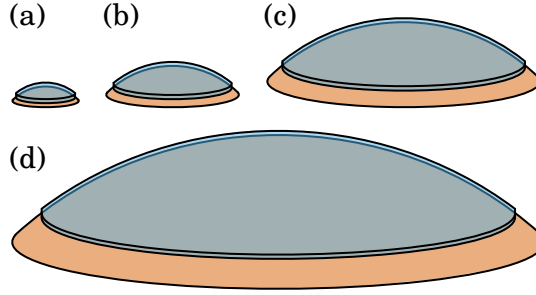
Figure 3.8: Schematic of differently scaled, but similar (in a geometrical sense) setups of wafer and spherical substrate which are in complete area stable contact.

Equations (2), (14) and (21) show that the strain energy release rate has to be proportional to the elastic strain squared, that is, $G \propto \varepsilon^2$. This implies $G_{\mathrm{max}} \propto \varepsilon^2$.

The elastic strain, ε, is essentially proportional to the normalized maximum vertical deflection of the wafer, $u_{z,\mathrm{max}}/\rho := u_z|_{r=R}\big/\rho$, where $1/\rho$ has been chosen as the normalization factor. This is because almost all of the elastic strain is stored at $r = R$, that is, at the outer perimeter of the wafer (in the case of complete area stable contact between wafer and substrate), as it was shown in Fig. 3.5. The normalized maximum vertical deflection is given by the TAYLOR's approximation of a circle function, that is,

$$\frac{u_{z,\mathrm{max}}}{\rho} = \sqrt{1 - \left(\frac{R}{\rho}\right)^2} - 1 \approx -\frac{1}{2}\left(\frac{R}{\rho}\right)^2 - \frac{1}{8}\left(\frac{R}{\rho}\right)^4 - \frac{1}{16}\left(\frac{R}{\rho}\right)^6. \tag{52}$$

In the case of the largest R-to-ρ ratio investigated in the frame of this thesis, the second term in Eq. (52) is already more than 1000 times smaller than the first term. The third term is accordingly smaller than the second one. Therefore, it is reasonable to only consider the first term. By doing this and applying the finding from above, Eq. (51) is obtained.

3.3.6 Majidi and Fearing's Model

In 2008, MAJIDI and FEARING [238] investigated the contacting behavior of a circular plate on a sphere, too, but they considered thin polyethylene plates instead of wafer direct bonding. By neglecting the non-contacted part of the wafer, as in the naïve azimuthal strain model, but approximating the sphere as a paraboloid and applying the FÖPPL-VON KÁRMÁN plate theory, cf. Sec. 2.6.2, they too found the characteristic quartic proportionality, however, with again a different pre-factor, namely

$$G_c \geq G_{\mathrm{max}} = \frac{B}{128}\left(\frac{R}{\rho}\right)^4 \approx \left(78.1 \times 10^{-4}\right) \times B\left(\frac{R}{\rho}\right)^4. \tag{53}$$

A sketch of their derivation is presented in the appendix, see Sec. A.1.4. MAJIDI and FEARING did not experimentally test their result.

In all models presented up to now, contributions from plate *bending* have been neglected, since they are comparatively small. MAJIDI and FEARING suggested to consider these contributions by simply adding the small deflection approximation from TURNER and SPEARING, see Eq. (2). This is a reasonable suggestion because Ψ_M and Ψ_N have been defined as being approximately independent quantities, see Eq. (14). As a result, Eq. (53) becomes

$$G_c \geq G_{\max} = \left(78.1 \times 10^{-4}\right) \times B \left(\frac{R}{\rho}\right)^4 + \frac{D\left(1+\nu\right)}{\rho^2}. \tag{54}$$

An analogous procedure is advised for the previous models, too.

3.3.7   Finite Element Method Model

All previous models were subjected to geometrical approximations. This allowed some analytical calculations. An alternative approach is the finite element method (FEM) which is a powerful numerical tool that divides the given geometry into a finite number of elements and then iteratively computes the resulting force and displacement field for a given set of mechanical boundary conditions [239].

For the previous geometry, the FEM is performed by using the software *Mechanical 2020 R1* by Ansys Inc., Canonsburg, PV, United States, where the displacement method is applied. It would be a highly complex venture to model the actual process of contact front propagation governed by the intermolecular forces between the surfaces. Therefore, the model has been simplified such that it consists of a circular wafer placed in between of two spherical shells of equal curvature radius, one convex and the other one concave, see Fig. 3.9. By decreasing the distance between these shells in a quasi-static way, the wafer is deformed accordingly. The shells' material is modeled to behave as steel where friction is neglected. The model is restricted to calculate the final strain energy, U_E, that is stored in the completely contacted wafer. As such, after achieving complete area stable contact, the maximum strain energy release rate is approximated by

$$G_{\max} = \frac{\mathrm{d}U_E}{\mathrm{d}A_c} \approx \frac{U_E}{2\pi R^2}. \tag{55}$$

The FEM simulation was run with 30 input values (in a range of $R \in [20\,\mathrm{mm}, 70\,\mathrm{mm}]$ and $\rho \in [0.3\,\mathrm{m}, 0.7\,\mathrm{m}]$). In all cases, a wafer thickness of $d = 100\,\mu\mathrm{m}$ is assumed, which ensures that the energetic contribution from longitudinal forces, Ψ_N, is much larger than that from plate bending, Ψ_M. As such, the numerically calculated
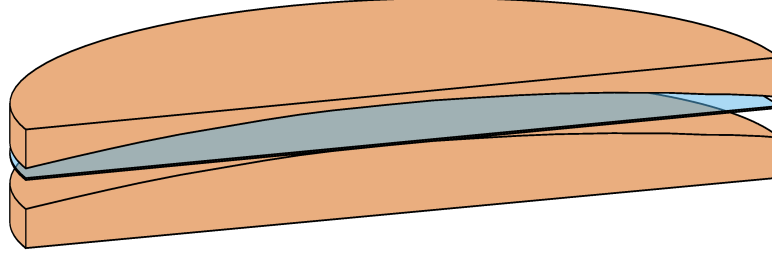
Figure 3.9: Schematic of the FEM model. Cutaway diagram. The depicted geometry has the parameters $d = 100\,\mu m$, $R = 30\,mm$ and $\rho = 300\,mm$.

strain energy release rate values are particularly accurate for large deflections. As a result, the characteristic quartic proportionality is obtained again, as expected, but in this case the pre-factor (which is the only fit parameter) is 25.2×10^{-4}. A visualization of the curve fitting process is shown in the appendix, see Sec. A.2.2.

In conclusion, the result is

$$G_c \geq G = \left(25.2 \times 10^{-4}\right) \times B \left(\frac{R}{\rho}\right)^4 + \frac{D\,(1+\nu)}{\rho^2}. \tag{56}$$

The deviation between the numerical result and Eq. (56) is smaller than $2\,\%$ (in a range of $R \in [20\,mm,\ 70\,mm]$ and $\rho \in [0.3\,m, 0.7\,m]$).

Note that the truncated cone model suggests that G takes on its maximum value already during partial contact, as shown in Fig. 3.6. The approach in Eq. (55) however essentially calculates the average strain energy release rate over the entire area, not considering possible local maximum values. The FEM model is therefore expected to underestimate the maximum value of the strain energy release rate, $G_{\max}$, because it does not allow to consider the propagation of the contact front.

3.3.8 Discussion and Summary of the Large Spherical Deflection Models

All discussed models lead to the same formula (if the pre-factor is neglected). The formula consists of two terms. The first term describes the energetic contribution from longitudinal forces, Ψ_N. It prevails when R becomes large or ρ becomes small. The second term describes the energetic contribution from plate bending, Ψ_M. It prevails when R becomes small or ρ becomes large as well as when d becomes large due to the fact that $D \propto d^3$ while $B \propto d$.

Due to the fact that the pre-factor of the first term is under debate, it will be referred to with the symbol Π. Concluding, the general equation is given by

$$G_c \geq G = \Pi B \left(\frac{R}{\rho}\right)^4 + \frac{D\,(1+\nu)}{\rho^2}. \tag{57}$$

The true numerical value will eventually have to be determined experimentally.

4 Experimental Framework

The wafer and substrate material, the surface preparation and characterization as well as the direct bonding process parameters are described in the following.

4.1 Choice of the Wafer and Substrate Material

Direct bonding for optical and opto-mechanical applications is generally applied using the materials Si, fused silica and other optical glasses, see Sec. 2.4. Among these materials is SCHOTT Borofloat® 33, in the following referred to as borofloat. It is a commonly used, versatile industrial oxide glass. In particular, borofloat has proven its suitability for the application of optical coatings, lithographic diffractive optical elements (DOEs) [240–242] as well as plasma-activated bonding (PAB) techniques [177]. Table III shows the relevant properties of the materials Si, fused silica and borofloat.

The workpieces on which the experiments are carried out exhibit large deflections, where an *in-situ* visual inspection of the contact front propagation is needed. Si is unsuited due to its anisotropic structure, relatively high YOUNG's modulus and opacity for visible light. A comparison of fused silica and borofloat shows that borofloat is more elastic. They have a similar bending strength. Borofloat is slightly more prone to react with water, which favors the investigation of the underlying mechanisms [243]. Borofloat is readily available in wafer geometry. Thus, borofloat is the material of choice.

Table III: Comparison of material properties. Data obtained from Refs. [99, 100, 103–106, 244–246]. For the ⋆-symbol, the first entry is a guaranteed value from the suppliers's data sheet [247] and the second entry is obtained from self-performed three-point flexural test experiments.

			Si	fused silica	borofloat
Mechanical Properties					
YOUNG's modulus	E /	GPa	130–170	72	64
POISSON's ratio	ν /	-	0.07–0.28	0.17	0.20
coeff. of thermal expansion	α /	$10^{-6}\,\mathrm{K}^{-1}$	3	0.57	3.25
bending strength	σ_b /	MPa	300	67	25, 87±8 ⋆
KNOOP's hardness (0.1/20)	H /	GPa	1100	550–570	480–490
Optical Properties					
application wavelength	λ /	µm	1.3–6.5	0.2–3.5	0.3–2.0
refractive index	n /	-	3.42–3.50	1.44–1.49	1.46–1.49
extinction coefficient	k /	-	$< 10^{-6}$	10^{-10}	10^{-8}
stress optical coefficient	C /	$\mathrm{m}^2\mathrm{N}^{-1}$	< 1	3.84	4.00–4.15
Structural Properties					
crystallinity			yes	no	no

4.2 Sample Procurement and Geometry

Wafers made of borofloat have been purchased from Nano Quarz Wafer GmbH, Langenzenn, Germany. In the case of experiments on cylindrical and acylindrical substrates, wafers of nominally 4 inches diameter, that is, $R = 50\,\text{mm}$, have been purchased which have then been diced into rectangular beams prior to bonding. In the case of experiments on spherical substrates, wafers of nominally 2 inches diameter, that is, $R = 25.4\,\text{mm}$, have been purchased. In all cases, four different nominal wafer thickness values, d, were investigated, namely $100\,\mu\text{m}$, $200\,\mu\text{m}$, $400\,\mu\text{m}$, $1000\,\mu\text{m}$.

Spherical lens substrates have been purchased from Eksma Optics, Vilnius, Lithuania. Four different curvature radii, ρ, were investigated, namely $518.7\,\text{mm}$, $1037.4\,\text{mm}$, $2593.6\,\text{mm}$ and $5187.2\,\text{mm}$. The direct bonding experiments performed with wafers on these lenses omit the annealing step such that coefficient of thermal expansion (CTE) matching is not required. Therefore, in this case, the lens material N-BK7 instead of borofloat has been chosen, which is easier available for lenses. Its surface is considered as chemically comparable to that of borofloat as long as no annealing is performed, which was the case. In the case of the demonstrator manufacture experiment, where annealing did take place, bi-convex cylindrical lenses custom-made of borofloat have been purchased from Optec Jena GmbH, Schorba, Germany.

4.3 Sample Preparation

For direct bonding, a surface roughness of $S_q < 0.5\,\text{nm}$ (obtained from an test area of $10 \times 10\,\mu\text{m}^2$) is typically required [73]. Surface topography measurements have revealed that the wafer surfaces are not sufficiently smooth. This is as expected, since due to manufacturing limitations roughness, waviness and shape variations increase as the wafers get thinner [248]. In order to obtain a sufficiently small and reproducible surface roughness, an additional polishing step was performed for all wafers. In particular, chemical-mechanical polishing (CMP) was applied. CMP, which is a key method in Si wafer technology for reducing surface roughness and waviness while additionally preserving the planarity by combining abrasive polishing and chemical etching [249], has been proven to be a suitable technique for realizing a surface roughness suitable for the application of direct bonding on a variety of glass materials [64, 250]. Here, if applicable, dicing of circular wafers to rectangular wafer beams was performed after the CMP step. This was done for ensuring a spatially homogeneous surface roughness.

4.4 Surface and Interface Characterization

After the CMP step and prior to direct bonding, the surfaces were characterized with regard to its surface roughness by using first, atomic force microscopy (AFM) and

second, vertical scanning interferometry which is also referred to as white light interferometry (WLI). As such, data from differently sized test areas, and consequently, from a large spatial frequency range, were obtained, cf. Sec. 2.3.1.

AFM uses a cantilevered physical probe that scans over the sample surface at a known spring constant. As the probe tip touches the sample surface, interactive forces are generated, and this leads to a deflection of the probe tip. A laser beam, which is reflected on the probe tip, measures its deflection. The resulting vertical imaging resolution is in the order of less than a nm. WLI is an optical technique where a light beam reflected by the sample surface recombines with a light beam reflected by an reference mirror. The resulting optical path difference then produces a pattern of interference fringes that is recorded. Vertical scanning is performed to acquire height data. WLI offers a lateral resolution of a few µm and a vertical resolution of around a nm [251].

Planarity measurements of the complete wafer surface could not be performed because the commonly used methods, for example, FIZEAU interferometry, do not work due to the wafers' back side reflections. Instead, tactile measurements were performed. In particular, thickness mappings were performed with the height measurement device TESA µHite, and surface altitude mappings were performed with the profilometer device PANASONIC UA3P.

After direct bonding, the interface was exemplarily characterized with regard to possible cavities of defects via microscopy. Here, a KEYENCE Digital Microscope VHX-6000 was used with top ring light illumination. The magnification is 200×. This setup allows a distinct observation of structures as small as approximately 1 µm. Another method for the inspection of bonding interface defects is scanning acoustic microscopy (SAM). This method works with ultrasonic sound waves instead of light. The lateral resolution of SAM is slightly worse than that of optical microscopes [252]. Because of this and due to the fact that borofloat is used which is optically transparent, optical microscopy is preferred over SAM.

4.5 Direct Bonding Process Parameters

In all cases, direct bonding was performed by conducting a typical PAB process flow, cf. Fig. 2.6, that is, prior to the contacting step the samples' surfaces were treated with a mixture of DIW, ammonia water and hydrogen peroxide (often referred to as "RCA1"-cleaning), a low-pressure plasma activation using the process gases O_2 and N_2, a mega-sonic assisted DIW rinse and a spin drying step before brought into contact. Contacting was performed in clean room conditions (class 2 according to the international standard [253]) to avoid particle contamination. After contacting, annealing at 200 °C for 10 h using a vacuum furnace without applying a static load was performed.

5 Development of a Novel Method for Determining the Bonding Energy (κ-Method)

In this section, a principle for measuring the bonding energy, G_c, is described and validated. This newly introduced principle will be referred to as κ-method.

5.1 Modeling Mixed Mode Bonding Energy Measurement

In Sec. 3.2.1, it has been derived that the strain energy release rate, G, is a function of the curvature, κ_{xx}, of acylindrical substrates, locally evaluated at the contact front position, x_c. The key idea is, that a measurement of the contact front position relates to a measurement of the bonding energy, G_c, according to

$$G_c = \frac{D}{2} \, [\kappa_{xx}(x = x_c)]^2 = \frac{D}{2} \, \kappa_{xx,c}^2, \tag{58}$$

given that the curvature at the contact front position, $\kappa_{xx,c}$, is known.

For this method to be able to provide suitable data that can be compared with other methods, for example with the DCB-method, the share of mode I bonding energy in the total bonding energy has to be determined. To start with, a wafer is considered which is put on an acylindrical substrate, where

(a) the substrate's curvature, $\kappa_{xx}(x)$, is strictly monotonically increasing (assuming that it increases from the right hand side toward the left hand side),

(b) during interface closure, the contact front propagation takes place leftwards, while at the right hand side, the wafer is already completely contacted, and

(c) the wafer is being assisted via an external force to fulfill complete area contact with the substrate. This process is assumed to be conducted in a frictionless way.

This makes it possible to regard a wafer which is already completely contacted with a convex acylindrical substrate. When removing the external force, separation will occur
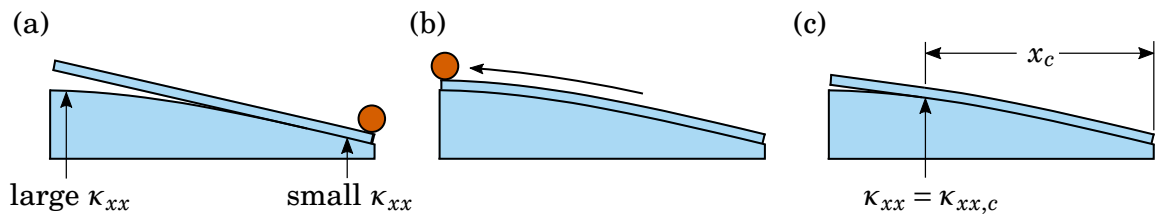

Figure 5.1: Schematic of the basic principle of the κ-method, where (a) a wafer is initially in contact with an acylindrical substrate, (b) then is completely contacted via an external force, and (c) after release of that force, it delaminates until its contact front reaches an equilibrium position.

such that the contact front will start propagating rightwards, given that at the wafer's edge the curvature is sufficiently large. The curvature at which the current contact front is located is equals $\kappa_{xx,c} := \kappa_{xx}(x = x_c)$, where x_c is the contact front position when static equilibrium is reached. A schematic of this process is shown in Fig. 5.1.

During interface closure, only bending moments in one direction will act on the wafer, that is, there is an uni-axial deformation. The non-contacted part of the wafer is not subjected to bending moments or longitudinal forces. Thus, Eq. (26) simplifies to

$$G_c = \Psi_M \Big|_{\partial \mathscr{A}_c} \tag{59}$$

which states that G_c is completely described by the strain energy per unit area evaluated *locally* at the contact front position.

Whenever a wafer is bent, for example downwards, the wafer's top side experiences a small stretching strain and the wafer's underside experiences a small compression (that is, squeezing) strain, ε_{xx}. An important question is therefore whether the contact front is subjected to mode I, mode II or mixed mode. Note that in Sec. 2.2.5, the DCB-method and the 4PT-method have been presented as examples for measurements methods of the bonding energy, G_c, in pure mode I and in mixed mode, respectively. In the case of the 4PT-method, debonding is performed after *changing* the curvature of the wafer pair.

In the case of the κ-method, debonding occurs with a *constant* substrate's curvature. Therefore, delamination is completely governed by the wafer's bending moment, M, evaluated at the contact front position. For one part of the bonding energy, that bending moment is related to a local curvature of the wafer, $\kappa_{xx}^{(\text{wafer})}$. This corresponds to mode I. The strain energy density is given by Ψ_I. For the other part of the bonding energy, that bending moment is related to a shear stress directly at the crack tip. This is because the partly bonded wafer's underside experiences a small but significant change in strain, ε, while separating from the substrate. This corresponds to mode II. The strain energy density is given by Ψ_{II}. Due to conservation of energy, it is assumed that $\kappa_{xx}^{(\text{wafer})}$ is slightly smaller than the local curvature of the substrate, $\kappa_{xx,c}$.

In total, the applicable strain energy per unit area due to bending is

$$\Psi_M = \mathscr{N} \times (\Psi_I + \Psi_{II}), \tag{60}$$

where $\mathscr{N} = \Psi_M/(\Psi_M + \Psi_{II})$ is a normalization factor, and Ψ_I and Ψ_{II} have been defined as unnormalized strain energy density values. The normalization will come in useful for expressing Ψ_I and Ψ_{II} with the local curvature of the substrate, $\kappa_{xx,c}$, as a variable, instead of using the local curvature of the wafer, $\kappa_{xx}^{(\text{wafer})}$, as a variable. The advantage of this procedure is that $\kappa_{xx,c}$ is easy to observe experimentally whereas

$\kappa_{xx}^{(\text{wafer})}$ cannot be observed directly. The bending part and the stretching part is equals

$$\Psi_I\Big|_{\partial\mathscr{A}_c} = \frac{1}{2}D\,\kappa_{xx,c}^2 \quad\text{and}\quad \Psi_{II}\Big|_{\partial\mathscr{A}_c} = \frac{1}{2}B\,\varepsilon_{xx,c}^2, \tag{61}$$

respectively, see Sec. 2.6.2, where $\varepsilon_{xx,c} := \varepsilon_{xx}(x = x_c)$. The calculation of Ψ_{II} evaluated at the contact front position requires to consider that the wafer's underside is in a compressed (that is, squeezed) state.

During delamination, any fixed point at the wafer's underside does not separate perpendicularly from the substrate, but follows a certain curve which can be calculated by the parametric representation of the substrate's involute where the corresponding path length scales according to the "relaxation" (that is, "decompression" or "unsqueezing") process, as shown in the appendix, see Sec. A.1.2. The curve's initial curvature radius is found to be

$$\rho^\star = \frac{\kappa_{xx,c}\,d^2}{4 - \kappa_{xx,c}^2\,d^2} \approx \frac{\kappa_{xx,c}\,d^2}{4}. \tag{62}$$

There is a local stress at the crack tip which distributes as a strain along the wafer's thickness according to

$$\varepsilon = \frac{\cos(\theta)\,\rho^\star}{d} \tag{63}$$

where the separation angle, θ, is yet to be determined. A consideration of the separation angle has proved useful in calculating the share of mode II bonding energy in the total bonding energy, see Refs. [254, 255]. With Eqs. (61) to (63), it is found that

$$\Psi_{II}\Big|_{\partial\mathscr{A}_c} = \frac{3\cos^2(\theta)}{8}D\,\kappa_{xx,c}^2. \tag{64}$$

Now, Eq. (60) can be solved to find $\mathscr{N} = 1/\left(1 + 3\cos^2(\theta)/4\right)$. An interim result is that

$$\frac{G_{Ic}}{G_c} = \frac{4}{3\cos^2(\theta) + 4} \tag{65}$$

is the share of mode I bonding energy in the total bonding energy. For the 4PT method, $\theta = 0$ holds, because the wafer pair is bent *after* contacting such that initial separation corresponds to in-plane shear movement. Therefore, $\cos^2(\theta) = 1$. As such, mode mixity is a function of how wafers were initially bonded.

In conclusion, with the presented approach it was possible to reproduce the result $G_{Ic}/G_c = 4/7$ from the 4PT-method, as presented in Sec. 2.2.5. In contrast, for the κ-method, the delaminating underside of the wafer follows a curve where at the approximated characteristic separation distance, $2\rho^\star$, the separation angle is

$$\theta = \arctan\left(\frac{2 + \sin(\kappa_{xx,c}\,d)}{1 - 2\sin(\kappa_{xx,c}\,d)}\right) \approx \arctan(2), \tag{66}$$

which is also derived in the appendix, see Sec. A.1.2 again. This implies $\cos^2(\theta) = 1/5$. Equation (65) becomes

$$\frac{G_{Ic}}{G_c} = \frac{20}{23} \approx 86.96\,\%. \tag{67}$$

When combining the results from above, the formula

$$G_c = \frac{D}{2}\kappa_{xx,c}^2 \times \Big(\underbrace{\frac{20}{23}}_{\text{mode I}} + \underbrace{\frac{3}{23}}_{\text{mode II}} \Big) \tag{68}$$

is obtained. The idea of splitting G_c comes from the fact that this is often done in crack propagation literature for the *fracture toughness* (defined as being proportional to the square of the bonding energy), where in this context the measure of mode I to mode II loading ratio is quantified by a so-called phase angle, ψ, see Ref. [256, Chap. II]. Equation (68) allows separately measuring the contributions of mode I and mode II bonding energy in the total bonding energy as a function of the observed static equilibrium curvature, $\kappa_{xx,c}$, observed at the substrate. This allows to compare the measured bonding energy values to those of the DCB-method.

5.2   Experimental Setup of the κ-Method

In order to accurately obtain the curvature from an observed contact front position, x_c, an acylindrical lens substrate is considered whose curvature is *linearly* increasing as a function of the x-coordinate, from $\kappa_{xx} = 0$ to $\kappa_{xx} = \kappa_{xx,\text{max}}$. Let $K := \mathrm{d}\kappa_{xx}/\mathrm{d}x$ be the proportionality factor, such that the relation

$$\kappa_{xx} = K\,x_c \tag{69}$$

holds. This geometry is exactly that of a cantilever which is clamped on one side and deflected by a force at its tip on the other side, see Fig. 5.2.
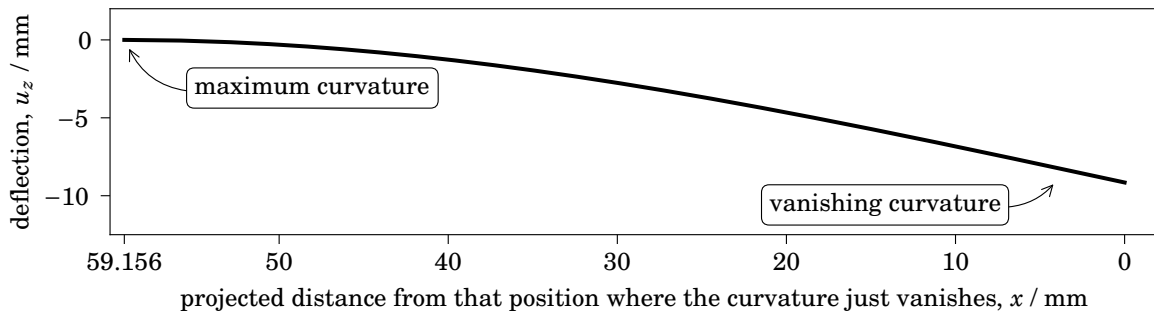
Figure 5.2: Shape of a clamped cantilever (with a free arc length of $L = 60\,\text{mm}$) which is deflected by applying a vertical force at the tip on the right-hand side. Here, $\kappa_{xx,\text{max}} = 7.69\,\text{m}^{-1}$. The x-axis is defined such that it yields the projected distance from the cantilever's tip where the curvature just vanishes. The force, P, has been chosen such that in any case the maximum bending stress is approximately equal to the guaranteed borofloat bending strength from the suppliers's data sheet, $\sigma_\text{b} = 25\,\text{MPa}$, cf. Tab. III. This gives $P = 17.639\,\text{mN} \times (d/100\,\mu\text{m})^2$.

When a wafer beam is placed on top of that substrate with first contact exactly at the end position (where the curvature, κ_{xx}, vanishes), then is completely contacted, and then is released, the contact front will spontaneously start propagating back towards decreasing curvature, as it has been shown in Fig. 5.1 (c). According to Eqs. (68) and (69), the mode I bonding energy is then calculated by

$$G_{Ic} = \frac{10D}{23} K^2 x_c^2.$$

(70)

Equation (70) allows a comparison to bonding energy values obtained by the DCB-method, see Sec. 2.2.5.

For practical reasons, instead of using a rigid lens substrate, another wafer beam is put on top of a milled brass support platform, fixed at both ends, so that it takes on the required shape, that is, the shape from Fig. 5.2. In particular, the κ-method experiments are performed with each two wafer beams of equal thickness, d, and width $B = 25.4$ mm. The *first* wafer beam, which is used as a substrate, has the length $L + 2 \times 3.5$ mm, with $L = 60$ mm. This wafer beam is placed and fixed on top of that brass support platform where those two parts of length 3.5 mm allow for the fixture on each side. The *second* wafer beam has the length L. It is put on top of the first wafer beam (with first contact at the end position where the curvature, κ_{xx}, vanishes). These two experimental procedure steps are shown in Figs. 5.3 (a) and (b). Prior to the annealing step, the second wafer beam is completely pressed down using a crossbar clamp, see Fig. 5.3 (c). Then, the complete tool which is holding the wafer beam pair is annealed. By removing that clamp after the annealing step, an intrinsic peeling (that is, bending) moment is introduced into the second wafer beam. This allows measuring the bonding energy again, see Fig. 5.3 (d).

If the design parameters L and K are given, the explicit geometry of the support platform can be calculated numerically. For the work presented in this thesis, four different support platforms (with $L = 60$ mm and different design parameters, K) were used to measure the bonding energy in different orders of magnitude according to the wafers' thickness. An overview is given in the appendix, see Sec. A.2.3. Also, an exemplary support platform's technical drawing is shown in the appendix, see Sec. A.2.4. A short approximation formula for calculating K from $\kappa_{xx,\mathrm{max}}$ and L, as well as a polynomial approximation for each of the support platforms' cantilever curves is given in the appendix, too, see Secs. A.2.5 and A.2.6.

The brass support platforms have been milled by a computerized numerical control (CNC) machine. It is conceivable that manufacturing limitations could create a manufacturing error of the proportionality factor. To quantify that error, ΔK, the support platforms were characterized with the profilometer presented in Sec. 4.4. It was
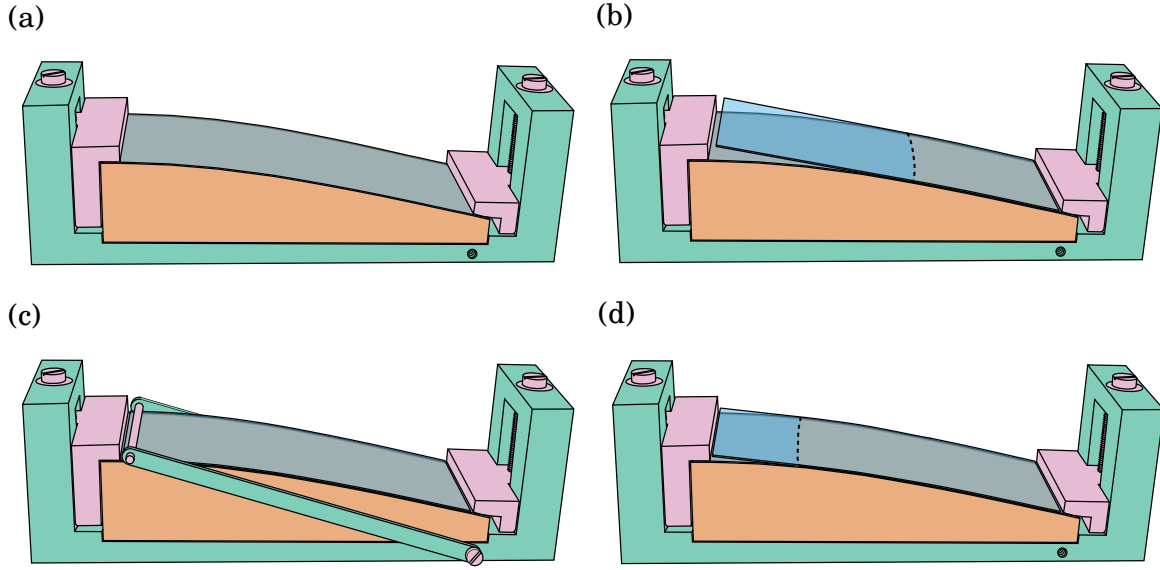
(a)

(b)

(c)

(d)

Figure 5.3: Non-planar direct bonding alignment and clamping tool, that is, the tool for the novel κ-method. Here, (a) shows the first wafer beam fixed on a brass support platform so that it takes on the required cantilever shape. (b) shows the second wafer beam put onto the first one, with the contact front (drawn as dashed curve) having reached its equilibrium position. (c) shows a crossbar clamp that is added prior to performing the annealing step for realizing complete area contact stable between both wafer beams. After the annealing step, see (d), the clamp is removed. In order to measure x_c, the contact front position projected to the x-axis has to be read, where $x = 0$ is located exactly at that position where the curvature just vanishes.

found that for the platform with the largest maximum curvature the deviation over the complete area is only up to 2 μm and it is very continuous and long-range like. This is less than the wafers' shape variation. At the critical area, that is, near $\kappa_{xx,\text{max}}$, the deviation is well below 0.5 μm. Thus, it is reasonable to neglect the manufacturing error of the proportionality factor.

5.3 Remarks on Method Validation and Data Evaluation

5.3.1 Application of the DCB-Method

For the validation of the results from the novel κ-method, the DCB-method was applied. With the DCB-method, the bonding energy is determined by the equation [118]

$$G_c = G_{Ic} = \frac{3}{16} \frac{E}{1 - \nu^2} \frac{w^2 d^3}{a^4} = \frac{9D}{4} w^2 a^{-4} \tag{71}$$

where w is the thickness of the razor blade (or thin, stiff gauge steel foil) and D is the wafer's flexural rigidity, see Sec. 2.6.2. A derivation of Eq. (71) is presented in the appendix, see Sec. A.1.5. Note that the κ-method's formula, see Eq. (70), and the DCB-method's formula, see Eq. (71), have different exponents of the measured length value.

The experiments were conducted on pairs of wafer beams. Here, the criterion $w < d/2.5$ needs to be maintained since Eq. (71) is derived from plate theory using the small-deflection approximation, cf. Sec. 2.6.1 and Ref. [216]. A blade insertion speed of

larger than $5\,\mathrm{mm\,s^{-1}}$ needs to be applied, so that any effect of insertion speed on the measurement result can be ruled out [257].

The steel foils are subject to manufacturing limitation. To quantify the corresponding thickness error, Δw, the foils were characterized with the height gauge presented in Sec. 4.4. For the thinnest foil, where $w = 40\,\mu\mathrm{m}$, the resulting thickness tolerance is below $0.05\,\mu\mathrm{m}$ with a total thickness variation below $0.15\,\mu\mathrm{m}$, so it is assumed that $\Delta w = 0.2\,\mu\mathrm{m}$. The results presented later are taking this error into account (even though it merely contributes to the total measurement error of G_{Ic}).

5.3.2 Measurement Length Correction

For the κ-method and the DCB-method, a length reading error of $\Delta x_c = 0.25\,\mathrm{mm}$ and $\Delta a = 0.10\,\mathrm{mm}$ is assumed, respectively. Note that for the κ-method, a larger reading error is assumed. This is because the contact front position, which is measured via the reflected light from interference fringes occurring in between of the two wafer beams, can be read more directly with the DCB-method than with the κ-method.

In both the DCB- and the κ-method, it is important to note that the real length, a or x_c, consists of a part that can be observed and another part that is invisible. This is because constructive wave interference requires the air gap between the bottom side of the top wafer and the upper side of the lower wafer to have a width of at least $\lambda/4$. If the air gap is becoming smaller, it is becoming invisible. In the context of the DCB-method, this has originally been pointed out by FOURNEL et al. [116]. In the frame of this thesis, it is assumed that $\lambda = 400\,\mathrm{nm}$ due to the use of visible light. The mathematical background as well as the reason for this assumption is explained in detail in the appendix, see Sec. A.1.6. In the case of the DCB-method, for each measured length, a_{meas}, the invisible length, a_{invis}, has been calculated numerically by exactly modeling the shape of one of the deflected wafer parts as a corresponding cantilever curve. In the case of the κ-method, it is much easier to correct the measured length, because the invisible part, $x_{c,\mathrm{invis}}$, is an explicit function of the local curvature, κ, the wavelength, λ, and the measured length, $x_{c,\mathrm{meas}}$. By using basic geometry, it can be shown that $\lambda/4 = 1/\kappa_{xx} \times (1 - \cos(\arcsin(\kappa_{xx} x_{c,\mathrm{invis}})))$. Rearranging yields

$$x_c = x_{c,\mathrm{meas}} - x_{c,\mathrm{invis}} = x_{c,\mathrm{meas}} - \sqrt{\frac{\lambda(8 - \lambda\kappa_{xx})}{16\kappa_{xx}}} \approx x_{c,\mathrm{meas}} - \sqrt{\frac{\lambda(8 - \lambda K x_{c,\mathrm{meas}})}{16 K x_{c,\mathrm{meas}}}} \qquad (72)$$

where the last approximation is valid because the proportionality factor, K, is small.

All measured bonding energy values have been corrected accordingly. In the case of the DCB-method, the calculated bonding energy is very sensitive with respect to performing that correction, whereas in the case of the κ-method, the calculated bonding energy is merely affected.

5.3.3 Method Validation Terminology

The term *accuracy* is defined as the closeness of the agreement between a test result, x, and the accepted reference value, x_{ref}. A test result can be a result calculated from several measurement values or it can be the measurement value itself. The term *accuracy* consists of trueness *and* precision: A true and precise test result is referred to as accurate [258, Secs. 3.1 & 3.5]. In the frame of this thesis, test results obtained from the DCB-method were considered as reference values.

If the test result stems from several measurement values, the term *trueness* refers to the closeness of the agreement between the expected value (that is, the arithmetic mean) and the accepted reference value. The term *precision* refers to the inverse of the imprecision, which is given by the range of scattering (that is, the empiric standard deviation) [258, Secs. 3.6 & 3.12].

If the test result stems from the measurement value itself, the term *trueness* refers to the closeness of agreement between the expected value (that is, the measurement value itself) and the accepted reference value. The term *precision* is in this case not applicable in the same way as above, instead, it is considered that the test result is subjected to random and systematic errors, which are, among other things, given by the discrimination threshold and bias, respectively, of the reading instrument [259, Secs. 3.2, 3.5 & 3.10].

A method is said to be *repeatable* if the range of scattering from several measurement values obtained under similar conditions is small [258, Secs. 3.13 & 3.14].

5.3.4 Calculation of the Error Bars

If a test result, z, is calculated indirectly from a given function, $z \propto x^b y^c$, where x and y are direct measurement values with given errors, Δx and Δy, respectively, the resulting error of the test result is given by the formula

$$\Delta z = \left| x^b y^c - (x \pm \Delta x)^b (y \pm \Delta y)^c \right| \tag{73}$$

$$\approx \left| b z \frac{\Delta x}{x} \mp \frac{b(1-b)}{2} z \left(\frac{\Delta x}{x} \right)^2 + c z \frac{\Delta y}{y} \mp \frac{c(1-c)}{2} z \left(\frac{\Delta y}{y} \right)^2 \right| \tag{74}$$

$$\approx b z \frac{\Delta x}{x} + c z \frac{\Delta y}{y}. \tag{75}$$

Equation (74) was obtained by calculating the TAYLOR series at $\Delta x = 0$, $\Delta y = 0$ for each factor. It shows that the error bar is asymmetrical if the function is not linear, that is, if $b, c \notin \{0, 1\}$. This is the case for both the κ-method and the DCB-method, where the bonding energy is given by $G_c \propto K^2 x_c^2$ and $G_c \propto w^2 a^{-4}$ according to Eqs. (70) and (71), respectively.
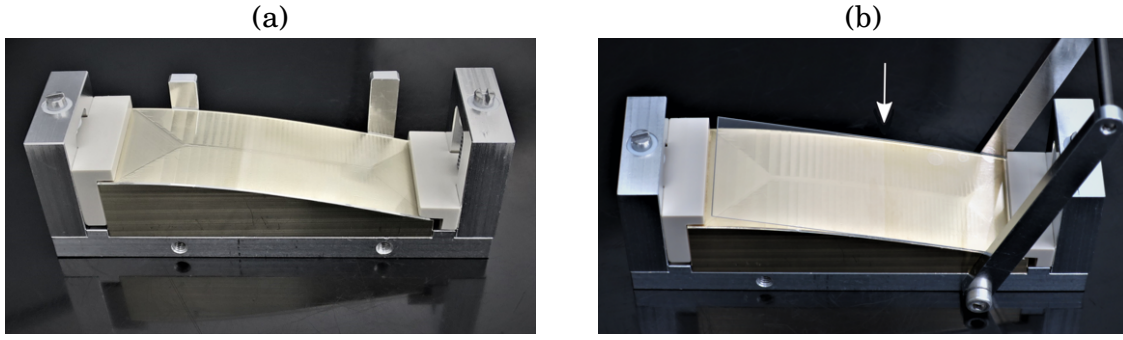
Figure 5.4: Photos of an experiment conducted with the novel κ-method. (a) shows the stage where the first wafer has been fixed on top of the support platform, (b) shows the stage where the contact front is taking on its equilibrium value after the annealing step, where an arrow indicates the contact front position. (Here, each wafer beam has a thickness of $d = 400\,\mu\text{m}$ and the support platform has a maximum curvature of $\kappa_{xx,\text{max}} = 7.69\,\text{m}^{-1}$.)

For the calculation of the error bars of any bonding energy measurement throughout this thesis, Eq. (73) is used. For a qualitative discussion of the accuracy of the κ-method and the DCB-method, Eq. (75) is used.

5.4 Bonding Energy Measurement Results

In the following, a comparison of the κ-method and the DCB-method with regard to measurement accuracy and repeatability is done. Photos of an actual experiment conducted with the κ-method are shown in Fig. 5.4. For now, only bonding energy measurement results of initially contacted samples are presented, that is, no annealing has been performed. Bonding energy measurement results of annealed samples will be presented later in Sec. 6. For all experiments presented in this section, a support platform with $\kappa_{xx,\text{max}}$ has been used.

In order to compare the measurement repeatability of the κ-method and the DCB-method, $N = 7$ identical contacting experiments on each two wafer beams were performed. In all cases, the nominal thickness of the wafer beams was $d = 200\,\mu\text{m}$. For the κ-method, a support platform that is defined by the design parameter $\kappa_{\text{max}} = 3.90\,\text{m}^{-1}$ was used, setting the measurement range to a maximum value of $441\,\text{mJ}\,\text{m}^2$. This is a reasonable value because for the initial contact, a bonding energy of about 100 to $400\,\text{mJ}\,\text{m}^2$ is expected [97]. For the DCB-method, a steel foil for insertion with a thickness of $w = 40\,\mu\text{m}$ was used.

The results are shown in Fig. 5.5. For each single measurement, both methods yield consistent results, but the resulting bonding energy error, ΔG_{Ic}, of the κ-method is more than five times smaller than that of the DCB-method. This shows that the κ-method is capable to more accurately measure the bonding energy. The κ-method's high accuracy is, first, due to the exponent 2 of the measured length, x_c, see Eq. (70), as compared to the exponent 4 of the DCB-method, see Eq. (71). Second, the DCB-method
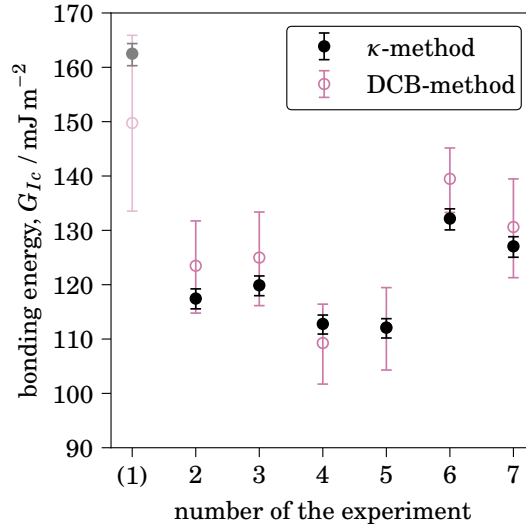
Figure 5.5: Bonding energy, G_{Ic}, between each two contacted wafer beams measured with the κ-method and the DCB-method. The wafers' nominal thickness is $d = 200\,\mu m$. The experiment has been conducted $N = 7$ times in order to study the repeatability. Each data point represents an individual measurement value. The error bars have been calculated from the length reading error, Δx_c or Δa, and the foil thickness error, Δw. The result of the first experiment is drawn in a lighter shade because it is considered as an outlier, see explanation in the text.

requires $w < d/2.5$, which makes a smaller, so that the ratio $\Delta a/a$ may become very large (particularly for very thin samples). In contrast, the κ-method allows to choose a platform that matches the correct measurement range, which increases x_c, so that $\Delta x_c/x_c$ becomes small.

By comparing the $N = 7$ results with each other, it can be seen that the first measurement result is significantly larger than the other results. This is because the first experiment has been conducted only three months after the CMP step, while the other six experiments have been conducted from 16 to 19 months after the CMP step. It is known that a glass surface may degrade over time due to storage in humid air [260, Chap. 11.2.1]. As such, the first experiment must not be considered as performed under identical conditions. Therefore, in Fig. 5.5 the first measurement result is drawn in a lighter shade.

In the case of the second to seventh experiment, any two neighboring measurement results have almost the same value. This is because each such experiments were conducted on the same day. It is assumed that there have been uncontrolled experimental parameters, such as lab air humidity or air pressure which may slightly change from day to day. The resulting scatter, which is observed with both methods, is therefore a consequence of the experimental setup. For the practical application, this means that it is important to carefully control such external experimental parameters if a highly reproducible test result is required. In that case, the κ-method is to be preferred over the DCB-method due to its higher accuracy.

5.5 Assessment of the κ-Method

The DCB-method is the established method for measuring the bonding energy, G_{Ic}, between the interfaces of glass wafers joined via direct bonding [118]. It has been shown that the novel κ-method is capable of accurately measuring the bonding energy between thin glass wafers. Both methods have in common that they require rectangular, thin wafer beams. The DCB-methods provides the pure mode I bonding energy, G_{Ic}. Stricly, this is true only if both wafer beams have the same thickness, or more precisely, the same flexural rigidity. The κ-method provides a mixed mode bonding energy where it is possible to calculate the mode I bonding energy, G_{Ic}. For the κ-method, only the thickness, or more precisely, the flexural rigidity, of the top wafer beam is relevant. A comparison of the advantages and disadvantages of the DCB-method and the κ-method is presented in the following.

Considering the equipment and tooling requirements in relation to the measurement accuracy achieved, the DCB-method requires only a razor blade or a thin stiff foil of a certain thickness w. Due to the condition $w < d/2.5$ on which Eq. (71) for the bonding energy calculation is based, the resulting gap opening length, a, can become very small, especially in the case of thin wafers and large expected bonding energy values. This results in a high measurement error, $\Delta G_{Ic} \approx 4 G_{Ic} \times \Delta a/a$, see Eq. (75). In contrast, the κ-method requires a bonding tool and a support platform, as shown in Fig. 5.4. This requires some initial manufacture effort. The geometry of the platform can be designed according to a certain maximum curvature value, $\kappa_{\max}$, so that the resulting measurement error, $\Delta G_{Ic} \approx 2 G_{Ic} \times \Delta x_c/x_c$, is considerably smaller. Another reason why for the κ-method the resulting measurement error is smaller is because the numerical prefactor is 2 instead of 4.

For thin wafers with large expected bonding energy values, measuring the bonding energy can be challenging, both in the case of the DCB-method and the κ-method. In the case of the DCB-method, the measurement error is very high, as explained above. When using the κ-method, a support platform would be required that has such a large value of $\kappa_{\max}$ that it would not fit into the currently used bonding tool frame. However, technically it is possible to design such a bonding tool frame.

When using the DCB-method to measure the bonding energy of an annealed wafer pair, there is a high risk of glass breakage during razor blade insertion. In contrast, with the κ-method, glass breakage is very unlikely, regardless of wafer thickness and bonding energy. The DCB-method leaves scratches at the interface, whereas the κ-method does not. Therefore, when using the κ-method, it would still be possible to perform a characterization of an undisturbed surface after surface separation.

The κ-method contacts the wafer pair in a non-planar way. This has some disadvantages when it comes to advanced characterization techniques. For example, scan-

ning acoustic microscopy (SAM) defect inspection of the bonded wafer pair is likely to be limited. Finally, in terms of process flow, the κ-method requires wafer cutting or dicing prior to the direct bonding step. In contrast, the DCB-method allows the wafer to be cut or diced both before and after the direct bonding step.

For a summary of the advantages and disadvantages of both methods, see Tab. IV. In conclusion, the κ-method is the preferred method when an accurate bonding energy measurement of directly bonded wafers is required.

Table IV: Overview of the advantages and disadvantages of the DCB-method and the κ-method.

	DCB-method	κ-method
sample geometry	rectangular wafer beams	rectangular wafer beams
crack growth mode	pure mode I (*if* both wafer beams have the same thickness)	mixed mode I and II
equipment	very low effort: provision of a razor blade or thin foil with a suitable thickness, w	moderate effort, once: manufacture of a platform with a suitable max. curvature value, $\kappa_{\max}$, and a clamping tool
measurement error	large: $\Delta G_{Ic} \approx 4 G_{Ic} \times \Delta a/a$ $+2 G_{Ic} \times \Delta w/w$, where a has an upper limit due to the condition $w < d/2.5$	small: $\Delta G_{Ic} \approx 2 G_{Ic} \times \Delta x_c/x_c$ $+2 G_{Ic} \times \Delta K/K$, where x_c may become substantially large depending on L and K
breakage of thin wafers	high risk during blade or foil insertion	low risk
defect inspection at the bonded wafer pair	no restrictions	scanning acoustic microscopy (SAM) is restricted
process flow	wafer cutting can be performed prior to or after the direct bonding step	wafer cutting has to be performed prior to the direct bonding step

6 Investigation of the Direct Bonding Mechanism

For studying the direct bonding mechanism and the underlying chemical reactions occurring at the direct bonding interface, direct bonding of wafers with different nominal thickness values was investigated, which corresponds to the investigation of wafers with different surface topography conditions.

6.1 Surface Topography Characterization

A high surface roughness is expected to directly reduce the bonding energy [112]. A large surface shape variation is expected to impose mechanical stress during the direct bonding contacting step. This reduces the adherence, that is, the work of separation, thus, indirectly yields smaller measured bonding energy values [176, 223]. Surface shape variation may also manifest as thickness variation [261]. The surface waviness plays an intermediate role, as it affects the measured bonding energy both directly and indirectly. As proposed by TURNER [262], the criterion for the surfaces to not separate, see Eq. (23), can be adjusted such that the bonding energy, G_c, becomes a function of the strain energy release rate, G, itself.

In the following, measurement results for the surface thickness variation, shape variation, waviness and roughness as a function of the wafer thickness are presented. As presented Sec. 4.4, tactile measurements, white light interferometry (WLI) and atomic force microscopy (AFM) were applied.

6.1.1 Wafer Thickness Variation Characterization

The spatial variation of the local thickness, d_{local}, was investigated for each wafer's nominal thickness value, d. It was exemplarily characterized at wafers of 4 inches diameter. From this data, the spatial variation of the relative flexural rigidity has been calculated, which is here defined as

$$\frac{D_{\text{local}}}{D_{\text{average}}} := 1 - \left(\frac{d_{\text{local}}}{d_{\text{average}}}\right)^3. \tag{76}$$

This is done because the flexural rigidity is a more meaningful quantity for predicting contacting success, as it correlates with the strain energy per unit area, see Eq. (19).

Figure 6.1 shows the spatial variation of the relative flexural rigidity. With a distance of 20 mm between each neighboring data point, the scanning resolution is low. Still, it can be seen that thin wafers have larger a variation than thick ones. This is as expected due to manufacturing limitations known for thin wafers [248].
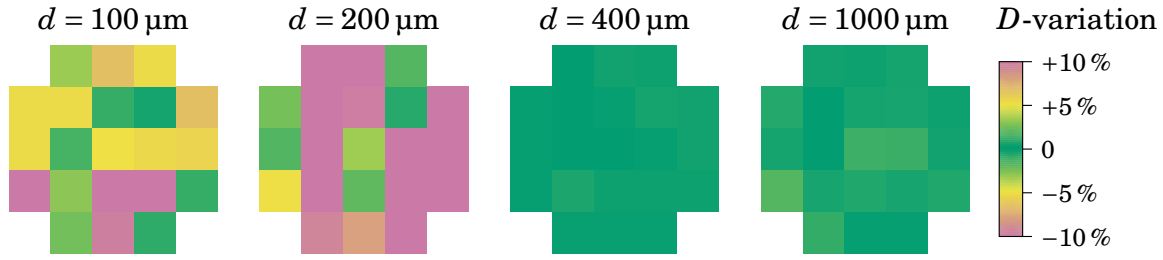
Figure 6.1: Heat maps of the variation of the relative local flexural rigidity, $D_{\mathrm{local}}/D_{\mathrm{average}}$, for each wafer thickness value, d. The test area is the complete wafer, that is, a circular area of 100 mm diameter. Data are calculated from measurements of the local thickness, d_{local}.
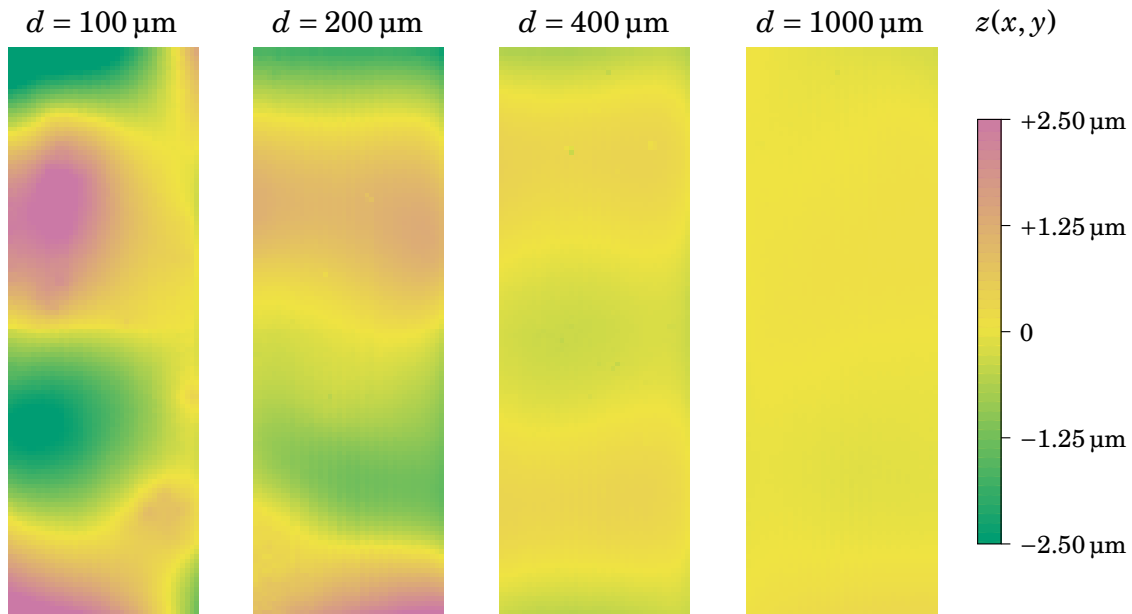

Figure 6.2: Heat maps of the surface topography, $z(x,y)$, of exemplary wafer beams, representing the wafers' shape variation. The test area is $20 \times 60\,\mathrm{mm}^2$ in all cases. The data are presented after subtracting a best fit paraboloid in order to remove the very large spatial frequency range data which would be redundant information as they are already considered in Fig. 6.1.

6.1.2 Surface Shape Variation Characterization

The surface shape variation refers to local deviations from a perfect plane in the low spatial frequency range (LSFR). It was exemplarily characterized at wafer beams via a profilometer at a test area of $20 \times 60\,\mathrm{mm}^2$ with a distance of $0.5\,\mathrm{mm}$ between each data point. It is useful here to define the LSFR as the measured range between $1/(20\,\mathrm{mm}) = 5 \times 10^{-5}\,\mathrm{\mu m}^{-1}$ and $1/(0.5\,\mathrm{mm}) = 2 \times 10^{-3}\,\mathrm{\mu m}^{-1}$. During the measurement, the wafer beams were placed on a sticky underground. Thus, the obtained shape variation may partly be a result of the wafer's thickness variation. For direct bonding, the cause of these shape variation is irrelevant, cf. Refs. [261, 263, 264].

The result is shown in Fig. 6.2. It can be seen that the surface becomes less planar with decreasing wafer thickness, d. This finding is confirmed by the calculated peak-to-valley (PV) and S_q-values, see Tab. V. According to Eq. (76), those PV values

Table V: Statistical values obtained from the shape variation data, see Fig. 6.2.

nominal wafer thickness	$d = 100\,\mu m$	$d = 200\,\mu m$	$d = 400\,\mu m$	$d = 1000\,\mu m$
PV/μm	7.66	4.95	1.12	0.55
S_q/μm	1.35	0.86	0.24	0.08

correspond to a relative flexural rigidity variation of $\pm 11\,\%$ and $\pm 0.1\,\%$ for the smallest and largest wafer thickness, respectively, assuming that the measured shape variation is due to thickness variation. This is consistent to the finding for the thickness variation, see Fig. 6.1.

6.1.3   Surface Waviness and Roughness Characterization

The surface waviness and roughness was exemplarily characterized at different spatial frequency ranges via WLI at the test areas $700 \times 520\,\mu m^2$ and $140 \times 105\,\mu m^2$ as well as via AFM at $10 \times 10\,\mu m^2$ and $1 \times 1\,\mu m^2$, as described in Sec. 4.4. All surface topography measurements were performed after the CMP step. It is useful to define the mid-spatial frequency range (MSFR) as the measured range between 2×10^{-3} and $5 \times 10^{-1}\,\mu m^{-1}$, and the high-spatial frequency range (HSFR) as the measured range between 5×10^{-1} and $2 \times 10^2\,\mu m^{-1}$.

The definitions for LSFR, MSFR and HSFR, which correspond to shape variation, waviness and roughness, corresponds to the typical definitions used in the field of optics. Note that some authors use the terms LSFR, MSFR and HSFR for slightly other spatial frequency ranges, depending on the authors' field of work.

Figure 6.3 shows the surface waviness as well as the surface roughness measured at exemplary wafers with $d = 100\,\mu m$ and $d = 1000\,\mu m$. At a very small test area (namely, $1 \times 1\,\mu m^2$) there is no significant difference, while at a very large test area (namely, $700 \times 520\,\mu m^2$) there is a significant difference where thin wafers have a much wavier surface than thick ones.

For each of the four considered wafer thickness values, d, the combined power-spectral density (PSD) function is shown in Fig. 6.4. The data are drawn on a log-log-scale. As expected, the curves appear approximately as straight lines, with an average negative slope of $\zeta = 2.751 \pm 0.005$ which is a typical value for polished glass surfaces, cf. Ref. [129]. The LSFR is shown on the left-hand side of the diagram. It is found that in the HSFR all curves lie closely together. However, towards the MSFR the curves are diverging away from each other, particularly for very low spatial frequencies. This divergence may look small, but the related surface waviness difference is significant, as it is shown in Fig. 6.3. Towards the LSFR, the curves diverge even more away from each other.
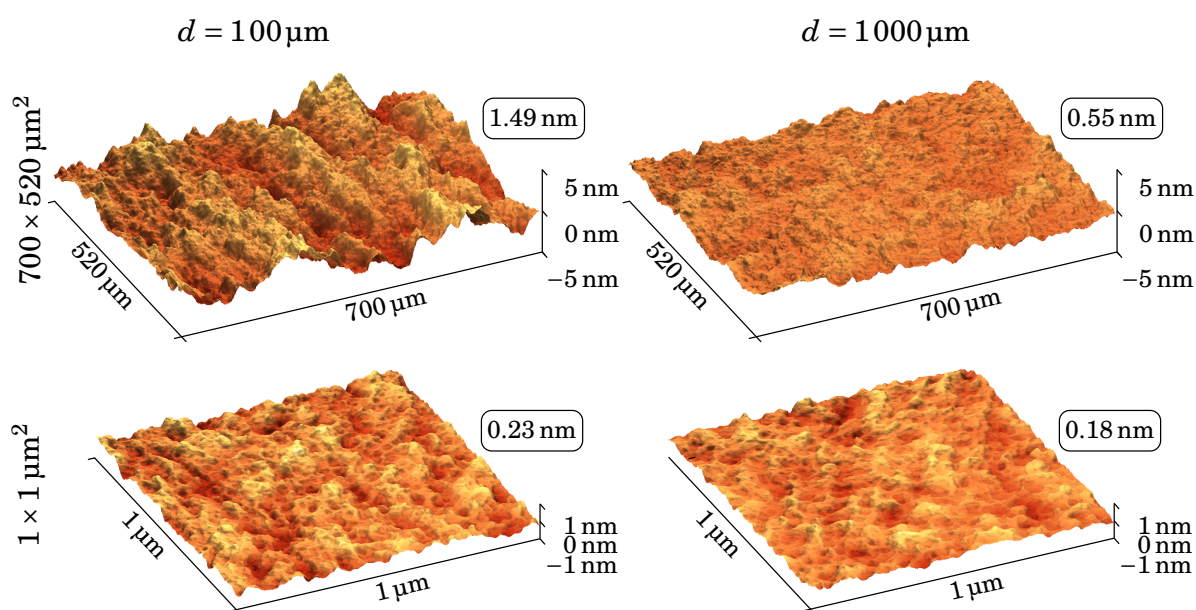
Figure 6.3: Exemplary surface topographies of a $d = 100\,\mu m$ thick wafer (left-hand side) and $d = 1000\,\mu m$ thick wafer (right-hand side). For each image, the S_q-value is presented in a box with round edges. Data have been obtained using WLI on a $700 \times 520\,\mu m^2$ test area (top) and AFM on a $1 \times 1\,\mu m^2$ test area (bottom). For a better visualization, a median filter of 7 px has been applied to the images.
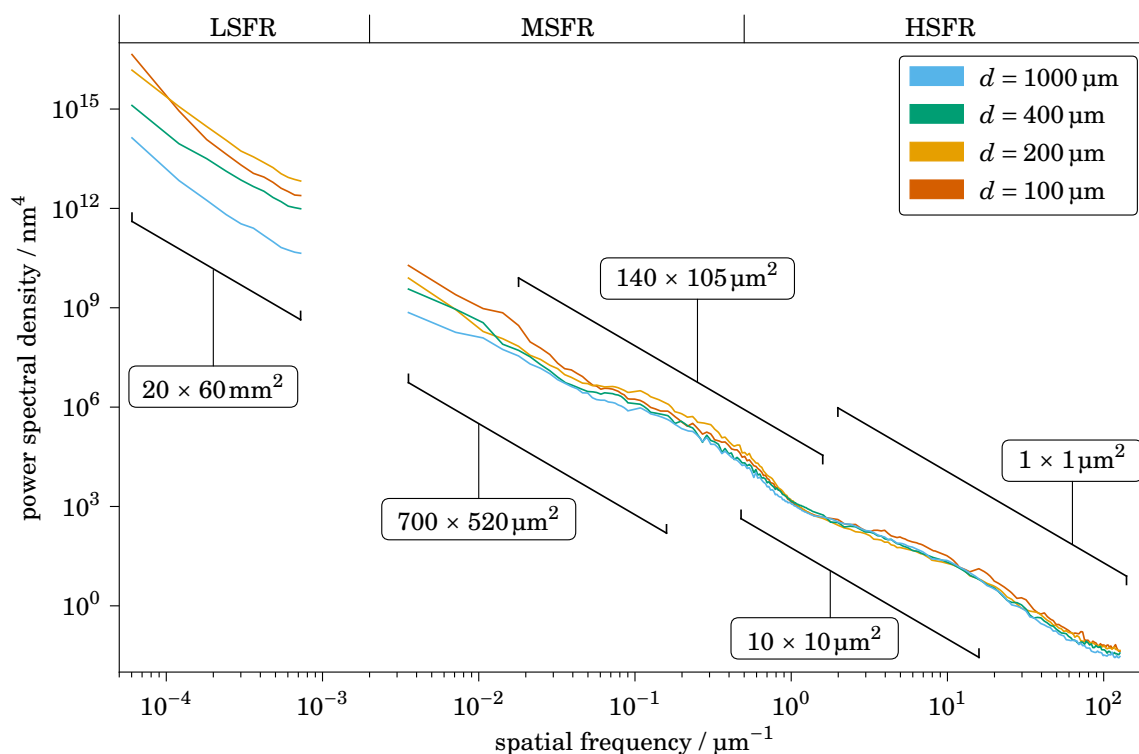

Figure 6.4: PSD functions, where for each thickness value, d, a wafer was measured exemplarily at five different test areas (see indications). Data is plotted on a log-log-scale. Each line gives the resulting combined PSD calculated according to Ref.[265]. The LSFR corresponds to the shape variation, the MSFR to waviness and the HSFR to roughness.

6.1.4   Summarized Correlation of Wafer Thickness and Surface Topography

For the borofloat wafer samples investigated in this thesis, a conclusion can now be drawn by considering all results from above. The conclusion is that the thinner a wafer gets, the more thickness variation and the more shape variation it has and the more wavy it becomes while still remaining very smooth. This corresponds to that what is expected according to the literature, see Ref. [248]. In the following, the focus of the data evaluation and discussion lies on waviness and roughness, because these parameters directly affect the bonding energy, as explained above.

In wafer direct bonding literature, the surface shape variation (as defined in this thesis) is often referred to as *warp*. The also often used term *bow* refers to more long range surface deviations which are not considered in this thesis because their effect vanishes when deforming the wafer during the non-planar direct bonding process.

6.2   Bonding Energy Measured via κ-Method and DCB-Method

In order to investigate the bonding energy for different direct bonding process steps, ac-

Table VI: Process step overview, defining when a measurement of the bonding energy takes place.

process step description	designation
after initial contacting (that is, prior to annealing)	"initial"
after annealing and $(10 \pm 2)\,$s after peeling moment introduction	"annealed"
after annealing and $(120 \pm 10)\,$s after peeling moment introduction	"corroded"

Figure 6.5: Bonding energy, G_{Ic}, between borofloat wafer beams with varying nominal thickness values, d, measured at different direct bonding process steps, see Tab. VI. Data are presented with a different scaling in the lower an upper part of the y-axis. Note that in some cases the κ-method could not be applied for measuring the annealed and corroded bonding energy because a support platform with a sufficiently large K-value could not be manufactured for the available clamping tool.

cording experiments were performed with the κ-method and the DCB-method. In the case of experiments conducted at annealed samples, the bonding interface was investigated visually for interface defects at the vicinity of the expected delamination front, with the result that no defects were observed.

6.2.1 Evolution of the Bonding Energy

The evolution of the mode I bonding energy, G_{Ic}, was studied by applying the κ-method and the DCB-method at three different process steps, namely those which are described in Tab. VI. The designation "corroded" is chosen due to a proposed water stress corrosion mechanism, as introduced in Sec. 2.5.3. It is worth recalling that the peeling moment is introduced either by removing the crossbar clamp (κ-method) or by pushing the razor blade or steel foil farther into the interface (DCB-method).

The bonding energy measurement results are shown in Fig. 6.5. The κ-method's error bars are smaller than those of the DCB-method. In fact, the κ-method's error bars are barely visible. The bonding energy increases by at least an order of magnitude from the initial to the annealed state. Both in the initial state and in the annealed state, thin wafers show smaller bonding energy values than thick wafers. In the corroded state, the bonding energy has dropped such that it is approximately the same for all wafer thickness values.

6.2.2 Bonding Energy and Surface Topography

It can be assumed that the wafer thickness, d, is not directly causing the observed differences in bonding energy, G_{Ic}. Instead, the wafer's waviness is, as it is shown in Sec. 6.1 that this properties correlates with the wafer thickness, d. Therefore, it is proposed that direct bonding of thin wafers would yield the same bonding energy as direct bonding of thick wafers when there is a comparable surface topography.

To test this hypothesis, a careful thinning process at a thick wafer ($d = 1000\,\mu m$) via multi-step grinding is performed for obtaining a thin wafer ($d = 100\,\mu m$), followed by a CMP step and then a dicing step to obtain wafer beams. Using AFM and WLI, the surface roughness of those wafer beams was characterized. The result is shown as purple curve in Fig. 6.6. The waviness of the thinned wafer is now much smaller than that of all other wafers, whereas roughness is still similar for all wafers. Presumably, the in-house thinning process is different than that of the wafer manufacturer, which is why the waviness is even better. As such, it is possible to predict that the bonding energy of the interface of such wafers should now have significantly increased.

Using the DCB-method, and if applicable also the κ-method, the bonding energy (for all three process steps according to Tab. VI) was measured. The result is shown in Fig. 6.7. Indeed, the thinned wafers' bonding energy is similar to that of thick wafers.

Figure 6.6: PSD functions for the ground and polished borofloat wafer's surface, along with data from Fig. 6.4. Only data from the MSFR (that is, waviness) and HSFR (that is, roughness) are shown.
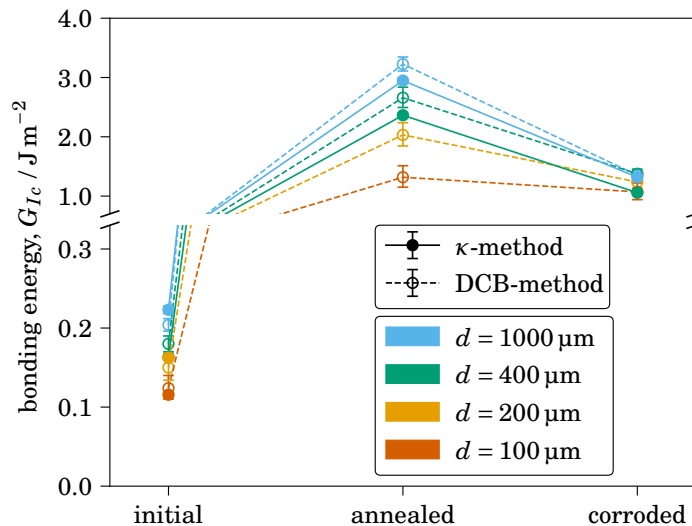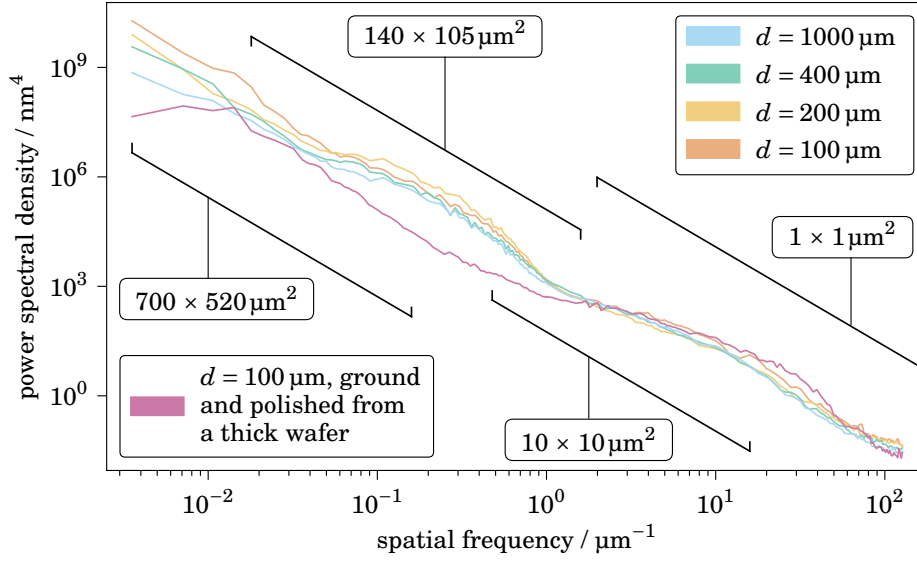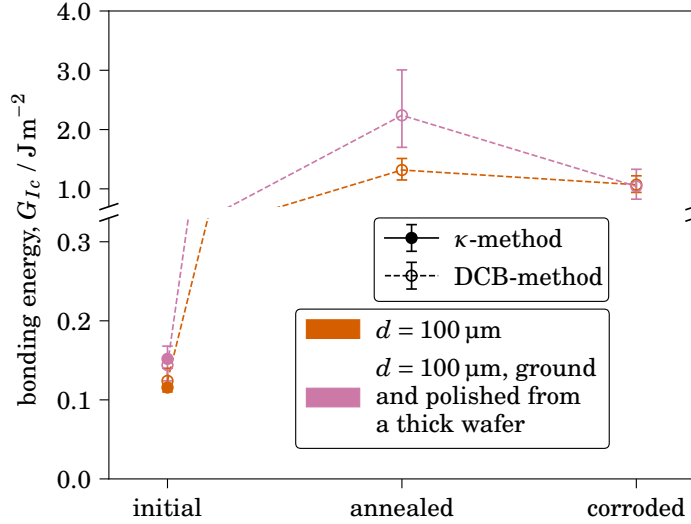

Figure 6.7: Bonding energy, G_{Ic}, between borofloat wafer beams with the same nominal thickness, d, for different direct bonding process steps, see Tab. VI. It shows a variation of the surface preparation, where the data of the orange curve are taken from Fig. 6.5. Again, note that in some cases the κ-method could not be applied for measuring the annealed and corroded bonding energy because a support platform with a sufficiently large κ_{max}-value could not be manufactured for the available clamping tool.

In the previous section, it was found that the bonding energy measured in the corroded state has dropped as compared to the bonding energy measured in the annealed state. This is proposed to be due to water stress corrosion.

6.3   Investigation of the Water Stress Corrosion Reaction

From the experimental data it does not become clear if in the annealed state

(a) the bonding energy which would be measured in the exact moment of the peeling moment introduction, that is, $G_{Ic}(t = 0)$, or

(b) the dropping rate, or   (c) both, that is, (a) *and* (b),

is / are correlated with the wafer surface topography, see Fig. 6.8. This is why time-resolved bonding energy measurements were conducted.
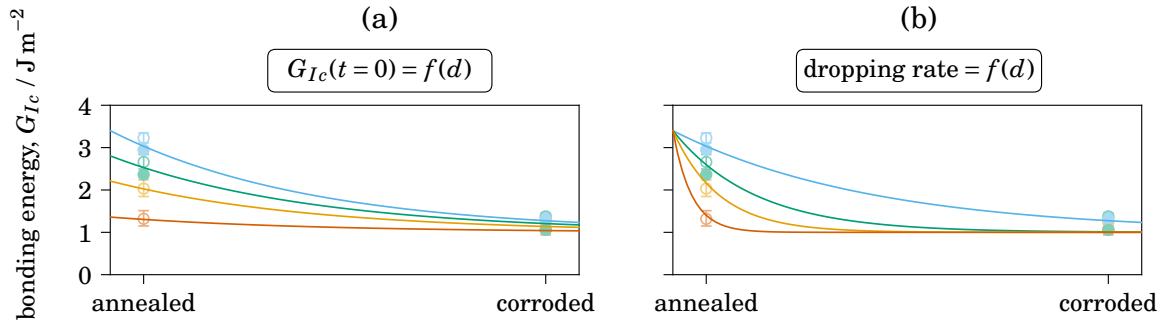
Figure 6.8: Qualitative depiction of two scenarios of the bonding energy time evolution, $G_{Ic}(t)$, with data points from Fig. 6.5 (a) drawn in a lighter shade. The curves' colors correspond to the wafers' nominal thickness values from Fig. 6.5. In scenario (a), the dropping rate is the same while $G_{Ic}(t = 0)$ is a function of the surface topography. In scenario (b), $G_{Ic}(t = 0)$ is the same while the dropping rate is a function of the wafer surface topography. (The wafer surface topography is represented by the wafer thickness, d, cf. Sec. 6.1.4.) In both scenarios, the settled bonding energy, $G_{Ic}(t \to \infty)$, is the same.

Figure 6.9: Measured values of the bonding energy, G_{Ic}, as a function of the time passed since the peeling moment introduction, t, where the experiments were conducted with the DCB-method. The surface separation took place in humid air (top) and in dry nitrogen (bottom). (The wafer surface topography is represented by the wafer thickness, d, cf. Sec. 6.1.4.)

6.3.1   Time-Resolved Bonding Energy Measurement

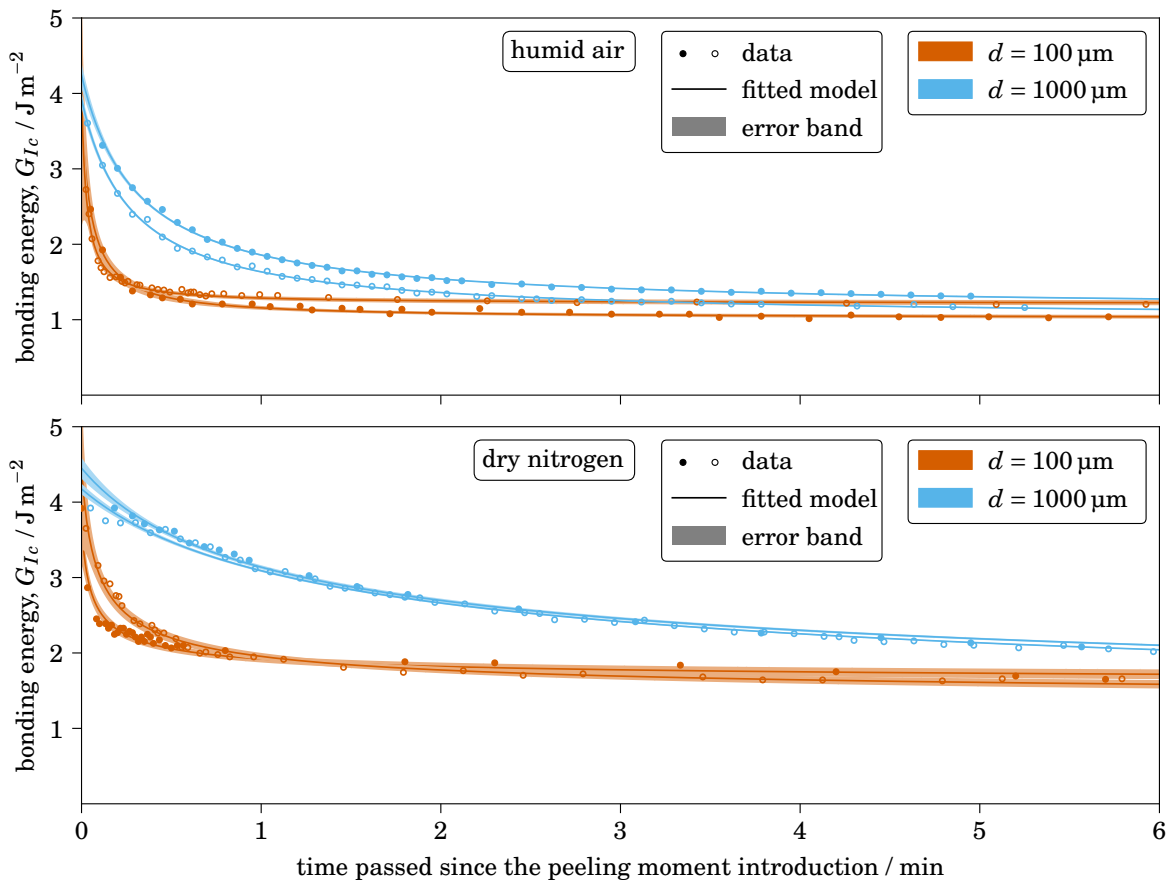The DCB-method was conducted at bonded pairs of borofloat wafer beams with nominal thickness $d = 100\,\mu\text{m}$ and $d = 1000\,\mu\text{m}$, first, in a laboratory environment with humid air ($\approx 7000\,\text{ppm}\ H_2O$), and second, in a glove box filled with dry nitrogen ($< 0.1\,\text{ppm}\ H_2O$). The contact front position is measured every few seconds until static equilibrium has set in. By doing this, the bonding energy, G_{Ic}, as a function of time, t, is measured. The experiment is performed twice for each value of d for each atmospheric condition. The results are shown in Fig. 6.9. For the following discussion, two parameters are introduced, namely, the incipient bonding energy, $G_{Ic,0} := G_{Ic}(t = 0)$, and the settled bonding energy, $G_{Ic,\infty} := G_{Ic}(t \to \infty)$.

In order to quantitatively investigate the underlying molecular mechanism, it is proposed that the water stress corrosion takes place within two different ways, depending on the atmosphere condition. In the following, both for humid air and for dry nitrogen, a chemical reaction kinetics model is derived.

In the case of humid air, it is proposed that the water stress corrosion reaction is described by a (pseudo) second order reaction. For the first reactant, H_2O, it can be assumed that its concentration, $C_{H_2O}(t)$, hardly changes from its original value, $C_{H_2O,0}$, because in humid air there is enough H_2O available. The second reactant, Si–O–Si, is of order two because it reacts to two Si–OH molecules. Its original concentration is $C_{\text{Si–O–Si},0}$. Thus, the rate law is given by

$$\frac{dC_{\text{Si–OH}}(t)}{dt} = -\frac{dC_{\text{Si–O–Si}}(t)}{dt} = k\,C_{H_2O,0}\,C_{\text{Si–O–Si}}^2(t) \tag{77}$$

where k is the reaction rate constant. The solution of that equation is $1 - C_{\text{Si–OH}}(t) = C_{\text{Si–O–Si}}(t) = 1 / \left(k\,t\,C_{H_2O,0} + 1/C_{\text{Si–O–Si},0} \right)$, see Ref. [266, Chap. 2-2]. Instead of considering the concentrations, it is more useful to consider the bonding energy. By assuming that the bonding energy in the incipient state and in the settled state is proportional to $C_{\text{Si–O–Si}}(t)$ and to $C_{\text{Si–OH}}(t)$, respectively, the equation can be rewritten as

$$G_{Ic}(t) = G_{Ic,\infty} + \left(G_{Ic,0} - G_{Ic,\infty} \right) / \left(1 + k_{\text{eff}}\,t \right). \tag{78}$$

In this equation, the effective reaction rate constant has been introduced as $k_{\text{eff}} := k\,C_{H_2O,0}\,C_{\text{Si–O–Si},0}$. There are three fitting parameters, namely, $G_{Ic,0}$, $G_{Ic,\infty}$ and k_{eff}.

In the case of dry nitrogen, the water stress corrosion reaction can be described by a third order reaction. Here, the first reactant, H_2O, is being consumed during the reaction. It is of order one. Note that H_2O is stored at the bonding interface [202]. The second reactant, Si–O–Si, is still of order two. Thus, the rate law is given by

$$\frac{dC_{\text{Si–OH}}(t)}{dt} = -\frac{dC_{\text{Si–O–Si}}(t)}{dt} = k\,C_{H_2O}(t)\,C_{\text{Si–O–Si}}^2(t). \tag{79}$$

This equation does not have a closed-form solution, unless it is assumed that the original concentrations of the reactants are the same, that is, $C_{\text{Si–O–Si},0} = C_{\text{H}_2\text{O},0}$, see Ref. [266, Chap. 2-6]. This assumption is realistic because during the direct bonding annealing step, for each covalent bond a water molecule is trapped at the bonding interface (neglecting evaporation). Now, it can be found that the solution is

$$G_{Ic}(t) = G_{Ic,\infty} + \left(G_{Ic,0} - G_{Ic,\infty}\right) \big/ \sqrt{1 + 2\,k_{\text{eff}}t}. \tag{80}$$

Here, the three fitting parameters are the same as above.

In summary, the general bonding energy time evolution can be modeled by

$$G_{Ic}(t) = G_{Ic,\infty} + \frac{G_{Ic,0} - G_{Ic,\infty}}{(1 - (1-n)\,k_{\text{eff}}t)^{1/(n-1)}}, \quad \text{with} \quad n = \begin{cases} 2 & \text{for humid air, and} \\ 3 & \text{for dry nitrogen.} \end{cases} \tag{81}$$

Thus, the atmosphere condition determines the order of the chemical reaction, n. (Note that for $n \to 1$, Eq. (81) would become an exponential function, which is expected for a first order chemical reaction.) A numerical algorithm was applied to fit the parameters of Eq. (81) to the measured data points for humid air and dry nitrogen, respectively, see Fig. 6.9. The error bands have been calculated from the resulting covariance matrix [267]. The curves agree very well with the data. This is remarkable because the number of fit parameters (that is, three) is very small.

An overview of the values obtained for the fit parameters is given in Fig. 6.10. The measured data points show that the incipient bonding energy is neither dependent of the surrounding atmosphere nor of the surface waviness. The same is found for the settled bonding energy. Considering the effective reaction rate constant, it is both a function of the surrounding atmosphere and of the wafer surface topography, where smaller values are observed in the case of dry nitrogen and overall smooth wafer surfaces. The measurement uncertainty in the case of the incipient bonding energy and effective reaction rate constants is relatively large for those wafers which are wavy. This is due to the fact that the underlying data show a sharp decline of the bonding energy at $t \approx 0$, see Fig. 6.9, which correlates to large values of the covariance matrix with regard to the entries for $G_{Ic,0}$ and k_{eff}.

The measurement data indicate that the contact front propagation, that is, the interface crack growth, is a time-dependent phenomenon where the crack continues to grow due to an underlying chemical reaction even at a comparably small external force. This phenomenon is known as *sub-critical crack growth*. A useful way to study sub-critical crack growth is to consider the growth rate, $v := \mathrm{d}a/\mathrm{d}t$, as a function of the bonding energy, G_{Ic}. This is shown in Fig. 6.11. (Here, only data obtained for those wafers with overall smooth surfaces are considered due to the smaller measurement uncertainty values of their fit parameters.) The fit model's transformation is derived
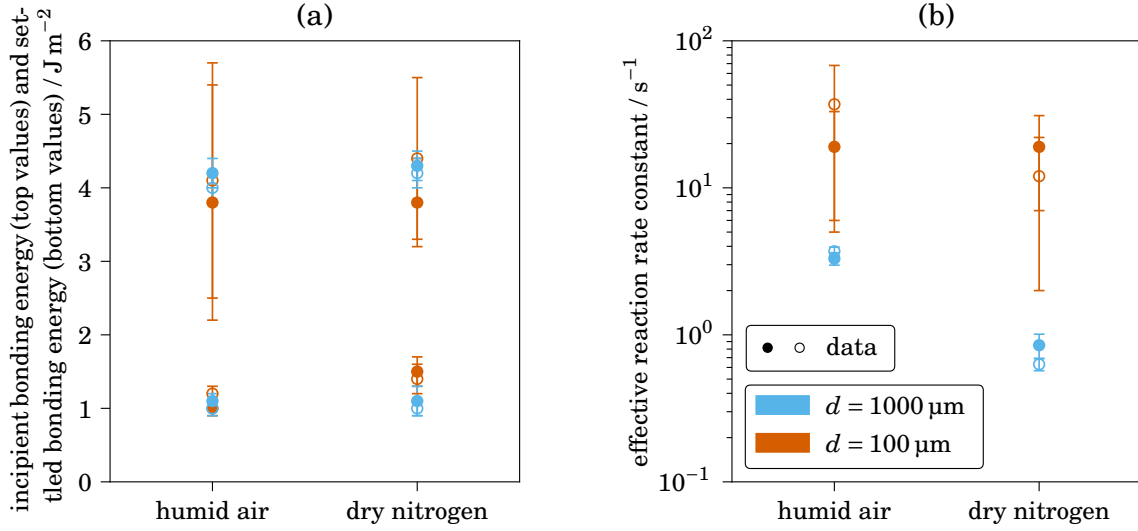
Figure 6.10: Overview of the fit parameters obtained from the bonding energy time evolution data, with (a) incipient and settled bonding energy, $G_{Ic,0}$ and $G_{Ic,\infty}$, and (b) the effective reaction rate constant, k_{eff}. (The wafer surface topography is represented by the wafer thickness, d, cf. Sec. 6.1.4.)
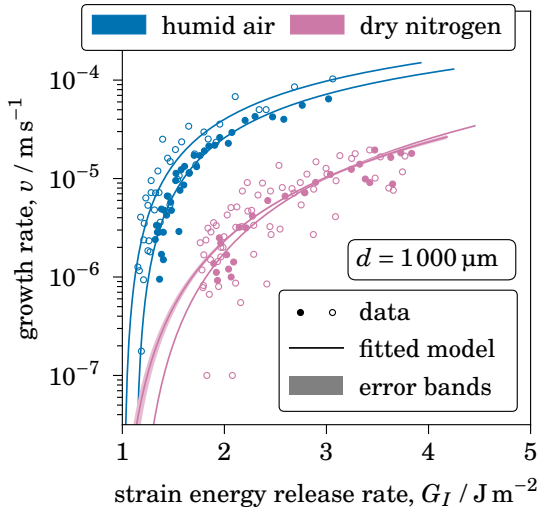
Figure 6.11: Data from Fig. 6.9, depicted in a transformed way in order to study the underlying sub-critical crack growth behavior. Note that the ordinate is scaled in a logarithmic way.
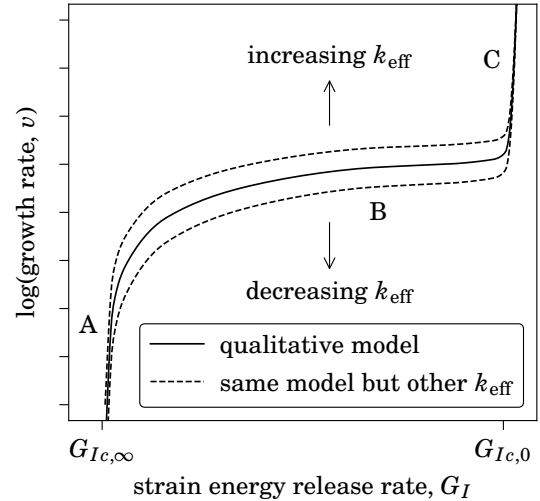
Figure 6.12: Schematic depiction of the three crack growth regimes. Note that the ordinate is scaled in a logarithmic way, which is why a change in the reaction rate constant causes the curve to shift vertically.

in the appendix, see Sec. A.1.7. The bonding energy energy, G_{Ic}, is in this case interpreted as the strain energy release rate, G_I, see Sec. 2.2.4.

If G_I falls below the settled bonding energy, $G_{Ic,\infty}$, sub-critical crack growth stops. In literature, that bonding energy is also referred to as the *equilibrium* bonding energy [268]. If G_I is slightly larger than $G_{Ic,\infty}$, the growth rate, v, is very slow and highly sensitive to G_I. This corresponds to regime A. If G_I is much larger than $G_{Ic,\infty}$ but still smaller than $G_{Ic,0}$, v becomes nearly steady, that is, less sensitive to G_I. This

corresponds to regime B. The largest growth rate measured corresponds to $G_I = G_{Ic,0}$. For $G_I > G_{Ic,0}$, critical crack growth is triggered, that is, the interface tears apart. In some literature, that bonding energy is also referred to as fracture toughness [269]. This corresponds to regime C. An overview of these three regimes, which are known from literature [268, 270], is shown in Fig. 6.12. Critical crack growth was not explicitly measured because data recording did not start until the razor blade or steel foil was fully inserted into the bonding interface. That is, razor blade or steel foil always rested during the bonding energy measurement.

6.4 Bonding Energy in the Case of Structured Surfaces

Encapsulated diffraction gratings, which can be manufactured via direct bonding by contacting a thin, transparent wafer with an optical substrate into which a diffraction grating has been inscribed, are a promising technology for laser and spectrometric applications with enhanced transmission. An additional advantage is that the sensitive grating structure is protected from contamination. KALKOWSKI et al. investigated direct bonding on rigid samples with grating orientation parallel to the contact front propagation direction [64, 271]. It is proposed that encapsulated diffraction gratings on non-planar substrates will promote the development of novel optical applications.

In order to investigate the bonding energy for the case of lithographically structured wafer surfaces, according experiments were performed with the κ-method and the DCB-method, such that direct bonding on planar and on non-planar substrates is considered, respectively, where each second wafer beam has a complete area binary diffraction grating with orientation perpendicular to the contact front propagation direction. The nominal thickness of each wafer is $d = 400\,\mu m$, that is, the wafer surfaces are overall smooth and planar, cf. Sec. 6.1.4. The purpose of these experiment is to investigate what has to be considered technologically when encapsulated diffraction gratings are applied to non-planar substrates.

6.4.1 Sample Preparation

Inscription of binary diffraction gratings is performed prior to wafer beam dicing using the following procedure. The grating pattern is exposed into a resist layer via electron-beam lithography and is then transferred via two reactive ion etching processes into the surface, with Cr serving as an intermediate masking layer. The grating period width is always 1500 nm and the plateau-to-total-surface ratios are varied, where the investigated ratios, that is, the grating fill factors, have nominal values of $\tau = 25\%$, 50% and 75%. A photo of an exemplary wafer beam during the direct bonding process is shown in Fig. 6.13.
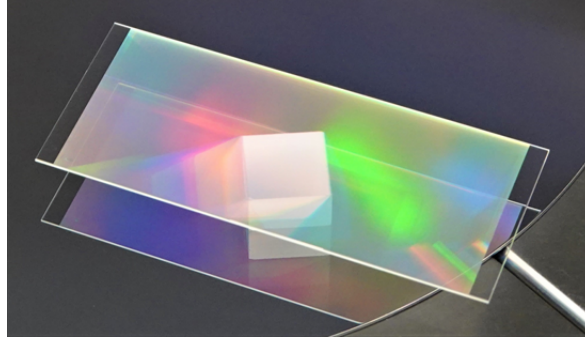
Figure 6.13: Photo of an exemplary structured wafer beam ($B = 25.4\,\text{mm}$, $L = 60\,\text{mm}$, $\tau = 25\,\%$) during the direct bonding process, in particular, prior to the plasma activation step. It is placed on top of a grinded quartz glass square which again is placed on top of a Si wafer.

6.4.2 Surface Structure Characterization

After grating inscription and prior to direct bonding, the wafer's surface structure is characterized via AFM, where line profile measurements perpendicular to the grating line direction and areal measurements on top of the plateaus were conducted. The resulting calculated *actual* fill factor values are shown in Tab. VII. The line profiles are shown in Fig. 6.14. It is found that for all nominal fill factor values, the desired period with of 1500 nm has been realized very well and that the plateaus are very flat, however, the actual fill factor values differ from the nominal ones.

Considering the surface roughness and waviness on top of the plateaus, it is found that they are comparable to those measured at the original wafers, that is, no surface degradation occurred during the grating structuring process.

6.4.3 Time-Resolved Bonding Energy Measurement

The bonding energy measurement results are presented in Fig. 6.15 (a). It is found, first, that for all states in which a measurement takes place ("initial", "annealed" and "corroded", as defined in Sec. 6.2.1), the measured bonding energy decreases with decreasing fill factor. Second, the amount of bonding energy reduction from the annealed state to the corroded state decreases likewise.

Table VII: Comparison of nominal and measured values of the grating fill factor, τ. The measurement was conducted on the basis of the data presented in Fig. 6.14.

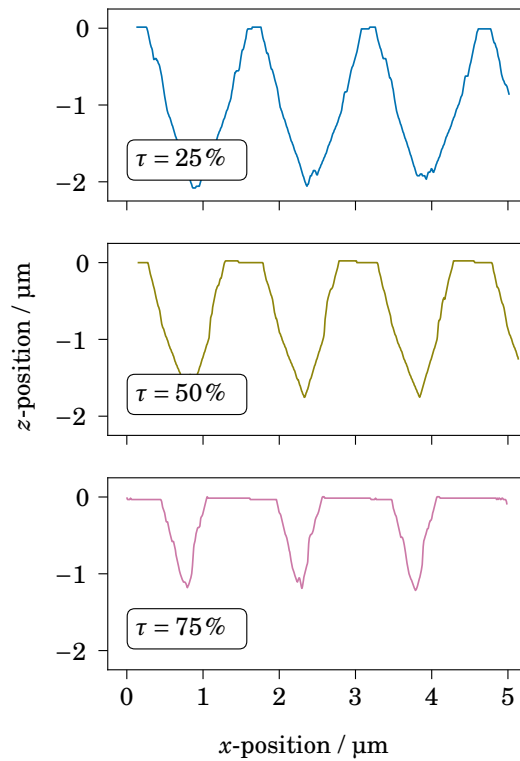| nominal value	measured value
25 %	$(12.6 \pm 1.0)\,\%$
50 %	$(33.6 \pm 0.4)\,\%$
75 %	$(60.8 \pm 0.2)\,\%$

Figure 6.14: Line profiles of the wafer surfaces with different grating fill factors, τ. Each measurement was conducted via AFM perpendicular to the grating direction.
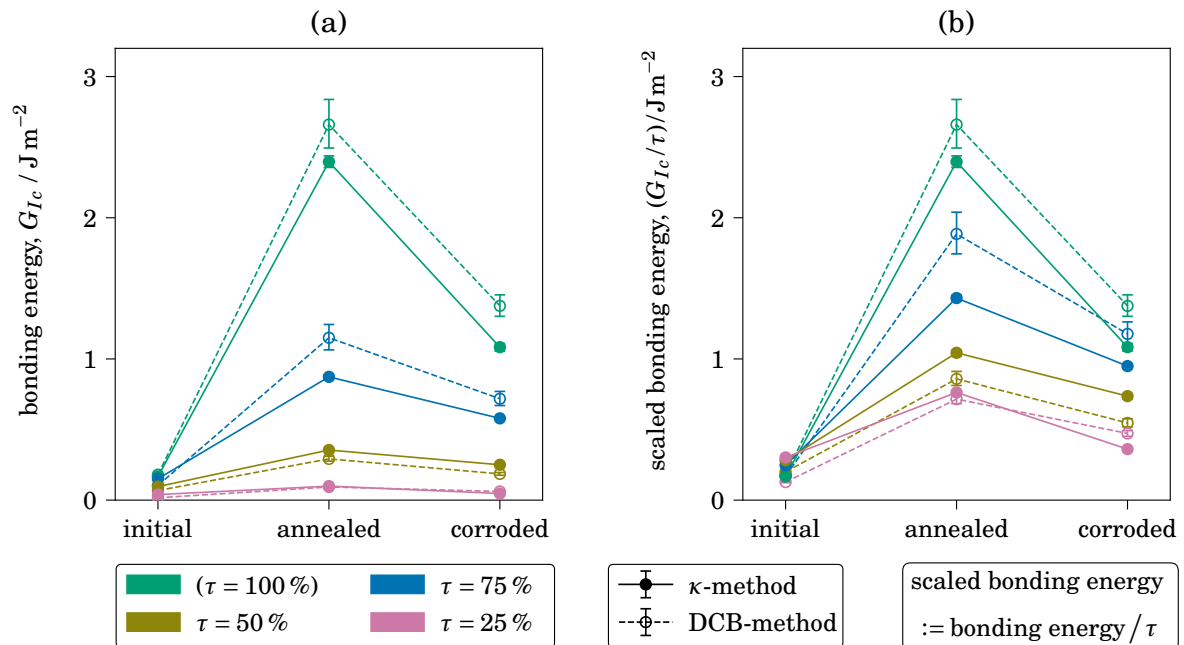

Figure 6.15: Bonding energy as a function of the grating fill factor, τ. In all cases, the nominal thickness of the wafers is $d = 400\,\mu\text{m}$, that is, the wafer surfaces are overall smooth, cf. Sec. 6.1.4.

In order to study whether the first observation can be contributed to the fill factor, which quantifies the effective bonding area, the scaled bonding energy, G_{Ic}/τ, has been calculated. Here, the actual fill factor values have been applied. The result is shown in Fig. 6.15 (b). It is found that there is still a distinct decrease in bonding energy with decreasing fill factor. However, the amount of bonding energy reduction from the annealed state to the corroded state has now become more similar.

6.4.4   Interface Inspection

The bonding interface was screened for homogeneously scattered cavities (which could determine the bonding energy) via microscopy, as described in Sec. 4.4. The result is that no homogeneously scattered cavities could be observed.

For bonded and later partly separated wafer pairs with a fill factor of $\tau = 50\,\%$, the contact front was inspected. An exemplary microscopy image is shown in Fig. 6.16. Here, the contact front is visible as a diagonal line. The grating orientation is exactly horizontally. Still, the contact front's path is not affected by the diffraction grating orientation. Therefore, it is suggested that the diffraction grating period is so small that the elastic deformation of the wafer is not affected by its orientation. Thus, the elastic deformation can be modeled by assuming homogeneous bonding surfaces where the bonding energy is scaled according to the effective area of contact.
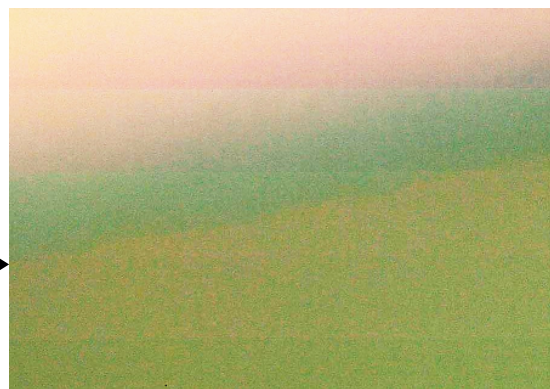
Figure 6.16: Microscopy image ($1.0 \times 0.7\,\mathrm{mm}^2$) of the contact front of a bonded wafer pair ($d = 400\,\mu\mathrm{m}$) where a diffraction grating ($\tau = 50\,\%$) has been inscribed into one of the wafer surfaces prior to bonding. The image contrast has been enhanced. The contact front position is shown by two arrows. The top half of the image shows the separated part where interference fringes are visible. The orientation of the diffraction grating is exactly horizontally. The horizontal lines with a period width of $150\,\mu\mathrm{m}$, that is, one hundred times the diffraction grating period width, is an artifact from the electron-beam lithography process caused by a strip-wise exposure processing.

6.5 Discussion of the Silanol Condensation Reaction

6.5.1 Assessment of the Time-Resolved Bonding Energy Measurement Data

For the bonding energy in the "initial" state (that is, prior to the annealing step), it was found that the waviness strongly correlates with the measured bonding energy. This is as expected: According to the current model, the bonding energy is determined by the real contact area, also called the contact point density, which is essentially determined by the waviness and roughness [198]. Already at room temperature, some covalent molecular bonds are formed according to the contact point density, which increases the adherence, as shown by FOURNEL et al. [199]. In addition, the contact points can be deformed. Thin induces mechanical stress in the material at the vicinity of the bonding interface (due to local elastic deformation), as shown by TURNER et al. [264]. This deformation is proposed to already occur during the contacting step when the wafers are lightly pressed together by the elastic pin.

The bridging of the remaining local asperities by water molecules also plays a role, provided that the separation is not too large: A separation of up to 1.4 nm can be bridged in the case of full wetting [112, 197] where a separation of up to 0.5 nm is suggested to contribute to adhesion [200]. For the very thin wafers, the waviness is associated with a peak-to-valley planarity deviation of up to 8 nm. Therefore, this mechanism can either only occur *after* sufficient contact point deformation or it is negligible. Which of the two is the case cannot be deduced from the data, as adherence is measured, not adhesion.

The bonding energy increases strongly during the annealing step. During the annealing step, the weakly hydrogen- and VAN-DER-WAALS-bonded surface molecules react to become covalently bonded via the so-called silanol condensation reaction [189].

For the bonding energy in the "annealed" state, or more precisely, for the incipient bonding energy which was determined by extrapolation of the time-resolved measurement data, it was found that the waviness does not affect that bonding energy. Instead, it is the corrosion rate that is affected. This suggests that the contact points due to the waviness have deformed in a sufficient way, and that, as explained above, there is an according amount of mechanical stress in the material at the vicinity of the bonding interface. Thus, for rough surfaces, there is more mechanical stress.

6.5.2 Estimation of the Actual Surface Area

Now, the question arises whether the actual contact area is affected by the waviness. This question is investigated now. A polished glass surface is not perfectly planar, but is characterized by roughness, waviness and shape variation, as explained in Sec. 2.3. Thus, the actual surface area differs from the projected surface area. Polished glass
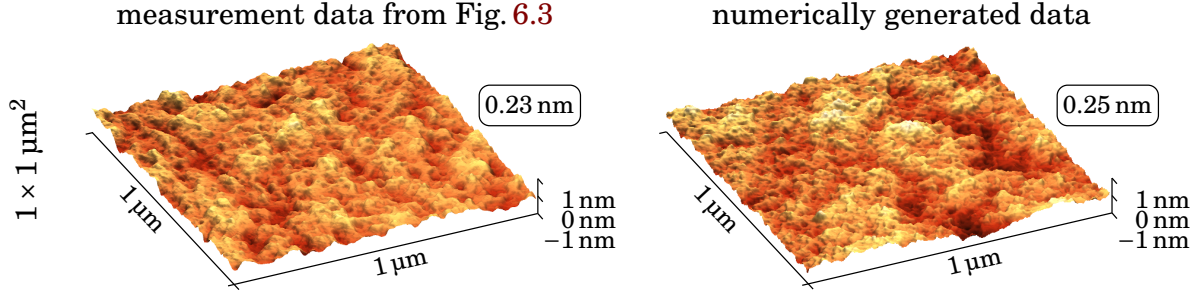
measurement data from Fig. 6.3 — 0.23 nm — $1 \times 1\,\mu m^2$ — 1 µm — 1 µm — 1 nm, 0 nm, −1 nm

numerically generated data — 0.25 nm — 1 µm — 1 µm — 1 nm, 0 nm, −1 nm

Figure 6.17: Exemplary surface topographies of a $d = 100\,\mu m$ thick wafer. For each image, the S_q-value is presented in a box with round edges. The measured surface (left-hand side) is the same as already presented in Fig. 6.3. The numerically generated surface has been obtained by using Eq. (82). For a better visualization, a median filter of 7 px has been applied to the images.

surfaces can be well described as self-affine profiles [272], for example, by the two-variable WEIERSTRASS-MANDELBROT function that is given by [273]

$$
z(x,y) = l \left(\frac{\psi}{l}\right)^{\zeta-2} \sqrt{\frac{\log\xi}{m_{\max}}} \times \sum_{m=1}^{m_{\max}} \sum_{n=1}^{n_{\max}} \xi^{(\zeta-3)n}
$$
$$
\times \left\{ \cos\omega_{mn} - \cos\left[\frac{2\pi\,\xi^n\,\sqrt{x^2+y^2}}{l} \times \cos\left(\arctan\left(\frac{x}{y}\right) - \frac{\pi\,m}{m_{\max}}\right) + \omega_{mn} \right] \right\}, \quad (82)
$$

with sample length, l, also referred to as profile evaluation length that is equal to the inverse of the profile's minimum spatial frequency, the fractal dimension, ζ, the height scaling parameter, ψ, the number of superposed ridges used to construct the surface, $m_{\max}$, the iteration depth, $n_{\max} = \lfloor \log(l/l_s)/\log\xi \rfloor$, which is determined by the molecular scale cut-off length, l_s, the frequency density scaling parameter, $\xi > 1$, and the random phase function, ω_{mn}. In order to numerically generate a surface which represents the measured surface of a polished borofloat wafer with thickness $d = 100\,\mu m$, a fractal dimension of $\zeta = 2.75$ and a height scaling parameter of $\psi = 2 \times 10^{-11}$ has been chosen, which agrees with the experimentally determined PSD function, see Sec. 6.1.3. As suggested in literature [274], it is useful to choose the other parameters as $\xi = 1.5$, $m_{\max} = 16$, and $l_s = 2\,\text{Å}$. By doing so, surface profiles have been generated for a lot of different spatial frequency ranges, that is, different values of l. The sampling resolution was chosen as 512×512 pixels. A corresponding computer code to implement Eq. (82) is given in the appendix, see Sec. A.3.4.

A measured surface compared to a numerically generated one for $l = 1\,\mu m$ (that is, a test area of $1 \times 1\,\mu m^2$) is shown in Fig. 6.17. It can be seen that both topography profiles are very similar. The resulting S_q-value is almost the same. Figure 6.18 shows the PSD function of the numerically generated surfaces (fitted by a power-law function with exponent ζ and cut off at $1/l_s$) as compared to that of the measured surface. Both curves are very close together. This is as expected since the parameters for Eq. (82) have been chosen such that the PSD function matches that of the measured surface.
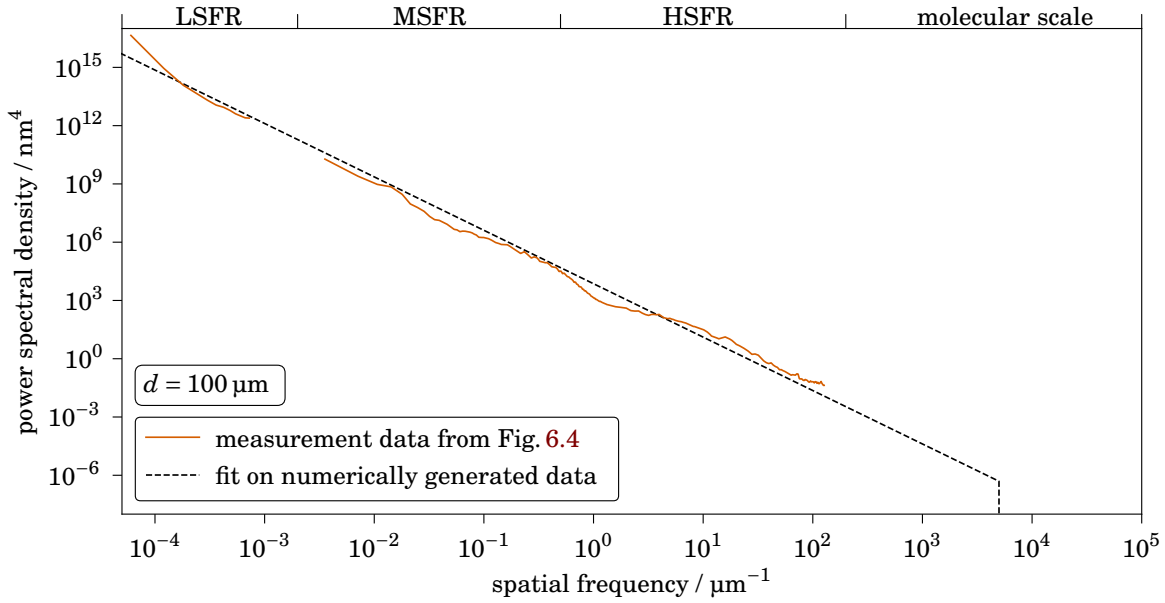
Figure 6.18: PSD function of the measured surface from Fig. 6.4, where the wafer has a thickness of $d = 100\,\mu m$, in comparison to that of the numerically generated surfaces, plotted on a log-log-scale. The LSFR corresponds to the shape variation, the MSFR to waviness and the HSFR to roughness.

For each surface topography data set, the relative actual surface area, that is, the actual surface area divided by the projected surface area, has been calculated. This is shown in Fig. 6.19. Considering the measured surfaces, there are data available only up to the HSFR because the measurement method with the highest spatial resolution available is AFM with a test area of $1 \times 1\,\mu m^2$. Considering the numerically generate surfaces, there are data available up to the molecular scale. It can be seen that up to the MSFR there is no significant difference between actual and projected surface area.

Figure 6.19: Calculated actual surface area increase, that is, the cumulative actual surface area for the according sample length, l. Note that there is no measurement data available for $l < 1\,\mu m$. In the case of the numerically generated data, each data point represents the average value of twelve numerically generated surfaces. The LSFR corresponds to the shape variation, the MSFR to waviness and the HSFR to roughness.

Only starting from the HSFR, the relative actual surface area increases up to $(56\pm7)\%$ in the molecular scale.

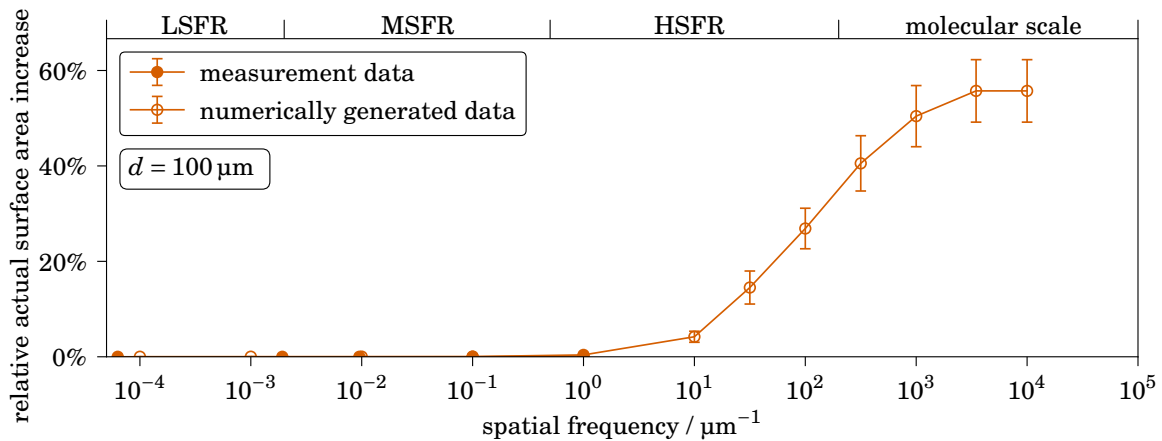In Sec. 6.1.4, it was shown that thick borofloat wafers in this work differ from thin ones with regard to the surface topography only in the shape variation and waviness, but are very smooth in the HSFR, that is, the roughness. Also, it can be assumed that there is no difference at the molecular level. It can therefore be concluded that all the polished borofloat wafers examined have the same relative actual surface area.

This agrees with the observation that the waviness does not affect the incipient bonding energy. In addition, this agrees with a very recent molecular dynamics simulation study by WU et al. where it was shown that the actual contact area between two rigid surfaces is only affected by the initial roughness of the surfaces, given a displacement of a few nm, see Fig. 11 in Ref. [274]. This finding is again consistent with the asperity deformation mechanism proposed by FOURNEL et al. [199]. Borofloat has recently been found to be relatively susceptible to water, allowing for near-surface structural changes [275], thereby enhancing contact point deformation. Therefore, it is proposed that the volume of interfacial voids for a sufficient amount of water storage, that is, the nanoscopic unbonded regions, is also negligible.

6.6   Discussion of the Water Stress Corrosion Reaction

6.6.1   Direct Bonding Interface Prerequisites

After annealing, when a peeling moment is applied, the bonding energy decreases with time. This is known to be due to the water stress corrosion reaction [116, 210] which is a *reversed* silanol condensation reaction, as explained in Sec. 2.5. Mechanical stress is a prerequisite for water stress corrosion to occur during peeling moment introduction [208, 209]. In particular, the effective reaction rate constant, k_{eff}, is a function of the mechanical stress. Another prerequisite is the amount of water stored at the bonding interface. In particular, the effective reaction rate constant, k_{eff}, is a function of the amount of water available for that chemical reaction. It is proposed that the amount of water stored at the bonding interface is determined by the actual surface area of the polished glass surface. Due to the fact that all the polished borofloat wafers examined have the same actual surface area, it can be concluded that the amount of water stored at the bonding interface is the same for all wafer surfaces.

6.6.2   Assessment of the Time-Resolved Bonding Energy Measurement Data

For now, only results from bonding energy measurement experiments carried out in humid air are considered. Based on an extrapolation of the time-resolved measurement data, it was found that the "corroded" bonding energy settles to approximately the same final value independently of the waviness, see Fig. 6.10 (b). For wavy sur-

faces, there is more mechanical stress stored in the material at the vicinity of the bonding interface, making the interface more susceptible to water stress corrosion. As a consequence, the reaction is very fast, so that the "annealed" bonding energy value has already partially decreased, as it is measured a few seconds after the peeling moment is introduced, see Tab. VI, as shown schematically in Fig. 6.8 (b). For surfaces that are smooth in all spatial frequency ranges, there is less mechanical stress stored in the material at the vicinity of the bonding interface, and the interface is less susceptible to water stress corrosion, which implies a lower corrosion rate.

If the experiments are carried out in humid air, water from the ambient atmosphere can be considered to be sufficiently available. Thus, all available sites will react as long as the applied mechanical stress or the internal stress at the bonding interface does not fall below a certain threshold. Thus, the bonding energy in the "corroded" state shows nearly the same settled value for all samples. The roughness determines the adherence in the "annealed" state, cf. Sec. 2.5, where an influence of nanoscopic unbonded regions is proposed to be small. In conclusion, it can be predicted that the bonding energy in the "corrected" state is only sensitive to the roughness value.

6.6.3   Water Stress Corrosion without Atmospheric Humidity

Now, results from bonding energy measurement experiments carried out in dry nitrogen are considered. Here, it was found that the bonding energy also decreases with time. But the effective reaction rate constant, k_{eff}, is reduced as compared to the case of humid air. A qualitatively very similar behavior for directly bonded "SiO_2" surfaces was measured by FOURNEL et al. [276], but they do not give any explanation for the decrease of the bonding energy with time. They only state that the bonding energy is more stable for experiments performed in dry nitrogen as compared to experiments performed in humid air. However, the experimental results presented in this thesis indicate that in dry nitrogen the bonding energy decreases just as much as in humid air, only more slowly and with a different underlying order of the chemical reaction.

In this thesis, borofloat instead of fused silica was investigated. Borofloat consists of approximately 80 % SiO_2, more than 10 % B_2O_3 as well as alkali metal oxides [247]. For the case of fused silica, it has been demonstrated by TAKEUCHI and SUGA that water required for the water stress corrosion is stored at the bonding interface [202]. For borofloat, it has been described that alkali ions are dissolving out of the surface when in contact with water [260, Chap. 11.2]. Therefore, it is proposed that not all interface sites are available for covalent SiO_2 bonds. The silanol condensation cannot proceed completely. This becomes clear when comparing the measured bonding energy, which is roughly $4\,\mathrm{J\,m^{-2}}$ as shown in Fig. 6.10, to the work of separation data of a virgin monolithic solid borofloat piece, which is roughly $11\,\mathrm{J\,m^{-2}}$ as shown in Tab. I.
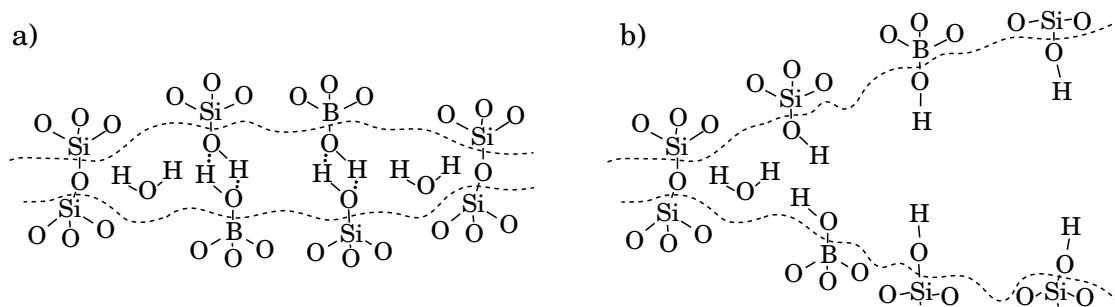
Figure 6.20: Proposed structural formulae of the proposed water stress corrosion for borofloat in dry nitrogen, with (a) before and (b) after the interface is torn apart by an external force. State (a) is essentially the same as the state shown in Fig. 2.9 (b) on page 21, that is, an incomplete silanol condensation.

There is also diffusion of water into the glass network where water is present as hydroxy groups, but this reaction occurs slowly [277]. For the fast water stress corrosion, a consideration of covalent SiO_2 bonds is a sufficient approximation for borofloat *if* the reduced amount of sites available for covalent bonds at the bonding interface is considered. It is proposed that water molecules are stored in between of covalent and hydrogen bond sites. This is why the water molecules are immediately available for the water stress corrosion reaction as soon as mechanical stress is applied, as shown in Fig. 6.20. A secondary role may play water that is stored in gaps due to microscopic surface fracture resulting from the wafer grinding or polishing step, cf. Ref. [278].

To the best of the author's knowledge, this is the first time that the rate at which water stress corrosion occurs at directly bonded interfaces was explicitly investigated. In particular, it was found that the surface roughness measured in the HSFR (as usually done by AFM in the literature, see for example Refs. [112, 159, 197, 198]), although important, is not a sufficient information for predicting that rate. Waviness must also be taken into account. The waviness can be measured by WLI.

For the application – independent of the atmospheric condition –, it is typically important to obtain a large bonding energy. In the case of mechanically relaxed bonding interfaces (that is, for planar direct bonding), it is particularly important to obtain a large incipient bonding energy, $G_{c,0}$, whereas in the case of mechanically stressed bonding interfaces (that is, in the case of non-planar direct bonding), it is particularly important to obtain a large settled bonding energy, $G_{c,\infty}$. The corrosion rate is not relevant. The rule that can be derived from this is that the requirement for surface roughness must be very good (typically, better than $S_q < 0.5\,\mathrm{nm}$ at a test area of $10 \times 10\,\mathrm{\mu m}^2$ [73]), while the requirement for surface waviness only concerns the corrosion rate, which is not relevant for most applications.

6.7   Proposition of a Molecular Model

It was found that the effective reaction rate constant, k_eff, of the water stress corrosion reaction is both a function of the surrounding atmosphere and of the wafer surface topography, where smaller values are observed in the case of dry nitrogen and overall
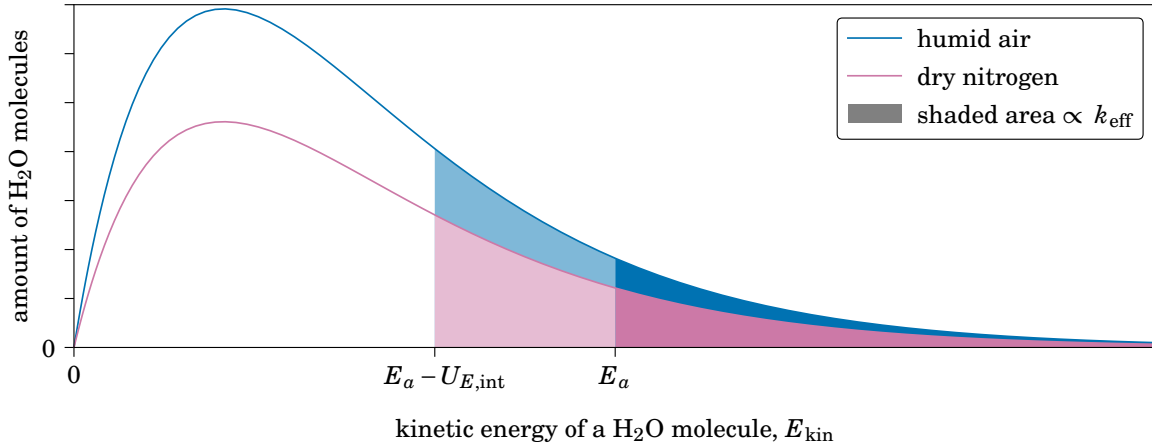
Figure 6.21: Proposed underlying model for the sub-critical crack growth mechanism of a general hydrophilic direct bonding interface. The shaded area, that is, the amount of water molecules with a sufficient kinetic energy to participate in the water stress corrosion is larger, first, in the case of humid air as compared to dry nitrogen, and second, in the case of mechanical stress stored in the bonding interface's vicinity which serves as offset in the activation barrier.

smooth wafer surfaces, see Fig. 6.10. As argued above, the effective reaction rate constant, k_{eff}, is determined by, first, the availability of water and, second, the internal mechanical stress stored at the bonding interface's vicinity due to contact point deformation related to the waviness. Here, it is again important to note that the waviness does not affect the amount of water stored at the bonding interface.

The internal mechanical stress stored at the bonding interface's vicinity can also be expressed as an internal strain energy, cf. Eq. (13), which is in the following referred to as $U_{E,\text{int}}$. From the point of view of physical chemistry, the reaction rate constant, k_{eff}, is determined by the ARRHENIUS equation, see Eq. (6). The equation states that k_{eff} increases with decreasing activation energy, E_a. This is because each molecule which could contribute to the chemical reaction has a certain kinetic energy, E_{kin}, which is statistically distributed, and only those molecules with $E_{\text{kin}} > E_a$ will react. As such, a decrease of E_a leads to a larger amount of reacting molecules.

For the consideration of sub-critical crack growth of inorganic glasses, it has been proposed to take the internal strain energy as an offset on the activation energy [279]. That is, those molecules with $E_{\text{kin}} > E_a - U_{E,\text{int}}$ will react. This increases the amount of reacting molecules, which increases k_{eff}. The reacting molecules worth considering are the water molecules. Thus, wavy direct bonding surface which are subjected to sub-critical crack growth show a large effective reaction rate constant, k_{eff}. Furthermore, when the chemical reaction takes place in humid air instead of dry nitrogen, the amount of reacting molecules becomes larger, too, which is why k_{eff} increases in the case of humid air as compared to dry nitrogen. In other words, the amount of water molecules with a sufficient kinetic energy to participate in the water stress corrosion is proportional to the effective reaction rate constant. This is visualized in Fig. 6.21.

When a peeling moment is applied to the interface (for example, when performing a

bonding energy measurement using the DCB-method, cf. Fig. 2.3, or when an initially planar wafer is bonded to a non-planar substrate, clamped during the annealing step and then released from the clamp, cf. Fig. 5.3), the locally available energy can be modeled as the sum of the elastic strain energy due to the externally applied stress, U_E, and the internal strain energy stored at the bonding interface's vicinity due to contact point deformation related to the waviness, $U_{E,\text{int}}$. Depending on this sum, the interface may be either stable, be subject to sub-critical crack growth or be subject to critical crack growth.

In the case of critical crack growth, the crack growth rate, v, is known to be very fast [257, 279]. However, the critical crack growth duration of the presented experiments is estimated to be so small that it does not affect the results of the model fit shown in Fig. 6.9. In the case of sub-critical crack growth, water stress corrosion determines the crack growth rate, v, of the bonding interface according to the proposed reaction kinetics model, see Eq. (81). The crack growth rate, v, decreases with time, which is equivalent to the bonding energy decreasing with time. This is due to relaxation of both the internal mechanical stress stored at the bonding interface's vicinity and the externally applied stress due to crack growth.

6.8 Discussion of the Case of Structured Surfaces

In the case of direct bonding of wafers with a grating inscribed in one surface, it was found that the bonding energy in the "annealed" and "corroded" states is reduced as compared to the bonding energy measured for unstructured wafers. While this is expected, it is worth noting that this is true even when considering the scaled bonding energy values, that is, the bonding energy divided by the grating fill factor, τ. It was also found that for smaller fill factors, the scaled bonding energy is further reduced, where this difference is less pronounced in the "initial" state.

It is not clear why this reduction in scaled bonding energy is found, since the surface roughness is comparable to that of the unstructured wafers. One possible explanation is that the diffraction grating grooves were not completely dried during the spin drying step (which is performed before the contacting step, see Sec. 4.5). Therefore, after the contacting step, and even after the annealing step, these trenches could still hold an amount of water large enough to enhance water stress corrosion once an external moment is applied, because the water stress corrosion reaction rate constant increases with increasing humidity as well as with increasing mechanical stress, as explained in Sec. 2.5.3. For this scenario, FOURNEL et al. have coined the term internal water stress corrosion [199]. Another hypothesis is that the contact area has been deformed due to mechanical stress induced by the lithography step. But this is unlikely, as the measured plateau's line profiles are flat, as shown in Fig. 6.14.

7 Direct Bonding of Wafers on Spherical Substrates

In the case of direct bonding of a wafer to a spherical substrate, bi-axial wafer bending has to be considered. Equation (57), , predicts complete and stable contacting success of wafer and spherical substrate. In this section, this equation is experimentally investigated, the results are evaluated qualitatively and quantitatively, and relevant technological considerations are discussed.

7.1 Experimental Approach

For experimentally verifying Eq. (57) and for the determination of the pre-factor of that equation, Π, circular wafers with different nominal thickness values were contacted with convex spherical lenses with different curvature radii, ρ, see Sec. 4.2. It was not necessary to vary the wafer radius, R, due to symmetry reasons, cf. Sec. 3.3.5. Only the initial contact step was investigated, that is, no annealing step was performed.

Practically speaking, a stack was build which consists of a concave spherical aluminum shell, a graphite wafer, the wafer to be bonded and the lens to be bonded, as depicted in Fig. 7.1. From the top, a small pressure was manually applied, such that the contact front can reach its equilibrium position while being subjected to radial-symmetric boundary conditions. The graphite wafer was used to reduce scratches.

7.2 Evaluation of the Contact Front Equilibrium Position

In all cases, $R = 25.4\,\text{mm}$. Therefore, additional load due to gravity can be assumed as negligible. In the case of not too thick wafers ($d \leq 400\,\mu\text{m}$) and substrates with a large curvature radius ($\rho = 2593.6\,\text{mm}$), complete and stable contact was observed. In contrast, in the case of thick wafers ($d = 1000\,\mu\text{m}$) and a substrate with a relatively small curvature radius ($\rho = 1037.4\,\text{mm}$), a point contact was observed. This is exemplarily shown in Figs. 7.2 (a) and (b), respectively. This result is as expected.
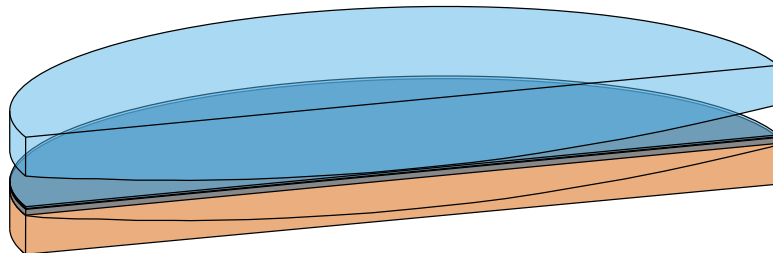

Figure 7.1: Schematic of the setup to experimentally verify Eq. (57). From bottom to top: Concave spherical aluminum shell, graphite wafer, wafer to be bonded, lens to be bonded.

The complete contact is characterized by vanished interference fringes over the complete wafer area (except some remaining small lines at the wafer's outer perimeter). The point contact is characterized by small, radial-symmetric interference fringes (in this case referred to as NEWTON rings) located at the substrate's center. It is well known that the diameter of the NEWTON rings give information about the substrate curvature radius given that the wafer is planar [280]. Indeed, by measuring the NEWTON rings' diameters, exactly the substrate curvature radius is obtained (within the scope of measurement accuracy, assuming visible light, cf. Sec. A.1.6). This implies that in the case of point contact, the wafer is not subjected to significant bending.

For two experiments – that is, in the case of a thick wafer ($d = 1000\,\mu m$) and a substrate with a large curvature radius ($\rho = 5187.2\,mm$) and in the case of a thin wafer ($d = 100\,\mu m$) and a substrate with a small curvature radius ($\rho = 518.7\,mm$) –, neither complete contact nor point contact was observed. Instead, partial contact was observed. This means, that there are three types of contact between wafer and spherical substrate, namely,

  i complete contact,

  ii point contact, and

 iii partial contact.

To qualitatively describe partial contact, the wafer area is split into four parts, namely,

1. the visibly contacted part,
2. the threshold area (where interference fringes are visible which implies that there is a very small distance between wafer and substrate surface),
3. the visibly not contacted part (that is, the remaining wafer area) and,
4. if applicable, the glass fracture area (where parts of the wafer have broken off).

For the four exemplary presented experiments, their resulting contact areas are shown schematically in Figs. 7.3 (a) to (d). Here, (a) shows complete contact, (b) shows no contact, and (c) and (d) show partial contact. In the case of (c), that is, a thick wafer has been contacted with a substrate that has a large curvature radius, the visibly contacted part is approximately circular. Around the contact front is an approximately 2 mm wide threshold area. In the case of (d), that is, a thin wafer that has been contacted with a substrate that has a small curvature radius, the visibly contacted part is irregularly shaped with some parts reaching toward the wafer's edge and some parts being merely expanded, that is, approximately star-shaped. The threshold area is very thin. At one position at the wafer's outer perimeter, glass fracture has occurred.

None of the models discussed in Sec. 3.3 is able to predict the partial contacting behavior. However, using simple assumptions, it can be qualitatively predicted. This is discussed later in Sec. 7.4.2.
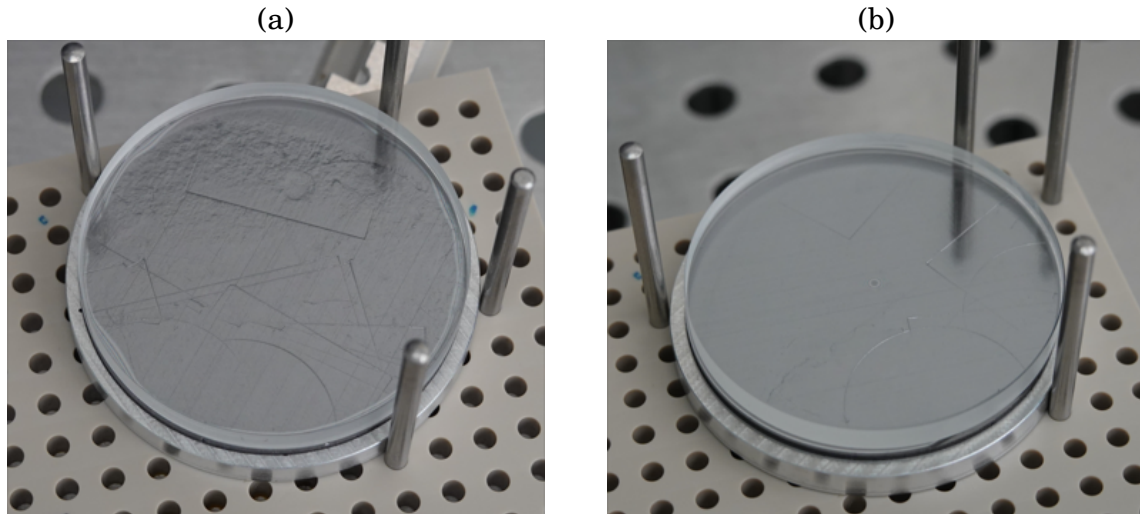
Figure 7.2: Photos of two different experiments where a circular wafer was contacted with a spherical substrate. Here, (a) shows complete contact, where the parameters are $d = 400\,\mu m$ and $\rho = 2593.6\,mm$, and (b) shows point contact, where the parameters are $d = 1000\,\mu m$ and $\rho = 1037.4\,mm$. In addition, (c) shows a detail view of the interference fringes that have been created by the point contact shown in (b). In all cases, the lens-wafer-pair is placed on a graphite wafer to prevent scratches. Those graphite wafers have imprints from previous experiments.
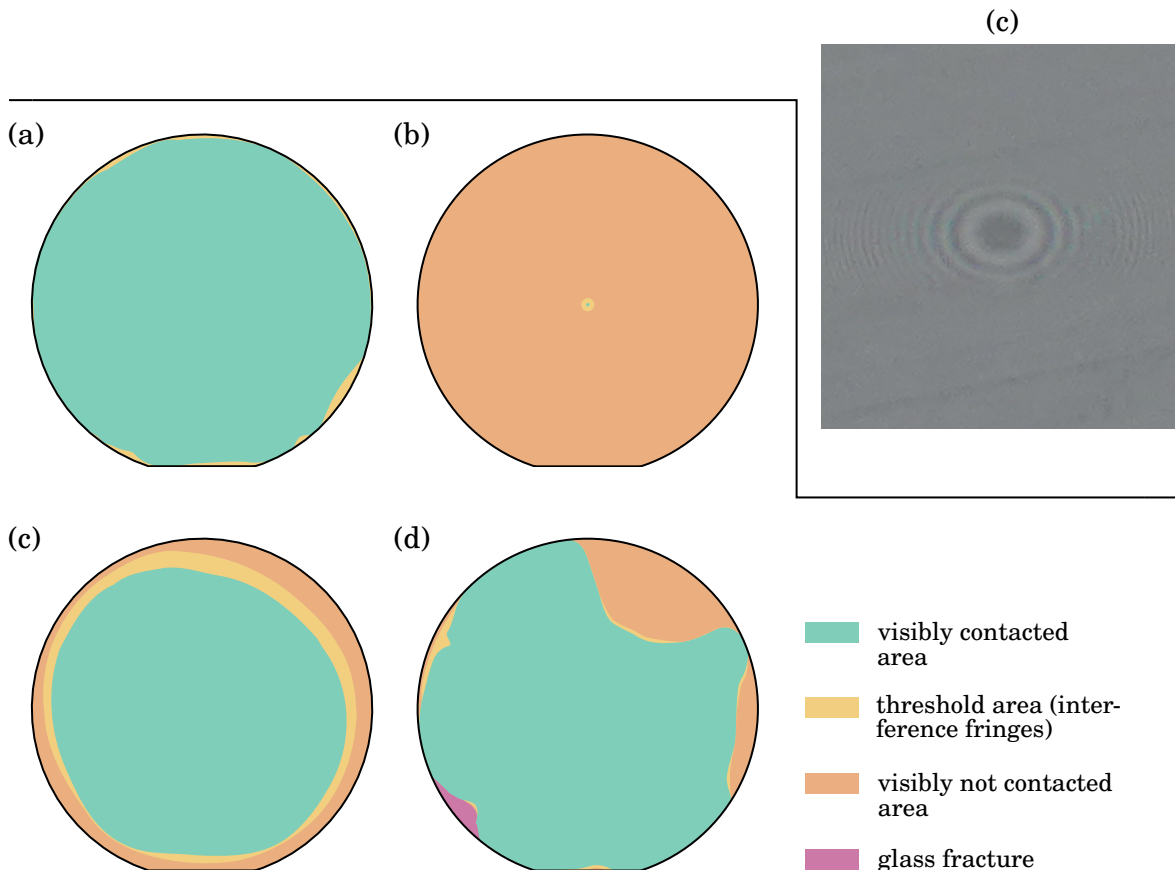
Figure 7.3: Schematic of the shape of the contacted part for four exemplary experiments. In (a), complete contact is shown where the underlying experiment corresponds to Fig. 7.2 (a). In (b), point contact is shown where the underlying experiment corresponds to Fig. 7.2 (b). In (c), partial contact is shown where the parameters are $d = 1000\,\mu m$ and $\rho = 5187.2\,mm$. In (d), partial contact is shown, too, where the parameters are $d = 100\,\mu m$ and $\rho = 518.7\,mm$.

7.3   Analysis of the Discrete Measurement Outcomes

With Eq. (57), a condition for complete and stable contact has been derived, where the numerical value of the pre-factor, Π, was found to turn out differently for different model assumptions. Therefore, the pre-factor will have to be determined (or at least narrowed down to a certain numerical range) experimentally.

The contacting experiments discussed above take on discrete measurement outcome values, namely, complete contact, partial contact and point contact. Therefore, it is reasonable to draw a (ρ, d)-diagram in which all measurement outcomes are represented by an accordingly colored data point. The result is shown in Fig. 7.4, where for now, only the colored data points are considered. The result is as expected, that is, in the case of thin wafers and substrates with a large curvature radius, there is complete contact, in the case of thick wafers and substrates with a small curvature radius, there is point contact, and in the other cases, there is partial contact.

In order to compare these discrete results with the derived condition for complete and stable contact, it is required to assume a value for the bonding energy, G_c. It is reasonable to assume the measurement values for the initial bonding energy as presented in Fig. 6.5 (column "initial"), where the mixed-mode bonding energy instead of the pure mode I bonding energy has to be taken into account, as explained in Sec. 3.3.8. This can be obtained by dividing G_{Ic} by the correction factor (20/23), cf. Eq. (68). The idea to this "correction factor approach" stems from Fig. 9 in Ref. [123].

Due to the fact that the measurement values are a function of the wafer thickness, d, it is reasonable to model the bonding energy accordingly. To do so, a linear model,

$$G_c(d) = \text{offset} + \text{slope} \times d, \tag{83}$$

is assumed. The result is shown in Fig. 7.5. The error bands have been calculated from the resulting covariance matrix [267]. The numerically calculated fit parameters are: offset $= (65 \pm 6)\,\mathrm{mJ\,m^{-2}}$, slope $= (68 \pm 17)\,\mathrm{J\,m^{-3}}$ and covariance $-0.064\,\mathrm{J^2\,m^{-5}}$. It can be seen that the linear model is a good assumption.

Now, the condition for complete and stable contact has to be rearranged such that is can be plotted in the d-ρ-diagram. The curve which divides the complete contact from the point contact measurement outcomes is defined by the assumption $G_c \overset{!}{=} G$. It is possible to find a closed-form expression, where the result takes on the form of a shifted hyperbola function. The result is

$$\rho^2 = C_1 + \sqrt{C_1^2 + C_2}, \tag{84}$$

$$\text{with coefficients} \quad C_1 = D(1+v)\big/\big(2G_c\big) = d^3 \times E\big/\big(24(1-v)G_c\big),$$
$$C_2 = B\,\Pi R^4\big/G_c \qquad = d \times \Pi E R^4\big/\big((1-v^2)G_c\big).$$

For those cases where d becomes very large or (R/ρ) becomes very small, Eq. (84) simplifies to

$$\rho^2 = \frac{D(1+\nu)}{G_c} \tag{85}$$

which is equivalent to the small spherical deflection approximation model from TURNER and SPEARING [110] which has been presented in Sec. 3.3.1.

Now, the experimentally determined bonding energy function, $G_c(d)$, from Eq. (83) is inserted into Eq. (84). The resulting function is plotted into the d-ρ-diagram, see
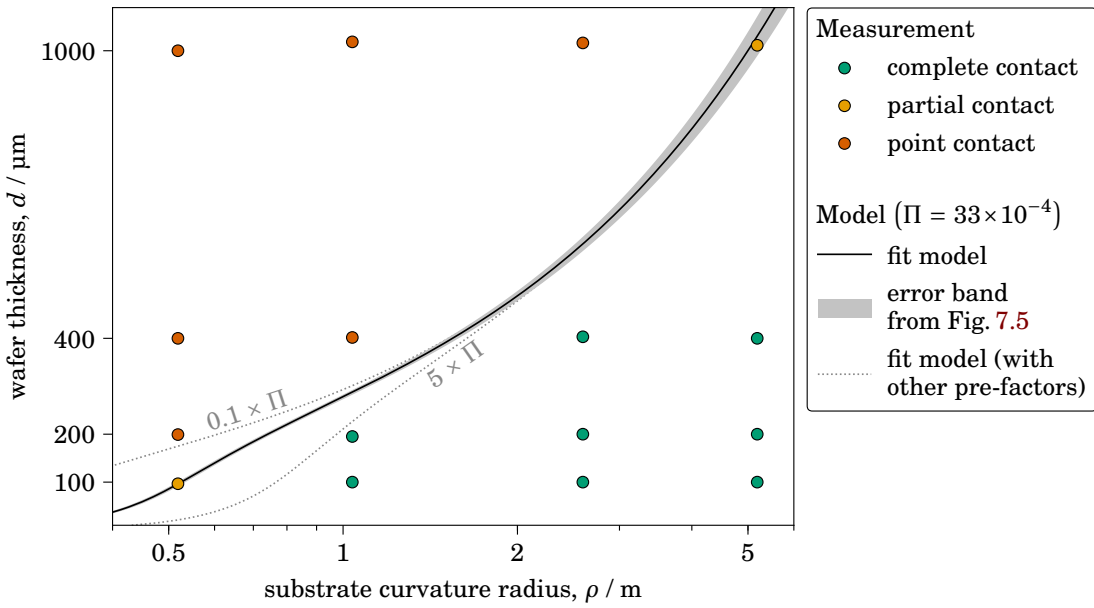
Figure 7.4: Discrete measurement outcomes for the contacting experiments of wafer and spherical substrate, where each data point is located at the corresponding position in the (ρ, d)-diagram. In all cases, $R = 25.4\,\text{mm}$. The model according to Eq. (57) is drawn into the diagram such that the different measurement outcomes are divided correctly, where the only fit parameter is Π.
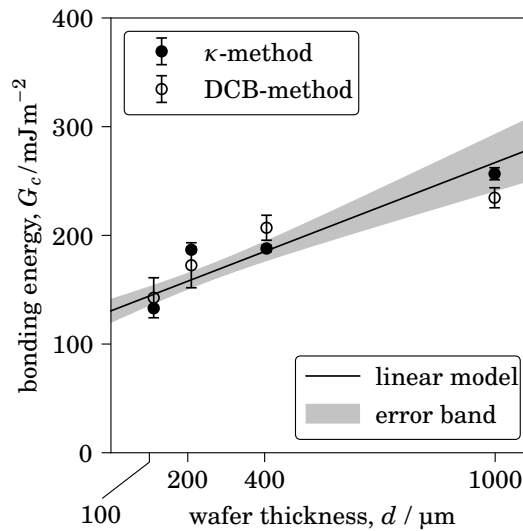
Figure 7.5: Mixed mode initial bonding energy, G_c, calculated from the data shown in Fig. 6.5, as a function of the wafer thickness, d. (The wafer thickness represents the surface topography, cf. Sec. 6.1.4.)

again Fig. 7.4. The only fit parameter is the pre-factor, Π. It is found that the best curve fit is obtained for $\Pi = 33 \times 10^{-4}$, that is, that fit value is the most probable estimation for the real pre-factor.

However, the bottom-left part of the curve is very sensitive with respect to changing the pre-factor, Π, and that any partial contact measurement outcome neither strictly corresponds to complete contact nor point contact. In fact, the real numerical value of the pre-factor could be up to ten times smaller or up to five times larger than the best fit value. As such, the estimated value and the error interval is given by $\Pi = \left(33^{+132}_{-30}\right) \times 10^{-4}$, or equivalently, $\ln(\Pi) = -5.7^{+1.6}_{-2.4}$.

7.4 Assessment of the Model Applicability

7.4.1 Numerical Pre-Factor of the Model

In Sec. 3.3, different models were presented to predict direct bonding of an initial planar wafer to a spherical substrate. As concluded in Sec. 3.3.8, all models yield qualitatively the same result, only the numerical value of the condition's pre-factor, Π, is under debate. An overview of the numerical pre-factors from the models as well as the experimental one is given in Tab. VIII.

It is reasonable to assume that the truncated torus model is the most exact model. This is due to the fact that it is the only model where

(a) the energetic contributions from the non-contacted part of the wafer during the contacting step are considered,

(b) the shape of the non-contacted part of the wafer is modeled approximately correctly, that is, it takes on the form of a truncated torus, and

(c) both radial stretching strain and azimuthal squeezing strain are considered.

Regarding point (a), note that the consideration of the non-contacted part of the wafer is important for correctly modeling the strain distribution in the contacted part of the wafer, cf. Sec. 3.3.3. The truncated torus model yields a pre-factor of $\Pi = 35.6 \times 10^{-4}$.

Table VIII: Overview of the numerical values for Π according to Eq. (57) for different models.

model	reference	$\Pi/10^{-4}$	assessment
TURNER and SPEARING [222]	Eq. (32)	0	valid for small deflections
FEM Model	Eq. (56)	25.2	underestimation
Experiment	Fig. (7.4)	33^{+132}_{-30}	measurement value
Truncated Torus Model	Eq. (50)	35.6	reasonable approximation
MAJIDI and FEARING [238]	Eq. (53)	78.1	still reasonable approxim.
Naïve Azimuthal Strain Model	Eq. (35)	138.9	rough approximation
Truncated Cone Model	Eq. (47)	320.4	overestimation

The experimentally determined pre-factor has been estimated as $\Pi = 33 \times 10^{-4}$. This is remarkably close to the value obtained for the truncated torus model. The truncated torus model is considered to be the most accurate model presented in this thesis. However, the experimentally determined pre-factor has a large measurement error, as it was shown in Tab. VIII. This is due to the fact that the sampling resolution of the experimental parameter set with respect to the nominal wafer thickness, d, and the lens curvature radius, ρ, is comparatively small. Thus, the model by MAJIDI and FEARING can also be considered suitable, although the underlying model assumptions are not as strict as those of the truncated torus model. The model by MAJIDI and FEARING is probably the most exact model where a fully analytical mathematical calculation is still possible.

It is worth noting that for almost all practical applications, only the order of magnitude of the pre-factor is relevant, and not its exact value, because first, as the ratio (R/ρ) becomes small, the effect of the numerical value of the pre-factor, Π, becomes negligible, cf. Eq. (84). Second, the measurement error of the bonding energy, G_c, may be larger than the model prediction error in predicting whether complete and stable direct bonding is possible, so that a safety margin has to be chosen. These two facts make the exact value of Π less important. Third, when the wafer thickness, d, becomes so small that the effect of Π becomes large, the issue of wafer glass fracture due to local bending stress may become predominant. This is discussed in the following.

7.4.2 Validity of the Model

The truncated torus model is proposed to be valid as long as the non-contacted part of the wafer takes the form of a truncated torus. For the case where the ratio (R/ρ) becomes large and the wafer thickness, d, becomes small, a large azimuthal compressive strain may occur in the outer perimeter of the non-contacted part of the wafer, while the wafer is highly susceptible to out-of-plane azimuthal bending, also referred to as buckling. In this case, a transition from the truncated torus geometry to a buckled truncated torus geometry can occur, as shown schematically (and in an exaggerated way) in Fig. 7.6. The reason for this buckling is a sensitivity of the stressed truncated torus to initial geometric imperfections [281], for example, to thickness variations in the outer wafer perimeter.

Wafer buckling causes the wafer to locally experience bending stress, or more specifically, tensile stress, that may exceed the bending strength. This can lead to local glass breakage. Indeed, this was observed experimentally, see Sec. 7.2, where in Fig. 7.3 (d), that is, for a thin wafer, the location of the glass fracture is shown for the case of an experiment where partial contact between a circular wafer and a spherical substrate was observed. Looking at this figure, it can be seen that the azimuthal vari-

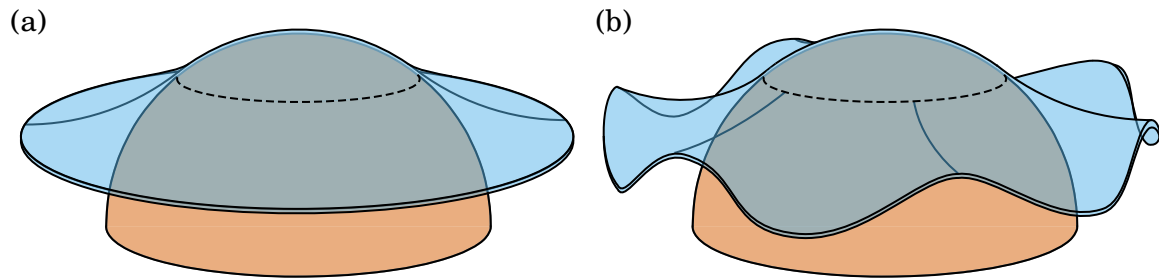(a)   (b)

Figure 7.6: Schematic of the geometry of a circular wafer partially in contact with a spherical substrate, where the non-contacted part of the wafer takes the form of (a) a truncated torus, and (b) a truncated torus where buckling has occurred. The contact front is shown as a dashed curve. The magnitude of the buckling is exaggerated.

ation of the contacted part, the non-contacted part as well as the glass fracture area is similar to the azimuthal periodic variation of the buckled truncated torus shown in Fig. 7.6 (b). In contrast, the non-contacted part was observed to be nearly radial-symmetric in the case of Fig. 7.3 (c), that is, for a thick wafer. This is in agreement with the experimental results from literature where the wrapping of an elastic film on an adhesive sphere was studied and it has been found that the deviation from a radial-symmetric contact front increases with increasing ratio (R/ρ) [282].

It is proposed that the resulting change in strain energy release rate, G, is small as compared to the truncated torus model. This is because the shape variation associated with buckling, u_z, have been found experimentally to occur only in an order of magnitude of the wafer thickness, d. Nevertheless, it is important to keep this effect in mind when considering direct bonding of very thin wafers to spherical substrates, as it can lead to glass breakage.

7.4.3   Extrapolation of the Model

Contacting of circular wafers with spherical substrates was investigated for wafers that have a diameter of two inches, only. (That is, $R = 25.4\,\text{mm}$.) Also, only the "initial" bonding energy was considered. (That is, no annealing step was performed.) It is possible to extrapolate the results beyond the experimentally verified range. To do so, the parameter R must be modified. Also, the assumed bonding energy must be modified. The extrapolated results are shown in Fig. 7.7. As expected, the parameter set where complete and stable contact is possible increases when the wafer diameter, $2R$, decreases, as well as when assuming the "corroded" bonding energy instead of the "initial" bonding energy.

It is not trivial to clamp the circular wafer during the annealing step such that it is in complete contact with the spherical substrate. The scenario where a concave spherical shell is used to press the wafer onto the substrate was investigated by an FEM simulation, see Fig. 7.8 (a) to (c). The state in the moment of the first contacting is shown in (a). The state where contacting has already started is shown in (b). Here,
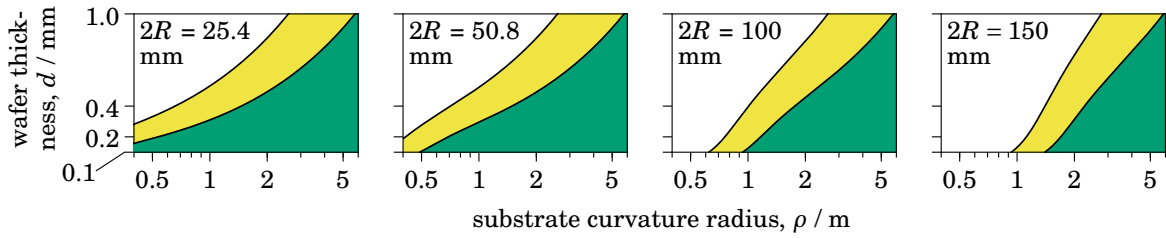
Figure 7.7: Parameter sets that allow (green and yellow area) and do not allow (white area) complete and stable contact of a circular wafer with given thickness, d, and diameter, $2R$, on a spherical lens substrate with given curvature radius, ρ. The curves were computed from Eq. (57) while assuming $\Pi = 35.6 \times 10^{-4}$. Here, the green area shows the result in the case of the state after the initial contacting step, where $G_c = 0.2\,\mathrm{J\,m^{-2}}$ is assumed, and the yellow area shows the result in the case of the annealed and corroded state, where $G_c = 1\,\mathrm{J\,m^{-2}}$ is assumed.
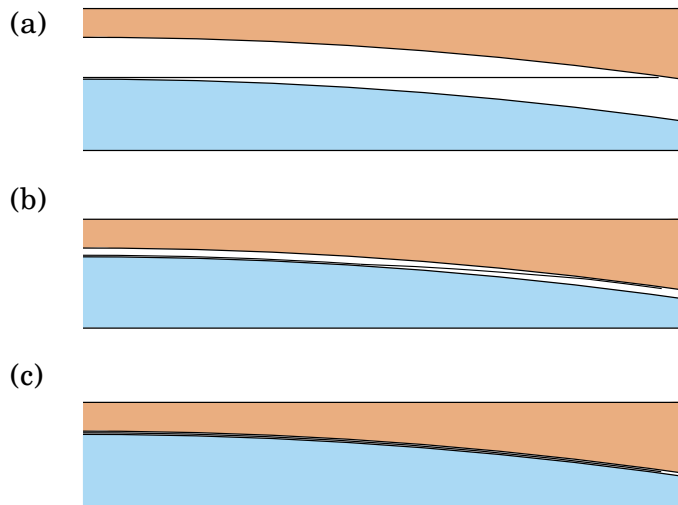
Figure 7.8: Schematic of the contacting process for a circular wafer and a spherical convex substrate (blue) where the external force is provided by a spherical concave shell (orange). The resulting wafer shape has been obtained by an FEM simulation with the parameters $\rho = 300\,\mathrm{mm}$, $R = 40\,\mathrm{mm}$ and $d = 100\,\mathrm{\mu m}$, assuming radial symmetry of the deformation behavior.

the strain distribution in the wafer causes the outer perimeter of the wafer to cling to the shell. This leads, at least locally, to a nearly parallel approach of the two surfaces. The state of complete contact is shown in (c). There is no continuous propagation of the contact front from the inside to the outside. Rather, the area near the wafer's outer perimeter touches the substrate instantly. That area is therefore very susceptible to an entrapment of bubbles at the bonding interface and to a significant accumulation of mechanical stress which can lead to wafer fracture. In addition, the air between wafer and spherical shell has nowhere to be pushed away during the contacting step, therefore, the spherical shell has be designed with ventilation holes or the contacting experiment has to be conducted in a vacuum. More sophisticated clamping tools are required for direct bonding of wafers with spherical substrates to allow a defect free and fracture-proof process.

8 Application of Non-Planar Direct Bonding

8.1 Discussion of Possible Direct Bonding Use Cases

For direct bonding of a wafer to a convex cylindrical lens substrate, a mathematical formula for predicting a complete area stable contact has been derived, see Eq. (29). For direct bonding of a wafer to a convex spherical lens substrate, a mathematical formula for predicting a complete area stable contact has been derived, too, see Eq. (57), where the pre-factor of the first term can be assumed to be equal to $\Pi = 35.6 \times 10^{-4}$ which is the result of the truncated torus model.

Tab. IX presents possible parameter sets where complete area stable contact is possible, for both substrate geometries discussed. It is assumed that the bonding energy is $G_c = 1\,\mathrm{J\,m^{-1}}$, which corresponds to the measured value for an annealed and then corroded borofloat bonding interface. If applicable, two different wafer diameters are considered, corresponding to the aperture diameters often used in optical applications, namely nominally 1 inch and 4 inches, that is, a radius of $R = 12.7\,\mathrm{mm}$ and $R = 50\,\mathrm{mm}$, respectively. Two wafer thickness values are also considered, namely $100\,\mathrm{\mu m}$ and $400\,\mathrm{\mu m}$, which corresponds to a low flexural rigidity wafer and to an overall smooth wafer surface, respectively.

For the material fused silica, it is possible to assume even higher bonding energy values [171, 199]. This would allow smaller curvature radius values than those presented in Tab. IX. Also, when designing real applications, it is important to include a safety margin when estimating the feasibility of possible optical design setups.

For spherical substrates, the possible curvature radii are more limited as compared to cylindrical substrates. For example, the imaging spectrometer's optical design presented in Sec. 1.2.1 would require an optical aperture of half its current size for al-

Table IX: Parameter sets that allow direct bonding of initial planar wafers on non-planar substrates. The abbreviation ROC stands for the lens' radius of curvature, that is, ρ_{cyl} (for cylindrical lenses, see Eq. (29)) or ρ (for spherical lenses, see Eq. (57)). The abbreviation N/A stands for and not applicable. In all cases, it is assumed that the bonding energy is equals $1\,\mathrm{J\,m^{-2}}$ and that borofloat is used as wafer material, which implies that $E = 64\,\mathrm{GPa}$ and $\nu = 0.2$.

substrate geometry	wafer diameter	wafer thickness, d	possible ROC
cylindrical	N/A	$100\,\mathrm{\mu m}$	$53\,\mathrm{mm}$
cylindrical	N/A	$400\,\mathrm{\mu m}$	$422\,\mathrm{mm}$
spherical	1 inch	$100\,\mathrm{\mu m}$	$169\,\mathrm{mm}$
spherical	4 inches	$100\,\mathrm{\mu m}$	$624\,\mathrm{mm}$
spherical	1 inch	$400\,\mathrm{\mu m}$	$658\,\mathrm{mm}$
spherical	4 inches	$400\,\mathrm{\mu m}$	$1007\,\mathrm{mm}$

lowing direct bonding with a wafer. But the advantages of using a more advanced DOE could compensate for the smaller optical aperture. Future research could go towards, first, a modification of the wafer geometry where, for example, a ring-shaped or a star-shaped geometry would enable direct bonding on spherical substrates with smaller curvature radii. Ring-shaped optical apertures have been proposed to be suitable for electron-beam lithography tools or telescope applications. Second, mechanical clamping is expected to prevent the onset of water stress corrosion, allowing to assume higher bonding energy values.

8.2   Discussion of Encapsulated Diffraction Gratings

For future applications requiring an optical lens with an encapsulated diffraction grating (or, more generally, an encapsulated DOE) on its non-planar side, predicting the possible radius of curvature from the bonding energy scaled according to its actual contact area is not a sufficient model. Instead, it should be considered that the real scaled bonding energy is smaller than the predicted one by a factor of up to three (in the case of the thinning wafer beams), as demonstrated in Sec. 6.4.3. However, this disadvantage can be overcome by reducing the clear aperture of the grating. It should also be considered whether the spin drying step can be performed for a longer period of time or if an additional annealing at 110 °C can be implemented in order to remove the water from the grating grooves such that the proposed internal water stress corrosion mechanism, as discussed in Sec. 6.8, is reduced.

8.3   Consideration of Optical Lens Manufacturing Tolerances

Due to manufacturing limitations, cylindrical and spherical optical lenses will always be subject to surface form tolerances, that is, deviations from a perfect cylinder or sphere surface, respectively. The formulae derived in this thesis, which predict direct bonding of an initially planar wafer to a cylindrical or spherical lens substrate, see Eqs. (29) and (57), respectively, assume that there are no such deviations. When it comes to applications, it is useful to modify these equations to account for these surface form tolerances. Reasonable tolerances to consider are radius of curvature and centering errors, as well as tilt, twist, and wedge errors [283, Chap. 36].

When cylindrical optical lenses are considered, none of these errors result in a deviation from the cylindrical shape. Thus, Eq. (29) is still valid. Only the radius of curvature has to be adjusted if necessary.

When considering spherical optical lenses, most of these errors correspond only to EUCLIDean transformations. However, when the radii of curvature in the meridional and sagittal planes are different, that is, ρ_x and ρ_y are different, an adjustment of Eq. (57) is required. This error is also called astigmatism error, that is, an imaging
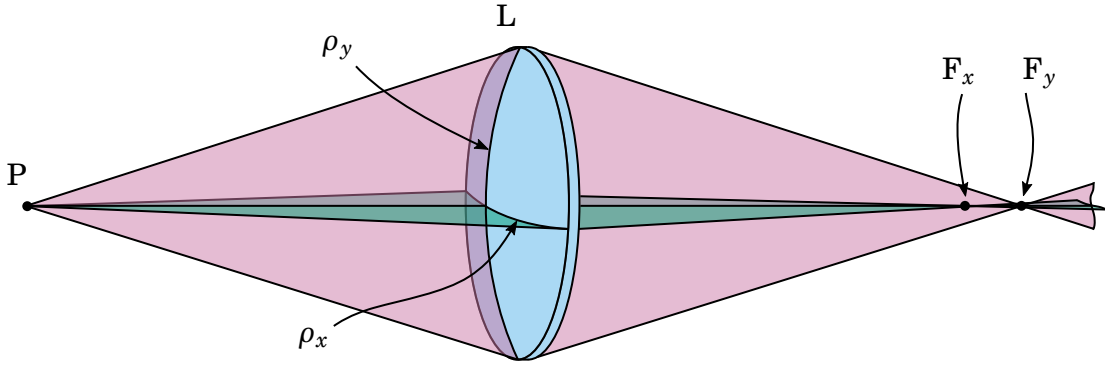
Figure 8.1: Schematic of the astigmatism imaging error due to a not perfectly spherically manufactured optical lens. The light which comes from a point source, P, is focused by the optical lens, L, where the focus points, F_x and F_y, for the sagittal plane (green) and tangential plane (red), respectively, are located at different positions along the optical axis according to the respective lens ROC values, ρ_x and ρ_y.

error where light rays propagating in two perpendicular planes have different foci, as schematically shown in Fig. 8.1. Equivalently, the lens is not spherical but an ellipsoid [284]. The success of direct bonding can still be predicted. This is done by assuming that the outer perimeter of the wafer changes according to that of an ellipse. Note that the outer perimeter of the wafer stores essentially all of the strain energy, cf. Sec. 3.3.3. A very good approximation for the perimeter of an ellipse is the calculation of the quadratic mean of the semi-axes, ρ_x and ρ_y. As such, the lens curvature radius needs to be modified via

$$\rho^2 \quad \longrightarrow \quad \frac{\rho_x^2 + \rho_y^2}{2}, \tag{86}$$

which needs to be applied to the first term of Eq. (57), which describes the energetic contributions from longitudinal forces, Ψ_N. Considering the second term of Eq. (57), which describes the energetic contributions from plate bending, Ψ_M, the modification

$$\frac{1+\nu}{\rho^2} = \frac{1}{\rho^2} + \frac{\nu}{\rho^2} \quad \longrightarrow \quad \frac{1}{2}\left(\frac{1}{\rho_x^2} + \frac{1}{\rho_y^2}\right) + \frac{\nu}{\rho_x \rho_y} \tag{87}$$

needs to be applied which directly follows from Eq. (19). In summary, Eq. (57) becomes

$$G_c \geq G = \Pi B \left(\frac{2R^2}{\rho_x^2 + \rho_y^2}\right)^2 + D\left[\frac{1}{2}\left(\frac{1}{\rho_x^2} + \frac{1}{\rho_y^2}\right) + \frac{\nu}{\rho_x \rho_y}\right]. \tag{88}$$

8.4   Demonstration of the Manufacture of a Novel Hybrid Lens

In Sec. 1.2, two ideas were presented where a combination of an optical lens with a diffractive optical element (DOE), realized via non-planar direct bonding, would be beneficial. Here, the realization of the second idea, that is, a novel hybrid lens for a volume BRAGG grating (VBG) inscription tool, is demonstrated.

8.4.1   Approach and Realization

The VBG inscription tool's current design makes use of a plano-convex cylinder lens, see Fig. 1.2. The new design will make use of a bi-convex cylinder lens with a wafer directly bonded on one of its surfaces. The wafer has a DOE for chromatic and spherical aberration reduction inscribed into its surface. The optical design is shown in Fig. 8.2.

The lens' curvature radius is specified as (80.0 ± 0.5) mm in both directions. The wafer thickness is (100 ± 10) µm where a total thickness variation of smaller than 1 µm is specified. The lens is square-shaped with side length (50.0 ± 0.5) mm and edge thickness (3.0 ± 0.1) mm where the relevant square-shaped optical aperture of the DOE has a side length of 25.4 mm. Both lens and wafer are made of borofloat. The calculated performance improvement with regard to the aberration reduction is shown in Fig. 8.3. It is equals a factor of one hundred. For the wafer, a thick, circular substrate of four inches diameter is used, and then with in-house technology a DOE is lithographically inscribed in its surface via direct-write grayscale lithography. Then, the wafer is thinned via multi-step grinding, polished via CMP and finally diced. The final wafer along with a detail image of the DOE structure's topography is shown in Figs. 8.4 (a) and (b), respectively.

According to Eq. (29), a bonding energy of $G_c = 0.59 \, \mathrm{J \, m^{-2}}$ is required for complete area stable contact. This can be achieved by an annealing step after the direct bonding contacting step, such that even in the corroded state, the expected bonding energy is still around $1 \, \mathrm{J \, m^{-2}}$, as shown Sec. 6.2.1. After the contacting step and during the annealing step, a fixture is required to prevent interface separation. The fixture must not get into contact with the optical aperture area. A tolerance analysis yields that a rotation error and a centration error between wafer and lens of smaller than ± 2.5 mrad and ± 100 µm is required, respectively. The contacting step must be performed such that

(a) the first contact is a line located lengthways along the substrate,

(b) the contact front propagates symmetrically towards the lens's edges,

(c) tilt and shift between wafer and lens are within the tolerances as specified above.

To tackle these challenges, a dedicated direct bonding tool has been developed. It is shown in Fig. 8.5. In the figure's caption, additional details are explained.

8.4.2   Characterization

The direct bonding process and the annealing process have been conducted according to the parameters described in Sec. 4.5. A photo of the contacting step and of the resulting novel hybrid lens is shown in Fig. 8.6 (a) and (b), respectively.

In the bonding interface, there are some defects visible, resulting supposedly from the wafer's thickness variations due to the grinding process. There is only one defect
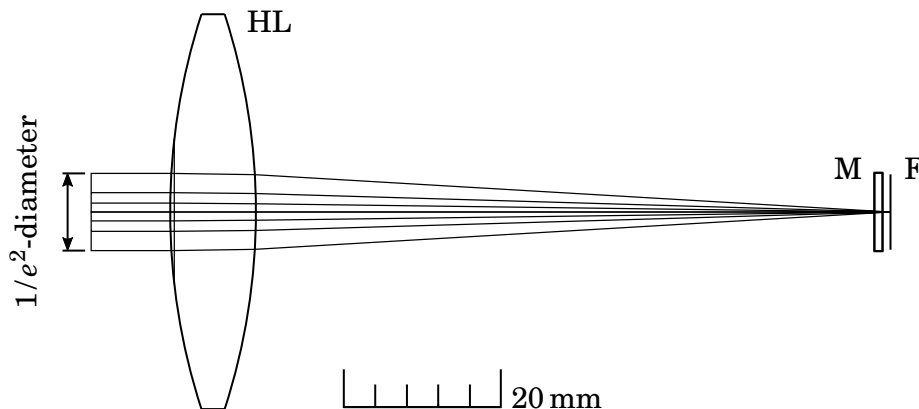
Figure 8.2: Schematic layout of the phase mask inscription tool's optical design. It consists of a hybrid lens (HL), that is, a bi-convex cylinder lens with a DOE, a phase mask (M), and a focus plane (F) that is located at the volume sample into which the grating will be written.
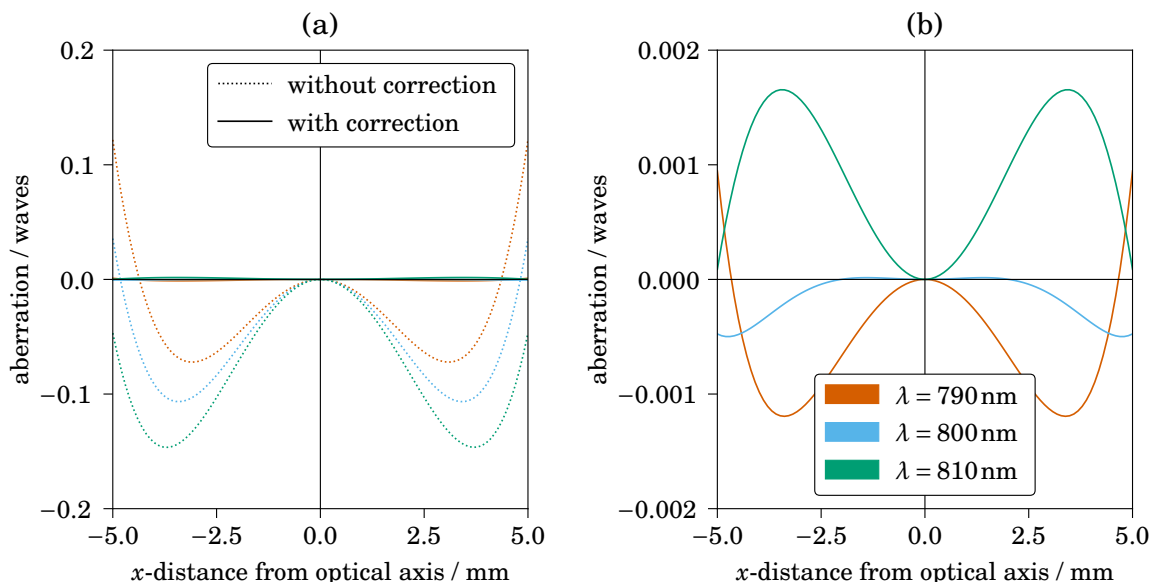
Figure 8.3: Optical design simulation results showing the aberration as a function of the x-distance from the optical axis for different wavelengths, λ. Note that (a) has a different ordinate scale than (b).
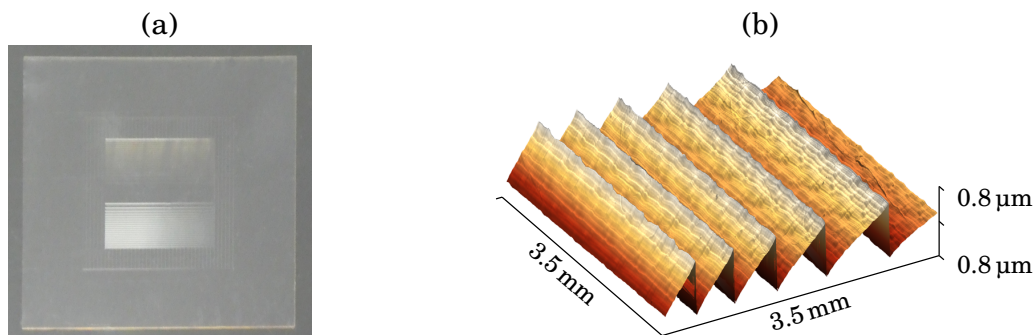
Figure 8.4: (a) Photo of one of the thinned borofloat wafers where a DOE structure has been inscribed in its surface. The wafer has a size of $(50.0 \times 50)\,\mathrm{mm}^2$ and is only $100\,\mu\mathrm{m}$ thick. (b) Surface topography of a part of the DOE structure. Data have been obtained using white light interferometery (WLI) on a $3.5 \times 3.5\,\mathrm{mm}^2$ test area.

in the area of the optical aperture, and it is located at its edge. The bonding interface is mechanically stable, even after weeks of storage in humid air. An optical characterization is planned to be performed in a real application laboratory setup of an VBG manufacture tool.

(a)   (b)

Figure 8.5: (a) Drawing (front face) and (b) cross-sectional drawing (side face) of the tool that allows direct bonding of a bi-convex cylinder lens with a 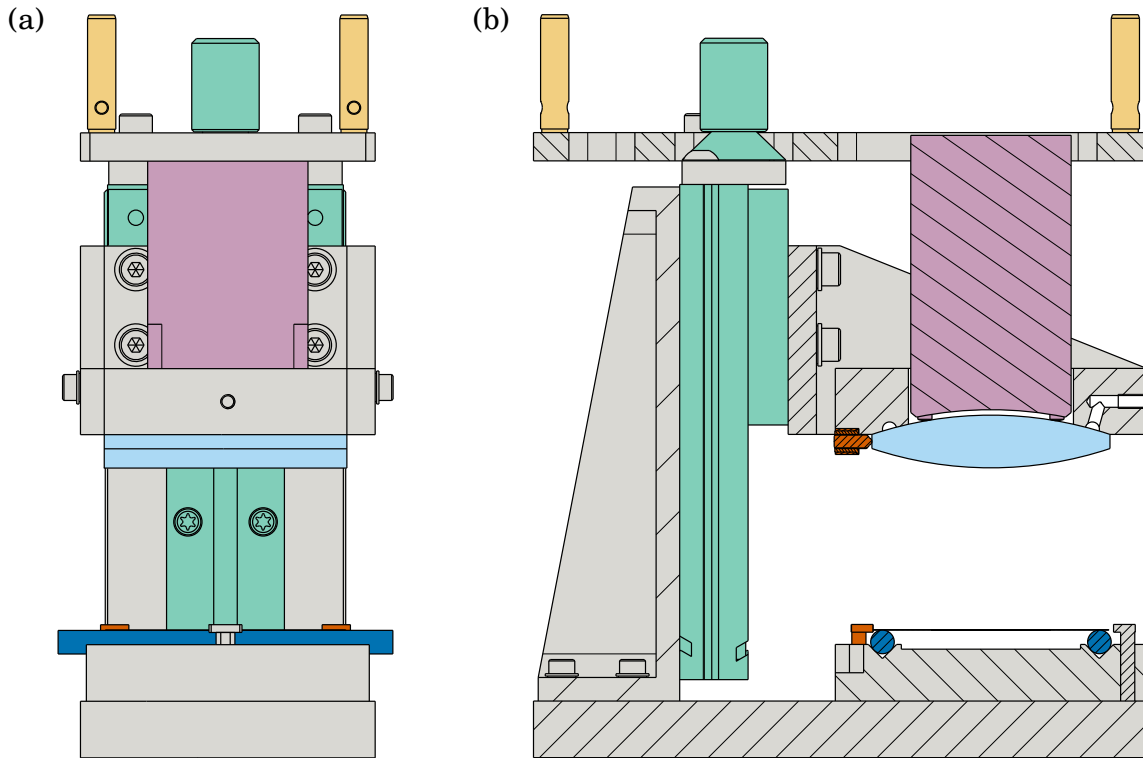thin wafer that has a diffraction grating inscribed in its outer surface. Procedure: The tool is turned upside down so that it stands on the pillars (yellow). Then, the lens (light blue) is placed on a ring-shaped vacuum chuck There is no mechanical contact to its optical aperture. The lens' position is fully determined by the chuck's shape and an alignment pin (orange). Then, the tool is turned around to its original position, and the wafer is placed on top of two test pins (dark blue). The wafer's DOE is facing downwards. The wafer's position is fully determined by these two test pins and by two alignment pins (orange). The lens is now descended via a dovetail slide (green) until an initial line contact sets in. By further descending the lens, the contact front increases symmetrically. As soon as the lens' movement is stopped by the test pins, a weight (purple) is put on top of the lens. Now, the vacuum is switched off, the tool is placed in a furnace and the dovetail slide is elevated. After annealing, the weight is removed and the hybrid lens is taken out.
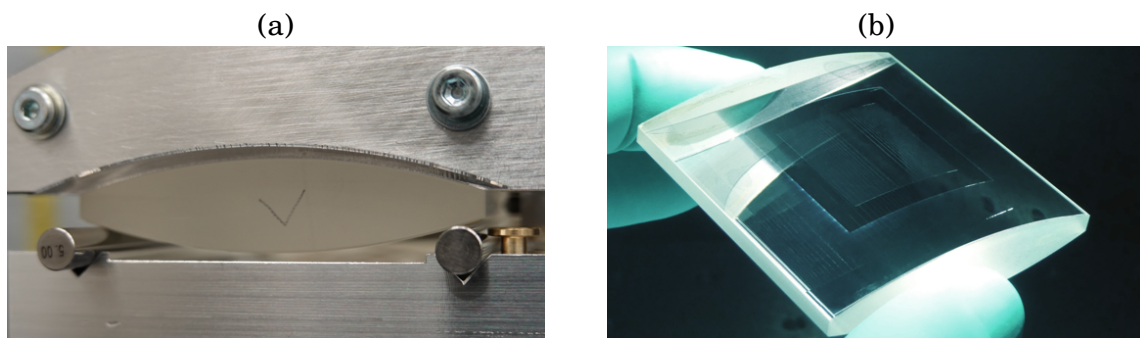
(a)   (b)

Figure 8.6: Photos of (a) the contacting step, and (b) the resulting novel hybrid lens.

9 Conclusion

In this thesis, direct bonding of wafers, that is, of thin, planar substrates, on non-planar substrates, in particular, convex cylindrical and spherical optical lenses, was investigated. As such, the paradigm that direct bonding requires both substrates' surfaces to be highly planar was tackled. The motivation stems from the field of optics, because there are advanced optical applications that would benefit from combining a diffractive optical element (DOE) with a non-planar substrate. This would reduce weight and assembly space and create new optical functionalities. Some advanced DOEs can only be inscribed in surfaces of planar substrates. Direct bonding of such structured wafers on non-planar substrates is proposed to open the door to that field of novel optical elements.

The following working packages have been completed within the scope of this thesis: Mathematical models have been developed to predict complete area stable contacting success. These models have been verified experimentally. A novel, highly accurate method for measuring the bonding energy has been developed. The underlying surface physics mechanism was investigated. A demonstrator that combines an optical lens and a DOE has been manufactured.

9.1 Methodology

Direct bonding experiments have been conducted using differently thick SCHOTT Borofloat® 33 wafers to study different conditions regarding surface quality and mechanical properties. In particular, plasma-activated bonding (PAB) was applied, which is a hydrophilic direct bonding method enabling low-temperature annealing.

The bonding energy was measured in the state after initial contacting (that is, prior to the annealing step), in the state after annealing and directly when a peeling moment has been introduced and, finally, in the state after water stress corrosion has set in. In order to study the surface physics mechanism of a bonded interface that is mechanically stressed in more detail, time-resolved contact front propagation experiments using the dual cantilever beam (DCB) method were performed in humid air and in dry nitrogen. In order to validate the mathematical models that predict complete area stable contacting success, direct bonding of wafers with convex cylindrical and convex spherical substrates was investigated. Here, the wafer's thickness and the substrate's radius of curvature was varied. The equilibrium contact front position was then analyzed.

For accurately measuring the bonding energy of non-planar interfaces that correspond to uni-axially bent wafers, a novel measurement method has been developed. It is referred to as "κ-method". Here, a wafer is placed on top of a non-planar substrate whose curvature, κ, is linearly increasing. The contact front's equilibrium position is directly related to a certain bonding energy value. The κ-method was evaluated with regard to reproducibility and accuracy as compared to the DCB-method.

9.2   Key Findings

It has been demonstrated that the κ-method, although requiring the equipment manufacture once in the beginning, has a distinctly improved measurement accuracy and a decreased risk of wafer breakage during the handling as compared to the DCB-method. These advantages are particularly pronounced in the case of directly bonded wafers which are very thin and have large expected bonding energy values. It gives a mixed mode I and II bonding energy value, where the share of the mode I bonding energy in the total bonding energy can be easily calculated. This allows a comparison with results obtained from the DCB-method. In conclusion, the κ-method is the preferred method when an accurate bonding energy measurement of directly bonded wafers is required.

Considering the direct bonding surface physics mechanism, it was found that, firstly, in order to predict the bonding energy, it is important to take into account not only the surface roughness but also the surface waviness. Second, the bonding energy of an interface affected by water stress corrosion drops and settles to the same value independently of the surface waviness, which is interesting, because during the contacting step, the bonding energy had been dependent of the these parameters. For explaining this phenomenon, it was proposed that a wavy surface leads to more elastic strain energy internally stored at the bonding interface's vicinity due to contact point deformation. The amount of water stored at the bonding interface is not affected by the surface waviness. The sum of the externally provided strain energy (due to the wafer being bent) and the internally stored elastic strain energy determines the water stress corrosion rate. In this thesis, an explicit reaction kinetics model has been developed which takes into account the atmospheric condition. For conceived practical applications of non-planar direct bonding, the rule that can be derived from this is that the requirement for surface roughness must be very good (much better than $S_q < 0.5$ nm, test area of $10 \times 10 \, \mu m^2$). This can be achieved by chemical-mechanical-polishing (CMP). The surface roughness determines the settled bonding energy, which is regarded as an important property. The surface waviness determines the properties corrosion rate and bonding energy during the contacting step, with the latter prop-

erty being potentially important for some applications. For very thin wafers, a very good surface waviness (much better than $S_q < 1\,\text{nm}$, test area of $700 \times 520\,\mu\text{m}^2$) can be achieved by a careful thinning process via multi-step grinding followed by CMP.

Considering direct bonding of wafers on convex cylindrical and convex spherical substrates, the mathematical models have been experimentally confirmed. This makes it possible to predict complete area stable contacting success for a large range of use cases. For cylindrical substrates, the required bonding energy scales with $(1/\rho)^2$, and for spherical substrates, it scales with $(R/\rho)^4$, where R is the wafer radius and ρ is the substrate curvature radius. For example, it was found that a $100\,\mu\text{m}$ thick borofloat wafer of one inch diameter can be bonded with a cylindrical lens substrate of curvature radius $53\,\text{mm}$ or with a spherical lens substrate of curvature radius $169\,\text{mm}$, assuming a bonding energy of $1\,\text{J}\,\text{m}^{-2}$.

In order to demonstrate the practical relevance of non-planar direct bonding, a combination of a cylindrical lens and a DOE for a volume BRAGG grating inscription tool has been manufactured. After lithographically inscribing the DOE in a wafer surface and then applying a thinning process on the wafer's backside, the direct bonding step could be performed just as predicted. Hereby, a novel hybrid lens has been manufactured which is expected to outperform state-of-the-art optical elements in terms of chromatic and spherical aberration. The proof of concept was successful.

9.3 Outlook

In various applied research fields, it is important to have a tool at hand for the accurate measurement of the bonding energy of interfaces. Relevant research fields are the development of adhesives [285], the engineering of structured interfaces [286–288] and wafer direct bonding. Particularly for wafer direct bonding, the κ-method's improved measurement accuracy may further stimulate research progress.

The presented mathematical models for predicting complete area stable contacting success as well as the new insights into the direct bonding surface physics mechanism give important guidelines for manufacturing optical, electronic, electromechanical or hybrid components which feature mechanically stressed interfaces that require long-term mechanical stability. Possible applications where this technology is expected to become important are, among others, space based imaging spectrometers and volume BRAGG grating inscription tools.

In conclusion, it has been shown that direct bonding of wafers into whose surface a DOE has been inscribed on non-planar substrates, in particular, optical lenses, is a possible way towards hybrid optical components with novel functionalities.

10 Acknowledgment

This thesis was developed during my occupation as a research employee at the Fraunhofer Institute for Applied Optics and Precision Engineering (IOF) in Jena, Germany. At the Fraunhofer IOF, I have always had the opportunity to work on a variety of exciting research and development projects together with great colleagues, for which I am very grateful.

First and foremost, I would like to thank my doctoral advisor, Prof. Dr. rer. nat. Uwe D. ZEITNER, for his commitment in taking over the supervision. He contributed a great deal of dedication by giving hands-on suggestions as well as encouragement and by guiding me to keep the focus throughout the whole time. Also, he conducted the optical design simulation of the novel hybrid lens, which is gratefully acknowledged.

Great thanks is also expressed to Prof. Dr. rer. nat. Stefanie KROKER for agreeing to take on the responsibility of being the co-referee for this thesis and for fruitful advice on how to tackle the presentation for the thesis defense. In addition, great thanks is expressed to Prof. Dr. Kevin T. TURNER, Ph. D., the third referee. His review contained a lot of insightful comments on how to improve the quality of this thesis. This is gratefully acknowledged.

I would also like to thank my head of department at the Fraunhofer IOF, Dr.-Ing. Stefan RISSE, for his practical and scientific advice, for keeping my back free in the face of heavy project load, for making possible the financial realization of this thesis and for his valuable hints on how I can maintain the "common thread" of this thesis. His great interest in the success of this work was always a source of motivation for me.

In addition, I would like to thank my group leader at the Fraunhofer IOF, Dr.-Ing. Carolin ROTHHARDT, because she was always available for scientific discussions. She provided a lot of good ideas, especially when it came to discussing the underlying physical mechanism at the borofloat interface. I learned from her how to keep a cool head when direct bonding experiments go wrong.

There are a lot of other colleagues to whom I hereby express my gratitude for their contributions to this thesis: The computer-aided design of the κ-method's bonding tool parts as well as that of the novel hybrid lens bonding tool parts was provided by Gerd HARNISCH, whom I also would like to thank for fruitful discussions on direct bonding contacting step aspects. The atomic force microscopy (AFM) and the white light interferometry (WLI) measurements were carried out by Dr. rer. nat. Nadja FELDE and Anna F. WENGER, whom I also would like to thank for fruitful discussions on the evaluation of the topography data. The electron beam lithography structures were

A Appendix

A.1 Formulae Derivations

In this section, the derivation of some important mathematical relations is presented.

A.1.1 Fundamental Plate Theory Equations for Bending and Twisting

For finding a plate's curvature, $\kappa_{\alpha\beta}$, as a function of its elastic strain, ε_{ij}, the inverse of the curvature is considered, that is, the curvature radius, $\rho_{\alpha\beta}$, which emerges from bending ($\alpha = \beta$) or twisting ($\alpha \neq \beta$) the plate by applying some stress, $\sigma_{\alpha\beta}$. Now, by considering the equation $\mathrm{d}x_\alpha = \rho_{\alpha\beta}\,\mathrm{d}\theta_\beta$, or equivalently

$$\mathrm{d}x_\alpha\,\kappa_{\alpha\beta} = \mathrm{d}\theta_\beta, \tag{89}$$

which holds at the mid-plane, that is, at $z = 0$, and by regarding a deformed length element which is *not* at the mid-plane, $\mathrm{d}x_\alpha'$, but parallel and shifted with respect to $\mathrm{d}x_\alpha$, see Fig. A.1, it can be derived that $\mathrm{d}x_\alpha' = (\rho_{\alpha\beta} - z)\mathrm{d}\theta_\beta$. By combining these equations with Eq. (10), cf. Ref. [289, Chap. 5], it is found that

$$\kappa_{\alpha\beta} = \kappa_{\beta\alpha} = \varepsilon_{\alpha\beta}/z. \tag{90}$$

Then, for finding the moment per unit length, $M_{\alpha\beta}$, as a function of the curvature, $\kappa_{\alpha\beta}$, it is assumed that a force, f_γ, is exerted on a plate's cross section acting on the edges parallel to the β-axis. This implies that β and γ are different, cf. Fig. 2.11 (a) and (b). This notation is in accordance with literature [215, Chap. 10]. Note that $M_{\alpha\beta} = M_{\beta\alpha}$. With Eqs. (11) and (15), the moment itself, that is, force times length z, is
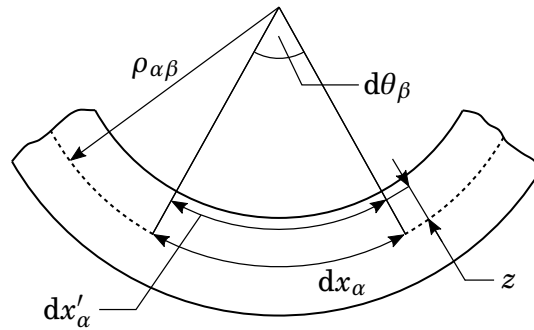

Figure A.1: Schematic drawing for the explanation of the relation between curvature, $\kappa_{\alpha\beta}$, and strain, $\varepsilon_{\alpha\beta}$, where the special case $\alpha = \beta$ is depicted. Taken from Ref. [289, Chap. 5.4], slightly modified.

given by the equations

$$\mathrm{d}M_{\alpha\beta}\,\mathrm{d}x_\gamma = \mathrm{d}^2 f_\gamma\, z = \frac{\partial f_\alpha}{\partial A_\beta}\,\mathrm{d}^2 A_\beta\, z = \sigma_{\alpha\beta}\,\mathrm{d}^2 A_\beta\, z = \sigma_{\alpha\beta}\,\mathrm{d}x_\gamma\,\mathrm{d}z\, z.$$

Now, both sides are divided by $\mathrm{d}x_\gamma$. By using Eq. (12) and again Eq. (15), inserting Eq. (90) and integrating with respect to z from $-d/2$ to $d/2$, the equation

$$M_{\alpha\beta} = D\,(1-\nu)\left(\kappa_{\alpha\beta} + \delta_{\alpha\beta}\frac{\nu}{1-\nu}\sum_\gamma \kappa_{\gamma\gamma}\right)$$

is found, with flexural rigidity, D, as defined in Sec. 2.6.2. Here, $\delta_{\alpha\beta}$ is the KRONECKER delta which is equal to one for $\alpha = \beta$ and equal to zero elsewise. This equation can be regarded as HOOKE's law of plate bending and twisting. In literature, this equation is often found in matrix notation and with the small deflection approximation, Eq. (20), applied, cf. Refs. [216, Chap. 2.3] and [236, Chap. 3.8].

Eventually, Eq. (89) is applied and it is considered that

$$\mathrm{d}U_E = \frac{1}{2}\sum_\alpha \sum_\beta M_{\alpha\beta}\,\mathrm{d}x_\alpha\,\mathrm{d}\theta_\alpha$$

holds, which is just a different way of expressing Eq. (13), cf. Ref. [215, Chap. 12]. From this and by using Eq. (14),

$$\mathrm{d}U_E = \frac{1}{2}\sum_\alpha \sum_\beta M_{\alpha\beta}\,\kappa_{\alpha\beta}\,\mathrm{d}x_\alpha\,\mathrm{d}x_\beta = \Psi_M\,\mathrm{d}x_\alpha\,\mathrm{d}x_\beta$$

is obtained. By inserting HOOKE's law of plate bending and twisting and comparing both sides of the equation, finally the explicit expression

$$\Psi_M = \frac{D}{2}\left(\kappa_{xx}^2 + \kappa_{yy}^2 + 2\nu\kappa_{xx}\kappa_{yy} + 2(1-\nu)\kappa_{xy}^2\right)$$

is found, which is valid for both small and large deflections.

A.1.2 Characteristic Separation Distance During Wafer Delamination

During the delamination of a wafer from an acylindrical substrate, any fixed point at the wafer's underside, $\mathbf{x}'$, does not separate perpendicularly from the substrate but follows a curve which can mathematically be described by the substrate's involute function, also referred to as evolvent function. For the given case, that function can be calculated by assuming that the curvature, κ_{xx}, is locally constant. The displacement

vector, given as a parametric representation, is

$$\mathbf{u} = \mathbf{x}' - \mathbf{x} = \begin{pmatrix} u_x \\ u_z \end{pmatrix} = \begin{pmatrix} \sin(\varphi) - \varphi \cos(\varphi)/(1-\varepsilon) \\ \cos(\varphi) + \varphi \sin(\varphi)/(1-\varepsilon) - 1 \end{pmatrix} \Big/ \kappa_{xx} \tag{91}$$

where $\mathbf{x}$ is the initial point fixed at the substrate where the delamination starts, φ is the angle between the line segment from the center of curvature to $\mathbf{x}$ and the line segment from the center of curvature to the current contact front position, $\mathbf{x}_c$, and $\varepsilon = \kappa_{xx} d/2$ is the elastic compression (that is, squeezing) strain stored locally at the wafer's underside. This is schematically shown in Fig. A.2. Note that for the case $\varepsilon = 0$, Eq. (91) would simplify to the well-known formula of the involute function of a circle with radius $1/\kappa_{xx}$ [290, Chap. 2.14.4].

Equation (91), with $\varphi > 0$ as a variable, is characterized by starting its path in a tangential way along the substrate and then following a nearly circular curve with gradually decreasing curvature moving away from the substrate. For $\varphi \to 0$, the local curvature radius of Eq. (91), that is, the inverse of the local curvature, is given by

$$\rho^\star = \frac{d^2 \kappa_{xx}}{4 - d^2 \kappa_{xx}^2} \approx \frac{d^2 \kappa_{xx}}{4}$$

where the approximation is valid due to the fact that $d\kappa_{xx} \approx 0$. By assuming $\kappa_{xx} = \kappa_{xx,c}$, the equation in question has been derived. Typical values obtained for the experiments conducted in the frame of this thesis are ranging from 20 nm to 125 nm.

Now, it will be shown that the absolute slope of Eq. (91),

$$S = \frac{\mathrm{d}u_z}{\mathrm{d}u_x} = \frac{\mathrm{d}u_z/\mathrm{d}\varphi}{\mathrm{d}u_x/\mathrm{d}\varphi} = \frac{\varepsilon \sin(\varphi) + \varphi \cos(\varphi)}{\varepsilon \cos(\varphi) - \varphi \sin(\varphi)}, \tag{92}$$

is equals zero in the case of $\varphi \to 0$ and equals 2 in the case defined by the condition $u_z(\varphi) = 2\rho^\star$, that is, when the wafer's underside has separated from the substrate surface by an amount that is assumed to be the approximated characteristic separation distance. This assumption is reasonable because only when the distance between substrate and wafer is smaller than $2\rho^\star$, surface separation is dominated by mixed mode crack formation behavior, whereas beyond that distance it is dominated by pure mode I crack formation behavior.

To show that $S = 0$ for $\varphi \to 0$ is trivial. To show that $S = 2$ for the condition $u_z(\varphi) = 2\rho^\star$ requires to find the value of the corresponding angle, φ. It can be shown empirically that the equation $u_z(\varphi) = 2\rho^\star$ has the solution $\varphi = \kappa_{xx} d$. The mathematical prove for this empirical finding is obtained by performing a TAYLOR approximation with respect to $\kappa_{xx} d$ and then assuming $\kappa_{xx} d \approx 0$. Finally, inserting the solution,
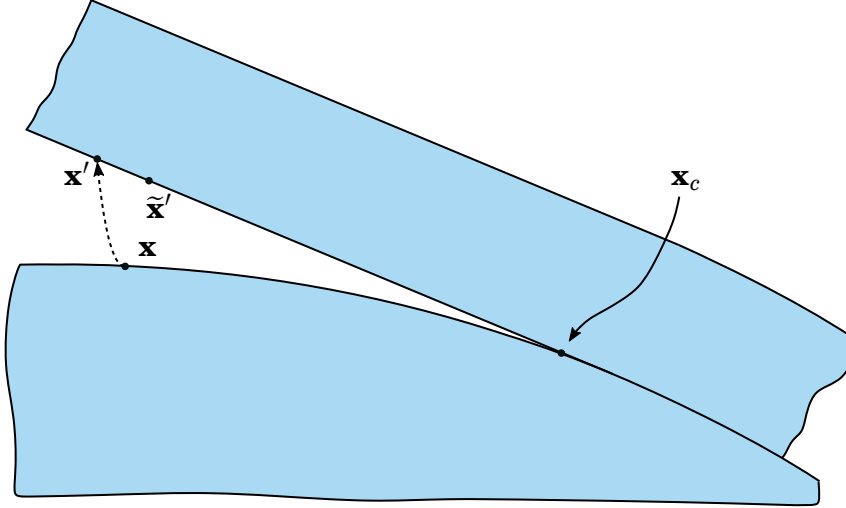
Figure A.2: Schematic of the delamination process of a wafer from a cylindrical substrate. The dashed line shows the trajectory of a fixed point at the wafer's underside, $\mathbf{x}'$, starting from the initial contact position, $\mathbf{x}$, see Eq. (91). Note that instead of the point $\mathbf{x}'$, the alternative point $\widetilde{\mathbf{x}}'$ would have been reached if there was no "relaxation" process (that is, "decompression" or "unsqueezing") occuring at the wafer's underside.

$\varphi = \kappa_{xx}\, d$, into to Eq. (92) yields the critical slope

$$S = \frac{2\cos(\kappa_{xx}\, d) + \sin(\kappa_{xx}\, d)}{\cos(\kappa_{xx}\, d) - 2\sin(\kappa_{xx}\, d)}$$
$$\approx \frac{2 + \sin(\kappa_{xx}\, d)}{1 - 2\sin(\kappa_{xx}\, d)} \approx 2. \tag{93}$$

A.1.3   Small Deflection Wafer Bending on a Spherical Substrate

TURNER and SPEARING [110] have presented a small deflection model for estimating complete area stable contacting success of two non-rigid wafers. In this thesis the special case of contacting of a non-rigid wafer and an infinitely rigid spherical lens is considered where a model can directly be derived from plate theory in a simple way.

Due to the fact that deflections are small and radially symmetric, the total strain energy is sufficiently described by bending moments only, see Tab. II, where the curvature is equal in both directions, that is, $\kappa = \kappa_{xx} = \kappa_{yy}$. Thus, Eq. (19) takes on the form

$$\Psi_M = \frac{D}{2}\left(2\kappa^2 + 2\nu\kappa^2\right) = D(1+\nu)\kappa^2.$$

With Eqs. (2) and (27), and by taking $1/\rho = \kappa$, it is found that

$$G_c \geq \frac{D(1+\nu)}{\rho^2}.$$

Due to $(1-\nu^2)/(1-\nu) = (1+\nu)$, the identity $D(1+\nu) = E\, d^3/(12(1-\nu))$ holds. This explains the relation to the equation by TURNER and SPEARING, see Eq. (24).

A.1.4   Derivation of MAJIDI and FEARING's Model

MAJIDI and FEARING [238] investigated the contacting behavior of thin polyethylene plates on convex spherical glass substrates. For the case of circular plates with a given radius, R, being pressed on a substrate with curvature radius, ρ, they calculated the strain energy release rate by using the following mathematical approach.

During the contacting step, a point in the mid-plane of the wafer displaces by an amount of u_r and u_z in the radial and vertical direction, respectively. The sphere is approximated as a paraboloid, such that $u_z = -r^2 / (2\rho)$. The wafer's radial strain is

$$\varepsilon_{rr} = \frac{\partial u_r}{\partial r} - z\,\kappa_{rr} + \frac{1}{2}\left(\frac{\partial u_z}{\partial r}\right)^2 = \frac{\partial u_r}{\partial r} - \frac{z}{\rho} + \frac{1}{2}\left(\frac{r}{\rho}\right)^2 \tag{94}$$

which is established by the approach explained in Sec. 2.6.2, that is, the FÖPPL-VON KÁRMÁN plate theory approach, and by inserting $\kappa_{rr} = 1/\rho$. Following the same approach, the wafer's azimuthal strain is given by

$$\varepsilon_{\varphi\varphi} = \frac{1}{r}\frac{\partial u_\varphi}{\partial \varphi} - z\,\kappa_{\varphi\varphi} + \frac{1}{2}\left(\frac{\partial u_z}{\partial \varphi}\right)^2 = \frac{u_r}{r} - \frac{z}{\rho}. \tag{95}$$

For understanding Eq. (95), it should be noted that $(1/r)\,(\partial u_\varphi / \partial \varphi) = (\tilde{p} - p)/p$, with p and $\tilde{p}$ being the wafer's original and strained perimeter as a function of r, respectively, as it has been explained in Sec. 3.3.2. By reducing the fraction by 2π and then identifying the remaining numerator with u_r, the term u_r/r is obtained.

Analogous to the second step of the derivation of the truncated cone model, see Sec. 3.3.3, by using Eqs. (21), (26) and (42), an integrand, $\mathscr{L}$, for the integral function for $G^{(\mathrm{nc})}$ can be calculated which can then be inserted into the EULER-LAGRANGE-equation, see Eq. (44). This yields an ordinary differential equation that has the exact solution

$$u_r = \frac{r\left(r^2\,(\nu - 3) - r_c^2(\nu - 1) - 16\,\rho\,z\right)}{16\,\rho^2}. \tag{96}$$

By inserting Eq. (96) back into the integral equation for $G^{(\mathrm{nc})}$ and then taking $r_c = R$ (such that $G^{(\mathrm{nc})}$ can be considered as being equal to G), the solution

$$G = \frac{B}{128}\left(\frac{R}{\rho}\right)^4 \approx \left(78.1 \times 10^{-4}\right) \times B\left(\frac{R}{\rho}\right)^4 \tag{97}$$

is obtained.

MAJIDI and FEARING use a completely different nomenclature when presenting their derivation. The derivation presented here is based on the nomenclature that has been introduced in Secs. 2 and 3.

A.1.5   Double Cantilever Beam Evaluation Formula

MASZARA et al. [119] give no derivation for their dual cantilever bending (DCB) formula but cite GILLIS and GILMAN [291] who give, unfortunately, a very complicated derivation. Here, a shorter and easier one is presented.

First, the opened wafer pair is regarded as two cantilevers of length a, width b and thickness d, being deflected symmetrically in opposite directions. It is assumed that the deflection is caused by inserting a razor blade with a certain thickness, w. At $x = 0$, both cantilevers are in contact. At $x = a$, the razor blade applies a vertical force, $F_z/2$, on each cantilever, so that for $0 \le x < a$ there is a bending moment per unit length, M_{xx}, with maximum value at $x = 0$. By assuming a linear and continuous relation,

$$M_{xx} = \frac{F_z}{2b}(a - x).$$

is obtained. Second, in order to describe the resulting geometry, HOOKE's law of plate bending and twisting is applied, see Eq. (17). Here, all contributions but κ_{xx} may be neglected, so that

$$M_{xx} = D\,\kappa_{xx} \approx D\,\frac{\mathrm{d}^2 u_z}{\mathrm{d}x^2}$$

where the small-deflection approximation, Eq. (20), has been applied. Now both equations can be combined. Solving for $\mathrm{d}^2 u_z/\mathrm{d}x^2$, integrating twice and applying the boundary conditions $u_z = 0\big|_{x=0}$ and $\mathrm{d}u_z/\mathrm{d}x\big|_{x=0} = 0$ yields

$$u_z = \frac{F\,a^3}{6\,b\,D}, \quad \text{or equivalently,} \quad F = \frac{6\,u_z\,b\,D}{a^3}.$$

The corresponding strain energy is given by

$$U_E = \int_0^{w/2} F\,\mathrm{d}u_z = \frac{3}{4}\frac{w^2\,b\,D}{a^3}.$$

With Eq. (2), the strain energy accumulation rate, G, is then given by

$$G = -\frac{1}{b}\frac{\mathrm{d}U_E}{\mathrm{d}a} = \frac{9}{4}\frac{w^2\,D}{a^4}.$$

When assuming a static equilibrium, the condition $G = G_c$ holds. Therefore,

$$G_c = \frac{9}{4}\frac{w^2\,D}{a^4}, \quad \text{or equivalently,} \quad G_c = \frac{3}{16}\frac{E}{1-v^2}\frac{w^2\,d^3}{a^4},$$

where the latter expression is more commonly found in literature, cf. Refs. [116, 118].

A.1.6   Wave Interference

Interference phenomena of superimposed light waves, that is, spatially structured distributions of the light intensity, can be observed if the light waves' path differences are small and certain conditions are fulfilled [292, Chap. 10]. For example, if two light waves from the same source that have the same wavelength, λ, and that have a phase shift of $\Delta\phi = 2k\pi$, with $k \in \mathbb{Z}$, are superimposed, constructive interference occurs such that the intensity takes on its maximum value. In contrast, for $\Delta\phi = (2k+1)\pi$, destructive interference occurs such that the intensity vanishes.

In the frame of this thesis, interference fringes have been observed during the contact front position measurement via the DCB-method and the κ-method. Here, the reflected light is observed. The air gap width, d_{air}, between top wafer and bottom wafer is related to the optical path length difference, Δx, between a light wave that is reflected at the under side of the top wafer and another light wave (from the same source) that is reflected at the upper side of the bottom wafer by the formula

$$\Delta x = 2\,d_{\mathrm{air}} + \frac{\lambda}{2} \tag{98}$$

where the second term describes the phase shift that occurs when a wave travels from an optically dense medium to air.

Due to the fact that $\Delta\phi = 2\pi\,\Delta x/\lambda$, the resulting phase difference is given by

$$\Delta\phi = 4\pi\,\frac{d_{\mathrm{air}}}{\lambda} + \pi. \tag{99}$$

This implies that constructive and destructive interference occurs if $d_{\mathrm{air}}/\lambda = (2k-1)/4$ and $d_{\mathrm{air}}/\lambda = k/2$, respectively. Now, $k \in \mathbb{N}$, due to $d_{\mathrm{air}} > 0$. As such, the first constructive wave interference is observed at an air gap width of $d_{\mathrm{air}} = \lambda/4$.

Between constructive and destructive interference, there is a smooth transition of the intensity profile. The relative intensity, that is, the local intensity divided by its overall maximum value, as a function of the air distance can be modeled by

$$I_{\mathrm{rel}} = \sin^2\!\left(2\pi\,\frac{d_{\mathrm{air}}}{\lambda}\right). \tag{100}$$

Equation (100) can be used to numerically simulate interference fringes that are typically observed during the contact front position measurement via the DCB-method and the κ-method. The resulting diagram, as well as a comparison to an experimental observation, is shown in Sec. A.2.7, and the underlying computer code is shown in Sec. A.3.2. There, it becomes clear that the assumption of $\lambda = 400\,\mathrm{nm}$ is a good approximation for defining the first interference fringe position.

A.1.7 Variable Transformation for Modeling Sub-Critical Crack Growth

The measurement data presented in Fig. 6.11 (a) are depicted as bonding energy, G_{Ic}, versus time, t. An alternative way to study sub-critical crack growth is to consider the growth rate, $v := \mathrm{d}a/\mathrm{d}t$. Strictly, the growth rate has to be a function of the strain energy release rate, G_I, and not of the bonding energy, G_{Ic}. This is because the bonding energy refers to a critical value, see Sec. 2.2.4, while the strain energy release rate refers to the intensity of the externally applied stress. To avoid ambiguity, the term strain energy release rate is used here.)

For the data points, the transformation from a (t, G_I)-diagram to a (G_I, v)-diagram is straight-forward: The growth rate, v, can be calculated by the central difference quotient of neighboring data points of the gap length, a. This is why the data points are more scattered after the transformation, see Figs. 6.11 (b).

In order to find the transformed representation of the proposed function for the bonding energy time evolution model, Eq. (81), the following procedure is applied. First, Eq. (81) is rewritten into its constituting non-linear ordinary differential equation (ODE) form, that is,

$$
\frac{\mathrm{d}(G_I)}{\mathrm{d}t} = -k_{\mathrm{eff}} \frac{(G_I - G_{Ic,\infty})^n}{(G_{Ic,0} - G_{Ic,\infty})^{n-1}}, \quad \text{with} \quad n = \begin{cases} 2 & \text{for humid air, and} \\ 3 & \text{for dry nitrogen.} \end{cases} \tag{101}
$$

Second, Eq. (71) is rearranged to

$$
a^{-4} = \frac{4}{9D} \frac{G_I}{w^2}. \tag{102}
$$

The derivative of a^{-4} with respect to G_I is given by

$$
\frac{\mathrm{d}(a^{-4})}{\mathrm{d}(G_I)} = \frac{4}{9DE} \frac{1}{w^2}, \tag{103}
$$

which will be useful in a moment. By using the chain rule of calculus [231, Chap. 2.9],

$$
v = \frac{\mathrm{d}a}{\mathrm{d}t} = -\frac{a^5}{4} \frac{\mathrm{d}(a^{-4})}{\mathrm{d}t} = -\frac{(a^{-4})^{-5/4}}{4} \frac{\mathrm{d}(a^{-4})}{\mathrm{d}(G_I)} \frac{\mathrm{d}(G_I)}{\mathrm{d}t} \tag{104}
$$

is obtained. Finally, inserting Eqs. (101), (102) and (103) into Eq. (104) yields

$$
v = \sqrt{\frac{3 w k_{\mathrm{eff}}^2}{32}} \sqrt{\frac{D}{G_I^5}} \times \frac{(G_I - G_{Ic,\infty})^n}{(G_{Ic,0} - G_{Ic,\infty}^2)^{n-1}}. \tag{105}
$$

The curves calculated from Eq. (105) are shown in Fig. 6.11 (b).

A.2 Additional Figures and Tables

A.2.1 Curve Fitting Procedure for the Truncated Cone Model Data

Figure A.3: Numerically calculated data (black points) and fit model (color plane) for the truncated cone model. The underlying fit model is given by $G = \Pi B (R/\rho)^4$, where Π is the only fit parameter. The point size is proportional to the percentage residuum, with a maximum value of 2%. Here, $d = 100\,\mu\text{m}$, $E = 64\,\text{GPa}$ and $\nu = 0.2$ has been assumed.

A.2.2 Curve Fitting Procedure for the FEM Model Data
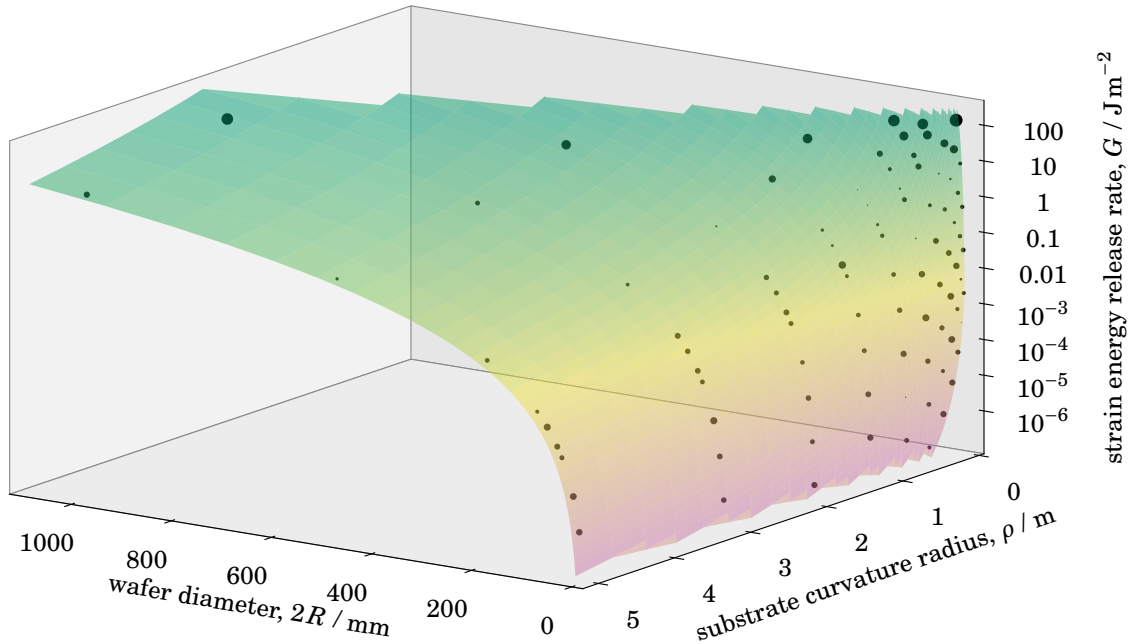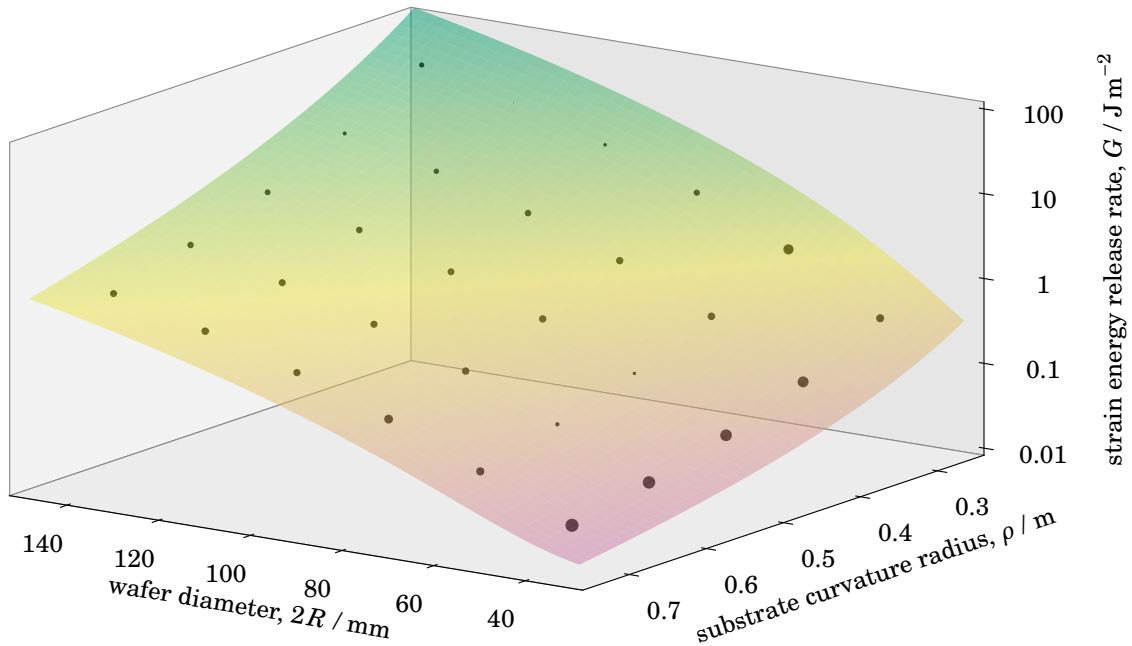
Figure A.4: Numerically calculated data (black points) and fit model (color plane) for the FEM model. The underlying fit model is given by $G = \Pi B (R/\rho)^4 + D (1+\nu)/\rho^2$, where Π is the only fit parameter. The point size is proportional to the percentage residuum, with a maximum value of 2%. Here, $d = 100\,\mu\text{m}$, $E = 64\,\text{GPa}$ and $\nu = 0.2$ has been assumed.
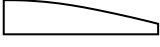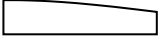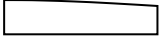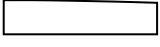
A.2.3 Overview of the Support Platforms

Four different support platforms, each with a different maximal curvature, $\kappa_{xx,\mathrm{max}}$, have been used in the frame of this thesis. This allows to accurately measure the bonding energy, G_{Ic}, for wafers of different thickness values, d, and for a wide range of expected bonding energy values.

Table X: Overview of maximally measurable bonding energy values when combining wafers of different thickness with different support platforms. Values are given in units of $\mathrm{mJ\,m^{-2}}$. Those combinations chosen for the experimental procedure are highlighted by a $\star$-symbol.

wafer beams' thickness	support platform type (with geometry according to the maximal curvature value, $\kappa_{xx,\mathrm{max}}$, see Sec. A.2.6 in the appendix)			
	$\kappa_{xx,\mathrm{max}} =$ $7.69\,\mathrm{m^{-1}}$	$\kappa_{xx,\mathrm{max}} =$ $3.90\,\mathrm{m^{-1}}$	$\kappa_{xx,\mathrm{max}} =$ $1.955\,\mathrm{m^{-1}}$	$\kappa_{xx,\mathrm{max}} =$ $0.783\,\mathrm{m^{-1}}$
$d\,/\,\mathrm{\mu m}$				
100	$\star 80.2$	20.9	5.25	0.851
200	642	$\star 167$	42.0	6.73
400	$\star 5\,134$	1\,338	$\star 335.9$	53.8
1\,000	80\,222	20\,909	$\star 5\,249$	$\star 841$

A.2.4 Technical Drawing of a Support Platform

There are four cantilever curves platform types. One curve is shown in Fig. 5.2 (which corresponds to a certain wafer beam's thickness of $d = 100\,\mathrm{\mu m}$). Its exact surface shape is shown in Fig. A.5.
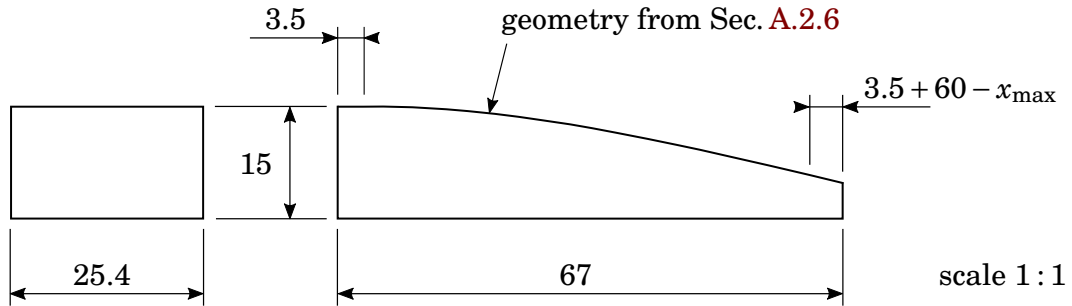
Figure A.5: Technical drawing of the support platforms. The geometry is exemplarily shown for the cantilever curve corresponding to $d = 100\,\mathrm{\mu m}$, but the annotations are valid for all support platform types. Note that left and right of the polynomially curved area there is an exactly 3.5 mm wide and an approximately 3.5 mm wide area, respectively, each with vanishing curvature. This is for the fixture of the first wafer beam (which has a length of 67 mm).

A.2.5   Proportionality Factor Calculation

The relation between the proportionality factor, K, the wafer beam length, L, and the maximal curvature, $\kappa_{xx,\mathrm{max}}$, is given by

$$K = \frac{1.000871 \times (\kappa_{xx,\mathrm{max}} L) - 0.003067 \times (\kappa_{xx,\mathrm{max}} L)^2 + 0.069410 \times (\kappa_{xx,\mathrm{max}} L)^3}{L^2}. \tag{106}$$

The validity of Eq. (106) can be proven by performing a TAYLOR's approximation at the data numerically obtained with the computer code in Sec. A.3.3.

A.2.6   Polynomial Approximations of the Cantilever Curves

In Sec. 5.2, a numerically calculated wafer beam cantilever curve have been shown. Their corresponding polynomial approximations for each wafer beam's thickness, d, is given in Tab. XI, where the polynomial function

$$u_z(x) = a_2 x^2 + a_3 x^3 + a_4 x^4 + a_5 x^5, \quad \text{with} \quad x \in [0, x_{\mathrm{max}}], \tag{107}$$

has been used. Again, the numerical data has been obtained with the computer code presented in Sec. A.3.3.

Table XI: Polynomial approximations for the cantilever curve from Fig. 5.2 and the other ones used.

wafer beams' thickness	characteristic values (coefficients, maximum value of the domain and maximum value of the curvature) according to Eq. (107)					
$d\,/\,\mu\mathrm{m}$	$a_2 \times 10^{-3}$ $/\mathrm{mm}^{-2}$	$a_3 \times 10^{-6}$ $/\mathrm{mm}^{-3}$	$a_4 \times 10^{-9}$ $/\mathrm{mm}^{-4}$	$a_5 \times 10^{-12}$ $/\mathrm{mm}^{-5}$	x_{max} $/\mathrm{mm}$	$\kappa_{xx,\mathrm{max}}$ $/\mathrm{m}^{-1}$
100	-3.85	20.69	-9.32	191.1	59.156	7.69
200	-1.948	10.86	-3.56	38.6	59.782	3.90
400	-0.977	5.50	-1.755	12.99	59.944	1.955
1 000	-0.391	2.208	-0.702	4.51	59.989	0.783

A.2.7   Wave Interference Fringes Visualization

When measuring the contact front position in the frame of the DCB-method, the air gap width, d_{air}, increases approximately quadratically as a function of the distance from the contact front, cf. Sec. A.2.6. Light waves constructively interfere at different distances from the contact front according to their wavelength. For the human eye, the superimposition of these intensity profiles appears as a range of different colors. An obvious method to simulate this superimposition is to calculate the intensity profiles of the colors red (R), green (G) and blue (B), which correspond to the colors of a typical light-emitting diode (LED) computer screen, and then let the computer screen

visualize the actual color by superimposing the light of all three LEDs for each pixel. The result of the simulated interference fringes is shown in Fig. A.6, along with the result of actual experimental data from literature [293].

The dotted line in Fig. A.6 corresponds to an air gap width defined by the condition $d_{air} = \lambda/4$ with $\lambda = 400\,nm$. Visible light has a wavelength range of approximately $380\,nm$ to $750\,nm$. In this sense, the dotted line is a very reasonable threshold to mark the visible border of the first interference fringe.
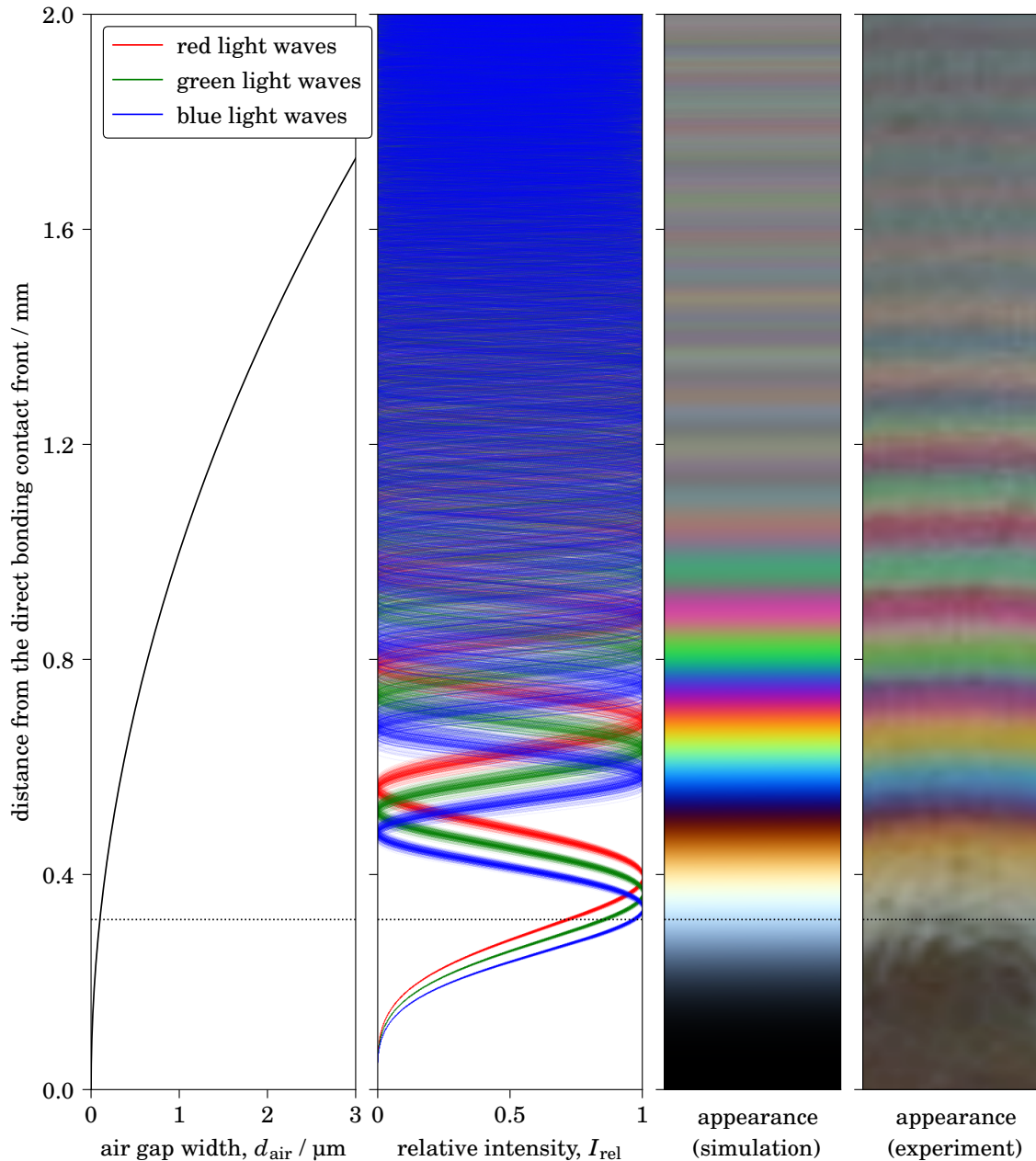
Figure A.6: Simulated and experimentally observed interference fringes for a reflective setup. Light waves are typically experimentally observed to cease interfering if the air gap width becomes too large, which is also referred to as decoherence. This phenomenon is modeled by slightly changing the wavelength value of each light wave from one of its three nominal values. The image of the experimental data has been taken from Ref. [293].

A.3   Computer Codes

For the numerical calculations, the programming language Python (Version 3.6.5) has been used. In the following, computer codes are presented in a minimal version where the focus is on a good comprehensibility rather than on an efficient computability.

A.3.1   Truncated Cone Model

While Fig. 3.4 shows the algorithm to calculate $\varepsilon_{\varphi\varphi}$ and $G^{(\mathrm{nc})}$ for the truncated cone model as a flowchart, the actual computer code is shown in Lst. 1.

Listing 1: Computer code for the numerical calculation of the contact front propagation within the truncated cone model. Here, the variables e and G correspond to $\varepsilon_{\varphi\varphi}$ and $G^{(\mathrm{nc})}$, respectively.

```python
from numpy import linspace, interp, sin

# Physical Parameters [-, Pa, m, m, m]
nu, E, t, rho, R = 0.2, 64e9, 400e-6, 0.5, 0.0254

# Numerical Precision
N = 1000

# Initial Conditions
integral_lst, r = [0], linspace(R/N, R, N)
e, e_prime, g, R_C_TLD = [0]*(N+1), [0]*(N+1), 1, 0

for r_c in r:
    r_lst = linspace(r_c, R, N+1)
    e_c = interp((r_c+(R/N)), r_lst, e)
    e_prime_c = interp((r_c+(R/N)), r_lst, e_prime)
    R_C_TLD += (R/N)*(1+e_c+r_c*e_prime_c)/g
    g = (1+sin(R_C_TLD/rho)**2)**(-0.5)
    c_1 = (g**2*e_c-g**2*nu-g*e_prime_c*r_c+g*nu+g-e_c -
            e_prime_c*r_c-1)/(2*g*(g+1))
    c_2 = (g*(e_c-nu)+e_c+e_prime_c*r_c+1)/(2*g)
    e = c_1*(r_lst/r_c)**(-g-1)+c_2*(r_lst/r_c)**(g-1)+(g*nu-1)/(g+1)
    e_prime = (c_1*(r_lst/r_c)**(-g-2)*(-g-1)/r_c +
                c_2*(r_lst/r_c)**(g-2)*(g-1)/r_c)
    L = r_lst*(e**2+((1+e+r_lst*e_prime)/g-1)**2 +
                e*((1+e+r_lst*e_prime)/g-1)*2*nu)
    integral_lst.append(sum(L)*(R-r_c)/N)
G = [0.5*(E*t/(1-nu**2))/r[i]*(integral_lst[i+1] -
            integral_lst[i])/(R/N) for i in range(N)]
for r_c, G_at_r_c in zip(r, G):
    print(r_c, "\t", G_at_r_c)

# End of File
```

A.3.2 Wave Interference Fringes Visualization

An example computer code to numerically simulate interference fringes that are typically observed during the contact front position measurement via the DCB-method, as shown in Fig. A.6, is shown in Lst. 2.

Listing 2: Computer code for the numerical calculation of the interference fringes observed during the DCB-method. Here, the variables x as well as d correspond to the distance from the direct bonding contact front as well as the air gap, d_{air}, respectively.

```python
from numpy import linspace, pi, sin, random
import matplotlib.pyplot as plt

# Physical Parameters [m, m, m, -, m, m]
Wavelength_R, Wavelength_G, Wavelength_B = 630e-9, 540e-9, 460e-9
Decoherence = 0.05
x_max, d_max = 20e-3, 100e-6

# Numerical Precision
M, N = 1000, 40

# Calculation
x = linspace(0, x_max, M)
d = (d_max/x_max**2)*x**2
line_r, line_g, line_b  = [[[0]*N]*M]*3
rand = random.normal(loc=0, scale=Decoherence, size=N)
lines = ([sin(2*pi*d/(Wavelength_R+d*rand[i]))**2 for i in range(N)],
         [sin(2*pi*d/(Wavelength_G+d*rand[i]))**2 for i in range(N)],
         [sin(2*pi*d/(Wavelength_B+d*rand[i]))**2 for i in range(N)])
a = [(sum([lines[0][j][i]/N for j in range(N)]),
      sum([lines[1][j][i]/N for j in range(N)]),
      sum([lines[2][j][i]/N for j in range(N)])) for i in range(M)]

# Plot Diagram
fig, axs = plt.subplots(3)
axs[0].set_ylabel(r"air gap width / m")
axs[0].plot(x, d, "k-")
axs[1].set_ylabel(r"relative intensity")
for line, color in zip(lines, ("r","g","b")):
    axs[1].plot([x]*N, line, c=color)
axs[2].set_ylabel("appearance")
axs[2].set_xlabel("distance from the contact front / m")
for i in range(M-1):
    axs[2].plot(x[i:i+2], [0,1], linewidth=1, color=a[i])
plt.show()

# End of File
```

A.3.3   Cantilever Deflection

The numerical calculation of the deformation of a cantilever which is subject to large deflections requires to solve the differential equation $M_{xx} = P \times (L - \delta - x) = D \kappa_{xx}$. Here, P is the applied load at the cantilever's tip, L is the cantilever's free length and δ is the tip's displacement along the x-axis. A convenient method to solve that differential equation via integral equations has been presented by BELÉNDEZ et al., see Eqs. (18) to (20) in Ref. [294]. An algorithm for solving these equations is presented in Lst. 3.

Listing 3: Computer code for the calculation of the deformation of a cantilever. The variables x and z correspond to the horizontal distance from the cantilever's position of fixture, x, and its vertical deflection, u_z, respectively.

```python
from numpy import linspace, sin, sqrt
from scipy.optimize import fsolve
from scipy.integrate import quad

# Functions
def approximate_a(phi_0, x_0):
    return((quad(lambda phi: 1./sqrt(sin(phi_0)-
    sin(phi)), 0, phi_0)[0]/2.0)**2.0-x_0)
def calculate_phi_0(a):
    return(fsolve(approximate_a, x0=1./N, args=a)[0])
def calculate_x(phi_0,phi,a,L):
    return((L/sqrt(a))*(sqrt(sin(phi_0))-sqrt(sin(phi_0)-sin(phi))))
def calculate_z(phi_0,phi,a,L):
    return((-L/(2.0*sqrt(a))) *
    quad(lambda phi: sin(phi)/sqrt(sin(phi_0)-sin(phi)), 0, phi)[0])

# Physical Parameters [-, Pa, m, m, m, N]
nu, E, L, b, t, P = 0.0, 64e9, 0.06, 0.0254, 100e-6, 0.017639

# Numerical Precision
N = 1000

# Calculation
a = P*L**2*6*(1-nu**2)/(b*E*t**3)
phi_0 = calculate_phi_0(a)
phi = linspace(0, phi_0, N)
x = [calculate_x(phi_0,phi[i],a,L) for i in range(N)]
z = [calculate_z(phi_0,phi[i],a,L) for i in range(N)]

for x_i , z_i in zip (x, z):
    print (x_i, "\t", z_i)

# End of File
```

A.3.4   Numerical Generation of the Topography of a Polished Glass Surface

The numerical generation of the topography of a polished glass surface requires an implementation of Eq. (82). A possible way to do this is presented in Lst. 4. By redirecting the output of this algorithm into, for example, an xyz-file, the result can be investigated by a scanning probe microscopy data visualization program, such as GWYDDION.

Listing 4: Computer code for the numerical generation of the topography of a polished glass surface.

```python
from numpy import sqrt, log, cos, pi, arctan, linspace
from numpy.random import uniform

# Functions
def phi(m, n):
    return (random_phase_m*(m+M)*random_phase_n*(n+n_max))

def z(x,y):
    prefactor = l*(psi/l)**(zeta-2)*sqrt(log(xi)/M)
    summands = sum([sum([xi**((zeta-3)*n)*(cos(phi(m, n)) -
            cos((2*pi*xi**n*sqrt(x**2 + y**2))/l *
        cos(arctan(y/x)-pi*m/M) + phi(m, n)))
        for n in range(1, n_max)]) for m in range(1, M)])
    return (prefactor*summands)

# Physical Parameters [m, m, -, -, -, -]
l, l_s, xi, psi, M, zeta = 1e-6, 2e-10, 1.5, 2e-11, 16, 2.75

# Number of pixels in each direction,
# that is, the sampling resolution
# (must be an even integer)
samples = 512

# Initial Conditions
x = linspace(l/samples, l+l/samples, samples+1)
y = linspace(l/samples, l+l/samples, samples+1)

# Calculation and Output
n_max = int(log(l/l_s) / log(xi))
random_phase_m = uniform(0, 2*pi)
random_phase_n = uniform(0, 2*pi)

for i in range(samples):
    for j in range(samples):
        print(x[i], "\t", y[j], "\t", z(x[i], y[j]))

# End of File
```

B References

[1] R. KINGSLAKE and R. B. JOHNSON. *Lens Design Fundamentals*, Volume PM 195. SPIE Press and Academic Press, Amsterdam, 2. edition, 2010.

[2] J.-Y. LABANDIBAR et al. Advanced Large FoV UV/VIS/NIR/SWIR Spectrometers. Final Report 100647037D. Thales Alenia Space, 2014.

[3] P. MOUROULIS and R. O. GREEN. Review of High Fidelity Imaging Spectrometer Design for Remote Sensing. *Opt. Eng.*, 57(4), 2018.

[4] CHANG Liu, C. STRAIF, T. FLÜGEL-PAUL, U. D. ZEITNER and H. GROSS. Comparison of Hyperspectral Imaging Spectrometer Designs and the Improvement of System Performance with Freeform Surfaces. *Appl. Opt.*, 56(24):6894–6901, 2017.

[5] T. FEIGL, M. PERSKE, H. PAUER, T. FIEDLER, U. ZEITNER, R. LEITEL, H.-C. ECKSTEIN, P. SCHLEICHER, S. SCHRÖDER, M. TROST, S. RISSE, R. STEINKOPF, F. SCHOLZE and C. LAUBIS. Sub-Aperture EUV Collector with Dual-Wavelength Spectral Purity Filter. In *Extreme Ultraviolet (EUV) Lithography VI*. *Proc. SPIE*, 9422:94220E, 2015.

[6] M. BURKHARDT, M. STEGLICH, M. HELGERT and D. LEHR. XUV Gratings Based on Holography. In *Advances in X-Ray/EUV Optics and Components XV*. *Proc. SPIE*, 11491:1149109, 2020.

[7] S. SCHRÖDER, L. BAHRENBERG, N. K. ERYILMAZ, S. GLABISCH, S. DANYLYUK, S. BROSE, J. STOLLENWERK and P. LOOSEN. Accuracy Analysis of a Stand-Alone EUV Spectrometer for the Characterization of Ultrathin Films and Nanoscale Gratings. In *Extreme Ultraviolet Lithography*. *Proc. SPIE*, 11517:115170S, 2020.

[8] S. SCHMIDT, S. THIELE, A. TOULOUSE, C. BÖSEL, T. TIESS, A. HERKOMMER, H. GROSS and H. GIESSEN. Tailored Micro-Optical Freeform Holograms for Integrated Complex Beam Shaping. *Optica*, 7(10):1279, 2020.

[9] H. OGAWA. Optical System with Refracting and Diffracting Optical Units, and Optical Instrument Including the Optical System. Standard Application. *Patent no.* 5,930,043. Canon Kabushiki Kaisha, 1999.

[10] C. M. Lee, M. L. Cable, S. J. Hook, R. O. Green, S. L. Ustin, D. J. Mandl and E. M. Middleton. An Introduction to the NASA Hyperspectral InfraRed Imager (HyspIRI) Mission and Preparatory Activities. *Remote Sens. Environ.*, 167:6–19, 2015.

[11] D. Krutz, R. Müller, U. Knodt, B. Günther, I. Walter, I. Sebastian, T. Säuberlich, R. Reulke, E. Carmona, A. Eckardt, H. Venus, C. Fischer, B. Zender, S. Arloth, M. Lieder, M. Neidhardt, U. Grote, F. Schrandt, S. Gelmi and A. Wojtkowiak. The Instrument Design of the DLR Earth Sensing Imaging Spectrometer (DESIS). *Sensors*, 19(7), 2019.

[12] Qian Shen-En, M. Bergeron, O. Djazovski, M. Maszkiewicz, R. Girard, M. Kappus, J. Bowles, A. Mannino, A. Matuszeski, M. Furlong, J.-P. Ardouin, G. Fournier, J. Levesque, L. Moreau, J.-F. Lavigne, J. Mandar, J. Busler and G. Buttner. A Spaceborne Coastal and Inland Water Color Hyperspectral Imager. In *IEEE International Geoscience and Remote Sensing Symposium*. *Proc. IEEE*, pages 447–450, 2017.

[13] J. Helbert. Mercury Radiometer and Thermal Infrared Spectrometer. A Novel Thermal Imaging Spectrometer for the Exploration of Mercury. *J. Appl. Remote Sens.*, 2(1):023528, 2008.

[14] J. Dyson. Unit Magnification Optical System Without Seidel Aberrations. *J. Opt. Soc. Am.*, 49(7):713, 1959.

[15] A. Offner. New Concepts in Projection Mask Aligners. *Opt. Eng.*, 14(2), 1975.

[16] C. G. Wynne. Monocentric Telescopes For Microlithography. *Opt. Eng.*, 26(4):300–303, 1987.

[17] D. W. Warren, D. J. Gutierrez, J. L. Hall and E. R. Keim. Dyson Spectrometers for Infrared Earth Remote Sensing. In *Infrared Spaceborne Remote Sensing and Instrumentation XVI*. *Proc. SPIE*, 7082:70820R, 2008.

[18] M. Taccola and M. Ahmad. Imaging Spectrometer with Reflective Grating. Standard Application. *Patent no.* US 10,184,833 B2. European Space Agency, 2019.

[19] D. Kwo, G. Lawrence and M. Chrisp. Design of a Grating Spectrometer from a 1:1 Offner Mirror System. In *Current Developments in Optical Engineering II*. *Proc. SPIE*, 818:275–279, 1987.

[20] KIM Seo Hyun, KONG Hong Jin, LEE Jong Ung, LEE Jun Ho and LEE Jai Hoon. Design and Construction of an OFFNER Spectrometer Based on Geometrical Analysis of Ring Fields. *Rev. Sci. Instrum.*, 85(8):083108, 2014.

[21] D. R. LOBB. Theory of Concentric Designs for Grating Spectrometers. *Appl. Opt.*, 33(13):2648–2658, 1994.

[22] WU Su, HUANG Chan, YU Lei, XUE Hui and LIN Jing. Optical Design and Evaluation of an Advanced Scanning DYSON Imaging Spectrometer for Ocean Color. *Opt. Express*, 29(22):36616–36633, 2021.

[23] ESTEC. Wide Band and High Efficiency Reflective Grating. Statement of Work TEC-MMO/2014/212. European Space Agency, 2015.

[24] P. M. STRZELECKI. Wide Band and High Efficiency Reflective Grating. ESA Open Invitation to Tender AO8458, 2015.

[25] F. BURMEISTER, T. FLÜGEL-PAUL, U. D. ZEITNER, M.-S.-L. LEE BOUHOURS, G. LEHOUCQ, J. CHOLET, B. LOISEAUX, N. TETAZ, R. WINDPASSINGER and M. TACCOLA. Binary Blazed Reflection Grating for UV/VIS/NIR/SWIR Spectral Range. In *Intl. Conference on Space Optics*. *Proc. SPIE*, 11180:111801J, 2019.

[26] J. THOMAS, C. VOIGTLÄNDER, R. G. BECKER, D. RICHTER, A. TÜNNERMANN and S. NOLTE. Femtosecond Pulse Written Fiber Gratings. a New Avenue to Integrated Fiber Technology. *Laser & Photon. Rev.*, 6(6):709–723, 2012.

[27] R. G. KRÄMER, C. MATZDORF, A. LIEM, V. BOCK, W. MIDDENTS, T. A. GOEBEL, M. HECK, D. RICHTER, T. SCHREIBER, A. TÜNNERMANN and S. NOLTE. Femtosecond Written Fiber BRAGG Gratings in Ytterbium-Doped Fibers for Fiber Lasers in the Kilowatt Regime. *Opt. Lett.*, 44(4):723–726, 2019.

[28] M. A. RIZA, Y. GO, II, S. W. HARUN and R. R. J. MAIER. FBG Sensors for Environmental and Biochemical Applications. A Review. *IEEE Sensors J.*, 20(14):7614–7627, 2020.

[29] T. J. STEINER, J. E. CASTRO, L. CHANG, Q. DANG, W. XIE, J. NORMAN, J. E. BOWERS and G. MOODY. Ultrabright Entangled-Photon-Pair Generation from an AlGaAs -On-Insulator Microring Resonator. *PRX Quantum*, 2(1):1, 2021.

[30] G. J. STECKMAN, W. LIU, R. PLATZ, D. SCHROEDER, C. MOSER and F. HAVER-MEYER. Volume Holographic Grating Wavelength Stabilized Laser Diodes. *IEEE J. Select. Topics Quantum Electron.*, 13(3):672–678, 2007.

[31] A. SEVIAN, O. ANDRUSYAK, I. CIAPURIN, V. SMIRNOV, G. VENUS and L. GLE-BOV. Efficient Power Scaling of Laser Radiation by Spectral Beam Combining. *Opt. Lett.*, 33(4):384–386, 2008.

[32] T. BARTULEVICIUS, S. FRANKINAS, A. MICHAILOVAS, R. VASILYEU, V. SMIR-NOV, F. TREPANIER and N. RUSTEIKA. Compact Fiber CPA System Based on a CFBG Stretcher and CVBG Compressor with Matched Dispersion Profile. *Opt. Express*, 25(17):19856–19862, 2017.

[33] D. RICHTER, M. P. SIEMS, W. J. MIDDENTS, M. HECK, T. A. GOEBEL, C. MATZDORF, R. G. KRÄMER, A. TÜNNERMANN and S. NOLTE. Minimiz-ing Residual Spectral Drift in Laser Diode Bars Using Femtosecond-Written Volume BRAGG Gratings in Fused Silica. *Opt. Lett.*, 42(3):623–626, 2017.

[34] T. BOILARD, R. VALLÉE and M. BERNIER. Probing the Dispersive Properties of Optical Fibers with an Array of Femtosecond-Written Fiber BRAGG Gratings. *Sci. Rep.*, 12(1):4350, 2022.

[35] L. TALBOT, D. RICHTER, M. HECK, S. NOLTE and M. BERNIER. Femtosecond-Written Volume BRAGG Gratings in Fluoride Glasses. *Opt. Lett.*, 45(13):3625–3628, 2020.

[36] H. A. ROWLAND. Preliminary Notice of the Results Accomplished in the Man-ufacture and Theory of Gratings for Optical Purposes. *Lond. Edinb. Dublin Philos. Mag. J. Sci.*, 13(84):469–474, 1882.

[37] H. G. BEUTLER. The Theory of the Concave Grating. *J. Opt. Soc. Am.*, 35(5):311–350, 1945.

[38] H. NODA, T. NAMIOKA and M. SEYA. Geometric Theory of the Grating. *J. Opt. Soc. Am.*, 64(8):1031, 1974.

[39] T. HARADA and T. KITA. Mechanically Ruled Aberration-Corrected Concave Gratings. *Appl. Opt.*, 19(23):3987–3993, 1980.

[40] K. MAJUMDAR and M. SINGH. On the Theory of Concave Transmission Grat-ing. *Opt. Commun.*, 1(7):329–333, 1970.

[41] S. SINGH. Diffraction Gratings: Aberrations and Applications. *Opt. Laser Technol.*, 31(3):195–218, 1999.

[42] CHEN Chungte W. Zoom Lens Employing Refractive and Diffractive Optical Elements. Std. Application. *Patent no.* 5,268,790. Hughes Aircraft Co., 1993.

[43] F. ZAMKOTSIAN, I. ZHURMINSKY, P. LANZONI, C. SCHNEIDER, N. TCHOUBAK-LIAN, S. FRICKE, M. SCHNIEPER, F. LÜTOLF, C. LUITOT and V. COSTES. Convex Blazed Gratings for High Throughput Spectrographs in Space Missions. In *International Conference on Space Optics*. *Proc. SPIE*, 11180:1118051, 2019.

[44] A. GEBHARDT, R. STEINKOPF, S. SCHEIDING, S. RISSE, C. DAMM, T. ZEH and S. KAISER. MERTIS: Optics Manufacturing and Verification. In *Infrared Remote Sensing and Instrumentation XVIII*. *Proc. SPIE*, 7808:78080Q, 2010.

[45] D. RADTKE and U. D. ZEITNER. Laser-Lithography on Non-Planar Surfaces. *Opt. Express*, 15(3):1167–1174, 2007.

[46] D. FLOREANO, R. PERICET-CAMARA, S. VIOLLET, F. RUFFIER, A. BRÜCKNER, R. LEITEL, W. BUSS, M. MENOUNI, F. EXPERT, R. JUSTON, M. K. DOBRZYN-SKI, G. L'EPLATTENIER, F. RECKTENWALD, H. A. MALLOT and N. FRANCES-CHINI. Miniature Curved Artificial Compound Eyes. *Proc. Natl. Acad. Sci. U.S.A.*, 110(23):9267–9272, 2013.

[47] SONG Young Min, XIE Yizhu, V. MALYARCHUK, XIAO Jianliang, JUNG Inhwa, CHOI Ki-Joong, LIU Zhuangjian, PARK Hyunsung, LU Chaofeng, KIM Rak-Hwan, LI Rui, K. B. CROZIER, HUANG Yonggang and J. A. ROGERS. Digital Cameras with Designs Inspired by the Arthropod Eye. *Nature*, 497(7447):95–99, 2013.

[48] S. SCHEIDING, A. Y. LI, A. GEBHARDT, LI Lei, S. RISSE, R. EBERHARDT and A. TÜNNERMANN. Freeform Manufacturing of a Microoptical Lens Array on a Steep Curved Substrate by Use of a Voice Coil Fast Tool Servo. *Optics Express*, 19(24):23938–23951, 2011.

[49] B. LANDGRAF, R. GÜNTHER, G. VACANTI, N. BARRIÈRE, M. VERVEST, D. A. GIROU, A. YANSON and M. J. COLLON. Direct Bonding of Multiple Curved, Wedged and Structured Silicon Wafers as X-Ray Mirrors. *ECS Trans.*, 75(9):331–338, 2016.

[50] C. VANHAVERBEKE, R. VERPLANCKE, J. DE SMET, D. DE CUYPERS and H. DE SMET. Microfabrication of a Spherically Curved Liquid Crystal Display Enabling the Integration in a Smart Contact Lens. *Displays*, 49:16–25, 2017.

[51] T. AONO, Y. EBATA, S. MATSUI and T. WATANABE. Curved Grating, Method for Manufacturing the Same, and Optical Device. Standard Application. *Patent no.* US 9,945,993 B2. Hitachi High-Technologies Corp., 2018.

[52] M.-S. L. Lee, J. Cholet, A. Delboulbé, R. Guillemet, B. Loiseaux, P. Garabédian, T. Flügel-Paul, T. Benkenstein, S. Sadlowski, N. Tetaz, R. Windpassinger and A. B. Mateo. Wide Band UV/Vis/NIR Blazed-Binary Reflective Gratings for Spectro-Imagers: Two Lithographic Technologies Investigation. *J. Eur. Opt. Society – Rapid Publ.*, 19(1):7, 2023.

[53] DIN 8593-0, Fertigungsverfahren Fügen. Teil 0: Allgemeines, Einordnung, Unterteilung, Begriffe. Beuth, Berlin, 2003.

[54] B. G. Yacobi, S. Martin, K. Davis, A. Hudson and M. Hubert. Adhesive Bonding in Microelectronics and Photonics. *J. Appl. Phys.*, 91(10):6227–6262, 2002.

[55] A. J. Hudson, S. C. Martin, M. Hubert and J. K. Spelt. Optical Measurements of Shrinkage in UV-Cured Adhesives. *J. Electron. Packag.*, 124(4):352–354, 2002.

[56] O. Gerberding, F. Guzmán Cervantes, J. Melcher, J. R. Pratt and J. M. Taylor. Optomechanical Reference Accelerometer. *Class. Quantum Grav.*, 52(5):654–665, 2015.

[57] J. Carter, P. Birckigt, O. Gerberding, Li Qingfeng, R. Strüning, T. Ullsperger and S. Köhlenbeck. An Experiment to Test the Mechanical Losses of Different Bonding Techniques in Fused Silica. *ArXiV PrePrint, Instrumentation and Detectors*, 2022.

[58] Gwo Dz-Hung. Ultraprecision Bonding for Cryogenic Fused-Silica Optics. In *Cryogenic Optical Systems and Instruments VIII*. *Proc. SPIE*, 3435:136–142, 1998.

[59] Gwo Dz-Hung. Ultra Precision and Reliable Bonding Method. Standard Application. *Patent no.* US 6,284,085 B1. The Board of Trustees of the Leland Stanford Junior University, 2001.

[60] E. J. Elliffe, J. Bogenstahl, A. Deshpande, J. Hough, C. Killow, S. Reid, D. Robertson, S. Rowan, H. Ward and G. Cagnoli. Hydroxide-Catalysis Bonding for Stable Optical Systems for Space. *Class. Quantum Grav.*, 22(10):S257–S267, 2005.

[61] A.-M. A. van Veggel and C. J. Killow. Hydroxide Catalysis Bonding for Astronomical Instruments. *Adv. Opt. Technol.*, 3(3):293–307, 2014.

[62] G. KALKOWSKI, S. FABIAN, C. ROTHHARDT, P. ZELLER and S. RISSE. Silicate and Direct Bonding of Low Thermal Expansion Materials. In *Material Technologies and Applications to Optics, Structures, Components, and Sub-Systems*. *Proc. SPIE*, 8837:88370U, 2013.

[63] V. MANGANO, A.-M. A. VAN VEGGEL, R. DOUGLAS, J. FALLER, A. GRANT, J. HOUGH and S. ROWAN. Determination of the Refractive Index and Thickness of a Hydroxide-Catalysis Bond Between Fused Silica from Reflectivity Measurements. *Opt. Express*, 25(4):3196–3213, 2017.

[64] G. KALKOWSKI, C. ROTHHARDT, P.-J. JOBST, M. SCHURMANN and R. EBERHARDT. Glass Direct Bonding for Optical Applications. In *Semiconductor Wafer Bonding 12: Science, Technology, and Applications*. *ECS Trans.*, 50(7):399–405, 2012.

[65] I. W. MARTIN, J. STEINLECHNER, A.-M. A. VAN VEGGEL, Z. TORNASI, A. S. BELL, J. HOUGH and S. ROWAN. Time-Evolution of NIR Absorption in Hydroxide-Catalysis Bonds. *Materialia*, 6(10):100331, 2019.

[66] S. RICHTER, S. NOLTE and A. TÜNNERMANN. Ultrashort Pulse Laser Welding. A New Approach for High-Stability Bonding of Different Glasses. *Phys. Procedia*, 39:556–562, 2012.

[67] A. PLÖSSL and G. KRÄUTER. Wafer Direct Bonding: Tailoring Adhesion Between Brittle Materials. *Mater. Sci. Eng. R Rep.*, 25(1-2):1–88, 1999.

[68] J. HAISMA and G. SPIERINGS. Contact Bonding, Including Direct-Bonding in a Historical and Recent Context of Materials Science and Technology, Physics and Chemistry. Historical Review in a Broader Scope and Comparative Outlook. *Mater. Sci. Eng. R Rep.*, 37(1-2):1–60, 2002.

[69] R. STRUTT (4th Baron RAYLEIGH). A Study of Glass Surfaces in Optical Contact. *Proc. R. Soc. Lond. A*, 156(888):326–349, 1936.

[70] TONG Qin-Yi and U. M. GÖSELE. *Semiconductor Wafer Bonding. Science and Technology*. The Electrochemical Society Series. Wiley, New York, 1999.

[71] M. J. SPARNAAY. Measurements of Attractive Forces Between Flat Plates. *Physica*, 24(6-10):751–764, 1958.

[72] L. L. PAYNE. Optical Contacting of Quartz. NASA/ASEE Summer Fac. Fellowship Program, Huntsville, 1982.

[73] P. BIRCKIGT, K. GRABOWSKI, G. LEIBELING, T. FLÜGEL-PAUL, M. HEUS-INGER, H. OUSLIMANI and S. RISSE. Effects of Static Load and Residual Stress on Fused Silica Direct Bonding Interface Properties. *Appl. Phys. A*, 127(12), 2021.

[74] M. ALEXE and U. M. GÖSELE, editors. *Wafer Bonding. Applications and Technology*, Volume 75 of *Springer Series in Materials Science*. Springer, Berlin, 2004.

[75] P. RAMM, J. J.-Q. LU and M. M. V. TAKLO, editors. *Handbook of Wafer Bonding*. Wiley-VCH, Weinheim, 2012.

[76] G. KALKOWSKI, S. RISSE, U. D. ZEITNER, F. FUCHS, R. EBERHARDT and A. TÜNNERMANN. (Invited) Glass-Glass Direct Bonding. In *Semiconductor Wafer Bonding 13: Science, Technology, and Applications*. *ECS Trans.*, 64(5):3–11, 2014.

[77] G. KALKOWSKI, K. GRABOWSKI, G. HARNISCH, T. FLÜGEL-PAUL, U. D. ZEITNER and S. RISSE. Fused Silica GRISMs Manufactured by Hydrophilic Direct Bonding at Moderate Heating. *CEAS Space J.*, 9(4):433–440, 2017.

[78] T. FLÜGEL-PAUL, C. ROTHHARDT, T. BENKENSTEIN, K. GRABOWSKI, S. RIS-SE, R. EBERHARDT, B. GULDIMANN and U. D. ZEITNER. All-Dielectric Prism-Grating-Prism Component Realized by Direct Hydrophilic Bonding Technology for Optical Applications in Space. In *International Conference on Space Optics*. *Proc. SPIE*, 11180:1118014, 2018.

[79] P. BIRCKIGT, C. ROTHHARDT, K. GRABOWSKI, K. JORKE, R. SCHLEGEL, F. DREISOW, G. KALKOWSKI, S. RISSE and R. EBERHARDT. Plasma-Activated Direct Bonding of Coated Optical Glasses. *Jpn. J. Appl. Phys.*, 59:SBBD01, 2020.

[80] C. ROTHHARDT, S. KLOSE, B. SATZER, S. SCHMIDL, K. GRABOWSKI, P. BIRCK-IGT, E. HILPERT, U. LIPPMANN, R. SCHLEGEL, S. SHESTAEVA, S. SCHWINDE and S. RISSE. Technical Layout and Fabrication of a Compact All-Glass Four-Channel Beam Splitter Based on a Kösters Design. *CEAS Space J.*, 120(866):405, 2022.

[81] J. N. ISRAELACHVILI. *Intermolecular and Surface Forces*. Academic Press, London, 2. edition, 2007.

[82] R. J. GOOD and R. R. STROMBERG, editors. *Surface and Colloid Science. Experimental Methods*, Volume 11. Springer US, Boston, 1979.

124

[83] E. M. LIFSHITZ. The Theory of Molecular Attractive Forces Between Solids. *J. Exp. Theor. Phys.*, 2:73–83, 1956.

[84] D. B. HOUGH and L. R. WHITE. The Calculation of HAMAKER Constants from LIFSHITZ Theory with Applications to Wetting Phenomena. *Adv. Colloid Interface Sci.*, 14(1):3–41, 1980.

[85] T. J. SENDEN and C. J. DRUMMOND. Surface Chemistry and Tip-Sample Interactions in Atomic Force Microscopy. *Colloids Surf. A*, 94(1):29–51, 1995.

[86] B. JANCZUK and A. ZDZIENNICKA. A Study on the Components of Surface Free Energy of Quartz from Contact Angle Measurements. *J. Mater. Sci.*, 29(13):3559–3564, 1994.

[87] I. ZGURA, R. MOLDOVAN, C. C. NEGRILA, S. FRUNZA, V. F. COTOROBAI and L. FRUNZA. Surface Free Energy of Smooth and Dehydroxylated Fused Quartz from Contact Angle Measurements Using Some Particular Organics as Probe Liquids. *J. Optoelectron. Adv. Mater*, 15(7–8):627–634, 2013.

[88] L. BERGSTRÖM. HAMAKER Constants of Inorganic Materials. *Adv. Colloid Interface Sci.*, 70:125–169, 1997.

[89] J. M. FERNÁNDEZ-VAREA and R. GARCIA-MOLINA. HAMAKER Constants of Systems Involving Water Obtained from a Dielectric Function that Fulfills the f Sum Rule. *J. Colloid Interface Sci.*, 231(2):394–397, 2000.

[90] J. W. WHALEN. Thermodynamic Properties of Water Absorbed on Quartz. *J. Appl. Phys.*, 64(10):1676–1681, 1961.

[91] C. G. ARMISTEAD, A. J. TYLER, F. H. HAMBLETON, S. A. MITCHELL and J. A. HOCKEY. Surface Hydroxylation of Silica. *J. Phys. Chem.*, 73(11):3947–3953, 1969.

[92] X. WU, E. SACHER and M. MEUNIER. The Effects of Hydrogen Bonds on the Adhesion of Inorganic Oxide Particles on Hydrophilic Silicon Surfaces. *J. Appl. Phys.*, 86(3):1744–1748, 1999.

[93] D. BASSETT, E. BOUCHER and A. ZETTLEMOYER. Adsorption Studies on Hydrated and Dehydrated Silicas. *J. Colloid Interface Sci.*, 27(4):649–658, 1968.

[94] M. L. HAIR. Hydroxyl Groups on Silica Surface. *J. Non-Cryst. Solids*, 19:299–309, 1975.

[95] P. HOBZA, J. SAUER, C. MORGENEYER, J. HURYCH and R. ZAHRADNIK. Bonding Ability of Surface Sites on Silica and Their Effect on Hydrogen Bonds. A Quantum-Chemical and Statistical Thermodynamic Treatment. *J. Phys. Chem.*, 85(26):4061–4067, 1981.

[96] S. K. RHEE. Surface Energies of Silicate Glasses Calculated from Their Wettability Data. *J. Mater. Sci.*, 12(4):823–824, 1977.

[97] G. SPIERINGS, J. HAISMA and T. M. MICHELSEN. Surface-Related Phenomena in the Direct Bonding of Silicon and Fused-Silica Wafer Pairs. *Philips J. Res.*, 49(1-2):47–63, 1995.

[98] D. TROMANS and J. A. MEECH. Fracture Toughness and Surface Energies of Covalent Minerals: Theoretical Estimates. *Miner. Eng.*, 17(1):1–15, 2004.

[99] H. MORICEAU, F. RIEUTORD, C. MORALES, A. M. CHARVET, O. RAYSSAC, B. BATAILLOU, F. FOURNEL, J. EYMERY, A. PASCALE, P. GENTILE, A. BAVARD, J. MÉZIÈRE, C. MALEVILLE and B. ASPAR. Direct Wafer Bonding for Nanostructure Preparations. *Solid State Phenom.*, 121-123:29–32, 2007.

[100] A. MASOLIN, P.-O. BOUCHARD, R. MARTINI and M. BERNACKI. Thermo-Mechanical and Fracture Properties in Single-Crystal Silicon. *J. Mater. Sci.*, 48(3):979–988, 2013.

[101] S. M. WIEDERHORN, H. JOHNSON, A. M. DINESS and A. H. HEUER. Fracture of Glass in Vacuum. *J. Am. Ceram. Soc.*, 57(8):336–341, 1974.

[102] S. W. MECHOLSKY, J. J., R. W. RICE and S. W. FREIMAN. Prediction of Fracture Energy and Flaw Size in Glasses from Measurements of Mirror Size. *J. Am. Ceram. Soc.*, 57(10):440–443, 1974.

[103] J. P. LUCAS, N. R. MOODY, S. L. ROBINSON, J. HANROCK and R. Q. HWANG. Determining Fracture Toughness of Vitreous Silica Glass. *Scr. Mater.*, 32(5):743–748, 1995.

[104] J. A. SALEM. Transparent Armor Ceramics as Spacecraft Windows. *J. Am. Ceram. Soc.*, 96(1):281–289, 2013.

[105] M. BERTOLDI and V. M. SGLAVO. Influence of Composition on Fatigue Behavior and Threshold Stress Intensity Factor of Borosilicate Glasses. *J. Am. Ceram. Soc.*, 85(10):2499–2506, 2002.

[106] G. D. QUINN and J. J. SWAB. Adventures and Misadventures in Applying ASTM Standard Test Method C 1421 to Measurements of the Fracture Toughness, K_{IC}, of Glasses. In *Mechanical Properties and Performance of Engineering Ceramics and Composites XI*. *Ceramic Engineering and Science Proceedings*, 37(2):29–43, 2017.

[107] P. HOFMANN. *Solid State Physics. An Introduction*. Wiley-VCH, Weinheim, 3. edition, 2012.

[108] C. CRETON and E. PAPON. Materials Science of Adhesives: How to Bond Things Together. *MRS Bull.*, 28(6):419–423, 2003.

[109] K. L. JOHNSON, K. KENDALL and A. D. ROBERTS. Surface Energy and the Contact of Elastic Solids. *Proc. Royal Soc. Lond. A*, 324(1558):301–313, 1971.

[110] K. T. TURNER and S. M. SPEARING. Mechanics of Direct Wafer Bonding. *Proc. Royal Soc. Lond. A*, 462(2065):171–188, 2006.

[111] D. GRIERSON and K. T. TURNER. Characterization of Hysteresis of Surface Energy in Room-Temperature Direct Bonding Processes. In *Semiconductor Wafer Bonding 11: Science, Technology, and Applications*. *ECS Trans.*, 33(4):573–580, 2010.

[112] V. LARREY, G. MAUGUEN, F. FOURNEL, D. RADISSON, F. RIEUTORD, C. MORALES, C. BRIDOUX and H. MORICEAU. Adhesion Energy and Bonding Wave Velocity Measurements. In *Semiconductor Wafer Bonding 14: Science, Technology and Applications*. *ECS Trans.*, 75(9):145–152, 2016.

[113] E. NAVARRO, Y. BRÉCHET, R. MOREAU, T. PARDOEN, J.-P. RASKIN, A. BARTHELEMY and I. RADU. Direct Silicon Bonding Dynamics. A Coupled Fluid/Structure Analysis. *Appl. Phys. Lett.*, 103(3):034104, 2013.

[114] N. IP, N. NEJADSADEGHI, C. FONSECA, N. KOHAMA and K. MOTODA. Multi-Physics Simulation of Wafer-To-Wafer Bonding Dynamics. In *Electronic Components and Technology Conference (ECTC)*. *Proc. IEEE*, 72:502–506, 2022.

[115] E. NAVARRO, Y. BRÉCHET, A. BARTHELEMY, I. RADU, J.-P. RASKIN and T. PARDOEN. Adhesion and Separation Models for Direct Hydrophilic Bonding. *J. Appl. Phys.*, 117(8):085305, 2015.

[116] F. FOURNEL, L. CONTINNI, C. MORALES, J. DA FONSECA, H. MORICEAU, F. RIEUTORD, A. BARTHELEMY and I. RADU. Measurement of Bonding Energy in an Anhydrous Nitrogen Atmosphere and Its Application to Silicon Direct Bonding Technology. *J. Appl. Phys.*, 111(10):104907, 2012.

[117] Ö. VALLIN, K. JONSSON and U. LINDBERG. Adhesion Quantification Methods for Wafer Bonding. *Mater. Sci. Eng. R Rep.*, 50(4-5):109–165, 2005.

[118] V. MASTEIKA, J. KOWAL, N. J. ST. BRAITHWAITE and T. ROGERS. A Review of Hydrophilic Silicon Wafer Bonding. *ECS J. Solid State Sci. Technol.*, 3(4):Q42–Q54, 2014.

[119] W. P. MASZARA, G. GOETZ, A. CAVIGLIA and J. B. MCKITTERICK. Bonding of Silicon Wafers for Silicon-on-Insulator. *Appl. Phys. Lett.*, 64(10):4943–4950, 1988.

[120] J. BAGDAHN, M. PETZOLD, M. REICHE and K. GUTJAHR. Characterization of Directly Bonded Silicon Wafers by Means of the Double Cantilever Crack Opening Method. In *Semiconductor Wafer Bonding: Science, Technology, and Applications IV*. *ECS Trans.*, 97-35:291–298, 1998.

[121] D30 Committee 7905-19, Standard Test Method for Determination of the Mode II Interlaminar Fracture Toughness of Unidirectional Fiber-Reinforced Polymer Matrix Composites. ASTM International, West Conshohocken, PA, 2019.

[122] P. G. CHARALAMBIDES, J. LUND, A. G. EVANS and R. M. MCMEEKING. A Test Specimen for Determining the Fracture Resistance of Bimaterial Interfaces. *Opt. Eng.*, 56(1):77–82, 1989.

[123] T. TABATA, L. SANCHEZ, F. FOURNEL and H. MORICEAU. Reliable Four-Point Flexion Test and Model for Die-To-Wafer Direct Bonding. *J. Appl. Phys.*, 118(1):015301, 2015.

[124] A. R. SHAHANI and S. A. TABATABAEI. Computation of Mixed Mode Stress Intensity Factors in a Four-Point Bend Specimen. *Appl. Math. Model.*, 32(7):1281–1288, 2008.

[125] S. ROHAM and T. HIGHT. Role of Residual Stress on Crack Penetration and Deflection at a Bimaterial Interface in a 4-Point Bend Test. *Microelectron. Eng.*, 84(1):72–79, 2007.

[126] DIN 4760, Gestaltabweichungen; Begriffe, Ordnungssystem. Beuth Verlag GmbH, Berlin, 1982.

[127] B. N. J. PERSSON and M. SCARAGGI. Theory of Adhesion: Role of Surface Roughness. *J. Chem. Phys.*, 141(12):124701, 2014.

[128] ISO 25178-2, Geometrical Product Specifications (GPS). Surface Texture: Areal. Part 2: Terms, Definitions and Surface Texture Parameters. ISO, Genève, 2021.

[129] A. DUPARRÉ, J. FERRE-BORRULL, S. GLIECH, G. NOTNI, J. STEINERT and J. M. BENNETT. Surface Characterization Techniques for Determining the Root-Mean-Square Roughness and Power Spectral Densities of Optical Components. *Appl. Opt.*, 41(1):154–171, 2002.

[130] J. M. BENNETT and L. MATTSSON. *Introduction to Surface Roughness and Scattering*. Optical Society of America, Washington, 2. edition, 1999.

[131] A. CLAUSET, C. R. SHALIZI and M. E. J. NEWMAN. Power-Law Distributions in Empirical Data. *SIAM Rev.*, 51(4):661–703, 2009.

[132] T. D. B. JACOBS, T. JUNGE and L. PASTEWKA. Quantitative Characterization of Surface Topography Using Spectral Analysis. *Surf. Topogr. Metrol. Prop.*, 5(1):013001, 2017.

[133] K. DEVELI and T. BABADAGLI. Quantification of Natural Fracture Surfaces Using Fractal Geometry. *Math. Geosci.*, 30(8):971–998, 1998.

[134] F. V. ZERNIKE. Beugungstheorie des Schneidenverfahrens und seiner Verbesserten Form der Phasenkontrastmethode. *Physica*, 1(7-12):689–704, 1934.

[135] V. LAKSHMINARAYANAN and A. FLECK. ZERNIKE Polynomials: A Guide. *J. Mod. Opt.*, 58(7):545–561, 2011.

[136] TONG Qin-Yi, E. SCHMIDT, U. M. GÖSELE and M. REICHE. Hydrophobic Silicon Wafer Bonding. *Appl. Phys. Lett.*, 64(5):625–627, 1994.

[137] TONG Qin-Yi, Q. GAN, G. HUDSON, G. FOUNTAIN, P. ENQUIST, R. SCHOLZ and U. M. GÖSELE. Low-Temperature Hydrophobic Silicon Wafer Bonding. *Appl. Phys. Lett.*, 83(23):4767–4769, 2003.

[138] J. B. LASKY. Wafer Bonding for Silicon-on-Insulator Technologies. *Appl. Phys. Lett.*, 48(1):78–80, 1986.

[139] TONG Qin-Yi and U. M. GÖSELE. Wafer Bonding and Layer Splitting for Microsystems. *Adv. Mater.*, 11(17):1409–1425, 1999.

[140] S. SPEARING. Materials Issues in Microelectromechanical Systems (MEMS). *Acta Mater.*, 48(1):179–196, 2000.

[141] M. HOWLADER, S. SUEHARA, H. TAKAGI, T. H. KIM, R. MAEDA and T. SUGA. Room-Temperature Microfluidics Packaging Using Sequential Plasma Activation Process. *IEEE Trans. Adv. Packag.*, 29(3):448–456, 2006.

[142] D. ANDO, K. OISHI, T. NAKAMURA and S. UMEDA. Glass Direct Bonding Technology for Hermetic Seal Package. *IEEE Tenth Annual International Workshop on Micro Electro Mechanical Systems*, pages 186–190, 1997.

[143] G. KALKOWSKI, S. RISSE, C. ROTHHARDT, M. ROHDE and R. EBERHARDT. Optical Contacting of Low-Expansion Materials. In *Optical Manufacturing and Testing IX*. *Proc. SPIE*, 8126:81261F, 2011.

[144] M. M. R. HOWLADER, P. R. SELVAGANAPATHY, M. J. DEEN and T. SUGA. Nanobonding Technology Toward Electronic, Fluidic, and Photonic Systems Integration. *IEEE J. Select. Topics Quantum Electron.*, 17(3):689–703, 2011.

[145] E. HIGURASHI. (Invited) Low-Temperature Bonding Technologies for Photonics Applications. In *Semiconductor Wafer Bonding 12: Science, Technology, and Applications*. *ECS Trans.*, 50(7):351–362, 2013.

[146] M. A. SCHMIDT. Wafer-To-Wafer Bonding for Microstructure Formation. *Proc. IEEE*, 86(8):1575–1585, 1998.

[147] T. MAYER, A. N. MARIANOV and D. W. INGLIS. Comparing Fusion Bonding Methods for Glass Substrates. *J. Micromech. Microeng.*, 5(8):085201, 2018.

[148] M. EICHLER, B. MICHEL, P. HENNECKE, M. GABRIEL and C.-P. KLAGES. Low-Temperature Direct Bonding of Borosilicate, Fused Silica, and Functional Coatings. In *Semiconductor Wafer Bonding 11: Science, Technology, and Applications*. *ECS Trans.*, 33(4):339–348, 2010.

[149] C. ROTHHARDT, J. ROTHHARDT, A. KLENKE, T. PESCHEL, R. EBERHARDT, J. LIMPERT and A. TÜNNERMANN. BBO-Sapphire Sandwich Structure for Frequency Conversion of High Power Lasers. *Opt. Mater. Express*, 4(5):1092, 2014.

[150] H. G. STENHOUSE, S. J. BEECHER and J. I. MACKENZIE. Direct Bonding Nd:YAG to Sapphire Wafers. In *Advanced Solid State Lasers*. *Laser Congress 2017*, JM5A:3, 2017.

[151] TONG Qin-Yi, G. CHA, R. GAFITEANU and U. M. GÖSELE. Low Temperature Wafer Direct Bonding. *J. Microelectromech. Syst.*, 3(1):29–35, 1994.

[152] TONG Qin-Yi. Low Vacuum Wafer Bonding. *Electrochem. Solid-State Lett.*, 1(1):52–53, 1999.

[153] M. ITANO, F. W. KERN, M. MIYASHITA and T. OHMI. Particle Removal from Silicon Wafer Surface in Wet Cleaning Process. *IEEE Trans. Semicond. Manufact.*, 6(3):258–267, 1993.

[154] W. KERN. The Evolution of Silicon Wafer Cleaning Technology. *J. Electrochem. Soc.*, 137(6):1887–1892, 1990.

[155] G. KISSINGER and W. KISSINGER. Void-Free Silicon-Wafer-Bond Strengthening in the 200–400 °C Range. *Sens. Actuator A-Phys.*, 36(2):149–156, 1993.

[156] YU Wei Bo, TAN Cher Ming, WEI Jun, DENG Shu Sheng and SHARON NAI MUI LING. Influence of Applied Load on Vacuum Wafer Bonding at Low Temperature. *Sens. Actuator A-Phys.*, 115(1):67–72, 2004.

[157] V. DRAGOI and P. LINDNER. Plasma Activated Wafer Bonding of Silicon: *In Situ* and *Ex Situ* Processes. In *Semiconductor Wafer Bonding 9: Science, Technology, and Applications*. *ECS Trans.*, 3(6):147–154, 2006.

[158] TAN Cher Ming, YU WEIBO and WEI JUN. Comparison of Medium-Vacuum and Plasma-Activated Low-Temperature Wafer Bonding. *Appl. Phys. Lett.*, 88(11):114102, 2006.

[159] XU Jikai, WANG Chenxi, WANG Te, WANG Yuan, KANG Qiushi, LIU Yannan and TIAN Yanhong. Mechanisms for Low-Temperature Direct Bonding of Si/Si and Quartz/Quartz *via* VUV/O_3 Activation. *RSC Adv.*, 8(21):11528–11535, 2018.

[160] WANG Chenxi, XU Jikai, QI Xiaoyun, LIU Yannan, TIAN Yanhong, WANG Chunqing and T. SUGA. Direct Homo/Heterogeneous Bonding of Silicon and Glass Using Vacuum Ultraviolet Irradiation in Air. *J. Electrochem. Soc.*, 165(4):H3093–H3098, 2018.

[161] O. ZUCKER, W. LANGHEINRICH, M. KULOZIK and H. GOEBEL. Application of Oxygen Plasma Processing to Silicon Direct Bonding. *Sens. Actuator A-Phys.*, 36(3):227–231, 1993.

[162] D. PASQUARIELLO, C. HEDLUND and K. HJORT. Oxidation and Induced Damage in Oxygen Plasma *In Situ* Wafer Bonding. *J. Electrochem. Soc.*, 147(7):2699, 2000.

[163] R. BENEYTON, F. FOURNEL, F. RIEUTORD, C. MORALES and H. MORICEAU. Effect of Prebonding Surface Treatments on Si-Si Direct Bonding. Bonding Void

Decrease. In *Semiconductor Wafer Bonding 9: Science, Technology, and Applications*. *ECS Trans.*, 3(6):239–248, 2006.

[164] H. MORICEAU, F. RIEUTORD, C. MORALES and A. M. CHARVET. Surface Plasma Treatments Enabling Low Temperature Direct Bonding. *Microsyst. Technol.*, 12(5):378–382, 2006.

[165] U. MISHRA and G. L. WITT. Wafer Cleaning and Pre-Bonding Module for Wafer Bonding. Defense Technical Information Center, 2007.

[166] T. M. MAYER, E. CHASON and A. J. HOWARD. Roughening Instability and Ion-Induced Viscous Relaxation of SiO_2 surfaces. *J. Appl. Phys.*, 76(3):1633–1643, 1994.

[167] WANG Chenxi, WANG Yuan, TIAN Yanhong, WANG Chunqing and T. SUGA. Room-Temperature Direct Bonding of Silicon and Quartz Glass Wafers. *Appl. Phys. Lett.*, 110(22):221602, 2017.

[168] HE RAN, A. YAMAUCHI and T. SUGA. Sequential Plasma Activation Methods for Hydrophilic Direct Bonding at Sub-200 °C. *Jpn. J. Appl. Phys.*, 57(2S1):02BD03, 2018.

[169] T. SUNI, K. HENTTINEN, I. SUNI and J. MÄKINEN. Effects of Plasma Activation on Hydrophilic Bonding of Si and SiO_2. *J. Electrochem. Soc.*, 149(6):G348–G351, 2002.

[170] MA Xiaobo, LIU Weili, SONG Zhitang, LI Wei and LIN Chenglu. Void-Free Low-Temperature Silicon Direct-Bonding Technique Using Plasma Activation. *J. Vac. Sci. Technol. B*, 25(1):229–234, 2007.

[171] M. EICHLER, B. MICHEL, M. THOMAS, M. GABRIEL and C.-P. KLAGES. Atmospheric-Pressure Plasma Pretreatment for Direct Bonding of Silicon Wafers at Low Temperatures. *Surf. Coat. Technol.*, 203(5-7):826–829, 2008.

[172] H. TAKAGI, K. KIKUCHI, R. MAEDA, CHUNG T. R. and T. SUGA. Surface Activated Bonding of Silicon Wafers at Room Temperature. *Appl. Phys. Lett.*, 68(16):2222–2224, 1996.

[173] R. W. BOWER and F. Y.-J. CHIN. Low Temperature Direct Silicon Wafer Bonding Using Argon Activation. *Jpn. J. Appl. Phys.*, 36(Part 2, No. 5A):L527–L528, 1997.

[174] H. MORICEAU, F. RIEUTORD, C. MORALES, S. SARTORI and A. M. CHARVET. Surface Plasma Activation Before Direct Wafer Bonding: A Short Review and Recent Results. In *Semiconductor Wafer Bonding VIII: Science, Technology, and Applications*. *ECS Trans.*, 05-02:43–49, 2005.

[175] V. DRAGOI, G. MITTENDORFER, C. THANNER and P. LINDNER. Wafer-Level Plasma Activated Bonding: New Technology for MEMS Fabrication. *Microsyst. Technol.*, 14(4-5):509–515, 2008.

[176] T. PLACH, K. HINGERL, S. TOLLABIMAZRAEHNO, G. HESSER, V. DRAGOI and M. WIMPLINGER. Mechanisms for Room Temperature Direct Wafer Bonding. *J. Appl. Phys.*, 113(9):094905, 2013.

[177] M. EICHLER, B. MICHEL, P. HENNECKE and C.-P. KLAGES. Effects on Silanol Condensation During Low Temperature Silicon Fusion Bonding. *J. Electrochem. Soc.*, 156(10):H786–H793, 2009.

[178] S. N. FARRENS. Chemical Free Room Temperature Wafer To Wafer Direct Bonding. *J. Electrochem. Soc.*, 142(11):3949–3955, 1995.

[179] P. AMIRFEIZ, S. BENGTSSON, M. BERGH, E. ZANGHELLINI and L. BÖRJES-SON. Formation of Silicon Structures by Plasma-Activated Wafer Bonding. *J. Electrochem. Soc.*, 147(7):2693–2698, 2000.

[180] M. WIEGAND, G. KRÄUTER and M. REICHE. Effect of O_2 Plasma Pretreatment on the Bonding Behavior of Silicon (100) Wafers. In *Semiconductor Wafer Bonding V: Science, Technology, and Applications*. *ECS Trans.*, 99-35:282–291, 2001.

[181] G. KALKOWSKI, M. ROHDE, S. RISSE, R. EBERHARDT and A. TÜNNERMANN. Direct Bonding of Glass Substrates. In *Semiconductor Wafer Bonding 11: Science, Technology, and Applications*. *ECS Trans.*, 33(4):349–355, 2010.

[182] DU Mao, LI Dongling and LIU Yufei. Investigation of Plasma Activated Si-Si Bonded Interface by Infrared Image Based on Combination of Spatial Domain and Morphology. *Micromachines*, 10(7), 2019.

[183] TONG Qin-Yi, LEE T.-H., U. M. GÖSELE, M. REICHE, J. RAMM and E. BECK. The Role of Surface Chemistry in Bonding of Standard Silicon Wafers. *J. Electrochem. Soc.*, 144(1):384–389, 1997.

[184] A. SANZ-VELASCO, P. AMIRFEIZ, S. BENGTSSON and C. COLINGE. Room Temperature Wafer Bonding Using Oxygen Plasma Treatment in Reactive Ion

Etchers With and Without Inductively Coupled Plasma. *J. Electrochem. Soc.*, 150(2):G155–G162, 2003.

[185] P. W. ATKINS and J. DE PAULA. *Physical Chemistry. Thermodynamics, Structure, and Change*. W. H. Freeman and Company, New York, 10. edition, 2014.

[186] S. ARRHENIUS. Über die Dissociationswärme und den Einfluss der Temperatur auf den Dissociationsgrad der Elektrolyte. *Z. Phys. Chem.*, 4U(1):96–116, 1889.

[187] M. GRUNDNER and H. JACOB. Investigations on Hydrophilic and Hydrophobic Silicon (100) Wafer Surfaces by X-Ray Photoelectron and High-Resolution Electron Energy Loss-Spectroscopy. *Appl. Phys. A*, 39(2):73–82, 1986.

[188] M. SHIMBO, K. FURUKAWA, K. FUKUDA and K. TANZAWA. Silicon-To-Silicon Direct Bonding Method. *J. Appl. Phys.*, 60(8):2987–2989, 1986.

[189] R. STENGL, TAN Te Yuh and U. M. GÖSELE. A Model for the Silicon Wafer Bonding Process. *Jpn. J. Appl. Phys.*, 28(Part 1, No. 10):1735–1741, 1989.

[190] TONG Qin-Yi and U. M. GÖSELE. A Model of Low-Temperature Wafer Bonding and Its Applications. *J. Electrochem. Soc.*, 143(5):1773–1779, 1996.

[191] M. MORITA, T. OHMI, E. HASEGAWA, M. KAWAKAMI and M. OHWADA. Growth of Native Oxide on a Silicon Surface. *J. Appl. Phys.*, 68(3):1272–1281, 1990.

[192] A. G. MILEKHIN, C. HIMCINSCHI, M. FRIEDRICH, K. HILLER, M. WIEMER, T. GESSNER, S. SCHULZE and D. R. T. ZAHN. Infrared Spectroscopy of Bonded Silicon Wafers. *Semiconductors*, 40(11):1304–1313, 2006.

[193] G. KRÄUTER, A. SCHUMACHER and U. GÖSELE. Low Temperature Silicon Direct Bonding for Application in Micromechanics: Bonding Energies for Different Combinations of Oxides. *Sens. Actuator A-Phys.*, 70(3):271–275, 1998.

[194] C. HIMCINSCHI, M. FRIEDRICH, K. HILLER, T. GESSNER and D. R. T. ZAHN. Infrared Spectroscopic Investigations of the Buried Interface in Silicon Bonded Wafers. *Semicond. Sci. Technol.*, 19(5):579–585, 2004.

[195] R. STENGL, AHN K.-Y. and U. GÖSELE. Bubble-Free Silicon Wafer Bonding in a Non-Cleanroom Environment. *Jpn. J. Appl. Phys.*, 27(Part 2, No. 12):L2364–L2366, 1988.

[196] C. GUI, M. ELWENSPOEK, TAS N. and J. G. E. GARDENIERS. The Effect of Surface Roughness on Direct Wafer Bonding. *J. Appl. Phys.*, 85(10):7448–7454, 1999.

[197] N. MIKI and S. M. SPEARING. Effect of Nanoscale Surface Roughness on the Bonding Energy of Direct-Bonded Silicon Wafers. *J. Appl. Phys.*, 94(10):6800–6806, 2003.

[198] F. RIEUTORD, H. MORICEAU, R. BENEYTON, L. CAPELLO, C. MORALES and A.-M. CHARVET. Rough Surface Adhesion Mechanisms for Wafer Bonding. In *Semiconductor Wafer Bonding 9: Science, Technology, and Applications. ECS Trans.*, 3(205):205–215, 2006.

[199] F. FOURNEL, C. MARTIN-COCHER, D. RADISSON, V. LARREY, E. BECHE, C. MORALES, P. A. DELEAN, F. RIEUTORD and H. MORICEAU. Water Stress Corrosion in Bonded Structures. *ECS J. Solid State Sci. Technol.*, 4(5):P124–P130, 2015.

[200] M. TEDJINI, F. FOURNEL, H. MORICEAU, V. LARREY, D. LANDRU, O. KONON-CHUK, S. TARDIF and F. RIEUTORD. Interface Water Diffusion in Silicon Direct Bonding. *Appl. Phys. Lett.*, 109(11):111603, 2016.

[201] C. VENTOSA, F. RIEUTORD, L. LIBRALESSO, C. MORALES, F. FOURNEL and H. MORICEAU. Hydrophilic Low-Temperature Direct Wafer Bonding. *J. Appl. Phys.*, 104(12):123524, 2008.

[202] K. TAKEUCHI and T. SUGA. Quantification of Wafer Bond Strength Under Controlled Atmospheres. *Jpn. J. Appl. Phys.*, 61(SF1010), 2022.

[203] F. FOURNEL, M. TEDJINI, V. LARREY, F. RIEUTORD, C. MORALES, C. BRI-DOUX and H. MORICEAU. Impact of Water Edge Absorption on Silicon Oxide Direct Bonding Energy. *ECS Trans.*, 75(9):129–134, 2016.

[204] S. BENGTSSON and P. AMIRFEIZ. Room Temperature Wafer Bonding of Silicon, Oxidized Silicon, and Crystalline Quartz. *J. Electron. Mater.*, 29(7):909–915, 2000.

[205] M. WIEGAND, M. REICHE and U. M. GÖSELE. Time-Dependent Surface Properties and Wafer Bonding of O₂-Plasma-Treated Silicon (100) Surfaces. *J. Electrochem. Soc.*, 147(7):2734–2740, 2000.

[206] S. KAYA, P. RAJAN, H. DASARI, D. C. INGRAM, W. JADWISIENCZAK and F. RAHMAN. A Systematic Study of Plasma Activation of Silicon Surfaces for Self Assembly. *ACS Appl. Mater. Interfaces*, 7(45):25024–25031, 2015.

[207] T. C. BAKER and F. W. PRESTON. The Effect of Water on the Strength of Glass. *J. Appl. Phys.*, 17(3):179–188, 1946.

[208] S. M. WIEDERHORN. Influence of Water Vapor on Crack Propagation in Soda-Lime Glass. *J. Am. Ceram. Soc.*, 50(8):407–414, 1967.

[209] T. A. MICHALSKE and S. W. FREIMAN. A Molecular Mechanism for Stress Corrosion in Vitreous Silica. *J. Am. Ceram. Soc.*, 66(4):284–288, 1983.

[210] M. PETZOLD, J. BAGDAHN and D. KATZER. Quality and Mechanical Reliability Assessment of Wafer-Bonded Micromechanical Components. *Microelectron. Reliab.*, 39(6-7):1103–1108, 1999.

[211] WANG Chenxi, LIU Yannan, LI Yue, TIAN Yanhong, WANG Chunqing and T. SUGA. Mechanisms for Room-Temperature Fluorine Containing Plasma Activated Bonding. *ECS J. Solid State Sci. Technol.*, 6(7):P373–P378, 2017.

[212] CHEN Wai-Fah and HAN Dan-Jie. *Plasticity for Structural Engineers*. Springer, New York and Berlin, 1988.

[213] L. LANDAU and E. M. LIFSHITZ. *Theory of Elasticity. Translated from Russian by S. B. Sykes and W. H. Reid*, Volume 7 of *Course of Theoretical Physics*. Pergamon Press, Oxford, 2. edition, 1970.

[214] M. F. ASHBY, H. SHERCLIFF and D. CEBON. *Materials. Engineering, Science, Processing and Design*. Butterworth-Heinemann, Amsterdam and Boston, 2007.

[215] S. P. TIMOSHENKO and S. WOINOWSKY-KRIEGER. *Theory of Plates and Shells*. McGraw-Hill, New York, 2. edition, 1959.

[216] E. VENTSEL, T. KRAUTHAMMER and E. CARRERA. *Thin Plates and Shells: Theory, Analysis, and Applications*, Volume 55. Marcel Dekker, New York, 2002.

[217] T. VON KÁRMÁN. Festigkeitsprobleme im Maschinenbau. *Encyklopädie der mathematischen Wissenschaften mit Einschluß ihrer Anwendungen*, 4-4(3):311–385, 1910.

[218] G. KIRCHHOFF. Über das Gleichgewicht und die Bewegung einer elastischen Scheibe. *J. Reine Angew. Math.*, 40:51–88, 1850.

[219] A. E. H. LOVE. *A Treatise on the Mathematical Theory of Elasticity*. Cambridge University Press, Cambridge, 2. edition, 1906.

[220] A. FÖPPL. *Die wichtigsten Lehren der höheren Elastizitätstheorie*, Volume 5 of *Vorlesungen über technische Mechanik*. B. G. Teubner, 1907.

[221] R. M. JONES. *Mechanics of Composite Materials*. Taylor & Francis, New York, 2. edition, 1999.

[222] K. T. TURNER and S. M. SPEARING. Modeling of Direct Wafer Bonding: Effect of Wafer Bow and Etch Patterns. *J. Appl. Phys.*, 92(12):7658–7666, 2002.

[223] W. P. MASZARA, B.-L. JIANG, A. YAMADA, G. A. ROZGONYI, H. BAUMGART and A. J. R. DE KOCK. Role of Surface Morphology in Wafer Bonding. *J. Appl. Phys.*, 69(1):257–260, 1991.

[224] TONG Qin-Yi and U. M. GÖSELE. Semiconductor Wafer Bonding: Recent Developments. *Mater. Chem. Phys.*, 37(2):101–127, 1994.

[225] TONG Qin-Yi and U. M. GÖSELE. Thickness Considerations in Direct Silicon Wafer Bonding. *J. Electrochem. Soc.*, 142(11):3975, 1995.

[226] C. ROTHHARDT. *Plasma-Aktiviertes Fügen von optischen Komponenten für Hochleistungslaser*. Dissertation, Friedrich-Schiller-Universität Jena, Jena, 2019.

[227] G. K. CELLER and S. CRISTOLOVEANU. Frontiers of Silicon-on-Insulator. *J. Appl. Phys.*, 93(9):4955–4978, 2003.

[228] S. H. CHRISTIANSEN, R. SINGH and U. M. GÖSELE. Wafer Direct Bonding: From Advanced Substrate Engineering to Future Applications in Micro/Nano-electronics. *Proc. IEEE*, 94(12):2060–2106, 2006.

[229] J. HAISMA, N. HATTU, J. T. C. M. PULLES, E. STEDING and J. C. G. VERVEST. Direct Bonding and Beyond. *Appl. Opt.*, 46(27):6793–6803, 2007.

[230] H. MORICEAU, F. RIEUTORD, F. FOURNEL, Y. LE TIEC, L. DI CIOCCIO, C. MORALES, A. M. CHARVET and C. DEGUET. Overview of Recent Direct Wafer Bonding Advances and Applications. *Adv. Nat. Sci: Nanosci. Nanotechnol.*, 1(4):043004, 2010.

[231] W. KAPLAN. *Advanced Calculus*. Addison-Wesley, Boston, 5. edition, 2003.

[232] R. L. NORTON. *Machine Design. An Integrated Approach*. Prentice Hall, Boston and Mexico City, 4. edition, 2011.

[233] M. PUJATTI. *Efficient Computation of the Strain Energy Density for the Assessment of Fracture and Fatigue of Welded Structures*. Dissertation, Università degli Studi di Padova, Padova, 2012.

[234] B. B. KIMIA, A. TANNENBAUM and S. W. ZUCKER. On the Evolution of Curves via a Function of Curvature. I. The Classical Case. *J. Math. Anal. Appl.*, 163(2):438–458, 1992.

[235] T. FLIESSBACH. *Mechanik. Lehrbuch zur Theoretischen Physik I*. Springer Berlin Heidelberg, Berlin, Heidelberg, 7. edition, 2015.

[236] J. N. REDDY. *Theory and Analysis of Elastic Plates and Shells*. Series in Systems and Control. CRC Press, Hoboken, 2. edition, 2015.

[237] D. ZWILLINGER. *Handbook of Differential Equations*. Academic Press, San Diego, 3. edition, 1997.

[238] C. MAJIDI and R. S. FEARING. Adhesion of an Elastic Plate to a Sphere. *Proc. R. Soc. A.*, 464(2093):1309–1317, 2008.

[239] T. R. CHANDRUPATLA and A. D. BELEGUNDA. *Introduction to Finite Elements in Engineering*. Prentice Hall, Englewood Cliffs, 2002.

[240] M. FLEMMING and A. DUPARRÉ. Design and Characterization of Nanostructured Ultrahydrophobic Coatings. *Appl. Opt.*, 45(7):1397–1401, 2006.

[241] D. S. HOBBS, B. D. MACLEOD and J. R. RICCOBONO. Update on the Development of High Performance Anti-Reflecting Surface Relief Micro-Structures. In *Window and Dome Techn. and Mater. X*. *Proc. SPIE*, 6545:65450Y, 2007.

[242] S. RICHTER, C. MIESE, S. DÖRING, F. ZIMMERMANN, M. J. WITHFORD, A. TÜNNERMANN and S. NOLTE. Laser Induced Nanogratings Beyond Fused Silica. Periodic Nanostructures in Borosilicate Glasses and ULE^{TM}. *Opt. Mater. Express*, 3(8):1161, 2013.

[243] R. E. YOUNGMAN. *Borosilicate Glasses*, Volume 29. Wiley, 2021.

[244] M. A. HOPCROFT, W. D. NIX and T. W. KENNY. What is the YOUNG's Modulus of Silicon?. *J. Microelectromech. Syst.*, 19(2):229–238, 2010.

[245] J. F. SHACKELFORD and W. ALEXANDER. *CRC Materials Science and Engineering Handbook*. CRC Press, Boca Raton, 3. edition, 2001.

[246] M. N. POLYANSKIY. Refractive Index Database. https://refractiveindex.info. Accessed on 2021-07-21.

[247] SCHOTT Technical Glass Solutions GmbH. Borofloat® 33. General Information and Properties. www.schott.com/borofloat. Accessed on 2021-05-20.

[248] M. AKILIAN and M. L. SCHATTENBURG. Reducing the Warp of Sheet Glass. *J. Soc. Inf. Display*, 18(3):240, 2010.

[249] ZHAO Gaoyang, WEI Zhen, WANG Weilei, FENG Daohuan, XU Aoxue, LIU Weili and SONG Zhitang. Review on Modeling and Application of Chemical Mechanical Polishing. *Nanotechnol. Rev.*, 9(1):182–189, 2020.

[250] C. GUI, M. ELWENSPOEK, J. G. E. GARDENIERS and P. V. LAMBECK. Present and Future Role of Chemical Mechanical Polishing in Wafer Bonding. *J. Electrochem. Soc.*, 145(6):2198–2204, 1998.

[251] E. O. FANIJO, J. G. THOMAS, Yizheng ZHU, Wenjun CAI and A. S. BRAND. Surface Characterization Techniques: A Systematic Review of Their Principles, Applications, and Perspectives in Corrosion Studies. *J. Electrochem. Soc.*, 169(11):111502, 2022.

[252] Hyunung YI. Scanning Acoustic Microscopy for Material Evaluation. *Appl. Microsc.*, 50(1):25, 2020.

[253] ISO 14644-1, Cleanrooms and Associated Controlled Environments. Part 1: Classification of Air Cleanliness by Particle Concentration. ISO, Genève, 2015.

[254] M. D. THOULESS and H. M. JENSEN. Elastic Fracture Mechanics of the Peel-Test Geometry. *J Adhes.*, 38(3-4):185–197, 1992.

[255] L. DE LORENZIS and G. ZAVARISE. Modeling of Mixed-Mode Debonding in the Peel Test Applied to Superficial Reinforcements. *Int. J. Solids Struct.*, 45(20):5419–5436, 2008.

[256] J. W. HUTCHINSON and Z. SUO. Mixed Mode Cracking in Layered Materials. *Adv. Appl. Mech.*, 29(2):63–191, 1991.

[257] Y. BERTHOLET, F. IKER, J. P. RASKIN and T. PARDOEN. Steady-State Measurement of Wafer Bonding Cracking Resistance. *Sens. Actuator A-Phys.*, 110(1-3):157–163, 2004.

[258] ISO 5725-1, Accuracy (Trueness and Precision) of Measurement Methods and Results. Part 1: General Principles and Definitions. ISO, Genève, 2023-07-01.

[259] DIN 1319-1, Grundlagen der Messtechnik. Teil 1: Grundbegriffe. Beuth, Berlin, 1995.

[260] H. JEBSEN-MARWEDEL and R. BRÜCKNER. *Glastechnische Fabrikationsfehler. "Pathologische" Ausnahmezustände des Werkstoffes Glas und Ihre Behebung ; eine Brücke Zwischen Wissenschaft, Technologie und Praxis.* Klassiker der Technik. Springer, Berlin and Heidelberg, 4. edition, 2011.

[261] C. YANG, F. MESS, K. SKENES, S. MELKOTE and S. DANYLUK. On the Residual Stress and Fracture Strength of Crystalline Silicon Wafers. *Appl. Phys. Lett.*, 102(2):021909, 2013.

[262] K. T. TURNER. *Wafer-Bonding. Mechanics-Based Models and Experiments*. Dissertation, Massachusetts Institute of Technology, Cambridge, 2004.

[263] I. D. VRINCEANU and S. DANYLUK. Measurement of Residual Stress in Single Crystal Silicon Wafers. In *International Advanced Packaging Materials Symposium*. *Proc. IEEE*, 2008:297–301, 2008.

[264] K. T. TURNER, S. M. SPEARING, W. A. BAYLIES, M. ROBINSON and R. SMYTHE. Effect of Nanotopography in Direct Wafer Bonding: Modeling and Measurements. *IEEE Trans. Semicond. Manufact.*, 18(2):289–296, 2005.

[265] J. FERRÉ-BORRULL, J. STEINERT and A. DUPARRÉ. Extending the Capabilities of Scanning Probe Microscopy for Microroughness Analysis in Surface Engineering. *Surf. Interface Anal.*, 33(2):92–95, 2002.

[266] J. H. ESPENSON. *Chemical Kinetics and Reaction Mechanisms*. McGraw-Hill, New York, 1981.

[267] J. TELLINGHUISEN. Statistical Error Propagation. *J. Phys. Chem. A*, 105(15):3917–3921, 2001.

[268] F. ROSTOM, A. RØYNE, D. K. DYSTHE and F. RENARD. Effect of Fluid Salinity on Subcritical Crack Propagation in Calcite. *Tectonophysics*, 583:68–75, 2013.

[269] CHEN Liguo, CHEN Tao and SUN Lining. Measurement Method of Bond Strength for Silicon Direct Wafer Bonding. In *2006 IEEE International Conference on Information Acquisition*. *Proc. IEEE*, pages 1021–1025, 2006.

[270] S. J. GRUTZIK, K. T. STRONG and J. M. RIMSZA. Kinetic Model for Prediction of Subcritical Crack Growth, Crack Tip Relaxation, and Static Fatigue Threshold in Silicate Glass. *J. Non-Cryst. Solids: X*, 16(1):100134, 2022.

[271] G. KALKOWSKI, U. D. ZEITNER, T. BENKENSTEIN, J. FUCHS, C. ROTHHARDT and R. EBERHARDT. Direct Wafer Bonding for Encapsulation of Fused Silica Optical Gratings. *Microelectron. Eng.*, 97:177–180, 2012.

[272] E. L. CHURCH. Fractal Surface Finish. *Appl. Opt.*, 27(8):1518–1526, 1988.

[273] K. KOMVOPOULOS and N. YE. Three-Dimensional Contact Analysis of Elastic-Plastic Layered Media With Fractal Surface Topographies. *J. Tribol.*, 123(3):632–640, 2001.

[274] Bing WU and Yunyun SUN. Normal Contact Analysis Between Two Self-Affine Fractal Surfaces at the Nanoscale by Molecular Dynamics Simulations. *Tribol. Lett.*, 71(2):0160101, 2023.

[275] R. BALZER, H. BEHRENS, S. SCHUTH, T. WAURISCHK, S. REINSCH, R. MÜLLER, M. FECHTELKORD and J. DEUBENER. The Influence of H_2O and SiO_2 on the Structure of Silicoborate Glasses. *J. Non-Cryst. Solids*, 519:119454, 2019.

[276] F. FOURNEL, V. LARREY, F. RIEUTORD, C. MORALES, C. BRIDOUX, G. MAUGUEN and S. LOBO. Impact of Multiple Debonding on Adhesion Energy. *ECS Transactions*, 86(5):49–53, 2018.

[277] J. SOHNS. *Modellierung von Transportprozessen in Alkaligläsern*. Dissertation, Universität Ulm, Ulm, 2008.

[278] B. R. LAWN and M. V. SWAIN. Microfracture Beneath Point Indentations in Brittle Solids. *J. Mater. Sci.*, 10(1):113–122, 1975.

[279] B. P. RODRIGUES, C. HÜHN, A. ERLEBACH, D. MEY, M. SIERKA and L. WONDRACZEK. Parametrization in Models of Subcritical Glass Fracture: Activation Offset and Concerted Activation. *Front. Mater.*, 4:1011, 2017.

[280] J. GUILD. Curvature Measurements. *Trans. Opt. Soc.*, 22(3):127–138, 1921.

[281] O. IFAYEFUNMI and J. BŁACHUT. Imperfection Sensitivity: A Review of Buckling Behavior of Cones, Cylinders, and Domes. *J. Press. Vessel Technol.*, 140(5):1, 2018.

[282] J. HURE, B. ROMAN and J. BICO. Wrapping an Adhesive Sphere with an Elastic Sheet. *Phys. Rev. Lett.*, 106(17):174301, 2011.

[283] M. BASS, editor. *Handbook of Optics*, Volume 1. McGraw-Hill, New York, 2. edition, 1995.

[284] N. BEN-TOVIM. Cylinder Dioptometry. *Arch. Ophthalmol.*, 84(3), 1970.

[285] A. OLÁH and G. J. VANCSO. Characterization of Adhesion at Solid Surfaces: Development of an Adhesion-Testing Device. *Eur. Polym. J.*, 41(12), 2005.

[286] YUAN Yue, M. P. HAYS, P. R. HARDWIDGE and KIM Jooyoun. Surface Characteristics Influencing Bacterial Adhesion to Polymeric Substrates. *RSC Adv.*, 7(23):14254–14261, 2017.

[287] M. D. SWIFT, C. B. HAVERKAMP, C. J. STABILE, D. HWANG, R. H. PLAUT, K. T. TURNER, D. A. DILLARD and M. D. BARTLETT. Active Membranes on Rigidity Tunable Foundations for Programmable, Rapidly Switchable Adhesion. *Adv. Mater. Technol.*, 18:2000676, 2020.

[288] S. HEIDE-JØRGENSEN, M. K. BUDZIK and K. T. TURNER. Mechanics and Fracture of Structured Pillar Interfaces. *J. Phys. Chem. Solids*, 137:103825, 2020.

[289] J. M. GERE and B. J. GOODNO. *Mechanics of Materials. Brief Edition*. Cengage Learning, Stamford, 2012.

[290] I. N. BRONSHTEIN, H. MUEHLIG, G. MUSIOL and K. A. SEMENDYAYEV. *Handbook of Mathematics*. Springer, Berlin, Heidelberg, 5. edition, 2007.

[291] P. P. GILLIS and J. J. GILMAN. Double-Cantilever Cleavage Mode of Crack Propagation. *J. Appl. Phys.*, 35(3):647–658, 1964.

[292] W. DEMTRÖDER. *Experimentalphysik II. Elektrizität und Optik*, Volume 2 of *Springer-Lehrbuch*. Springer, Berlin, 5. edition, 2009.

[293] ALAN E. SHAPIRO. Fundamental Problems of 17th-Century Physics: The Nature of Light. *Lecture Notes Presentation*, 2016.

[294] T. BELÉNDEZ, C. NEIPP and A. BELÉNDEZ. Large and Small Deflections of a Cantilever Beam. *Eur. J. Phys.*, 23(3):371–379, 2002.

Declaration of Originality
Selbstständigkeitserklärung

Die Promotionsordnung der Physikalisch-Astronomischen Fakultät der Friedrich-Schiller-Universität vom 20. November 2018 ist mir bekannt. Die vorliegende Dissertation habe ich selbstständig angefertigt. Ich habe keine Textabschnitte eines Dritten oder eigener Prüfungsarbeiten ohne Kennzeichnung übernommen. Ich habe alle von mir benutzten Hilfsmittel, persönlichen Mitteilungen und Quellen in meiner Arbeit angegeben. Dritte haben von mir keine geldwerten Leistungen für Arbeiten erhalten, die im Zusammenhang mit dem Inhalt dieser Dissertation stehen. Ich habe diese Dissertation weder in gleicher noch in ähnlicher Form einer anderen Prüfungsbehörde vorgelegt.

Jena, den 31. Mai 2024   Pascal Birckigt